NUMERICAL MODELLING OF WAVE-CURRENT INDUCED TURBIDITY MAXIMUM IN THE PEARL RIVER ESTUARY

by

WANG CHONGHAO

B. Sc., M. Eng.

A thesis submitted in partial fulfillment of the requirements for the Degree of Doctor of Philosophy

Department of Civil and Structural Engineering

The Hong Kong Polytechnic University

March 2006

CERTIFICATE OF ORIGINALITY

I hereby declare that this thesis entitled **"Numerical Modelling of Wave-Current Induced Turbidity Maximum in the Pearl River Estuary"** is my own work and that, to the best of my knowledge and belief. It reproduces no material previously published or written, nor material which has been accepted for the award of any other degree or diploma, except where due acknowledgement has been made in the text.

Signed

WANG Chonghao

Abstract of thesis entitled

NUMERICAL MODELLING OF WAVE−CURRENT INDUCED TURBIDITY MAXIMUM IN THE PEARL RIVER ESTUARY

Submitted by

WANG Chonghao

for the Degree of Doctor of Philosophy

at The Hong Kong Polytechnic University

March 2006

ABSTRACT

The dissertation describes a study of the hydrodynamics and sediment transport characteristics as well as the formation and development processes of turbidity maximum in the Pearl River Estuary under the interaction of both wave and current through field data analysis and numerical modelling.

Data from a large-scale synchronous hydrographic survey carried out along the main navigational channels are used to study the sediment transport processes in the Pearl River Estuary and subsequently to analyze the formation mechanisms of turbidity maximum. The results show that turbidity maximum widely exists in the Pearl River Estuary and is not only related to the intrusion of salt water, but also to the freshwater runoff from the three western river outlets. Gravitational circulation and tidal trapping are the main causes to form the turbidity maximum in the West Channel. However, turbidity maximum in the East Channel is mainly caused by the sediment resuspension and deposition processes. Sediment input from the Pearl River outlets and tidal Stokes drift are the important factors for the formation of turbidity maximum.

To investigate the horizontal characteristics of hydrodynamics and sediment transport, a depth-integrated 2D model is adopted. The model result is also verified against available measurements in the Pearl River Estuary and good agreement has been obtained. An analysis of computed residual flow shows that the Eulerian component from the non-tidal drift is the dominant one with a maximum velocity of about 0.3 m/s near river outlets, compared with that of the Stokes drift of less than 0.05 m/s. Model results also show that sediment resuspension plays an important role within tidal cycles due to the surplus

sediment-carrying capacity. The sediment concentration in deep channels is smaller than that in the nearby shoals.

With the background knowledge obtained from the data analysis and 2D modelling, a 3D hydrodynamics and sediment transport model is developed based on the work by Wai and Lu (1999 and 2000) to model the turbidity maximum in the Pearl River Estuary. The present 3D model has high efficiency and extended applicability through optimizing the old algorithm and taking into account the baroclinic terms in the momentum equations as well as coupling a level 2.5 turbulence closure scheme with the Navier-Stokes equations. The 3D model is validated comprehensively by comparing the computed tidal level, current, salinity and sediment concentration in a spring tide and a neap tide with available field data and good agreement is obtained.

The 3D model is able to capture the formation and development processes of turbidity maximum in the Pearl River Estuary. Model results show turbidity maximum occurs during spring tides and disappears during neap tides with a cruising range of about 22 km over the sand bars in the main channels. The turbidity maximum fully develops when ebbing during a spring tide in the wet season. Gravitational circulation, tidal pumping and resuspension are the main factors in the formation of turbidity maximum in the wet season. However, local resuspension is the main cause in the dry season.

To study the wave effect, a wave propagation model, developed by Chen (2001), is coupled with the present 3D hydrodynamics and sediment model. Applications in the Pearl River Estuary show that the coupled wave-current model can solve combined wave-current problems efficiently. The computed results show that the island sheltering and shoaling factors significantly influence the propagation of wave into the Pearl River Estuary. Also, the results indicate that the combined wave-current interaction only increases the sediment concentration mainly near the sand bars and in shoals, resulting in a thicker high sediment concentration vertical core in the turbidity maximum without significant modification of the general characteristics of the turbidity maximum including the location and excursion amplitude of the TM. However, the credibility of this result is yet to be verified with field measured data.

ACKNOWLEDGEMENTS

This thesis cannot be completed without the valuable advices from my supervisors. Here, I would like to express my deepest appreciation to my supervisors, Prof. Y.S. Li and Dr. Onyx, W.H. Wai, for their all-round suggestion and guidance to my thesis and for their warmhearted encouragement and support during my Ph.D. study. I am deeply impressed with their profound professional knowledge, precise and aggressive attitude to research, as well as their open-mindedness and friendly characters.

I also want to thank Dr. Y. Chen and Dr. Y.W. Jiang very much for their sharing of modelling experience, and exchange of research idea and achievement.

Special thanks are given to The Hong Kong Polytechnic University and the Hong Kong Research Grants Council for the funding supports.

Particular thanks are due to Prof. C.H. Hu and other colleagues of China Institute of Water Resources and Hydro-power Research, for their supports and the conveniences given to my visa application.

Finally, I am truly indebted to my families for their long-time spiritual encouragement and patience.

CONTENTS

LIST OF FIGURES

LIST OF TABLES

LIST OF NOTATIONS

1. VARIABLES

a	reference height above mean seabed
A	wave action, $A = \dfrac{H^2}{8\omega}$
c	suspended sediment concentration; wave speed
$\bar{c}_0$	tidally mean value of vertically averaged sediment concentration
c_a	near bed reference sediment concentration
$c_{a,c,w}$	bed-boundary concentration by waves and currents
c_b	near bed sediment concentration
C_d	bottom drag coefficient of flow
C_d^w	drag coefficient of air
c_g	wave group speed
Cl	chlorinity
c_v	deviation of sediment concentration at any depth from the vertically averaged value
C_x, C_y	phase speeds along the x and y directions
c_{*b}	near bed sediment-carrying capacity
c_*	vertical-averaged seidment-carrying capacity
d	distance between the ‘sponge’ layer and the boundary in wave model
d_s	‘sponge’ layer thickness in wave model
D	downward sediment flux
D_1	sediment deposition rate to the bed
D_{50}	median diameter of sediment of which 50% by weight is finer

D_*	dimensionless sediment particle parameter, $D_* = D_{50}\left[\frac{(\rho_s-\rho)g}{\rho\upsilon^2}\right]^{1/3}$
e	computational element
E	upward sediment flux
E_1 .	sediment entrainment rate from the bed
f	Coriolis parameter
f_w	wave friction factor
F	coefficient expressing the effect of flocculation to settling velocity
g	gravitational acceleration
H	total water depth; wave height
H_0 , H_t	tidally averaged water depth and its deviation
k	wave number
k_s	bed roughness height
K	modified wave number
l	turbulence macroscale
n	time steps
N	buoyancy frequency
P	pressure
q_s	vertical sediment exchange flux
$q^2/2$	turbulent kinetic energy
Ri	Richardson number
s	salinity of sea water
s_d	relative density of sediment to water
$\bar{s}$	vertical averaged salinity
S	unit-width salinity flux over water column
t	time
T	temperature; tidal period
T_*	bed shear stress parameter, $T_* = \tau_b/\tau_{b,cr} - 1$
u , v , w	velocity components in x , y and z directions
$\bar{u}$, $\bar{v}$	depth-averaged current velocity in the x and y directions

$\bar{u}_0$	tidally mean value of vertically averaged velocity
u_b, v_b	velocity components near seabed in the x and y directions
$u_{b,cr}$	critical bottom threshold current velocity
$\bar{u}_{b,cr}$	vertically averaged critical threshold current velocity
u_n^{γ}	velocity normal to the closed boundary
u_v	deviation of velocity at any depth from the vertically averaged value
u^w, v^w	wind velocity components in the x and y directions
u_*	friction velocity
U_c	near bed current-induced flow velocity
U_w	the near-bed wave orbital velocity amplitude
x, y, z	Cartesian coordinate system
z_0	bottom roughness
z_b	distance from seabed of the first grid nearest to bottom
α	sediment recovery coefficient
α_c	current direction
α_d	deposition probability of the sediment settling to the seabed
α_s	erosion probability of sediment particles from seabed
α_w	wave propagation direction
β	suspension probability of sediment particles,
σ	relative depth from seabed
γ'	dry-bulk density of sediment
$\varepsilon_h, \varepsilon_z$	eddy viscosities in the horizontal and vertical directions
ε_q	eddy diffusion coefficient for turbulence energy
$\varepsilon_{s,h}, \varepsilon_{s,z}$	horizontal and vertical diffusion coefficients of salinity (and sediment)
ζ	tidal level

θ_{cr}	dimensionless parameter, $\theta_{cr} = \dfrac{\tau_{b,cr}}{(\rho_s - \rho) g D_{50}}$
κ	von Kármán constant
ξ	coefficient related to viscosity forces
ρ	density of sea water
ρ_0	constant reference density of water
ρ_a	density of air
ρ_b	density of porous sediment on seabed.
ρ_{b0}	density of consolidated sediment on seabed
ρ_s	density of sediment particle
ρ'	local variation from the reference density
$\tau_b, \tau_{b,x}, \tau_{b,y}$	bottom shear stress and its components in x, y direction
$\tau_{b,cr}$	critical bottom shear stress for erosion
τ_c, τ_w	bottom shear stresses due to the current alone and wave alone
$\tau_m, \tau_{\max}$	mean and maximum combined wave-current induced bottom shear stress
$\tau_{s,x}, \tau_{s,y}$	wind-induced shear stress at water surface in the x and y directions
υ	kinematic viscosity of water
φ	latitude
ϕ	four node isoparametric shape function
ω	wave angular frequency
ω_{D50}	settling velocity of basic sediment particles without flocculation
ω_{F50}	setting velocity of a floc
ω_s	settling velocity of sediment particles
ω_{sb}	settling velocity of sediment particle near bottom
Γ	boundary around the domain
Δ	bed-form height

ΔZ_b	evolution of seabed level
Ω	speed of earth's rotation; computational domain

2. MATRIX AND VECTOR

J	Jacobian matrix
S	vector of salinity, sediment concentration, turbulence turbulent kinetic energy and turbulence macroscale
V	velocity vector
$\boldsymbol{\varepsilon}_{\mathbf{s,h}}$	diffusion coefficients vector
RV	vector of barotropic terms
RS	vector of sediment deposition flux and generation and dissipation of turbulence energy
B	a triangular coefficient matrix
D	stiffness matrix
M	mass matrix

3. ABBREVIATION

1D	One-dimensional
2D	Two-dimensional
3D	Three-dimensional
ELM	Eulerian-Lagrangian method
FDM	Finite difference method
FEM	Finite element method
FND	Finite node method
GJ	Gauss-Jacobian iteration method
CRM	Conjugate residual method
PRD	Pearl River Delta
PRE	Pearl River Estuary
TM	Turbidity maximum

CHAPTER 1

INTRODUCTION

1.1 Background and motivation

An estuary, which connects a river with the open sea, is the transition from the freshwater zone to the saltwater zone, where the complicated physical, chemical, biological and geological processes interact with each other. These special features result in abundant natural resources and distinctive physiognomy. Basically, the estuary is an economic zone with animated human activities. As estuaries are always very important to the national economy, many scientists and researches have paid great attention to study the evolution of estuaries and their hydrodynamics as well as the fate and transport of masses within and across their boundaries.

With the opening to the world since the end of 1970s, China has made tremendous progresses in different aspects of its economy. The importance of estuarine economy and marine economy has been brought out. Numerous hydraulic engineering projects, such as the regulation of estuaries, construction of harbors and navigation channels and coastal protection works, have been undertaken. The study of estuaries has been given great attention in China in the last two decades to support the exploitation of coastal resources. The research includes both important theoretical issues and the solution of engineering problems.

An estuary is a complex natural system, which is not only affected principally by runoff and tidal current, but also by waves, Coriolis force, along-shoal current, bores and so on. Some phenomena, which involve complicated hydrodynamics and mass transport, have not been fully understood. For example, the phenomenon of the turbidity maximum (TM) needs further study to elucidate its formation mechanism.

The TM is a common phenomenon in the fresh-salt water interaction region in many mesotidal or macro-tidal estuaries. The main characteristic of the TM is that the suspended sediment concentration there is markedly higher than that either upstream or downstream. Its position is in general near the apex of the salt intrusion wedge. However, its exact position and magnitude are influenced by many factors, such as the relative intensity of river runoff to tidal dynamics, sediment sources both from river and ocean, sediment particle size distribution, and wind stress for shallower estuaries.

The TM is significant not only because of its high sediment concentration, but also because of its potentially high concentrations of hydrophobic contaminants associated with the sediments, especially with the fine-grained fraction of the sediments.

The suspended sediment concentration in the TM is always very high, and its occurrence always coincides with the deposition of suspended sediments, resulting in the formation of river-mouth bars. Thus the investigation of the TM is helpful to understand the formation and evolution of river-mouth bars and to tackle other related problems, such as estuary regulation and navigation channel maintenance.

The TM in the Pearl River Estuary (PRE) P.R. China has been noticed, and its importance to the PRE has been duly recognized since the 1980s. Some formation mechanisms had also been proposed based primarily on analyzing a limited amount of field data. However, there is obvious inadequacy in our knowledge both in terms of the spatial extent and the degree of impact of the TM in the PRE, because of the complicated influence factors and the scarcity of field measurements. With the rapid economic development in the PRE region and the implementation of the close economic partnership arrangement between Hong Kong and mainland China, the PRE plays a more and more important role in the economic development of the Pearl River Delta (PRD) region. Therefore, it would be beneficial to the sustainable development of the PRE to have a clear understanding of the TM formation mechanisms, including the processes of formation, development and dissipation under the interaction of runoff, tidal current, wave, and salt water intrusion.

Mathematical modelling is now an effective research tool to study hydrodynamics and mass transport after the great advances made in the last three decades. It has been used to solve many complex engineering problems in estuaries successfully. However, it is still a challenging task to apply this technique to the PRE due to the complicated river system and coastline, complex fine cohesive sediment transport mechanisms, and the influence of wave and current. There is an urgent need to develop and perfect a three-dimensional hydrodynamics and mass transport numerical model to study the TM in the PRE and other engineering problems in view of the continuing rapid economic development in the region.

1.2 Objectives of study

The study of the turbidity maximum in the Pearl River Estuary has great significance in both theoretical development and in practical applications. The main objectives of this study are to investigate the characteristics of hydrodynamics and cohesive sediment transport in the large body of coastal waters of the PRE which have complex coastlines, to study the formation mechanisms of the turbidity maximum in the PRE, and to reveal the variations of the turbidity maximum in different seasons under the combined action of wave and tidal current using advanced three-dimensional hydrodynamics and mass transport mathematical models coupled with a turbulence model.

1.3 Outlines of dissertation

This dissertation consists of eight chapters. In the first chapter, the background and motivation to study the turbidity maximum in the Pearl River Estuary using mathematical modelling is introduced, and the objectives of this research are also stated.

Chapter 2 reviews the history of turbidity maximum research, including the previous works on the formation mechanisms of TM, as well as the approaches for studying TM in estuaries.

Chapter 3 is devoted to the formation mechanisms of TM in the PRE. The hydrodynamics, salinity and sediment transport processes in the PRE are studied, making use of field data. The temporal and spatial variations of TM in the PRE are discussed and the net sediment fluxes in the East and West channels are analyzed. By comparing the magnitude of each component of the net sediment fluxes, the contributions of each physical process to the TM in the PRE are discussed. To understand the vertical sediment transport processes, the sediment settling velocity is analyzed by inversely solving the Rouse Profile, and a one-dimensional vertical sediment transport model is used to elucidate the importance of the settling and resuspension mechanism.

In Chapter 4, a two-dimensional vertically integrated model is used to study the general characteristics of hydrodynamics and sediment transport in the PRE. The model is verified by field data obtained in the wet season of 1992 and the dry season of 1993. Tidal and seasonal variations of characteristics of hydrodynamics and sediment transport in the PRE are analyzed based on the computed results and the effects of Coriolis force and surface wind stress on residual flow, salinity and sediment transport are discussed.

Chapter 5 introduces an advanced three-dimensional hydrodynamics and mass transport model, coupled with a 2.5 turbulence model. Hydrodynamics, salinity and sediment concentration during spring and neap tides obtained from the model are extensively validated by field data in the PRE obtained in 1998. Characteristics of hydrodynamics and mass transport are discussed further.

Chapter 6 focuses on the study of temporal and spatial variations of TM in the PRE using the three dimensional model described in Chapter 5. Here, a panorama of modeled TM in the PRE is depicted. Formation and variations of TM with tidal cycle and seasonal changes of freshwater runoff are discussed.

In Chapter 7, a wave propagation model is introduced and coupled with the three-dimensional hydrodynamics and sediment transport model to study the sediment transport and turbidity maximum in the PRE with wave-current interaction.

In Chapter 8, some conclusions on the characteristics of hydrodynamics and mass transport, formation mechanisms of TM in the PRE, and the numerical modelling results are drawn. Lastly, deficiencies of this study are pointed out and recommendations for further research are also proposed.

CHAPTER 2

LITERATURE REVIEW

2.1 Review of TM study

TM is a region in a partially mixed or density-stratified estuary where a higher suspended sediment concentration occurs relative to regions both upstream and downstream (Dyer, 1988; Dyer *et al.*, 2002). TM generally occurs near the upstream limit of the seawater intrusion, which is called the salt intrusion wedge and its position and magnitude vary with the tidal cycles and seasonal variability of the river fresh water flow. TM is widely observed in estuaries in various climate zones of the world. It has an important effect on the finer grain-size sediment transport and on the transport and fate of heavy metals and organisms in the estuarine environment. TM is an important index of the intensity of suspended sediment transportation in a region, where the physical properties of water and suspended matter transform from salt to freshwater characteristics or vice versa. It is characterized by steep gradients of density and suspended sediment concentration. TM consists of fine-grained suspended particles, which move back and forth many times in cycles of deposition and resuspension. Martin *et al.* (1986) indicated that the residence time of the particles that constitute the turbidity maximum is at least several months and probably of the order of years for the Gironde estuary. Finally, some of the particles deposit locally and consolidate during slack tides, and the remainder move out of the estuary to offshore regions to form the submarine coastal delta.

Since Glangeaud (1938) discovered this phenomenon in the Gironde estuary, France, many investigations and researches on TM have been carried out in estuaries of the world. For instance, Chesapeake Bay (Schubel, 1968), Thames estuary (Odd and Owen, 1972), Gironde estuary (Allen, 1973), James estuary (Office, 1980), Weser estuary (Wellershaus, 1981), Columbia River estuary (Gelfenbaum, 1983) and Tamar estuary (Uncles *et al.*, 1985a) had been studied on the turbidity maxima.

2.2 TM study in China

China has long coastlines of over 21000 km and more than 60 estuaries with the length over 100 km. Turbidity maximum is also a common phenomenon in these estuaries. Since the study on the formation and variation of the turbidity maximum in the Changjiang Estuary by Shen *et al*. (1980), Chinese researchers have put great efforts to study the turbidity maximum in the different kinds of estuaries, especially in the Yangtze River Estuary, resulting in some fruitful publications. For examples, He (1983) analyzed the formation of deposition zones inside and outside the Ou Jiang Estuary. Bi and Sun (1984) and Li *et al.* (1999) studied the sediment transport processes and particle size distribution in the turbidity maximum in the Jiao Jiang Estuary. Tian (1986) analyzed the field data to study the formation of turbidity maximum in the Pearl River Estuary. Based on field data, Pang *et al.* (2000) found that the turbidity maximum in the Yellow River Estuary is mainly caused by the numerous riverine sediment, sediment induced density flow, saltwater intrusion and turbulence. More in-depth studies focus on the turbidity maximum in the Yangtze River Estuary with regard to its formation mechanisms and spatial and temporal variations are also available (Shen *et al.*, 1992; Shi and Li, 1995; Pan *et al.*, 1999; Shi and Chen, 2000; Zhu *et al.*, 2004).

Shen *et al*. (2001) opined that both the availability of abundant supply of fine sediment and hydrodynamic forces for sediment convergence are the necessary conditions to form the turbidity maximum in an estuary. Based on the sources and convergence of estuarine fine sediment, Shen *et al*. (2001) also proposed that the turbidity maxima in Chinese estuaries can be classified into five different types, namely: 1) tidally induced with terrigenous sediment sources, e.g. the Yellow River Estuary; 2) induced by saltwater intrusion with terrigenous sediment sources, such as the Pearl River Estuary; 3) induced by combined action of tidally and saltwater intrusion with terrigenous sediment sources, such as the south branch of the Changjiang Estuary; 4) tidally induced with marine sediment sources in some fully mixed estuaries, such as Qiantang Estuary, Ou Jiang Estuary and Jiao Jiang Estuary; and 5) induced by saltwater intrusion with marine sediment sources.

2.3 Formation mechanisms of TM

Because of the significance of the turbidity maximum in an estuary and its complicated hydrodynamic characteristics, researchers have paid great attention to study the formation mechanisms in different estuaries for a long time from the different view points of hydrodynamics, sediment transport, salt intrusion, and chemical and biological processes. The understanding of the mechanisms of turbidity maximum formation has improved progressively.

In general, many former investigators indicated that the turbidity maximum is mainly caused by vertical gravitational circulation (e.g., Hansen and Rattray, 1966; Postma, 1967; Fisher *et al*., 1979). It is well known that in a partially mixed or density-stratified estuary, a two-layer circulation pattern tends to form with the upper layer of fresh river water flowing downstream and a bottom layer of denser seawater flowing slowly upstream. Suspended sediments are carried downstream with the river water and tend to settle down as they reach the deeper and less turbulent parts of the estuary. As the suspended sediments in the upper layer settle toward the bottom, the upstream flowing seawater near the bottom can transport parts of these sediments back upstream. Moreover, where the upstream flow meets the downstream current in a strongly stratified estuary, vertical velocities occur which are relatively larger than those present in non-stratified flows. These vertical velocities carry sediments upward toward the surface where they are then transported downstream and tend to settle down again. These re-circulation results in the convergence of sediments in the lower portion of the water column near the head of the salt intrusion wedge and hence a higher sediment concentration zone, which is called turbidity maximum, occurs.

Postma (1967) gave a particularly lucid account of this hypothesized mechanism. He postulated that the magnitude of the turbidity maximum depends on the amount of suspended materials at both the river and ocean sources, the settling velocity of the sediment, and the strength of the estuarine circulation. Two other processes, flocculation and deflocculation (Ippen *et al*., 1966) have been offered as alternative or contributing mechanisms. At steady state, two-dimensional model developed by Festa and Hansen (1978) demonstrated Postma's hypothesis. In addition, after studying the sediment flux stream functions and the influence of the sediment settling velocity on the turbidity maximum, Festa and Hansen (1978) concluded that the sufficient condition for the development of the turbidity maximum was that the downward sediment flux by particle settling in the seaward portion of the estuary must be sufficient to counterbalance the upward flux due to advection and diffusion. However, their model neglected the influence of the bottom boundary layer on the magnitude of the turbidity maximum, and the simplified assumption of steady-state rendered the model incapable of predicting the variations of the turbidity maximum in an intertidal cycle or neap-spring tidal cycle.

Vertical gravitational circulation qualitatively explains the generation of the turbidity maximum and its relation to the salt seawater intrusion. Hence its location and magnitude depend on the relative magnitude of the freshwater runoff and tidal current. However, Wellershaus (1981) proposed that vertical gravitational circulation cannot cause the TM and it is now accepted by many researchers that vertical gravitational circulation is only one of the main formation mechanisms of TM. It plays an important role in the TM formation in highly stratified or partially mixed estuaries.

Sediment resuspension and deposition are also important factors that have bearing on the existence of the turbidity maximum (Schubel, 1968; Wellershaus, 1981; Gelfenbaum, 1983). The suspended sediment concentration in the turbidity maximum varies by an order of magnitude or more during tidal cycles due to sediment resuspension and deposition. This great variability of the suspended sediment concentration in the turbidity maximum is caused by the tidal asymmetry and the deposition and resuspension of near-bed fluidized mud or bed materials in the location coinciding with the turbidity maximum. Based on the analysis of measurements and with the help of mathematical models, many researchers placed particular emphasis on the importance of the combined effects of gravitational circulation, tidal asymmetry and resuspension on the turbidity maximum in more recent investigations.

The possible importance of the resuspension of bottom sediments by tidal currents on the formation of the turbidity maximum in mesotidal and macrotidal estuaries has been recognized for some time. Allen *et al.* (1980) attributed the formation of the turbidity maximum in the Gironde estuary in France to three tidal processes: (a) asymmetry in the tidal currents in which flood currents exceed ebb currents and high-water slack periods exceed low-water slack periods; (b) suspension of eroded bottom sediments; and (c) the existence of an up-estuary maximum in the tidal currents and thus in the erosion of sediments.

Officer and Nichols (1980) used a simple box model to investigate the behavior of non-conservative quantities in estuaries. After analyzing the sediment flux in estuaries, the conclusion that the turbidity maximum could be caused by a combination of gravitational circulation effects and local resuspension of bottom sediments by tidal currents or by either separately was drawn. Evidently this conclusion also emphasized the importance of the local resuspension on the magnitude of the turbidity maximum. Although turbidity maxima in most mesotidal estuaries can be explained by the combination of gravitational circulation and local resuspension in many cases, other mechanisms have also been put forward. Allen *et al.* (1980) proposed that in an estuary with sharp changes in its geometry, turbidity maximum could even occur in the absence of a gravitational circulation.

Officer (1981) and Dyer (1986, 1988 and 1997) proposed that three processes contributed to the generation and maintenance of the turbidity maximum: vertical gravitational circulation, tidal pumping and sediment dynamics. Vertical gravitational circulation as described above includes barotropic circulation in the seaward direction generally due to the free-surface slope and baroclinic circulation in the riverward direction generally caused by the density gradient. Tidal pumping is caused by the asymmetry of tides. Consequently, there is a preferential movement of sediment, transporting riverward to the head of the estuary until the point where the ebb current due to the river flow becomes dominant. This energy balance point coincides with the null point. But Dyer (1997) also indicated that tidal pumping alone would not lead to the turbidity maximum. It would induce a turbidity maximum only when interacting with sediment settling and re-entrainment during the tidal cycle. Similar conclusions were drawn by Uncles *et al*. (1985b and 1989). Based on the analysis of the measurement data in the Tamar estuary and a tidal resuspension model which ignored density effects but had a spatially independent, runoff dependent (but otherwise time independent) erodibility constant as a single ‘free parameter’, Uncles *et al.* (1985b and 1989) pointed out that the sediment flux due to tidal pumping is much larger than that due to the vertical shear stress. The magnitude of the turbidity maximum corresponds to the relative intensity of tidal current to river flow. High concentrations of suspended sediments in the turbidity maximum at spring tides appear to be a consequence of enhanced resuspension of bed sediments by the strong tidal currents. The location of the maximum is affected by freshwater runoff and may be also affected by both gravitational circulation and intratidal variations in vertical stability within the water column. At the period of neap tides or during larger freshwater runoff, the turbidity maximum in the Tamar estuary seldom occurs because of little tidal pumping and high stratification suppresses the turbulence and reduces local sediment resuspension due to smaller bottom shear stresses. Therefore, Uncles *et al*. (1985b and 1989) concluded that the sediment resuspension and tidal pumping are the major causes of the occurrence of a turbidity maximum in an estuary. The gravitational circulation and intratidal variations in water column stability may also influence the formation and behavior of the turbidity maximum.

Hamblin (1989) also discussed the effect of tidal pumping due to tidal asymmetry on turbidity maximum. After investigating the turbidity maximum in the upper Saint Lawrence estuary by the analysis of field data and simulation of the deposition of fine-grained sediments using a vertical transport model, Hamblin (1989) found that the landward sediment flux in the lower layer is maintained by the ebb-flood asymmetry mechanism. The asymmetry in vertical mixing due to fluctuations in stratification is related to the intrusion of the salt wedge, and the magnitude of the turbidity maximum depends on the local resuspension and vertical diffusion.

With respect to the influence of stratification on the turbidity maximum as mentioned above, Geyer (1993) revealed the importance of the suppression of turbulence by stratification. He stressed that the reduction in turbulence due to stratification greatly enhances the trapping of suspended sediment that occurs at the estuarine turbidity maximum. In moderately and highly stratified estuaries, the turbulent diffusivity decreases markedly between the region upstream of the salinity intrusion, where the turbulence is uninhibited by salt stratification, and the stratified regime within the salinity intrusion, where turbulence is reduced by the inhibitory influence of salt stratification. This reduction in turbulence diffusion results in reduction in the quantity of sediment that can be carried by the flow. Jay and Musiak (1994) supported the above viewpoint. After a harmonic analysis of sediment fluxes using integrated sediment balance between two cross sections in the Columbia River estuary, they suggested that the internal residual and overtide circulations generated by time-varying stratification through a process known as internal tidal asymmetry are primarily responsible for the landward sediment transport on the seaward side of the turbidity maximum located near the upstream limits of the salinity intrusion. Density stratification may enhance particle trapping through its influence on the vertical distributions of both suspended sediment and velocity at various frequencies, because it is the correlation between velocity shear and suspended-sediment stratification in the residual circulation at various tidal frequencies that traps particles.

With further investigations, many more subtle mechanisms for the generation and maintenance of the turbidity maximum in an estuary have been revealed. In fact, the turbidity maximum is the resultant of the energy balance between the riverine and estuarine motions. So far, the generation mechanisms can be summarized as the combination of the following main factors: (1) vertical gravitational circulation due to the intrusion of salt water; (2) tidal pumping due to tidal asymmetry and the sediment settling and scouring lag; (3) sediment deposition and resuspension during tidal cycles and (4) sediment particle trapping due to stratification and turbulence suppression.

However, the hydrodynamic behavior of the turbidity maximum is very complicated. Its location and magnitude are influenced by other factors, which include estuary topography, the type of estuaries, the relative intensity of river discharge to tidal water volume, sediment property in the turbidity maximum such as particle sizes and flocculation and deflocculation, and whether there exists a fluidized mud, and the influence of wave-tidal current interactions. So the establishment of a universal mechanism for the formation of the turbidity maximum in different types of riverine-estuarine systems is very difficult. In a particular estuary, the formation mechanism of the turbidity maximum has its own characteristic features because of the different boundary conditions both at the river outlets and the open sea and particular sediment sources and sediment particle properties. For example, in a macrotidal estuary, because of the topography convergence, tide from the open sea becomes more and more asymmetric riverward, resulting in a great amount of sediment transport from the open sea. In this situation, tidal pumping due to tidal asymmetry may be the predominant factor in the formation of the turbidity maximum. In a highly stratified estuary, due to the vertical density gradient, inhibition of the vertical mixing by stratification near the salt intrusion wedge decreases the upward flux associated with vertical mixing relative to the downward flux of sediment. Sediment particles both from riverine and oceanic sources will be trapped, which leads to the formation of the turbidity maximum. A particular estuary has its distinctive mechanisms of formation and development of the turbidity maximum. Up to now, it is still not possible to establish a complete theory for the formation mechanism of the turbidity maximum that includes all the above-mentioned factors. However, it is still feasible to quantitatively reveal the main characteristics of the turbidity maximum in a particular estuary by theoretical analysis of measurement data and sediment transport mathematical models.

2.4 Methodology for TM study

The core of TM is fine-grained cohesive sediments, so the traditional tools for cohesive sediment research, either they are based on field investigations, experiments, physical modelling, or numerical modelling, are also suitable for the study of TM. Flux analysis and numerical modelling are the most widely used tools for studying TM.

2.4.1 Field data analysis

Field data analysis is an effective approach to disclose the formation mechanisms of the turbidity maximum in an estuary based on systematic field measurements in an estuary. Tian (1986) discussed the formation mechanisms of the turbidity maximum in the Lingding Sea of the PRE by the analysis of longitudinal distribution of barotropic and baroclinic pressures, residual flow patterns and near-bed shear stresses based on observed data. Zhou (1992) and Shen *et al*. (1995) decomposed the sediment flux in the turbidity maximum in the Yangtze River estuary, analyzed the origin of the suspended sediments in it and deduced the causes of its formation. Shi (1993) emphasized the resuspension effects on the formation of the turbidity maximum in the Yangtze River estuary after analyzing the relationship between the vertical diffusion coefficient for sediments and the near-bed sediment concentrations. Field data analysis was also used broadly by many other researchers, such as Jay and Musiak (1994) for Columbia River Estuary, Uncles *et al*. (1998) for the Humber-Ouse Estuary in the

UK, Sylaios and Boxall (1998) for Southampton Water and the Test Estuary and Fettweis *et al*. (1998) for the Scheldt Estuary.

2.4.2 One-dimensional and two-dimensional models

The second approach is to use simple mathematical models. This method was generally used to reveal the predominant mechanisms of the formation of the turbidity maximum and the less important processes were neglected. For example, the turbidity maximum in an estuary is largely induced by the vertical gravitational circulation and tidal pumping due to the tidal asymmetry, so a laterally averaged two-dimensional model is applicable to study the turbidity maximum. Festa and Hansen (1978) first simulated the turbidity maximum in an experimental estuary by a 2D steady state model. The mechanisms of gravitational circulation and salt intrusion wedge and variation of the magnitude and location of the turbidity maximum were revealed successfully. In general, 2D vertical models were used in estuaries with small lateral variations of physical variables. Guan *et al*. (1998) used this kind of models to study both the turbidity maximum of Gironde Estuary in France and Jiaojiang Estuary in China. Some simpler mathematical models were also explored to study the turbidity maximum. Under the assumption that the longitudinal exchanges are small with respect to the vertical exchanges within a tidal cycle, Uncle and Stephens (1989), Hamblin (1989) and Shi and Chen (2000) used an 1D vertical sediment transport model to investigate the resuspension effect on the turbidity maximum in the Tamar estuary, Upper Saint Lawrence estuary and Yangtze River estuary, respectively. Moreover, Officer and Nichols (1980) applied a box model to study the sediment flux in the

Rappahannock estuary and the sediment source of the turbidity maximum in the estuary was revealed.

2.4.3 Three dimensional models

The third approach is to use advanced 3D sediment transport models. Although the simplified 1D and 2D simulations are useful for studying the formation mechanisms of the turbidity maximum, however, they can not simulate the real 3D physical processes. In partially mixed estuaries, especially those with complex topography, physical parameters such as velocity, salinity and sediment concentration vary significantly laterally and vertically, hence a 3D model is required to reproduce the turbidity maximum. Fortunately, with the development of computer hardware and numerical schemes, many effective 3D sediment transport models have been developed (Nicholson and O'Connor, 1986; Sheng and Villaret, 1989; Lin and Falconer, 1996; Wai *et al*., 1996; Wai and Lu, 1999) and applied to study the turbidity maximum (Zhou, 1992; Pickens *et al*., 1993; Wu *et al*., 1998). Recently, sediment transport driven by wave-tidal current interaction has also been studied. However, the researches were mostly focused on the variations of the near bed velocity and bed roughness (Fredsøe, 1984; Qin, 1991; Cao and Wang, 1993; Mimura, 1993; Lian and Zhao, 1998; Fan *et al*., 1999; Marin, 1999). Sediment transport models including real-time coupling of wave and tidal current are scarce. Up to now, no attempt has ever been made by other researchers to use a sediment transport model, taking into account both wave and tidal current, to study the turbidity maximum in an estuary to the best knowledge of the author.

CHAPTER 3

SEDIMENT DYNAMICS
IN THE PEARL RIVER ESTUARY

3.1 Introduction

In this chapter, based on two large scale simultaneous field measurements of current, salinity and suspended sediment concentration, conducted along the East Channel and the West Channel of the Pearl River Estuary (PRE) in the wet season of 1978 (July of 1978) and the dry season of 1979 (March of 1979), the fine cohesive sediment dynamics in the PRE was analyzed. The relationship between the effective settling velocity, bottom shear stress and sediment concentration was studied, and a 1D vertical model was used to study the vertical resuspension mechanism. Furthermore, by analyzing the net sediment flux at different locations of measurement, the characteristics of the turbidity maximum in the PRE, due to its complex and particular topography, are revealed, and the basic formation mechanisms of TM are also studied.

3.2 Pearl River Estuary

Pearl River Delta (PRD), including Hong Kong and Macau, is one of the most important economic zones in South China, (see Fig. 3.1). Through this delta, sediment-laden fresh water from upstream Pearl River flows into the South China Sea through eight outlets, namely from the east to the west, Humen, Jiaomen, Hongqimen, Hengmen, Modaomen, Jitimen, Hutiaomen and, Aimen. The total average annual freshwater runoff and sediment discharge from the outlets are 302 billion m^3 and 83.6 million tons, respectively (Xu *et al*., 1985).

The first four outlets discharge water into the Lingding Sea, which is also traditionally named Pearl River Estuary (PRE). In this study, the PRE is used to refer to the sea area comprising Lingding Sea, and Hong Kong and Macau waters unless otherwise stated.

PRE is a conical shaped estuary (see Fig 3.2) with two open boundaries, and covering more than 2000 km^2 of surface area. The main upstream open boundary, 5 km wide, is located at Humen, which is the largest river outlet in the PRE, and the sea boundary is 30 km wide between Hong Kong and Macau. The longitudinal (north-south) length from Humen to Hong Kong is approximately 65 km. The total average annual freshwater runoff, from Humen, Jiaomen, Hongqimen and Hengmen, is 179.3 billion m^3 (Xu *et al*., 1985). The mean annual runoffs from the four outlets (from east to west) are about 62.0 billion m^3, 58.2 billion m^3, 21.5 billion m^3 and 37.6 billion m^3, respectively (Tong, 1986).

There are two major natural waterways, namely East and West Channel in the PRE, with water depth varying from 5 to 20 m. The rest of the PRE, separated by the two waterways into three shoals, namely East Shoal, Middle Shoal and West Shoal, is generally less than 5 m deep. The sediment discharge from the four river outlets is the major source of sediments in the PRE. Although the largest freshwater runoff is through Humen, over 70 percent of the sediment discharge is from Jiaomen and Hengmen.

Sediments in the PRE are principally transported in the form of suspension. The suspended sediment concentration is lower than that in other major rivers in China. The mean concentration is about 0.172 g/l and the annual flux is about 30.64 million tons. About 92-96% of the suspended sediment is discharged during the wet season, with about 80% of the sediment deposited in the PRE and the remaining transported to the South China Sea (Xu *et al.*, 1985). The median size of the suspended sediment particle is around 21.5 μm. Bedload transport is mainly found in the northwestern part of the PRE and is relatively insignificant compared with the amount of sediment transported in suspension.

The bottom sediment particle sizes vary widely from 2 to 250 μm. Median silts to fine sands (31 μm to 250 μm) are found in the western part and near the sea boundary of the PRE. The bed sediments in other parts of the PRE are mainly made up of clay and silt particles. The dominant sediment classes in the deeper regions (water depth larger than 5 m) and in the shoal regions of the PRE are silty sand (size larger than 63 μm) and silty clay (size less than 63 μm), respectively (Xu *et al*., 1985).

The tide in the PRE is of the asymmetric, semi-diurnal and partially mixed type in which the tidal range of two consecutive tides may have different magnitude. The average tidal range is about 2.0 m, and the largest tidal range is 3.66 m. The tidal current mainly comes from the eastern side and propagates into the PRE through the Victoria Channel, Lamma Channel and the Tonggu Waterway (see Fig. 3.1). The ratios of the annual mean runoff to the tidal flooding discharges are about 0.35, 3.33, 5.14 and 10.36 at Humen, Jiaomen, Hongqimen and Hengmen, respectively (Xu *et al*., 1985). Obviously, tidal current is the dominant hydrodynamic force in the Humen outlet, while river runoff is the principal force in the other three outlets.

Salt water, from the South China Sea during flooding, mixes with the fresh water from the four river outlets, with the degree of mixing depending on the relative strength of runoff to the tidal flow. Salinity varies from 0 to 33 ppt from Humen to the South China Sea. The presence of salt water helps the flocculation of fine cohesive sediments, which often occurs in coastal areas where the salinity is between 3 and 10 ppt (Chen, 2001).

Besides the effects due to fresh water and tidal current, the hydrodynamics in the PRE is also influenced by winds and waves. Based on field measurements near Deep bay, the most frequent wind direction in the wet season is from the E and SE, the stronger winds are from the E and SW, and the highest wind speed is over 40 m/s, which occurs during the passage of typhoons. On average, 1.3 typhoons affect the PRE every summer, creating high wind waves (Xu *et al*, 1995; Chen, 2001). Swells occur much more frequently. According to a one-year wave record collected at Wanshan Islands from October 1991 to September 1992, the percentage of swell occurrence is 97.2%. The most frequent swells are from the SE and ESE directions. The percentage of wave heights between 0.5 m and 1.5 m is 75.8%.

3.3 Field data

A field survey in the PRE was conducted along the two waterways in the wet season of 1978 and in the dry season of 1979 by the Chinese Authority. The aim of this exercise was to obtain a comprehensive database for (1) studying the characteristics of hydrodynamics and sediment transport; and (2) analyzing and predicting the development and evolution of submerged deltas for general planning purposes (Report on hydrological investigation in Lingding Bay, 1982). The measurements comprised tidal level, water depth, flow velocity, suspended sediment concentration, salinity and temperature. Tidal level was recorded by automatic tide-recorders and calibrated by hydrometric gauges twice daily. The velocity profile at each station was measured by a cup-type current meter and a direct-reading current meter. In situ collected water samples at one-hour intervals at five different layers were analyzed in the laboratory to determine the suspended sediment concentration and salinity. A total of six sets of measurements were collected under different freshwater input and tidal conditions. In each set, water samples were collected over two consecutive tidal cycles. Because several floods and typhoons occurred during the measurement period in the wet season of 1978, the data of some sets were discontinuous.

To have a consistent and accurate analysis, measurements collected synchronously in both the East Channel and West Channel in July 1978 from 6:00 9th to 9:00 10th and March 1979 from15:00 27th to18:00 28th are selected for the present analysis. The locations of the field stations are also shown in Fig. 3.2. A summary of the tidally averaged flow rate and sediment concentration is shown in Table 3.1.

Although the field measurement was conducted more than 20 years ago and the PRD region has seen dramatic changes in terms of economic development over the past two decades, the systematic data set is still useful and effective for studying the sediment dynamics and turbidity maximum in the PRE qualitatively because only their intensities, but not the transport patterns, have changed.

Table 3.1 Mean flow rate, suspended sediment concentration and net sediment flux in the PRE

		6:00 9th to 9:00 10th July 1978		15:00 27th to18:00 28th March 1979		Annual mean
		Flow rate (m^3/s)	SSC (g/l)	Flow rate (m^3/s)	SSC (g/l)	Net sediment flux (million tons /years)
Humen	Flooding	16000	0.11	21400	0.36	6.59
	Ebbing	12100	0.10	19800	0.34	
Jiaomen	Flooding	2170	0.12	5360	0.13	12.90
	Ebbing	3750	0.16	4990	0.14	
Hongqimen	Flooding	315	0.095	1360	0.10	5.17
	Ebbing	1240	0.22	1290	0.098	
Hengmen	Flooding	916	0.014	1930	0.059	9.24
	Ebbing	1040	0.27	2140	0.057	

3.4 Sediment dynamics

3.4.1 Sediment processes

Turbidity maximum in the PRE was observed at stations Gu3 to Gu6 in the East Channel and from Gu4 to Gu7 in the West Channel (Tian, 1986). In this study, measurements of tidal current, sediment concentration and salinity at these stations were used to analyze the sediment processes in the PRE.

a. Wet season (July, 1978)

Fig. 3.3 to Fig.3.6 show the contours of current, sediment concentration and chlorinity in the wet season at stations Gu3, Gu6, Gu4 and Gu7, respectively. Tidal current varies with the stages of flooding and ebbing, and the fresh water runoff from the Pearl River outlets. Ebbing velocity is much larger than flood velocity generally. The maximum ebb speed is at the water surface. However, the maximum flood speed is usually at the middle of the water column. At station Gu3, the current is much more uniform vertically during flooding than during ebbing. The maximum velocities are about 0.85 m/s and 1.5 m/s, and the velocity differences from bottom to surface are about 0.1 m/s and 0.8 m/s during flooding and ebbing, respectively. Salt water starts to intrude into the bottom layer during tidal flooding about 3 hours after the lower tidal slack and disappears 7 hours after the start of ebbing. The maximum chlorinity is about 5.5 ppt at the bottom of the water column, occurring about 1 hour after the high slack. The station is located near the head of the salt water wedge in the East Channel, with salt water only present in the lower water column. The sediment concentration is less than 0.05 g/l during flooding. However, its value could reach 0.45 g/l at the bottom layer during maximum ebbing. The maximum sediment concentration lags the occurrence of the maximum velocity during ebbing by one hour, and occurs when the salt water disappears. That implies sediment resuspension at this station is suppressed during the intrusion of salt water, and sediment is mainly from upstream sources and local resuspension.

At station Gu6, the maximum velocities during flooding and ebbing are about 1.0 m/s and 2.2 m/s, and the maximum velocity differences along the water column are about 0.4 m/s and 1.3 m/s from bottom to water surface, respectively. Salt water intrudes all the time into the entire water column during high slack and at the lower water column during low slack. The maximum chlorinity is about 11 ppt, occurring at about one hour after the high slack. Obviously, the stratification of the water column at this station is much higher than that at station Gu3. The characteristic of the sediment concentration at this station is thus different from that at station Gu3. The maximum suspended sediment concentration is about 0.36 g/l, occurring during tidal flooding, which implies more sediment particles were transported from the open sea to this station.

Stations Gu4 and Gu7 are located along the West Channel. The tidal current and the mass transport are affected to a great extent by the strong fresh water input from the three western outlets in the PRE. At station Gu4, maximum velocities of 0.9 m/s and of 1.4 m/s are found at the lower layer during flooding and the surface layer during ebbing, respectively. Sediment concentration varies with the stage of the tidal flooding and ebbing, and sediments can be resuspended from the seabed. However, the maximum sediment concentration is about 0.35 g/l occurring near the middle of the water column during ebbing, which is a little larger than the simultaneous concentration at the bottom. Hence, it is reasonable to say that the sediment there comes from river water upstream, supplemented by local resuspension. With the saltwater intrusion, the sediment concentration decreases quickly to less than 0.10 g/l. The station is located near the head of the salt water wedge in the wet season. Saltwater could still intrude into the lower water column at this station, with maximum chlorinity of about 3 ppt after the high slack. Station Gu7, relatively farther away from the western outlets, is also heavily affected by the strong freshwater runoff. The maximum velocities during flooding and ebbing are about 0.9 m/s and 1.9 m/s, respectively. A large velocity difference of about 1.2 m/s along the water column occurs during ebbing. The maximum sediment concentrations during flooding and ebbing are 0.22 g/l and 0.36 g/l, respectively. The high sediment concentration also occurs 1 hour after the disappearance of the salt water. The maximum chlorinity is about 12 ppt occurring around high slack. The saltwater recession after the low slack lasts for about 3 hours.

b. Dry season (March, 1979)

Fig. 3.7 to Fig. 3.10 show the contours of current, sediment concentration and chlorinity in the dry season at Gu3, Gu6, Gu4 and Gu7, respectively. In the dry season, the flow rates of freshwater from the Pearl River outlets weaken; hence saltwater could intrude further upstream, resulting in fully mixed water columns and more uniform vertical velocity profiles. Consequently, the sediment concentrations during flooding are generally larger than those during ebbing, which mean that sediment particles are transported landward. At station Gu3, the maximum velocities during flooding and ebbing are about 1.0 m/s and 2.0 m/s, respectively. The corresponding vertical velocity differences are 0.2 m/s and 0.7 m/s. The sediment concentration at this station reaches 1.0 g/l during maximum flooding. However, the maximum sediment concentration during ebbing is only 0.6 g/l. Salinity at this station is uniform vertically with a maximum chlorinity of about 16 ppt, except during the low slack when a small vertical salinity gradient appears. At station Gu6, the maximum velocities during flooding and ebbing are 1.2 m/s and 1.4 m/s, respectively. The sediment concentration during flooding with the maximum value of 0.44 g/l is also larger than that during ebbing period.

Chlorinity at this station is very uniform vertically, with a maximum chlorinity of about 18 ppt. At station Gu4, the maximum velocities during flooding and ebbing are 1.4 m/s and 1.8 m/s, respectively. The maximum sediment concentration is 0.2 g/l during flooding and the maximum chlorinity is about 17 ppt., the effect of freshwater runoff at station Gu7 is larger compared with that at the other three stations. This station has greater vertical gradients of velocity and salinity. The maximum velocities during flooding and ebbing are about 1.2 m/s and 2.0 m/s, respectively. The corresponding vertical velocity differences are about 0.6 m/s and 1.0 m/s. The sediment at this station is affected both by the river runoff and the tidal flow. Every flooding and ebbing process can cause a similar high sediment concentration at the bottom layer, around 0.55 g/l.

3.4.2 Locations of turbidity maximum

Fig. 3.11 shows the tidally averaged longitudinal distributions of suspended sediment concentration and chlorinity (salinity s /chlorinity Cl relationship: $s = 1.80655Cl$) in the East and West channels. The figures clearly reveal the existence of TMs along both the channels in the different seasons. In the wet season (Fig. 3.11a, b), due to the effect of the strong freshwater runoff, saltwater intrusion is suppressed, with stratification occurring downstream of stations Gu3 and Gu4. In the East Channel, two TMs have been observed. One is located upstream of the salt water wedge and the other is just adjacent to the wedge. The locations of the two tidally averaged TMs are near station Gu1 and station Xun22, which are about 12 and 31 km downstream of the Humen outlet, respectively. The two tidally averaged TMs in the West Channel are located between stations Xun12 and Gu4, and near station CS4, which are about 20 and 47 km downstream of the Humen outlet, respectively. Two regions with relatively lower sediment concentration can be found in the upper layer of the saltwater wedge. This may be attributed to the increased settling velocity of fine sediment particles where enhanced flocculation is taking place in the region between fresh water and salt water. It may also be the result of tidal trapping due to salinity stratification. In the dry season, the runoff from the outlets is weak and brackish water could intrude into the up-estuary region. The chlorinity at station Dahu is higher than 3 ppt. Tidal currents become the major forcing in this season. In general, the estuary in the dry season is well mixed, especially in the reaches upstream of Gu3 and Gu4 in the East and West channels, respectively. However, downstream of Gu3 and Gu4, moderate salinity stratification is also observed in both channels which is caused by the freshwater runoff from the three western Pearl River outlets. Besides the existence of TM located near station Dahu, there exists another TM located around Gu3 in the East Channel, which is about 25 km downstream from Humen, and between stations Gu4 and Gu7 in the West Channel. Each identified TM is labeled in Fig. 3.11.

3.4.3 Tidally averaged sediment transport profiles

The locations of TMs in the PRE can also be roughly determined from the shapes of the vertical profiles of the sediment transport flux, which is the product of the velocity and sediment concentration profiles (Fig. 3.12). In a short reach, if the sediment flux changes direction from landward to seaward or vice versa, this indicates the possibility of the merger of two turbid water zones and consequently the formation of a turbidity maximum. Fig. 3.12 shows that sediment is transported seaward uniformly in the entire water column at stations Dahu and

Gu3 in the wet season. However, further downstream from station Xun22 in the East Channel and station Gu4 in the West Channel onwards, sediment in the lower layer is transported back landward. Stations Xun22 and Gu4 are situated at the core and at the front of saltwater wedges, respectively. This suggests that the formations of TM2 and TM4 are closely related to the intrusion of salt water in the wet season. Sediment is transported landward at station Gu1. This means that the flow upstream of the two channels is greatly influenced by the freshwater runoff from Jiaomen.

In the dry season, because salt water intrudes all the way upstream of the PRE into Dahu channel, the net sediment transport in the lower layer is in the landward direction in all stations. This suggests that TM may occur upstream of Dahu channel as well. The formation of TM5 in Fig. 3.11 can be related to the saltwater intrusion. However, two TMs, which are namely TM6 and TM7, also occur in the middle reaches of the two navigational channels as shown in Fig. 3.11(c) and (d). It is observed from Fig. 3.12(b) that the magnitude of the near bed landward sediment transport reaches maximum at stations Gu3 in the East Channel and at Gu4 in the West Channel. These two stations correspond with the locations of TM6 and TM7 in the dry season. From Fig. 3.11(c), (d) and Fig. 3.12(b), it can be found that the formation of TMs in the middle reaches of the East and West channels is related to the stratification due to the freshwater runoff from the three western river outlets, although this stratification is less intensive than that in the wet season.

3.4.4 Net sediment transport flux analysis

3.4.4.1 Methodology

Based on the method of mass transport flux suggested by Dyer (1997), neglecting the short period turbulence, velocity u and sediment concentration c at any depth could be written as

$$u = \overline{u} + u_v \quad \text{and} \quad c = \overline{c} + c_v \tag{3.1}$$

where u_v and c_v are the deviations at any depth from the mean values $\overline{u} = \frac{1}{H}\int_0^H udz$ and $\overline{c} = \frac{1}{H}\int_0^H cdz$, H is the total water depth from water surface to bottom, and z is the vertical coordinate.

Because of tidal fluctuations, $\overline{u}$ and $\overline{c}$ will vary over tidal cycles. Consequently, $\overline{u}$ and $\overline{c}$ can be expressed by the sum of tidally averaged value and its deviation, $\overline{u} = \overline{u}_0 + \overline{u}_t$ and $\overline{c} = \overline{c}_0 + \overline{c}_t$, where

$$\overline{u}_0 = \frac{1}{T}\int_0^T \overline{u}dt \quad \text{and} \quad \overline{c}_0 = \frac{1}{T}\int_0^T \overline{c}dt \tag{3.2}$$

and T is the tidal period. $\overline{u}_0$ and $\overline{c}_0$ are the mean values of vertically averaged velocity and sediment concentration over a tidal cycle, respectively. $\overline{u}_t$ and $\overline{c}_t$ are the corresponding deviations of vertically averaged values from the means.

The diagrammatic representation of decompositions of velocity along the water column and over a tidal cycle are depicted in Fig. 3.13.

The instantaneous flux of sediment through a unit width of a section perpendicular to the mean flow is given by

$$F = \int_0^H ucdz = \int_0^1 Hucd\sigma \tag{3.3}$$

where σ is the relative water depth from seabed ($\sigma = 0$) to the water surface ($\sigma = 1$).

Averaging Eq. (3.3) over tidal cycles, the net sediment flux can be partitioned into seven major components as given by the following equation.

$$\begin{aligned}\langle F \rangle &= \frac{1}{T}\int_0^T \int_0^1 Hucd\sigma dt \\ &= H_0 \bar{u}_0 \bar{c}_0 + \bar{c}_0 \langle H_t \bar{u}_t \rangle + \bar{u}_0 \langle H_t \bar{c}_t \rangle + H_0 \langle \bar{u}_t \bar{c}_t \rangle + \langle H_t \bar{u}_t \bar{c}_t \rangle + H_0 \langle \overline{u_v c_v} \rangle + \langle \overline{H_t u_v c_v} \rangle\end{aligned} \tag{3.4}$$

T1 T2 T3 T4 T5 T6 T7

where the bracket $\langle \; \rangle$ denotes the tidally averaged value of a vertically integrated variable; the over bar denotes the vertically averaged value; $H = H_0 + H_t$ where H_0 and H_t are tidally averaged water depth and its deviation, respectively.

The first term T1 is the flux due to the non-tidal drift, resulting from the Eulerian velocity. T2 is the flux due to Stokes drift, which results from the correlation between the deviations of the water depth and the vertically averaged velocity from their corresponding tidally averaged concentration values. Together these two terms provide the downstream advective sediment flux, which is the total flux due to the Lagrangian velocity (Zhou, 1992; Shen *et al.*, 1995). T3, T4, and T5 are the tidal pumping terms that are produced by the phase differences

(Dyer, 1997). T3 is the correlation term between the tidal level and sediment concentration. T4 mainly arises from the consequence of the sediment erosion threshold and its time lag, which is the result of sediment resuspension and deposition. T5 is the correlation term between the tidal level, velocity and sediment concentration, and it expresses the role of tidal trapping (Shen *et al.*, 1995). T6 is the vertical gravitational circulation, arising from the correlation between the landward bottom mean flow with high near-bed sediment concentration and the seaward mean surface flow with lower concentration. T7 arises from the changing forms of the vertical profiles of velocity and concentration within the tide, mainly due to the scour and settling lags. In this study, Eq. 3.4 is used to compute the sediment sources for the identification of the formation mechanisms of TM in the PRE.

3.4.4.2 Net sediment transport flux

To quantitatively investigate the physical processes that generate TM in the PRE, the partitioned net sediment fluxes calculated by Eq. 3.4 over two tidal cycles have been analyzed in detail.

Table 3.2 and Table 3.3 list the components of tidally averaged sediment transport flux calculated per unit width in the wet and dry seasons, respectively. In the tables, positive values represent the seaward net sediment transport and negative values denote the landward net sediment transport. Stokes drift is always in the direction of wave or tidal propagation, and brings sediment particles from the open sea into the estuary. Therefore, the net sediment fluxes due to Stokes drift, i.e. term T2 in Table 3.2 and Table 3.3, are negative.

Table 3.2 Components of net sediment flux in the wet season, 1978

	Stations	T1	T2	T3	T4	T5	T6	T7	Total
Humen	Dahu	100.3	-19.1	0.6	3.2	-1.2	-2.8	0.2	81.2
Channel	Gu1	-81.8	-27.2	-0.2	-18.7	-6.9	9.2	0.5	-125.1
East	Gu3	77.2	-20.4	-2.2	155.5	-7.7	-7.7	0.5	195.3
Channel	Xun22	102.9	-18.8	-3.7	137.2	-16.5	-22.3	0.5	179.3
	Gu6	74.9	-18.8	1.3	-31.5	-4.0	-3.4	1.3	19.8
	CS2	57.7	-10.5	-1.9	45.5	-3.0	-6.5	1.7	82.9
West	Gu4	53.1	-28.0	-1.1	46.0	-9.2	-7.5	0.4	53.8
Channel	Gu7	44.9	-9.5	-0.9	-13.5	-8.8	-10.0	2.3	4.5
	CS4	-17.0	-14.6	0.2	53.7	-1.8	-17.3	2.2	5.5

Unit: g/s/m

Table 3.3 Components of net sediment flux in the dry season, 1979

	Stations	T1	T2	T3	T4	T5	T6	T7	Total
Humen	Dahu	226.1	-62.9	0.9	-157.4	-13.5	-31.0	2.6	-35.2
Channel	Gu1	-39.5	-25.2	0.3	33.7	-4.4	-0.4	0.8	-34.8
East	Gu3	419.2	-88.7	2.4	-289.4	-10.5	-46.6	4.6	-9.0
Channel	Gu6	208	-75.9	1.1	-99.4	-3.9	-7.8	1.0	23.0
	CS2	124.8	-41.8	-0.5	-38.2	-7.1	-5.7	3.3	34.8
West	Gu4	-3.1	-68.6	0.0	15.4	-3.3	-10.5	1.8	-68.1
Channel	Gu7	193.5	-71.3	-0.8	59.8	-6.0	-33.5	6.2	147.9
	CS4	33.1	-36.2	0.1	-83.3	-2.0	0.9	0.7	-86.7

Unit: g/s/m

Fig. 3.14 shows the variations of each component along the two deep channels and Humen channel. Since the contributions of T3 and T7 to the net sediment transport are small (less than 1% of the total flux contribution), these two terms are not shown in Fig. 3.14.

a. Wet season (July, 1978)

In the wet season, sediment is generally transported seaward at all stations except in the regions near stations Gu1 and Xun12. The Eulerian advection component T1 (due to river runoff) conveys sediment to the open sea. Its contribution is between 33.1% and 96.1% of the total seaward sediment flux. However, at station Gu1 (in the East Channel), station Xun12 and station CS4 (in the West Channel), T1 is in the landward direction. The locations of these stations clearly correlate with the locations of several TM, labeled as TM1, TM3 and TM4 in Fig. 3.11. Landward transport of sediment at Gu1 and Xun12 are caused by the freshwater runoff with slightly higher sediment concentration at Jiaomen as compared with that from Humen as shown in Table 3.1. The intrusion of salt water is limited downstream of station Xun12.Thus, the landward sediment transport due to the mechanisms of T1, T2 and T4 causes the occurrence of TM1 near station Gu1 and TM3 near station Xun12. The contributions of T1, T2 and T4 to the total sediment fluxes are 60.0%, 30.0% and 13.7% at station Gu1, and about 14.3%, 23.7% and 45.2% at station Xun12, respectively. This implies that TM1 is predominantly caused by the river runoff. On the other hand, sediment resuspension and deposition (T4) is the predominant formation mechanism of TM3.

The presence of Neilingding Island is the main cause for the formation of TM4. The landward direction of T1 flux at station CS4 is the result of the clockwise flow around Neilingding Island in the wet season (Wang *et al.*, 1992). At this station, T4 is the only flux transporting sediment to the open sea. The contributions of the landward fluxes, T1, T2, T5 and T6, to the total sediment transport are of 16.2%, 14.0%, 1.7% and 16.6%, respectively. In fact, Eulerian advection, Stokes drift and gravitational circulation play almost equally important roles in the formation of TM4.

TM2 is located near station Xun22 where T1 and T4 are in the seaward direction and the landward sediment transport is attributed to T2, T5 and T6. The contributions of the seaward fluxes, T1 and T4, are 34.5% and 46.1% of the total sediment flux, respectively, and of landward fluxes, T2, T5 and T6 are about 6.3%, 5.3% and 7.5%, respectively. Because the location of station Xun22 is near the head of the saltwater wedge, sediment particles are trapped. The magnitudes of the different sediment flux components reveal the important role of the combined action of tidal trapping and gravitational circulation in the formation of TM2. The other important mechanism of TM2 formation is the flux reversal of T4 from seaward at station Xun22 to landward at station Gu6, resulting in the convergence of sediment particles in the reach between station Xun22 and station Gu6.

b. Dry season (March, 1979)

In the dry season, the freshwater runoffs from the river outlets are much weaker, so the salt water can intrude all the way into Dahu channel and sediments can as well be carried into the estuary from the South China Sea (Xu *et al*., 1985).

Fig. 3.14 (b) shows that T1, due to the Eulerian advection, is the only flux transporting sediment out of the Dahu Channel. On the other hand, Stokes drift (T2) plays an important role in preventing sediment from being transported to the open sea and is also the main transporting agent that carries sediment from the open sea into the estuary in the dry season. Because the formation of TM is related to the intrusion of salt water, the occurrence of TM5 in Dahu channel is anticipated. However, there is no information upstream of the station Dahu; hence the spatial extent of the TM inside Dahu channel is not known.

TM6 is located near station Gu3, where T2, T4, T5 and T6 are in the landward direction. The contributions of these four fluxes to the total sediment transport are 10.4%, 33.9%, 1.2% and 5.4%, respectively. This indicates that the occurrence of TM6 is mainly due to the sediment resuspension and deposition activities (T4) at that location. The gravitational circulation also plays a role due to the moderate stratification caused by the freshwater input from the three western river outlets. Furthermore, the mixing process between the higher sediment concentration runoff from Humen and the lower sediment concentration runoff from Jiaomen leads to a relatively high sediment concentration belt located near Gu3. This is also one of the reasons that TM6 is quite prominent in the East Channel in the dry season.

In the reach between stations Gu4 and Gu7 in the West Channel where TM7 is located, T4 transports sediment seaward because of the runoff from the three western river outlets. The runoff has a greater impact on the West Channel than on the East Channel. At stations Gu7, Stokes drift (T2), tidal trapping (T5) and gravitational circulation (T6) convey sediment landward, contributing 19.6%, 1.6% and 9.2% to the total sediment transport, respectively. The Stokes drift and gravitational circulation are the major formation mechanisms of TM7.

3.5 Settling velocity

Within the TM of an estuary, there is a considerable increase in the suspended sediment concentration above background levels. Since the size of the flocs increases with concentration, it can therefore be anticipated that the sizes of the flocs will also increase in the TM. Even though the larger flocs are more porous and have a lower effective density, these macro flocs nevertheless have a greatly enhanced settling velocity, thereby contributing significantly to sediment deposition. This settling flux is a crucial factor in sediment accumulation and morphological change, and many mathematical models have been developed to predict its magnitude. There is also a large amount of laboratory and fieldwork devoted to identifying the relationship between the size and the settling velocity. Since the distribution of floc sizes may change with both concentration and shear, it is a challenging task to estimate the settling velocity from the floc aggregation and break-up processes.

Although mechanisms of flocculation and disaggregation are very complex, the effective settling velocity has to be estimated as accurately as possible because it is an important parameter for studying sediment dynamics in estuaries. Many researchers have devoted a lot of efforts to study the settling velocity of fine-grained sediment particles (Dyer, 1989; Lick *et al*., 1993; Fennessy *et al*., 1994). However, most of the findings were obtained from experiments in particular estuaries at very low velocity condition. This greatly limits the applicability of these equations to other estuaries. Up to date, very few studies on the settling velocity in the PRE have been conducted.

A simple and effective approach to estimate the settling velocity is to assume that the distribution of sediment concentration throughout the water column can be described by the Rouse profile. Zhou (1992) and Orton and Kineke (2001) used this method to estimate the effective settling velocity. After comparing several methods for estimating the settling velocity, Orton and Kineke (2001) concluded that the use of the Rouse profile could provide an acceptable alternative to the in situ measurement approach, in addition to a convenient means for parameterization of the concentration profile for 2D numerical modelling.

If it is assumed that under quasi-steady condition the settling flux of suspended sediment is balanced by the upward flux of sediment resulting from turbulent diffusion and a further assumption is made that the eddy diffusivity is of the parabolic form,

$$\varepsilon_z = \kappa u_* z\left(1 - \frac{z}{H}\right) \tag{3.5}$$

where ε_z is the vertical eddy viscosity, H is the water depth, z is the height above bed, κ is von Kármán constant (=0.4), and u_* is the friction velocity. Then it can be shown that the suspended sediment concentration profile is of the form:

$$\frac{c}{c_a} = \left[\frac{z(H - z_a)}{z_a(H - z)}\right]^{\frac{\kappa u_*}{\omega_s}} \tag{3.6}$$

where subscript a denotes the value at the near-bed reference height..

Some sediment concentration profiles are shown in Fig. 3.15 in the logarithmic scale. It can be seen that the measured sediment concentration profiles can be approximately described by the Rouse profile during both flooding and ebbing. However, during the transition period between flooding and ebbing, the sediment concentration cannot be described by Eq. 3.5 as expected. Fig. 3.16 shows the relationship between the settling velocity and the near bed shear stress. Although the measurements are not of high accuracy, the settling velocity in the PRE can be roughly approximated by the linear regression equation as follows:

$$\omega_s = A\tau_b + B \tag{3.7}$$

Here A and B are coefficients, and τ_b is the bottom shear stress.

Eq. 3.7 indicates that the effective settling velocity increases linearly with the bottom shear stress. Stations Gu3 and Gu4 are located at the turbidity maximum zones in East and West channels, where a large amount of fine cohesive sediment particles have aggregated or are trapped. High bed shear stress implies higher turbulence intensity, which in turn increases the probability of collision between fine cohesive sediment particles and enhances the formation of flocs, resulting in a larger effective settling velocity. However, the effective settling velocity will not increase with the shear stress infinitely. It has been observed that the effective settling velocity will start to decrease if the turbulence is strong enough to break up the flocs and hinder the flocculation process.

3.6 Vertical sediment diffusion modelling

In partially mixed and well-mixed estuaries, sediment deposition and resuspension usually play an important role in the magnitude of TM, and turbulence suppression due to stratification helps to promote sediment congregation in the lower water column. To reveal these two mechanisms in detail, a vertical sediment transport model was applied.

Because the gradient of sediment concentration in the horizontal direction is much smaller than that in the vertical direction, $\frac{\partial}{\partial x} = \frac{\partial}{\partial z}$, and the settling velocity of the fine sediment particles is small, the vertical sediment advection and diffusion equation can be simplified to the following form after neglecting the horizontal advection and diffusion terms.

$$\frac{\partial c}{\partial t} = \frac{\partial}{\partial z}(\omega_s - w) + \frac{\partial}{\partial z}\left(\varepsilon_{s,z}\frac{\partial c}{\partial z}\right) \tag{3.8}$$

where ω_s is the sediment settling velocity; w is the vertical velocity and $\varepsilon_{s,z}$ is the vertical diffusion coefficient of the suspended sediment. To include the effect of the damping of turbulence due to the stratification in a partially mixed estuary $\varepsilon_{s,z}$ should be a function of the Richardson number Ri in the following form.

$$\varepsilon_{s,z} = \varepsilon_{s,z0}(1+10Ri)^{-1/2} \tag{3.9}$$

where $\varepsilon_{s,z0}$ is the vertical diffusion coefficient without the effect of stratification, which can be determined by the widely used parabolic-constant distribution expressions (van Rijn, 1986).

$$\varepsilon_{s,z0} = \begin{cases} \kappa u_* z\left(1-\frac{z}{H}\right) & for \quad \frac{z}{H} < 0.5 \\ 0.25\kappa u_* H & for \quad \frac{z}{H} \geq 0.5 \end{cases} \tag{3.10}$$

The Richardson number, Ri, is a measure of vertical stability based on the ratio of the local density gradient, which damps turbulence, to the velocity shear, which generates turbulence

$$Ri = -\frac{\rho}{g}\frac{\partial \rho}{\partial z} \bigg/ \left(\frac{\partial u}{\partial z}\right)^2 \tag{3.11}$$

Here ρ is the fluid density, which is related to temperature, sediment concentration and salinity. The effects of stratification are negligible until $Ri > 0.03$, and mixing is completely suppressed when $Ri \geq 0.25$ (Dyer, 1986).

The boundary condition for Eq. 3.8 at the water surface is taken as no sediment exchange between water and atmosphere. The mechanism of sediment deposition and resuspension near the seabed is more complex (Shi and Chen, 2000), and the measured suspended sediment concentration was used in the present model as the boundary condition. So the surface and bottom boundary conditions were prescribed as:

$$c = \begin{cases} \omega_s c + \varepsilon_{s,z}\dfrac{\partial c}{\partial z} = 0 & z = H \quad \textit{water surface} \\ c_a(t) & z = a \quad \textit{near seabed} \end{cases} \tag{3.12}$$

After transforming the above equations into the σ-coordinate, Eq. 3.8 coupled with the boundary conditions of Eq. 3.12 could be easily solved by the fully implicit finite difference method (Wai and Lu, 1999).

The simulated sediment concentration profiles at stations Gu3 and Gu4 from 7:00, July 9 to 7:00, July 10, 1978 are shown in Fig. 3.17. The computed results are in agreement with the observations at stations Gu3 and Gu4 in general. There is a kink in the computed sediment concentration profile for the case at Station Gu4 at hr 13:00 on July 9, which can be attributed to the inaccurately measured bottom sediment concentration at this point of time. The simulated results demonstrate the importance of the resuspension and deposition mechanism on sediment transport in the PRE. However, it should be noted that the simulated results at station Gu3 are better than that at Gu4. As discussed above, the resuspension and deposition mechanism is more dominant at station Gu3 in the wet season because hydrodynamics in the West Channel is more complicated and it is affected to a larger extent than the East Channel by the fresh water input from the three western outlets. Consequently, net sediment transport at station Gu4 is also dominated by advective transport in addition to resuspension and deposition. Comparing the accuracy of simulated results at these two stations, it is observed that a more sophisticated model is needed to more accurately represent the equally important mechanisms of advection and resuspension in the West Channel.

3.7 Summary

Based on the analysis of the sediment flux in the major navigational channels in the PRE, the formation mechanisms of TM have been revealed. Because of the complexity of the topography and the presence of river outlets along the western coastline, the formation mechanisms in the PRE are not only related to the intrusion of salt water, but also to the freshwater runoff from the three western river outlets, namely Jiaomen, Hongqimen and Hengmen. In general, in the wet season, TM far upstream of the wedge of saltwater intrusion is closely related to the effect of freshwater runoff from Jiaomen. Gravitational circulation and tidal trapping are the principal formation mechanisms of the TM that are located adjacent to the head of the saltwater wedge. The clockwise flow around Neilingding Island is also one of the formation mechanisms of TM in the West Channel during the wet season. In the dry season, salt water intrudes into Dahu Channel. Thus, TM occurring upstream of Dahu is related to the intrusion of salt water. However, the location of the upstream low concentration region associated with TM5 is not known from the present data set, hence the formation mechanisms of TM5 should be further studied when upstream measurements are available. TM in the East Channel is mainly caused by the sediment resuspension and deposition processes. On the other hand, gravitational circulation is the predominant formation mechanism of TM in the West Channel. In addition, it is found that Stokes drift plays a vital role in conveying sediment from the South China Sea into the PRE in the dry season, which is an important source of sediment for the formation of TM.

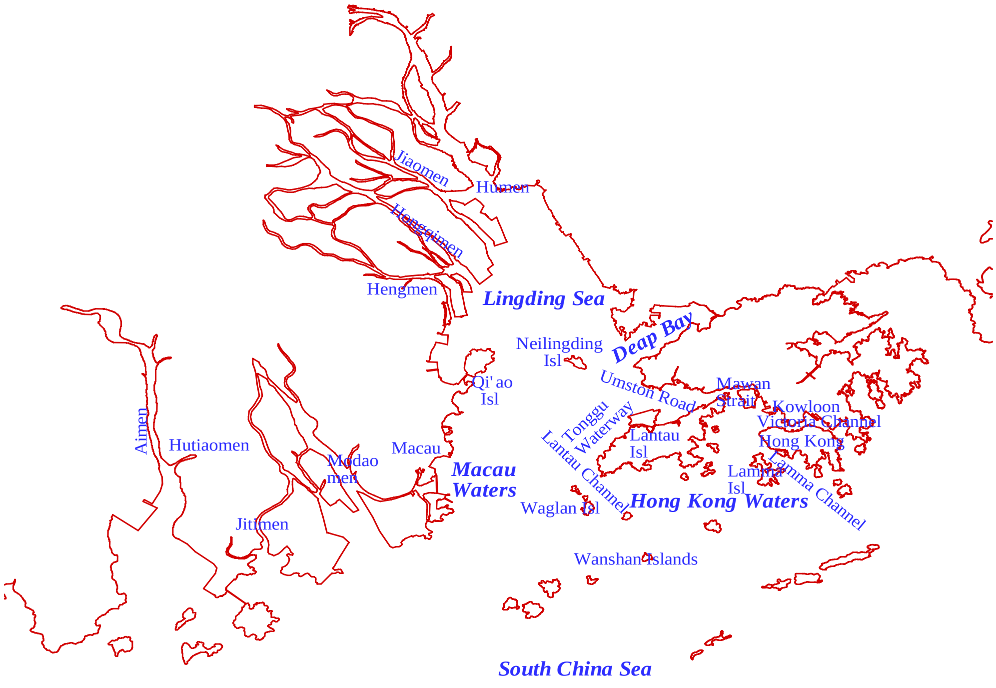

Fig. 3.1 Coastline of the Pearl River Delta

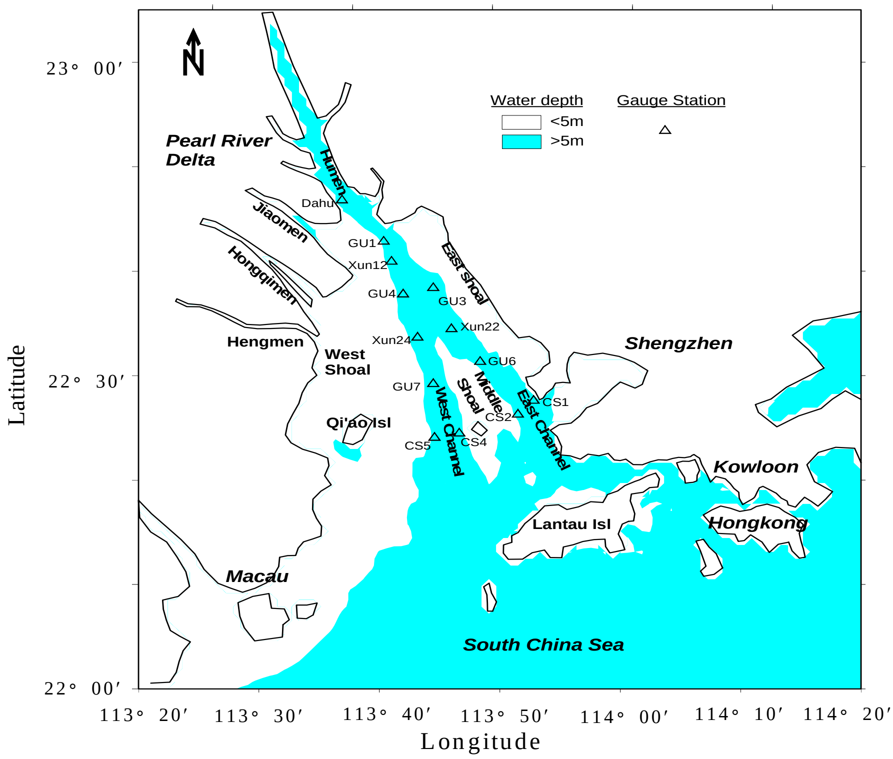

Fig. 3.2 Map of the PRE and locations of the field stations for the surveys in 1978 and1979.

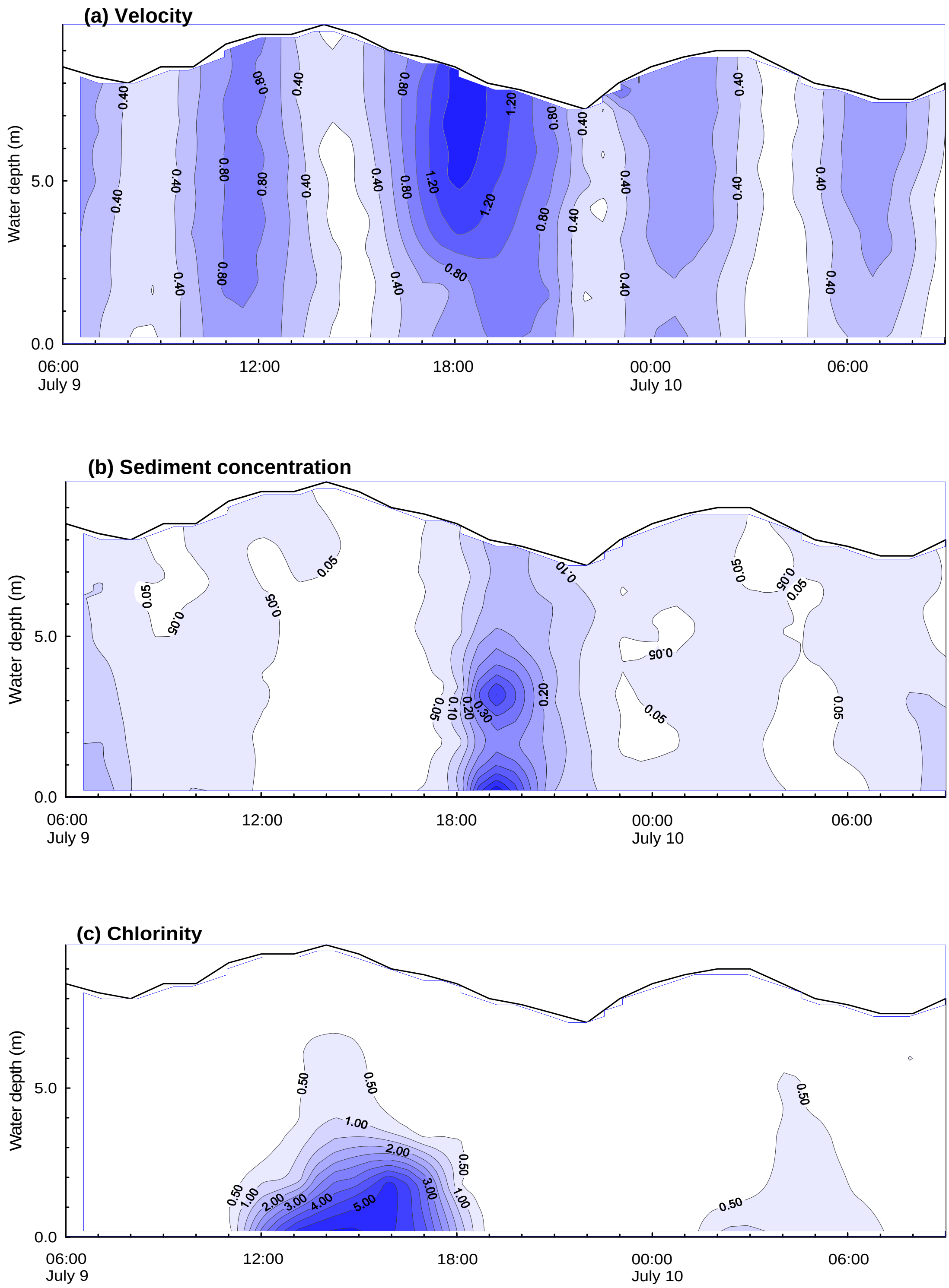

Fig. 3.3 Time series of velocity (m/s), suspended sediment concentration (g/l) and chlorinity (ppt) at station Gu3 in the wet season (July 1978)

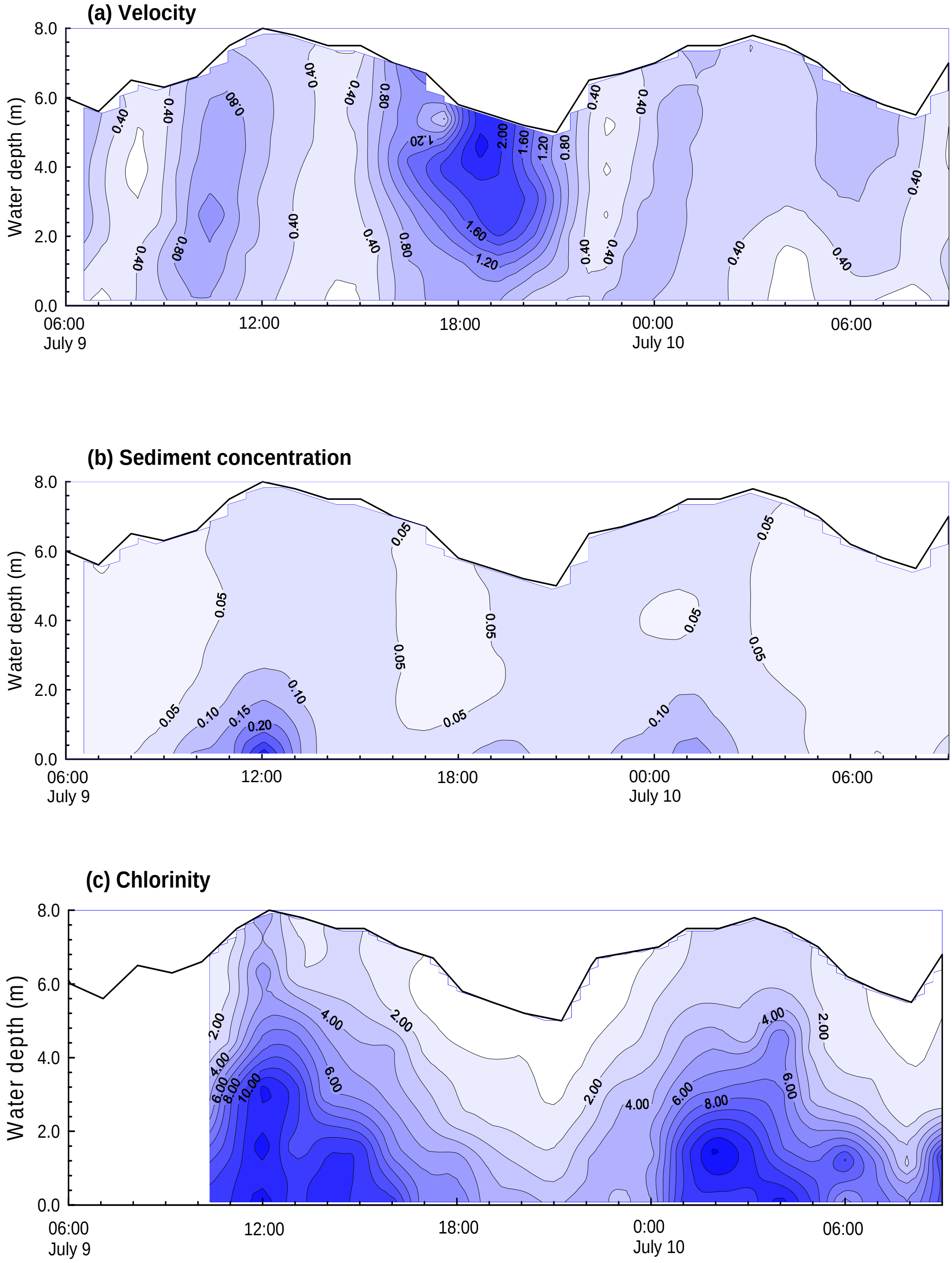

Fig. 3.4 Time series of velocity (m/s), suspended sediment concentration (g/l) and chlorinity (ppt) at station Gu6 in the wet season (July 1978)

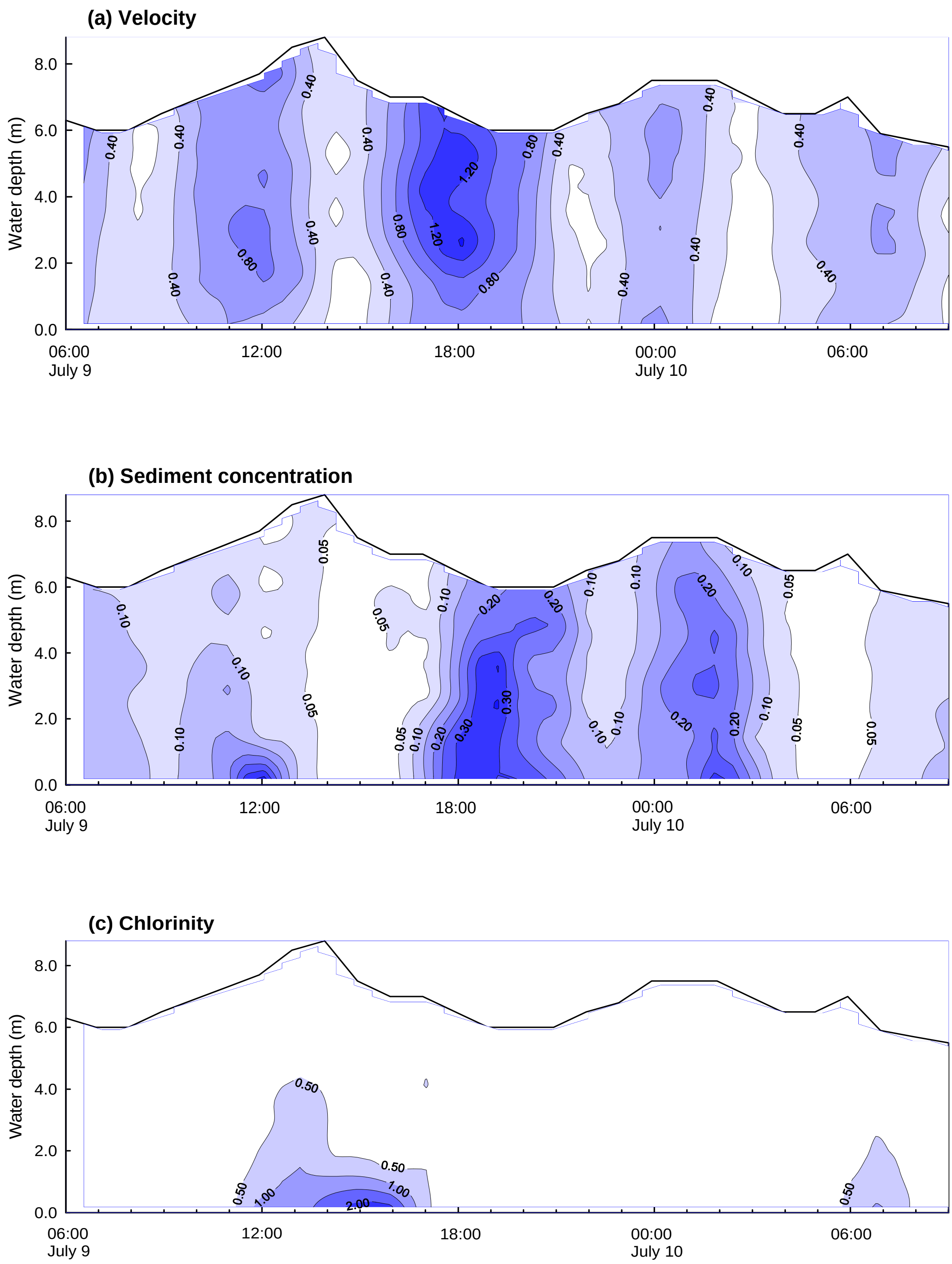

Fig. 3.5 Time series of velocity (m/s), suspended sediment concentration (g/l) and chlorinity (ppt) at station Gu4 in the wet season (July 1978)

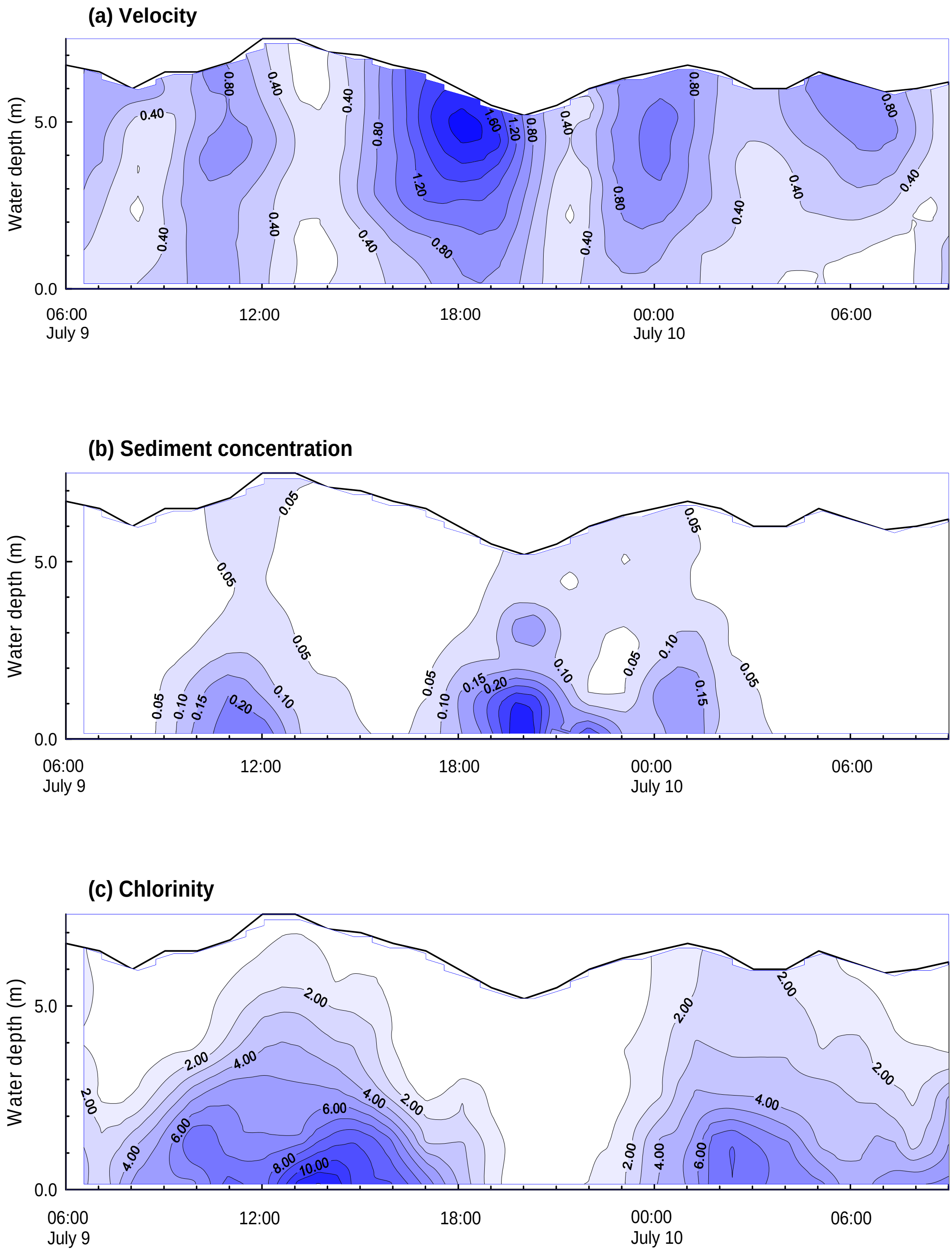

Fig. 3.6 Time series of velocity (m/s), suspended sediment concentration (g/l) and chlorinity (ppt) at station Gu7 in the wet season (July 1978)

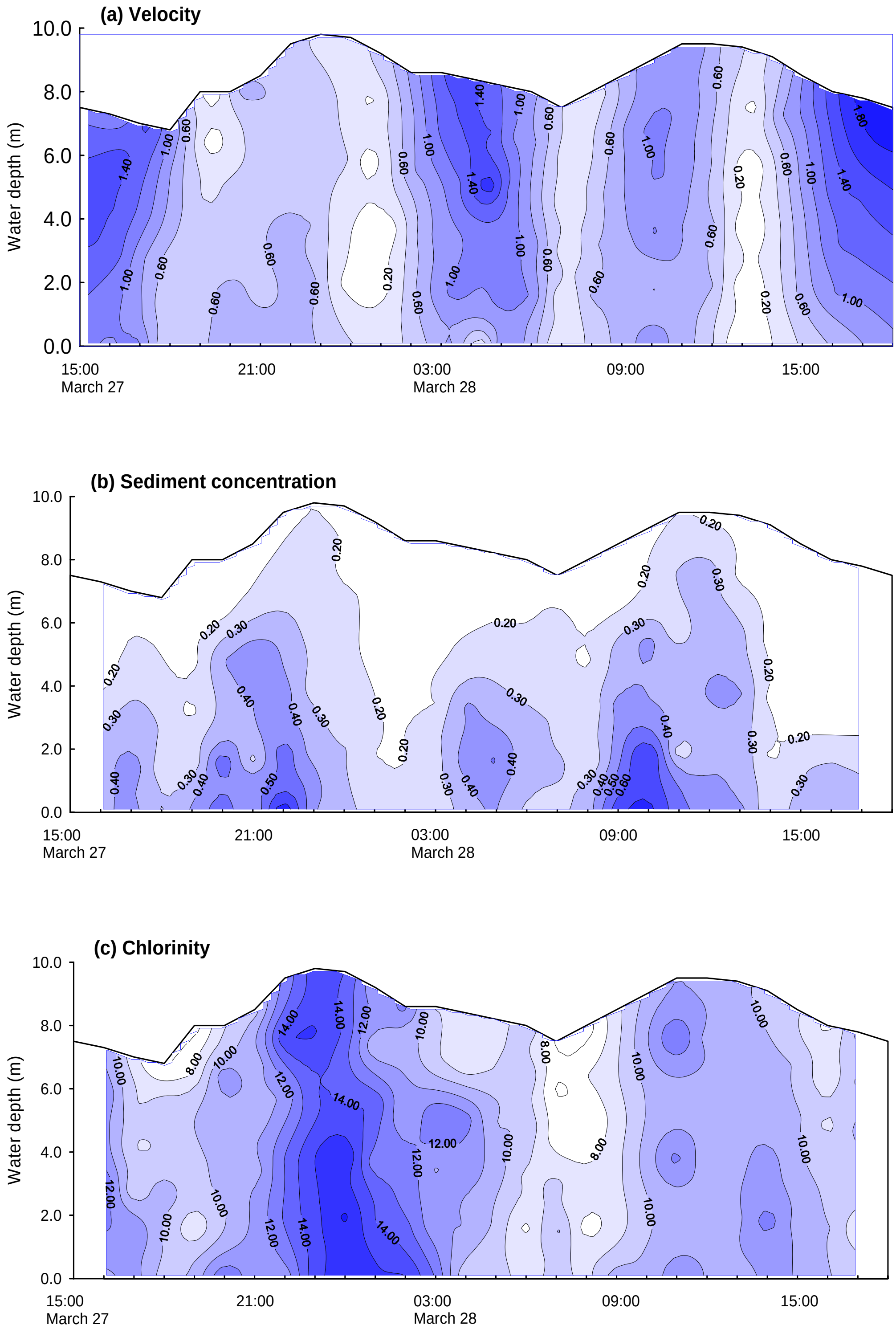

Fig. 3.7 Time series of velocity (m/s), suspended sediment concentration (g/l) and chlorinity (ppt) at station Gu3 in the dry season (March 1979)

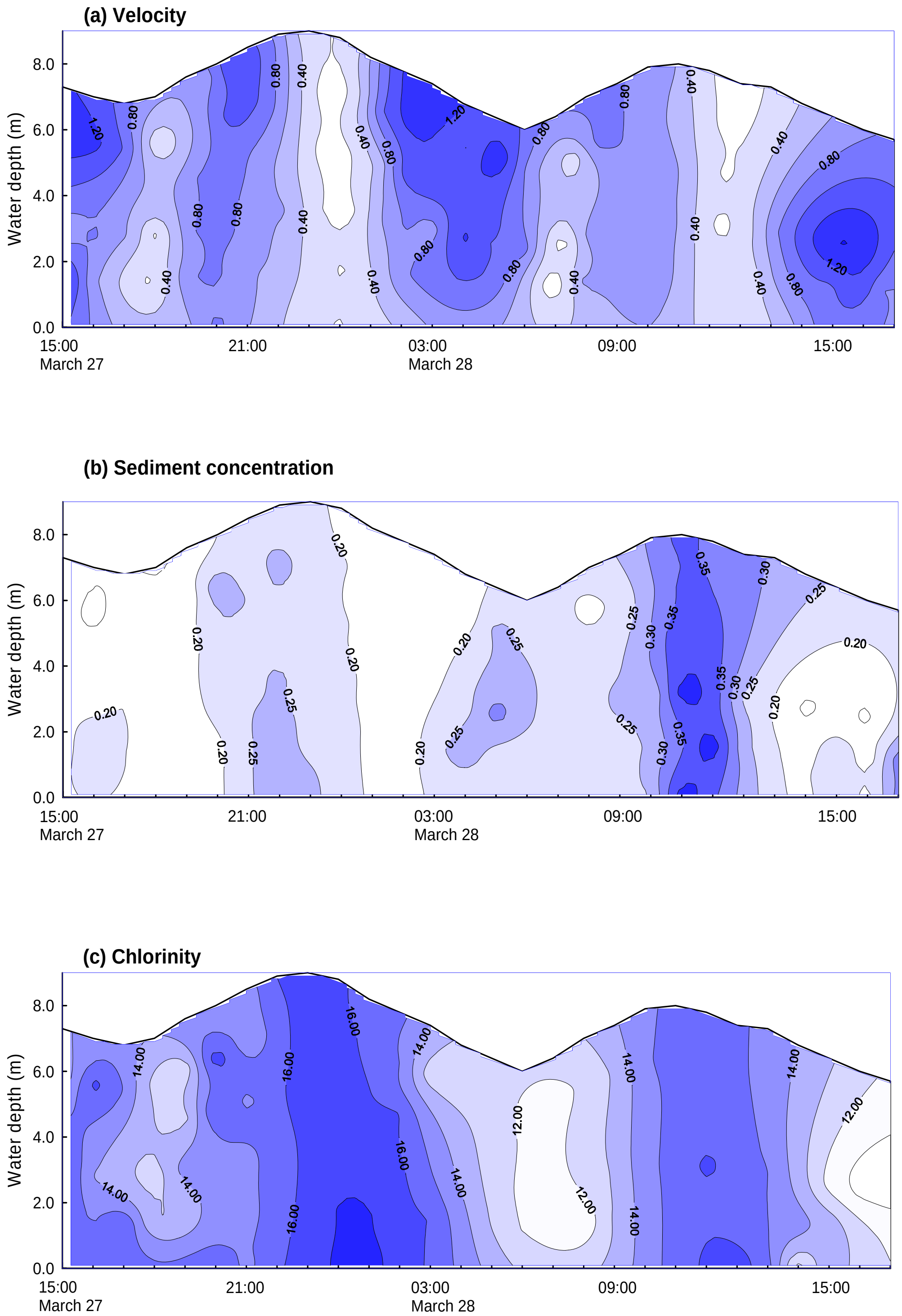

Fig. 3.8 Time series of velocity (m/s), suspended sediment concentration (g/l) and chlorinity (ppt) at station Gu6 in the dry season (March 1979)

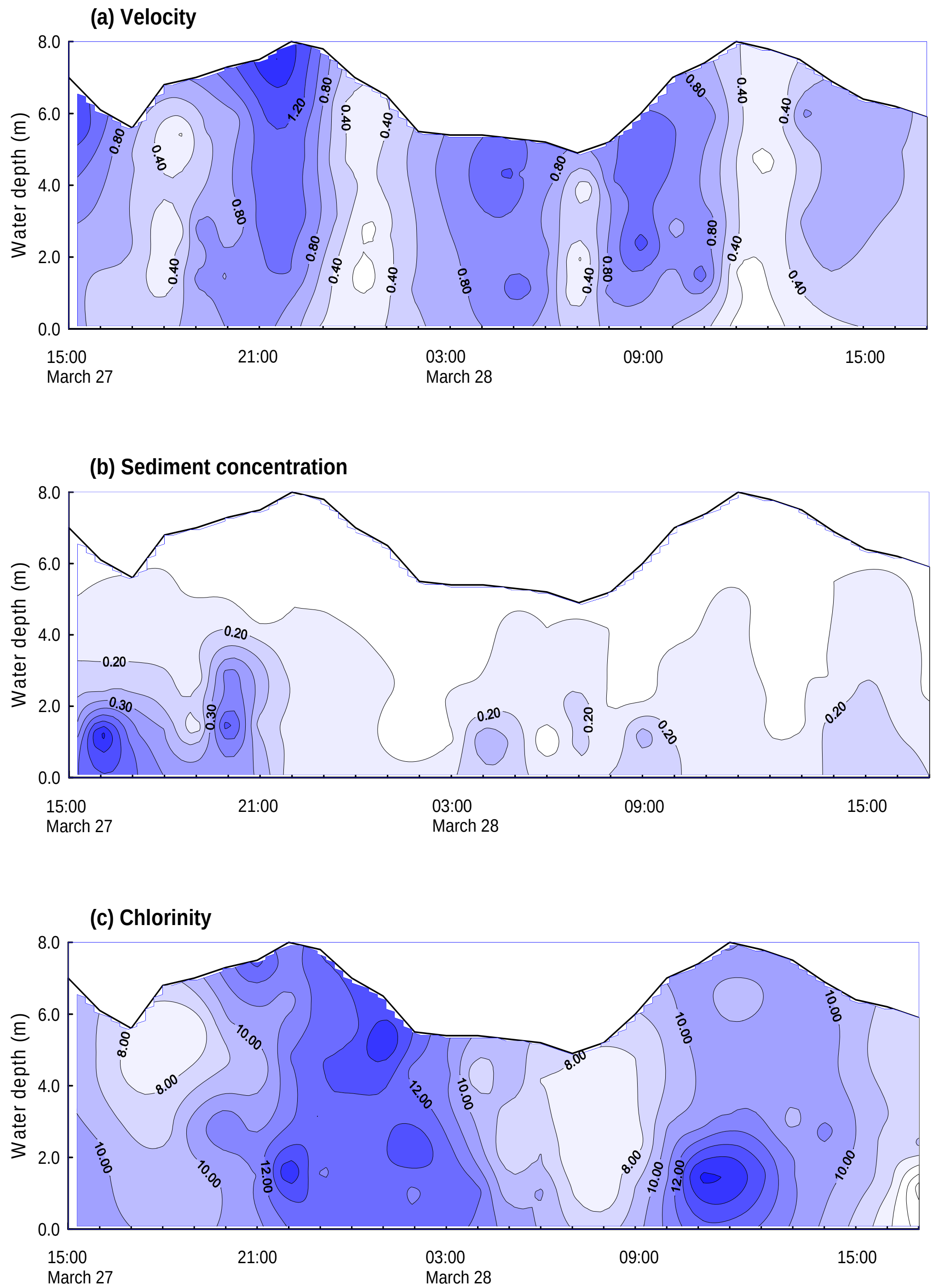

Fig. 3.9 Time series of velocity (m/s), suspended sediment concentration (g/l) and chlorinity (ppt) at station Gu4 in the dry season (March 1979)

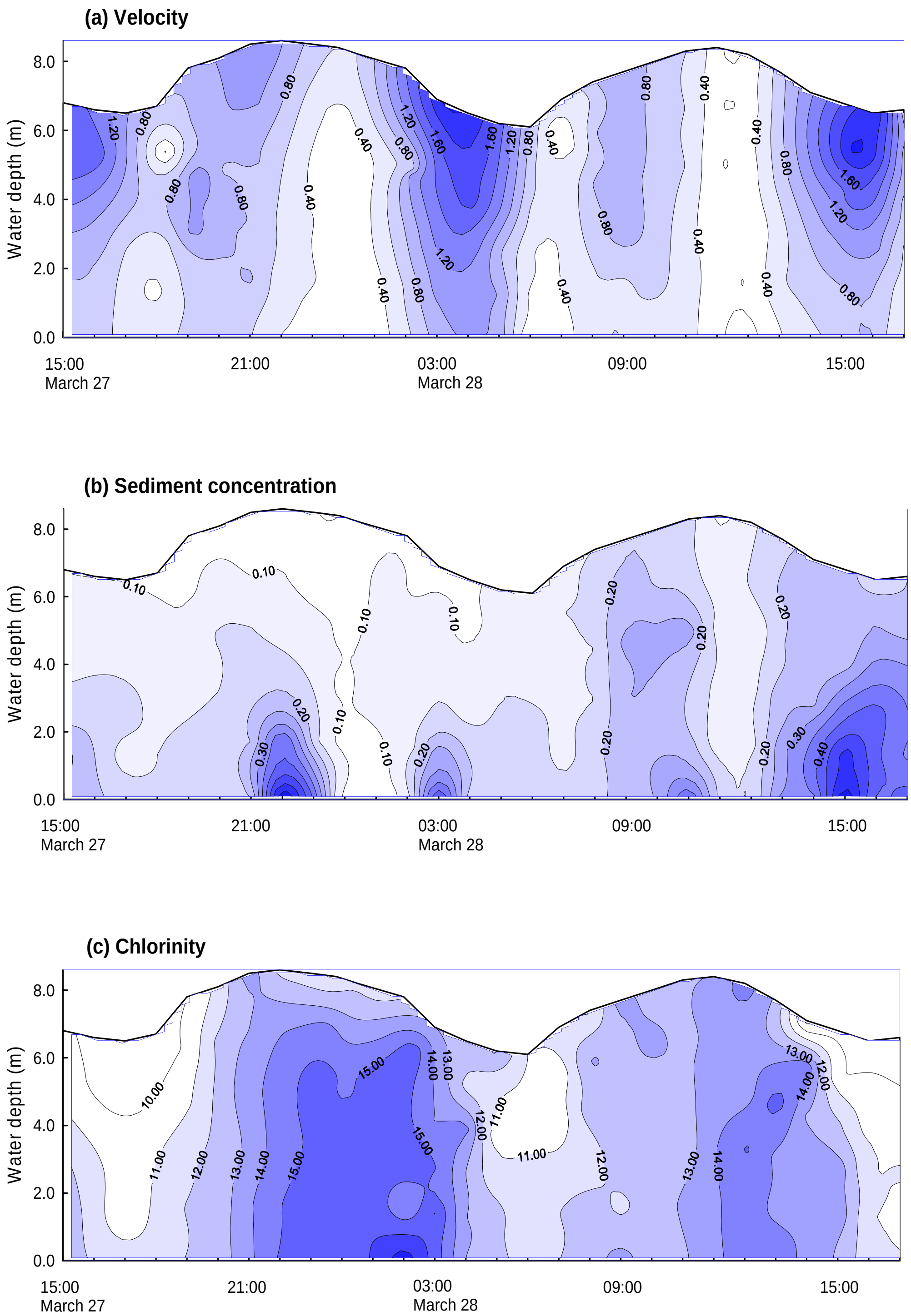

Fig. 3.10 Time series of velocity (m/s), suspended sediment concentration (g/l) and chlorinity (ppt) at station Gu7 in the dry season (March 1979)

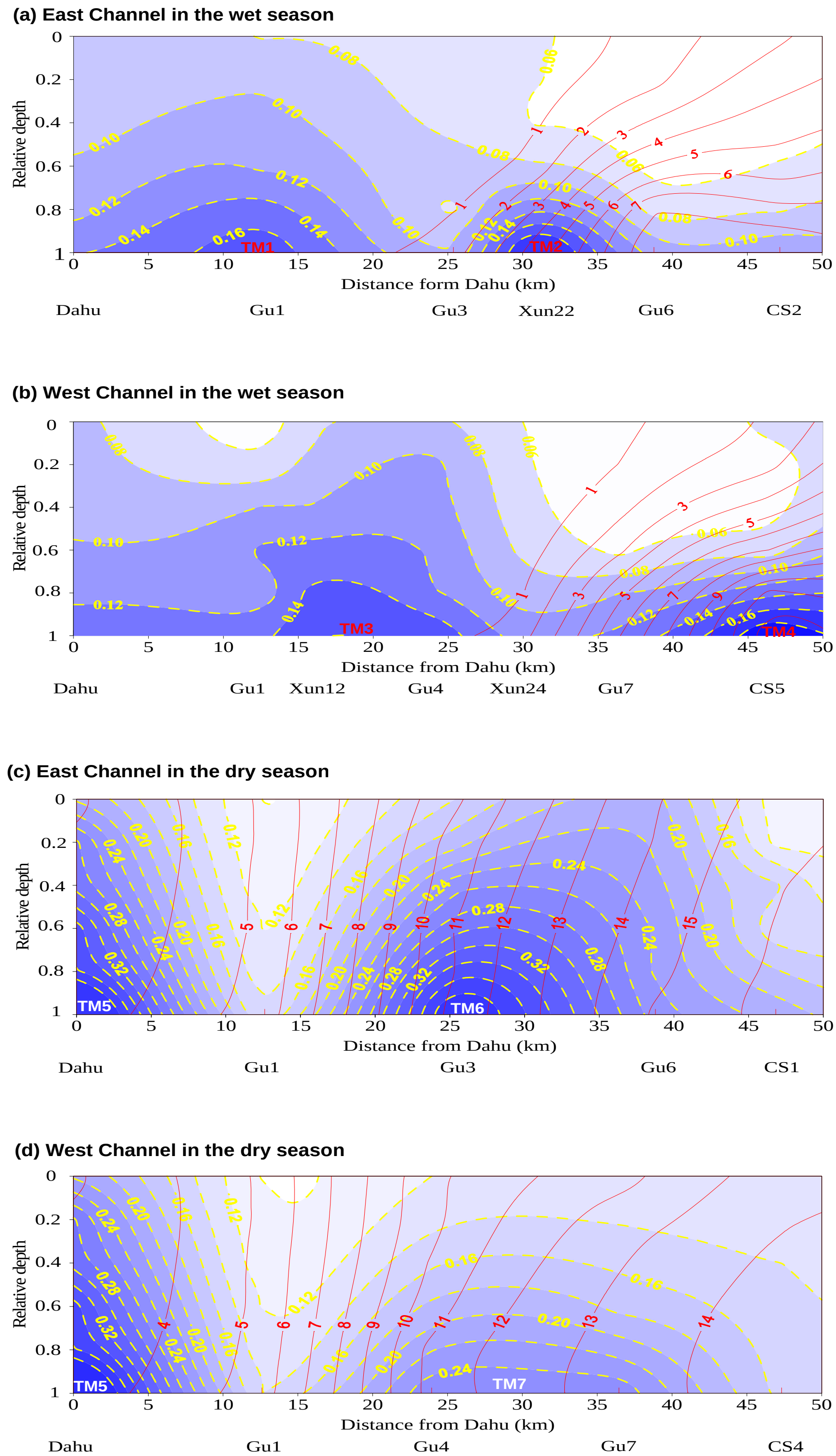

Fig. 3.11 Contours of tidally averaged sediment concentration, chlorinity and locations of turbidity maxima: Dash lines represent sediment concentration (g/l) and solid lines represent chlorinity (ppt)

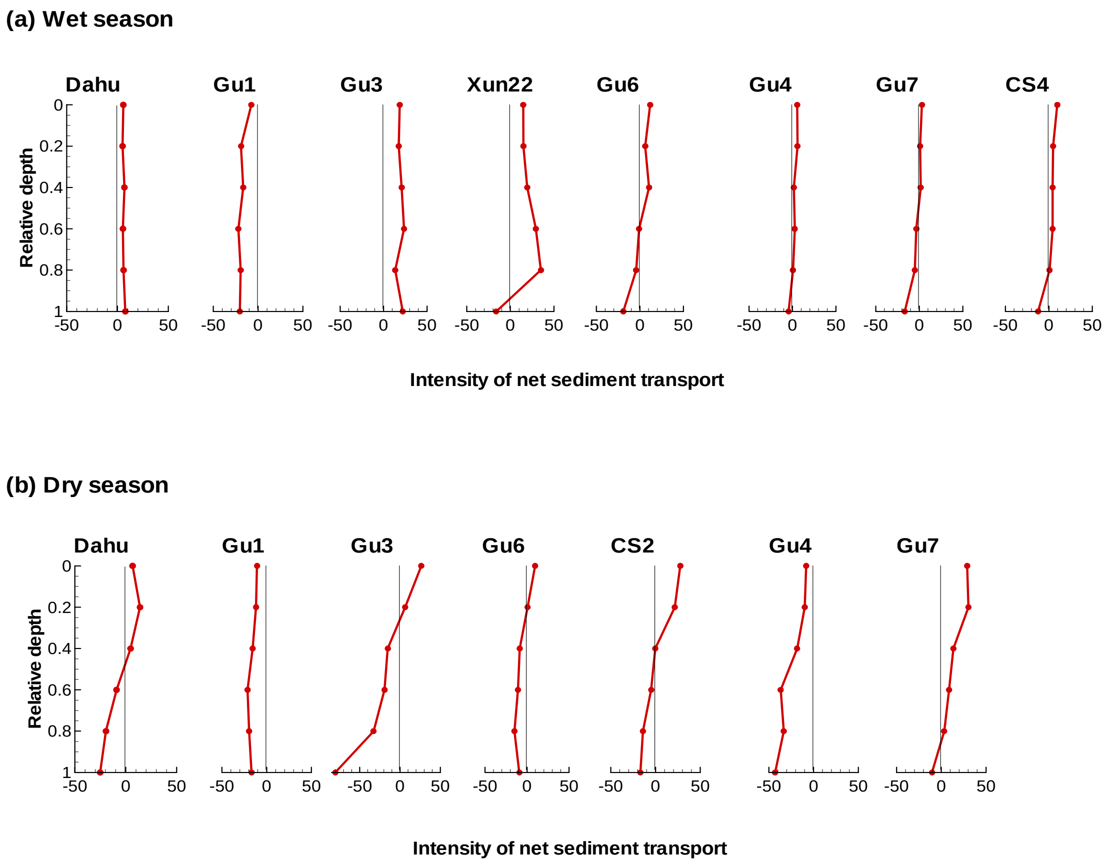

Fig. 3.12 Tidally averaged net sediment flux ($g{\cdot}s^{-1}{\cdot}m^{-2}$): positive values denote seaward transport, negative values denote landward transport

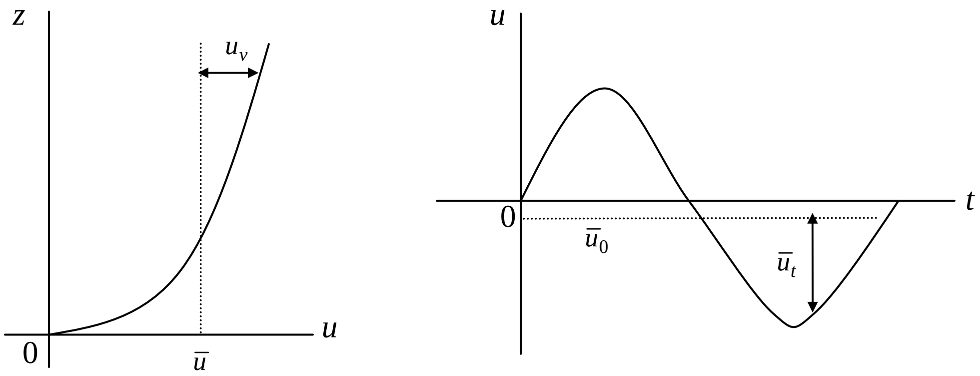

Fig. 3.13 Diagrammatic representations of decompositions of velocity along water column and over a tidal cycle

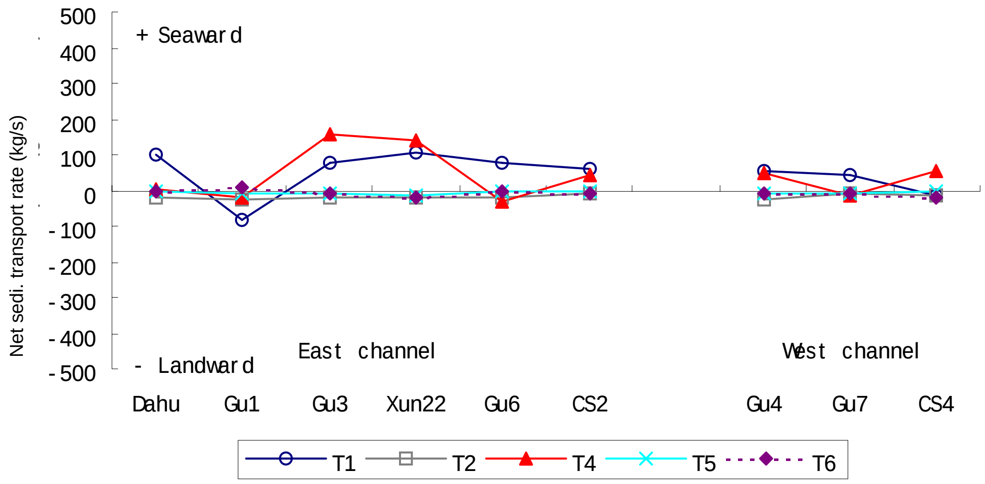

(a)

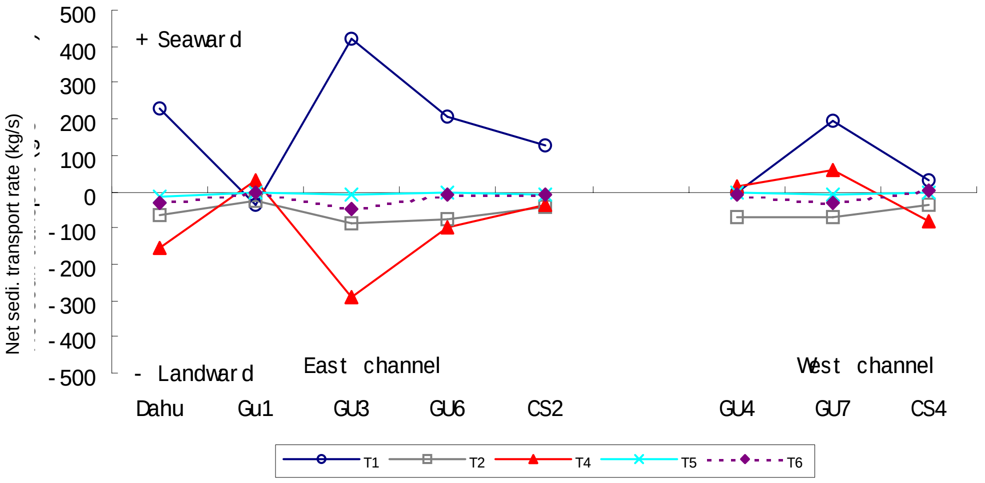

(b)

Fig. 3.14 Components of net sediment flux in the wet season (July 1978) and dry season (March 1979): T1—due to Eulerian velocity; T2—due to Stokes drift; T4—due to resuspension/deposition; T5—due to tidal trapping; T6—due to gravitational circulation

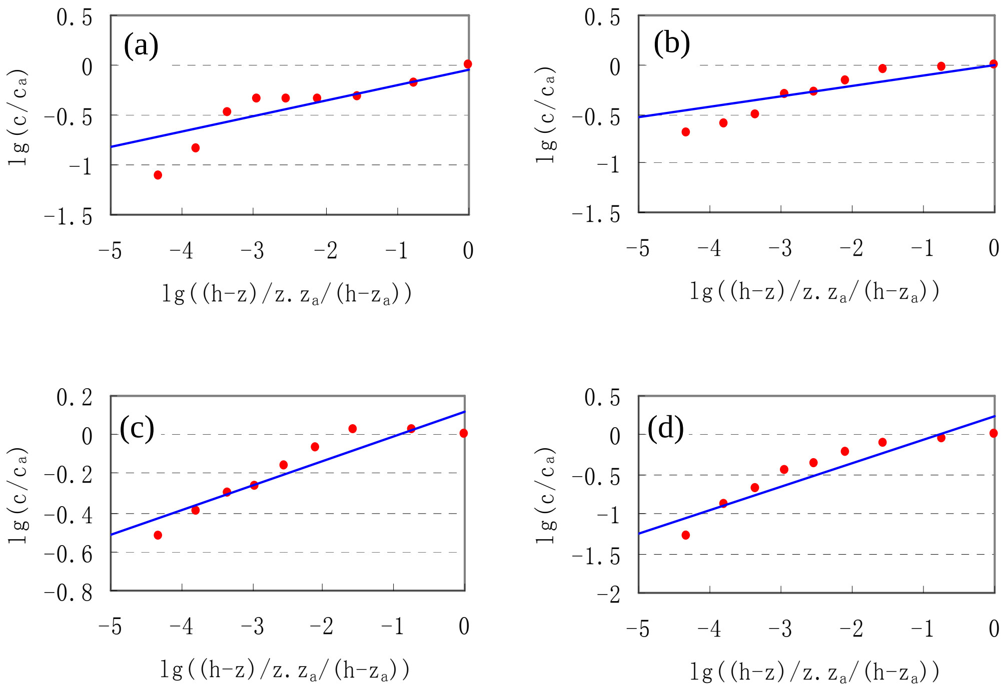

Fig. 3.15 Sediment concentration profiles derived from Rouse profile during (a) flooding at Gu3, (b) ebbing at Gu3, (c) flooding at Gu4, and (d) ebbing at Gu4.

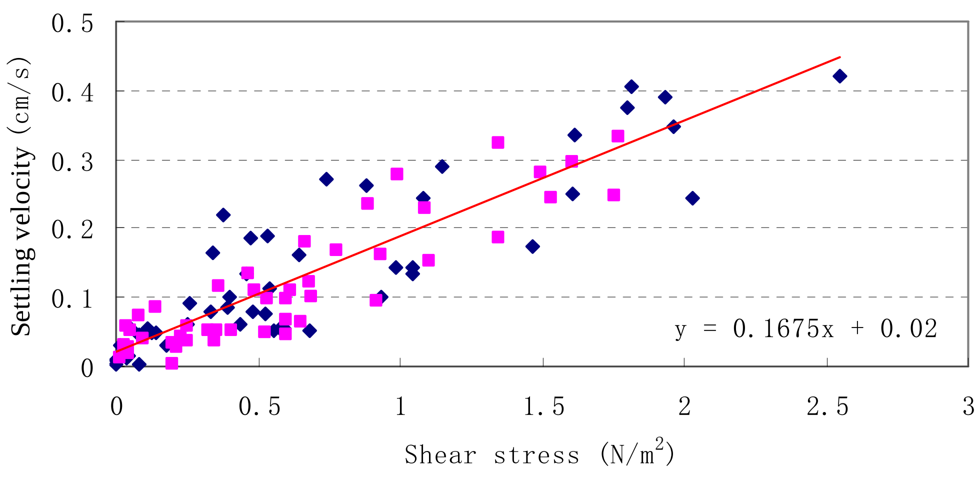

Fig. 3.16 Relationship between effective velocity and near bed shear stress ◆ at Gu3, ■ at Gu4.

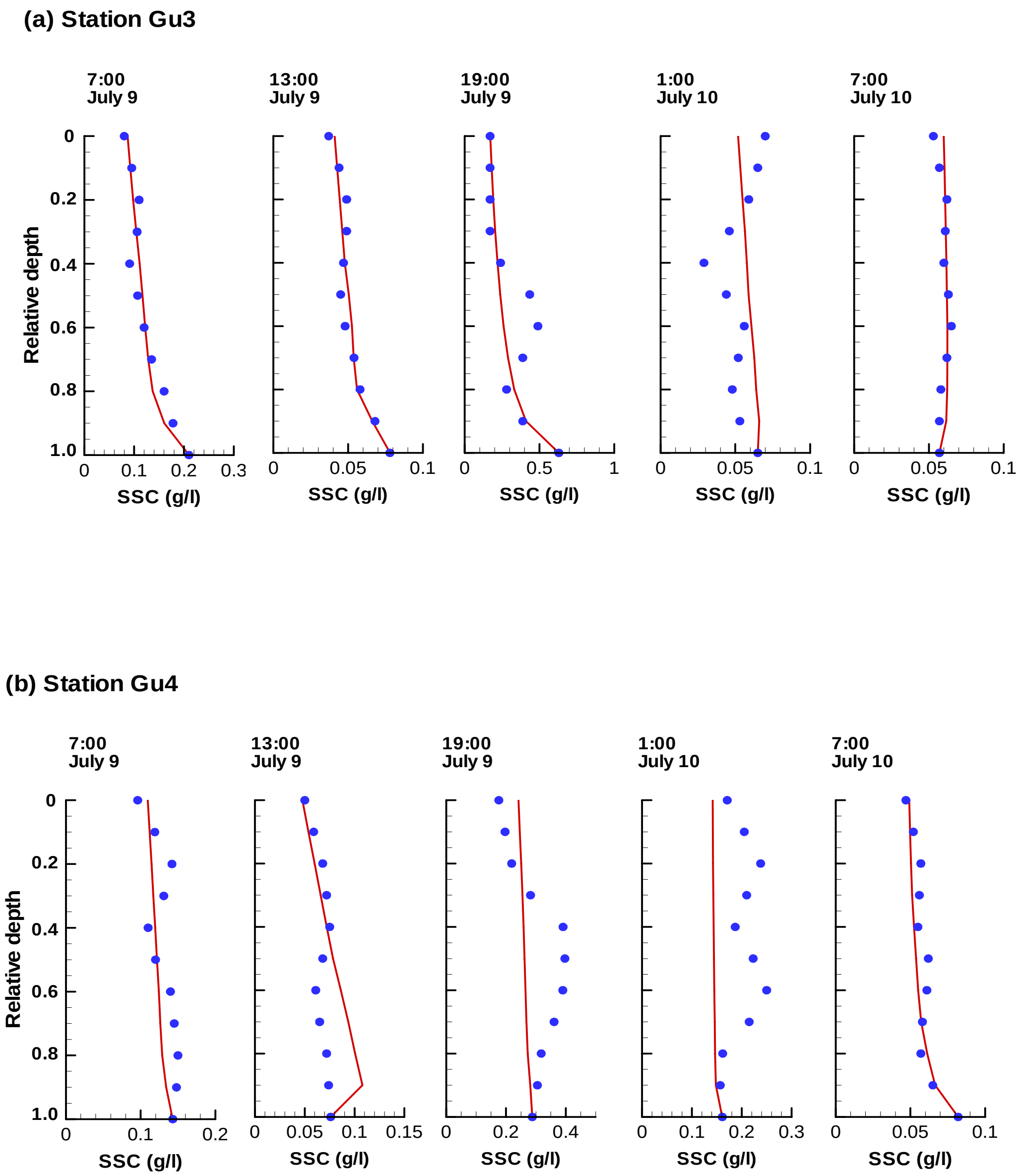

Fig. 3.17 Comparison of computed and measured suspended sediment concentration (SSC): Solid lines represent computed results and dots represent measured values.

CHAPTER 4

TWO-DIMENSIONAL CHARACTERISTICS OF HYDRODYNAMICS AND MASS TRANSPORT IN THE PEARL RIVER ESTUARY

4.1 Introduction

In Chapter 3, sediment dynamics in the PRE has been analyzed based on field measurements. Although field surveys can provide the first-hand information on hydrodynamics, sediment transport, and the fate of pollutants and heavy metal, field surveys are always carried out at a limited number of sites, and it is difficult to have a large-scale survey carried out over an extended time period. In the PRE, due to the complex coastline and river outlets distributed along the west coastline, a few field surveys are definitely insufficient to gather enough information on details of hydrodynamics and mass transport.

In order to gain more knowledge on the hydrodynamics and mass transport in the PRE, a depth-integrated model, which was modified from the three-dimensional multi-layer model by Wai *et al*. (1996), was employed. The model was verified by field data obtained in the wet season of 1992 and the dry season of 1993. Then, tidal and seasonal variations of characteristics of hydrodynamics and mass transport in the PRE were analyzed based on the computed results. The spatial distribution of vertically averaged suspended sediment concentration was studied and compared with satellite imagery. The phenomenon of sediment-laden flow in the main channels appears to be clearer than that in shoals was explained through the analysis of the sediment-carrying capacity of flow. Finally, the effects of Coriolis force and surface wind stress on residual flow, salinity and sediment transport were discussed.

4.2 Model description

4.2.1 Governing equations

The present depth-integrated two-dimensional hydrodynamics and mass transport model was modified from the three-dimensional multi-layer model developed by Wai *et al*. (1996). Under the assumption of (a) hydrostatic approximation for the vertical distribution of pressure and, (b) small vertical variations of the mass and momentum distributions, the vertically integreted continuity and Navier-stokes equations are as follows:

Continuity

$$\frac{\partial \zeta}{\partial t}+\frac{\partial U}{\partial x}+\frac{\partial V}{\partial y}=0 \tag{4.1}$$

Momentum eqations

for x-direction

$$\frac{\partial U}{\partial t}+\frac{1}{H}\frac{\partial UU}{\partial x}+\frac{1}{H}\frac{\partial VU}{\partial y}-fV=-gH\frac{\partial \zeta}{\partial x}+\varepsilon_h\left(\frac{\partial^2 U}{\partial x^2}+\frac{\partial^2 U}{\partial y^2}\right)+\frac{1}{\rho}\left(\tau_{s,x}-\tau_{b,x}\right) \tag{4.2}$$

for y-direction

$$\frac{\partial V}{\partial t}+\frac{1}{H}\frac{\partial UV}{\partial x}+\frac{1}{H}\frac{\partial VV}{\partial y}+fU=-gH\frac{\partial \zeta}{\partial y}+\varepsilon_h\left(\frac{\partial^2 V}{\partial x^2}+\frac{\partial^2 V}{\partial y^2}\right)+\frac{1}{\rho}\left(\tau_{s,y}-\tau_{b,y}\right) \tag{4.3}$$

where, ζ is tidal level; f is the Coriolis parameter; $H=\zeta+h$ is total water depth, and h is water depth under mean sea surface level; g =9.81 m/s^2 is gravitational acceralation; ρ is sea water density, a function of water temperature, salinity and sediment concentration. $\tau_{s,x},\tau_{s,y}$ are wind stress components in x and y directions respectively; $\tau_{b,x},\tau_{b,y}$ are bed shear stress components in x and y directions respectively; and ε_h is the horizontal eddy viscosity. The capital letters express the fluxes of variables through a unit width of the whole water column,

$$U=\int_{-h}^{\zeta} udz, \qquad V=\int_{-h}^{\zeta} vdz \tag{4.4}$$

where u , v are the velocity components in the x , y Cartesian coordinates, respectively.

The salinity conservation equation is

$$\frac{\partial S}{\partial t}+\frac{1}{H}\frac{\partial US}{\partial x}+\frac{1}{H}\frac{\partial VS}{\partial y}=\varepsilon_{s,h}\left(\frac{\partial^2 S}{\partial x^2}+\frac{\partial^2 S}{\partial y^2}\right) \tag{4.5}$$

and the sediment transport equation is

$$\frac{\partial C}{\partial t}+\frac{1}{H}\frac{\partial UC}{\partial x}+\frac{1}{H}\frac{\partial VC}{\partial y}=\varepsilon_{s,h}\left(\frac{\partial^2 C}{\partial x^2}+\frac{\partial^2 C}{\partial y^2}\right)-\left(\omega_s c\right)_b-\left(\varepsilon_{s,z}\frac{\partial c}{\partial z}\right)_b \tag{4.6}$$

where $\varepsilon_{s,h}$ and $\varepsilon_{s,z}$ are eddy diffusion coefficients in horizontal and vertical directions, respectively; $S=\int_{-h}^{\zeta} sdz$, $C=\int_{-h}^{\zeta} cdz$, in which s and c are salinity and suspended sediment concentration respectively; ω_s is settling velocity; the subscript b denotes the value of variables near seabed.

4.2.2 Near bottom sediment exchange

The last two terms in Eq. 4.6 express the sediment exchange between the seabed and the water column. The mechanisms of cohesive sediment resuspension from the seabed to the water column and deposition from the water column to the seabed are very complex. The net flux of sediment exchange near the bottom is closely related to the relative intensity of particle gravity force to the near bottom shear stress. The rate of resuspension depends on the excess bed shear stress above a critical value or the deficient bed shear stress below a critical value in case of deposition (Partheniades, 1962; Einstein and Krone, 1962), and this theory has been applied successfully in many laterally integrated two-dimensional models and three-dimensional modes.

However, in a vertically integrated model, it is difficult to get the information on near bed velocity and sediment concentration, and the time-scale of vertical diffusion is also unknown. Here the sediment-carrying capacity was introduced to describe the local overall sediment exchange between suspended particles and bed material.

When the equilibrium state of a particular velocity magnitude is established, there is no net deposition or erosion of sediment particles. The amount of sediment moving upward due to turbulent motion should be equal to the downward amount due to gravitational settling, and the corresponding sediment concentration is called the sediment-carrying capacity. When the amount of sediment supply is greater than the capacity, net deposition occurs, which leads to a decrease in sediment concentration until the carrying capacity of a lower velocity magnitude is reached. Conversely, if the sediment supply is less than the capacity and the bed is erodable, net scour may occur. The sediment concentration will then increase consequently, until the carrying capacity is reached again.

The near bed sediment concentration c_b is defined as the sediment-carrying capacity c_{*b} near bed.

$$\left(\varepsilon_{s,z}\frac{\partial c}{\partial z}\right)_b = -\omega_{sb}c_{*b} \tag{4.7}$$

Further assuming that the relationship Eq. 4.7 is applicable under nonequilibrium condition and expressing c_{*b} as vertically averaged sediment-carrying capacity $c_{*b} = \alpha_1 c_*$, Eq. 4.7 can be rewritten as

$$\left(\varepsilon_{s,z}\frac{\partial c}{\partial z}\right)_b = -\alpha_1\omega_{sb}c_* \tag{4.8}$$

In addition, assuming that the concentration near the bed c_b also has a relationship with the vertically averaged value $\bar{c}$, say $c_b = \alpha_2\bar{c}$, the term $\left(\omega_s c\right)_b$ in Eq. 4.6 becomes

$$\omega_{sb}c_b = \alpha_2\omega_{sb}\bar{c} \tag{4.9}$$

for uniform size sediment particles. The mean settling velocity ω_s can be used to replace the settling velocity near the bed ω_{sb}. In practical situations, $\alpha_1 \approx \alpha_2 = \alpha$ (Chen, *et al.*, 1999) and α is called the sediment recovery coefficient. Han and

He (1990), Fang (1998) and Zhou and Lin (1998) studied in detail the sediment recovery coefficient, which is related to the flow and sediment conditions. In general α =0.5 is a good approximation. Thus the sediment transport equation Eq. 4.6 can be expressed as

$$\frac{\partial C}{\partial t}+\frac{1}{H}\frac{\partial UC}{\partial x}+\frac{1}{H}\frac{\partial VC}{\partial y}+\alpha\omega_s\left(\bar{c}-c_*\right)=\varepsilon_{s,h}\left(\frac{\partial^2 C}{\partial x^2}+\frac{\partial^2 C}{\partial y^2}\right) \tag{4.10}$$

The sediment-carrying capacity is both a function of the hydrodynamic conditions (such as velocity and depth) and sediment conditions (such as sediment particle size and effective density). The concept of sediment-carrying capacity is widely used in river systems, in which the effect of wave-induced flow can be neglected and the hydrodynamic condition can be treated as steady. A representative formula for the sediment-carrying capacity of 1D river flow (Zhang, 1963; Bagnold, 1973), based on the principle of the balance of gravity and turbulence energy, is extended to the 2D situation in the present study as follows.

$$c_* = k\left(\frac{\left(\sqrt{\bar{u}^2+\bar{v}^2}\right)^3}{gH\omega_s}\right)^m \tag{4.11}$$

where k and m are coefficients, m is given a value of 0.92 (Han and He, 1987), and k should be verified by field data.

The principal parameter in Eq. 4.11 is the product of $\left(\bar{u}^2+\bar{v}^2\right)/gH$ and $\sqrt{\bar{u}^2+\bar{v}^2}/\omega_s$. The term $\left(\bar{u}^2+\bar{v}^2\right)/gH$ is the square of Froude number, which represents the ratio of the local inertial force to the gravity force. For flow with a specified velocity, the Froude number is inversely proportional to the water depth, which means the turbulence of the specified flow is decreasing with increasing water depth. The term $\sqrt{\bar{u}^2+\bar{v}^2}/\omega_s$ is proportional to u_*/ω_s, which represents the ratio of flow turbulence to gravity force on the sediment particles. For cohesive particles in estuaries, the sediment settling velocity increases because of the occurrence of flocculation, and hence stronger turbulence is required to keep sediment particles in suspension or to erode sediment from bed. An effective settling velocity, which takes into account the size of suspended sediment and bed materials is required if the sediment particles are non-uniform. Detail discussions of effective settling velocity can be found in He and Han (1989 and 1990).

4.2.3 Numerical scheme

Based on the above governing equations and boundary conditions, the computational domain is discretized using four-node isoparametric finite elements for easy adaptation to complex boundary configurations. The two-step Lax Wendroff scheme, following Kawahara *et al*. (1978), is used for time marching. Details can be found in Wai *et al*. (1996).

4.3 Computational domain and boundary conditions

4.3.1 Computational domain

Fig. 4.1 shows the domain of interest, which covers the whole of the eight Pearl River outlets and the whole of the Hong Kong Waters. To the east, part of Mirs Bay is included and to the west, the model extends to include the three major river outlets near Macau. To the south, the model domain extends to 70 m water depth contour at the south-east corner and the 55 m water depth contour at the south-west corner. Although the hydrodynamics and mass transport in Lingding Sea and the Hong Kong Waters are the objective of this study, the purpose of setting the open sea boundary far enough is to minimize the errors due to possible inaccuracy of the open sea boundary conditions.

The total area covered by the computational domain is about 20,400 km^2. In this model, the area to be simulated was divided into 4799 four-node elements of different elemental areas from 0.13 km^2 at Victoria Harbor to 14.8 km^2 outside the estuary, and the total node number is 5176.

4.3.2 Boundary conditions

Tidal levels can be used as the open sea boundary conditions. Because of insufficient information on observed tidal levels near the open sea boundaries, the four major harmonic tidal components, M2, S2, K1, and O1, which are known from tidal records at the tidal gauges shown in Fig. 4.1, were used to estimate the tidal water-surface elevations to drive the flow field. The amplitudes and phases of the four tidal components at the open boundary were extrapolated from the data recorded at the nearest tide gauge stations.

The upstream boundary conditions are the average fresh water discharges and sediment concentrations at the eight Pearl River outlets. Since the sea boundary was set far from the eight outlets and salt water could hardly reach the outlets (Xu *et al.*, 1985; Ying *et al.*, 1993), especially in the wet season, the river outlets are thus treated as net inflow systems of fresh water and only net fresh water flow rates and suspended sediment concentration were imposed there. Table 4.1 listed the long-term seasonal average river discharges and suspended sediment concentrations at river boundaries of eight outlets based on the DELFT report entitled “Upgrading of the water quality and hydraulic mathematical models, Part2” (1998) and Xu *et al*. (1985).

Table 4.1 Mean seasonal flow rates and sediment concentrations at the boundaries upstream of river outlets

Boundaries upstream of river outlets	Flow rate (m^3/s)		Sediment concentration (mg/l)	
	Dry season	Wet season	Dry season	Wet season
Humen	795	3436	50	136
Jiaomen	700	3304	70	200
Hongqimen	225	1207	200	300
Hengmen	441	2154	200	300
Modaomen	1145	5387	200	300
Jitimen	205	975	200	300
Hutiaomen	240	1143	200	300
Aimen	365	1737	200	300

The vertically averaged salinity and sediment concentrations, listed in Table 4.2, were based on field measurements and represent the approximate open sea conditions, which a fairly constant during the two seasons. The values at boundary nodes between two corner nodes were linearly interpolated from the known corner values. At the north-west corner, salinity and sediment concentration are more easily affected by the riverine flow and the more turbid water discharging from Aimen and Hutiaomen, a slightly smaller salinity and a slightly higher sediment concentration could be used.

Table 4.2 Mean salinity and sediment concentration at the open sea boundary

	Salinity (ppt)		Sediment. Concentration
	Dry season	Wet season	(mg/l)
NE corner	35	34	30
SE corner	35	35	10
SW corner	35	35	10
NW corner	25	15	100

4.3.3 Model parameters

In addition to the above-mentioned boundary conditions, some other parameters should be specified in advance in the model, such as the flow diffusion and mass dispersion coefficients, sea-bed roughness, and sediment-carrying capacity.

In general, the bed roughness is inversely proportional to the water depth. In this study, where water depth is less than 3 m in shallow shoals, a bed roughness of 0.025 was used. A value of 0.015 was used in the deeper water where water depth is greater than 6 m. In the transitional reach, Manning coefficient was linearly interpolated from the above two limits according to the water depth.

With the rapid advancement in computer software and hardware, many types of turbulence models, from simple mixing length model to complex two-equation models, were exploited to simulate the horizontal and vertical diffusion processes (ASCE Task Committee, 1988). However, as indicated in ASCE Task Committee Report (1988), in many large-water-body calculations a constant eddy viscosity or diffusivity over the whole flow field can be used. This crude assumption, employed mainly in connection with the depth-averaged model, is often sufficient in simulations of large regions because horizontal turbulent momentum transport is not important in such cases, and the heat and mass transfer cannot be separated from dispersion effects due to vertical non-uniformities and from numerical diffusion effects. In this model, a constant horizontal eddy viscosity/diffusion coefficient and mass dispersion coefficient of 100 m^2/s was used, which was the same value as that used by Wang *et al*. (1992) in simulating the tidal current in Lingding Sea.

The coefficients for determining the sediment-carrying capacity given by Eq. 4.11 should be determined from field data. As a simulation to identify the general characteristics, a value of k =0.010 was adopted based on the author’s experience in other rivers in China.

4.4 Field data

The Hong Kong Government commissioned a number of strategic studies to assess cumulative impacts of coastal development schemes. Strategic Sewage Disposal Scheme Stage II was carried out from July 1992 to July 1993, which covered both Hong Kong and part of China mainland waters. At each station (see Fig. 4.1), vertical profiles of temperature, salinity, and flow velocity at 1 m interval through the water column were recorded by ADCP and CTD continuously for 26 hours at time intervals of 10 minutes.

The vertically averaged current and salinity from 6:00, August 5 to 18:00, August 6, 1992, during neap tide and, from 0:00, August 12 to 12:00, August 13, 1992, during spring tide, were used as the wet season condition. The vertically averaged current and salinity from 6:00, January 9 to 18:00, January 10, 1992, during spring tide and from 6:00, January 17 to 18:00, January 18, 1993, during neap tide, were used as the dry season condition.

4.5 Model validation

To investigate the hydrodynamics and mass transport in the PRE, it is necessary to do some model validation to show the appropriateness of the chosen model parameters. The four main harmonic tidal components predicted from the measured tidal levels at stations Humen (HM), Chiwan (CW), Tap Shek Kok (TSK), Lok On Pai (LOP), Tsing Yi (TY), Macau (Mac), Tai O (TO), H09, H11 and Tung Lung (TL) in the wet season were compared with the computed results as shown Fig. 4.2. The computed tidal process at off-shoal station H09 is in very good agreement with the predicted one. Computed tidal processes at the outer part of Lingding Sea, such as Macau along the west coastal line and Lok On Pai in the Hong Kong Waters, are satisfactory. However, at stations Humen and Chiwan, differences obviously exist between predicted and computed tidal levels, especially during low tide. The computed levels during low tide are higher than the corresponding predicted values. This may be due to the rather coarse finite elements, and the average boundary conditions adopted at the river outlets. As a whole, the computed results can represent the tidal processes in Lingding Sea quite well, with both the amplitude and phase of the tide in good agreement with corresponding predicted values.

Fig. 4.3 and Fig. 4.4 show the comparison of computed and observed tidal current in the wet season (August 1992) and the dry season (January 1993), respectively at several stations. Computed tidal currents are in good agreement with the observed ones generally. This means that the tidal dispersion coefficient and the bed roughness used in this model are appropriate to the PRE.

Fig. 4.5 and Fig. 4.6 compare the computed and observed salinity in the wet season and the dry season, respectively at the same stations. Salinity in the PRE due to brackish water intrusion depends greatly on the freshwater input from the Pearl River outlets. The differences of salinity between neap and spring tides are small. However, the computed values of salinity at stations WF1 and WQ9 near the west coastline are obviously smaller than the corresponding observed values, especially in the wet season. This can be attributed to the approximate upstream boundary conditions adopted at the river outlets. As mentioned in the above section, because information of real-time flow rates is not available, long-term seasonal mean flow rates were used at the Pearl River outlets. It is possible that great differences exist between the long-term seasonal mean flow rates and the particular flow rates in August 1992 and January 1993. More accurate flow rates through outlets are necessary for accurate prediction of salinity pattern during particular time periods. However, for qualitative investigations, the computed results of both tidal current and salinity are adequate to capture general characteristics.

4.6 Results and discussions

After the model validation, three different cases of model simulation were performed for studying the characteristics of hydrodynamics and mass transport in the PRE with the same boundary conditions. CASE 1 considered the Coriolis force but excluded surface wind stress. In CASE 2, neither Coriolis force nor surface wind stress were considered. CASE 3 considered both the Coriolis force and surface wind stress. The following analysis is based on the results of CASE 1 except stated otherwise.

4.6.1 Hydrodynamics

4.6.1.1 Tides and tidal current

Tide in the PRE is of the irregular semidiurnal and partially mixed type. The tidal oscillations from the Pacific Ocean first spread into the South China Sea from the NE direction, coming through Taiwan Strait and Bashi Channel, and then pass through the Hong Kong Waters into Lingding Sea. When tides pass through the Hong Kong Waters, Ma Wan strait (see Fig. 3.1) forms a major barrier to the tidal wave propagation (DELFT report, titled ‘Model calibration and validation report, Part 1’, 1998). Fig. 4.7 illustrates the tidal propagation in the PRE. Tides from Waglan Island (see Fig. 3.1) arrive at Chiwan and Macau after about 1 to 2 hours. Because of the effects of coastline configuration and submarine topography of the PRE, tidal energy converges when tide propagates into the Lingding Sea, resulting in tidal range increases. Under the actions of seabed friction and the strong freshwater input from the Pearl River outlets, tidal deformation exists in the PRE in which the ebbing duration is lengthened (Xu *et al*., 1985; Wang *et al*., 1992; Ying *et al*., 1993). This feature can also be seen from Fig. 4.3 and Fig. 4.4. The strong freshwater input boosts up the ebbing flow and restrains the intrusion of seawater.

Tidal current in the PRE is mainly dominated by the tidal wave from the open sea, freshwater discharge from river outlets, density current, topography and wind.

Fig. 4.8 shows the tidal current during flooding and ebbing under spring tides in both the dry and wet seasons. The flow patterns in flooding and ebbing in the PRE are very complex. During flooding, tidal flow coming from offshore and the Hong Kong Waters, passes though the Lantau channel and Urmston channel (see Fig. 3.1) into Lingding Sea. With the effect of Coriolis force and the transverse surface slope, which is generally inclined in the SE direction (Wang *et al*. 1992, Ying *et al*. 1993), the salt water flows riverward along the channels, the flow direction nearly aligned with the coastline in the eastern part of the estuary. In the west shoals, because of the higher seabed roughness, tidal energy dissipates quickly, and hence the flow is relatively smaller. During ebbing, the flow velocity in the west shoals is relatively larger, which is due to the transverse surface slope and strong freshwater discharge from Jiaomen, Hongqimen and Hengmen. Flows in the west shoals, mostly go into the West Channel and partly pass though the Middle Shoal into the East Channel, then discharge into the South China Sea through Lantau and Urmston channels.

Fig. 4.9 and Fig. 4.10 show the residual flows during neap tide and spring tide in the wet and dry seasons, respectively. It can be seen that the Eulerian residual flow due to freshwater runoff is dominant in the PRE. The effect of Stokes drift from tidal asymmetry is relatively slight, especially in the wet season. The maximum Eulerian residual flow velocities are more than 30 cm/s in the wet season and 10cm/s in the dry season and are located at the Pearl River outlets. However, the velocity reduces quickly away from the outlets and is around 10-20 cm/s in both the East and West channels in the wet season. In the dry season, the residual flow in the West Channel is larger than that in the East Channel due to the larger effect of the residual flows from Jiaomen, Hongqimen and Hengmen on the West Channel. It is obvious that the Eulerian residual flow in the Hong Kong Waters is small. Most of the Eulerian residual flow discharges into the South China Sea through shoals and channels located west of Lantau Island. This feature of the Eulerian residual flow indicates that only a small quantity of sediment from the Pearl River can transport into the Hong Kong Waters. This is the main reason why sediment concentration in the Hong Kong Waters is always much lower than that in the western part of Lingding Sea. The direction of the Eulerian residual flow is consistent with the ebbing tidal currents. At the west shoals, it is in the SE to ESE direction. The Eulerian residual flow from the East Channel and East Shoal, which flows parallel to the east coastline of Lingding Sea, separates into two branches, with one branch flowing into the Hong Kong Waters through Urmston Channel and the other merging with flows from the West Channel before flowing into the South China Sea. Under the dual action of the Coriolis force and the off-shoal Eulerian residual flow in the SW direction, the Eulerian residual flows from Lingding Sea turn eventually to the west.

Stokes drift due to tidal asymmetry is an important mechanism to transport the sediment and salinity from the open sea into the estuary. Stokes drifts from the South China Sea are enhanced with the increase of the tidal range landward in the PRE with their directions basically opposite to the Eulerian residual flows. In general, Stokes drifts in shallow shoals are larger than those in deep channels. This phenomenon is due to the higher bottom friction in shallow regions, which causes asymmetric tides. The maximum Stokes drift occurs around Neilingding Island, irrespective of the season and tidal type. Wang *et al*. (1992)'s simulation also revealed this maximum Stokes drifts region. Stokes drifts larger than 2 cm/s during spring tides and larger than 1 cm/s during neap tides can also be found at the shoal between Lantau channel and Macau, shoals between west outlets, the East Shoal and some shoals in the Hong Kong Waters.

In general, the dominant residual flow in the PRE is Eulerian one, which resulting from strong freshwater input from the Pearl River. The maximum Eulerian residual flow occurs in the vicinity of the west three outlets. The magnitude of Eulerian residual flow in the West Shoal is larger than that in the West Channel, which is larger than that in the East Channel. Most of the Eulerian residual flow discharges through the west shoals and channels of Lantau Island into the South China Sea. The direction of Eulerian residual flow is consistent with the tidal ebbing in the PRE. Stokes drifts due to tidal asymmetry are also significant in transporting mass from open sea, especially during spring tide in dry season (Xu *et al*., 1985; Ying *et al*., 1993). Maximum Stokes drifts occur around Neilingding Island, and Stokes drifts in shoals are greater than in deep channels because of the higher seabed roughness in shallow regions.

4.6.1.2 Effects of Coriolis and wind on current

In order to ascertain the effects of the Coriolis force and monsoon on the tidal current, salinity and sediment transport in the PRE, two more cases were also studied. Case 2 considered neither Coriolis force nor wind stress; Case 3 considered both Coriolis force and a wind blow with a velocity of 5 m/s from the SW direction in the wet season or 3 m/s from the NE direction in the dry season. The monsoons considered are the typical ones in the PRE. The computed results of these two cases are also plotted in Fig. 4.3 and Fig. 4.4 together with those of Case1 for comparison. It can be seen that the effects of the Coriolis force and surface wind stress on the tidal current in the PRE are not significant. The differences in the computed flow velocities are within several centimeters per second. This is expected as the magnitudes of the Coriolis force and wind are much smaller than those of river runoff and tides. However, these two factors still have effects on the sediment transport in the long term, especially the wind which could generate wave and increase the turbulence level. The long-term effect of the Coriolis and wind on the flow field could be seen from the change of the residual flow.

Fig. 4.11 and Fig. 4.12 show the Eulerian residual flow for Case 2 and 3 in the wet and dry seasons, respectively. Comparing with the Eulerian residual flows in Fig. 4.9 and Fig. 4.10, it can be seen that under the action of the Coriolis force, the direction of the residual flow turns to SWW from SSW. This means that the Coriolis force further concentrates the suspended sediment to the western part of the PRE. The wind stress affects the residual flow in both magnitude and direction. In the wet season with the typical monsoon blowing from the SW direction at about 5 m/s, the Eulerian residual flow in Lingding Sea is changed to the SSE direction. Furthermore, the residual flow direction is reversed from SW to NE after it flows out of Lingding Sea. Undoubtedly, this residual flow pattern transports more sediment into the Hong Kong Waters. In the dry season, because the direction of the typical monsoon from NE is consistent with the direction of the Eulerian residual flow, the wind will drive the residual flow to the SW direction and finally to the west after it flows out of Lingding Sea. The Eulerian residual flow is enhanced between Macau and Hong Kong. These help to transport more sediment to the western part of the estuary.

4.6.2 Suspended sediment transport

Sediment transport in the PRE is very complex. It is not only affected by the fresh water from the Pearl River, but also by the tidal pumping, local resuspension, flocculation, monsoon, and wave. The main sources of sediment in the PRE are suspended sediments from the river outlets. The sediment transport near the three west outlets basically is dominated by the river discharge, except near Humen where the effect of tidal current is strong. Sediments are transported into Lingding Sea from the open sea only in the dry season, but the quantity is small (Xu *et al.*, 1985). Besides the seasonal variation of sediment input from the Pearl River, local resuspension is also an important factor affecting the suspended sediment pattern within tidal cycles in the PRE. Fig. 4.13 shows the variation of computed sediment concentration at several stations during a tidal cycle. It can be seen that there are large variations in sediment concentrations within a spring tidal cycle. Deposited sediments are resuspended after the occurrence of the maximum ebbing or flooding tidal velocities, with the maximum sediment concentration lagging behind the maximum tidal current by about 3 hours. Fig. 4.14 shows the relationship of suspended sediment concentration and sediment-carrying capacity with velocity at stations WF5 and WF6. It can be seen that the critical flow velocity for resuspension or deposition is about 0.4 m/s. When velocities rise above this critical value, sediment-carrying capacities in these two stations exceed the suspended sediment capacity. The maximum sediment-carrying capacities are several times larger than the suspended sediment concentration. Because of the short duration of each ebb or flood and the lag between maximum sediment concentration and velocity, the suspended sediment in the PRE is always in a state of non-equilibrium, with the sediment concentration below the sediment-carrying capacity most of the time. The sediment concentrations shown in Fig.4.14 are independent of each other, which have different background sediment concentration. Therefore, Fig. 4.14 shows no relationship between sediment concentration and sediment carrying capacity.

Fig. 4.15 compares the computed sediment pattern during an ebbing neap tide in August 1992 with a satellite imagery taken on September 14, 1997, which is near the end of the wet season. Although at different calendar dates, it could also be seen that the computed sediment concentration pattern in the PRE resembles the turbidity pattern captured in the satellite image.

Fig. 4.16 shows the computed suspended sediment concentration distributions during spring tides in both wet and dry seasons. The suspended sediment concentration in channels is less than that in shoals. Great differences of concentration near river outlets between wet and dry seasons indicate that seasonal variation in sediment input from the Pearl River has a great effect on the suspended sediment concentration in the PRE. Sediments coming from the Pearl River will deposit quickly when sediment-laden flow enters into Lingding Bay due to the reduction in flow velocity and sediment flocculation in the brackish water (Xu *et al*., 1985; Ying *et al*., 1993). Higher concentration regions also can be found at the West Shoal, East Shoal, south of the Middle Shoal around Neilingding Island, Tonggu Shoal to the NW of Lantau Island, and some shallow parts around Lantau Island. These are predominantly the result of resuspension. The 100 mg/l concentration contour basically coincides with the 5 m depth contour in the western part during ebbing. During the slack period, the 100 mg/l concentration contour shifts upstream, especially in the shoal to the south of Qi’ao

Island and east of Macau, where suspended sediments are dominated by deposition and resuspension associated with the change of tidal current. Sediment concentrations in the West and East Channels, especially in the East Channel, vary slightly during tidal cycles or seasonally. This phenomenon suggests that most of the sediments from the three west Pearl River outlets in Lingding Bay are transported into the South China Sea through west shoals, and only a small quantity of sediment particles travels across the West Shoal and enters the West Channel, which transports downstream part of the sediments from Humen. The East Channel is a passage for a large portion of the sediment from Humen. In general, the layout of the outlets and the characteristics of sediment and runoff from the Pearl River determine the characteristics of the suspended sediment distribution in the PRE. The strong runoff from the three west outlets and higher sediment concentration in the West Shoal enhances the development of the West Shoal, resulting in a gradual spread of the West Shoal to the east (Xu *et al*., 1985; Ying *et al*., 1993). As discussed above, the Eulerian residual flow in the PRE discharges into the South China Sea through Lingding Sea in the SW direction, resulting in lower suspended sediment concentration in the Hong Kong Waters. Except for the shallow regions near the coastline, the sediment concentration is less than 50 mg/l in the Hong Kong Waters.

In general, the suspended sediment concentration in the PRE varies seasonally and tidally. The seasonal variation is due to the corresponding changes in sediment input from the Pearl River, and the variation within tidal cycles is mainly due to the deposition and resuspension of sediment. The sediment concentration in channels is less than that in shoals basically due to the lower sediment concentration in the runoff from Humen which discharges into the East and West channels. Except for the deposited sediment in Lingding Sea due to the reduction in flow velocity, most of the sediments are transported into the South China Sea through the West Shoal and channels to the west of Lantau Island. Sediment concentration in the Hong Kong Waters is much lower than that in the western side of the estuary.

4.7 Summary

The hydrodynamics and sediment transports in the PRE are complicated as seen from the computed results. In this study, a depth-integrated two-dimensional hydrodynamics and sediment transport model, modified from a multi-layer three-dimensional model, was applied. Tidal levels were verified using four main tidal components. The simulated results were in very well agreement with the predicted ones from recorded tidal levels. Model results show that tidal flow can penetrate more riverward along the East and West channels. However, in the west shoals, the tidal wave energy dissipates quickly due to the shallow water. The flooding current is smaller than the ebbing current due to the strong riverine runoff. An analysis of residual flow shows that the Eulerian component from non-tidal drift is the dominant one in the PRE. The maximum residual velocity is about 30 cm/s, and the direction of the residual flow is consistent with the direction of tidal flooding and ebbing. The Stokes drift velocity is less than 5 cm/s, but it is an important source of energy to drive the sediment transport from the open sea. The effect of Coriolis force on the magnitude of tidal current is insignificant. However, the Coriolis force deflects both the ebbing current and Eulerian residual flow to the west. This is one of the important factors causing higher sediment concentrations in west shoals. Monsoon in the PRE has some influence on the

Eulerian residual flow. In the wet season, wind from SW direction causes a reverse of the Eulerian residual flow direction from SW to NE when it flows out of Lingding Sea. In the dry season, Eulerian residual flow is enhanced because the wind blows in the same direction, resulting in more sediments transport through west shoals into the open sea.

The computed results qualitatively reveal the characteristics of the salinity pattern in the PRE. Salinity in west shoals is lower than those in the east channels because of the runoffs from the three western outlets. It varies tidally and seasonally. However, because of the lack of data on real-time runoffs from the outlets and omission of the baroclinic term in the flow momentum equations, the accuracy of the simulated salinity field is not very realistic.

The characteristics of suspended sediment concentration were also investigated. Model results show that the sediment concentration in the West Shoal is high due to the inputs from the three western outlets and local resuspension. Resuspension plays an important role within tidal cycles because of the surplus sediment-carrying capacity. The sediment concentration in deep channels is smaller than that in the nearby shoals. This computed suspended sediment concentration pattern is consistent with a satellite image.

In this study, the effects of stratification due to summer runoffs have not been taken into account. However, the PRE is a partially mixed estuary with density stratification in wet seasons, intrusion of salt water and occurrence of turbidity maxima (Xu *et al.*, 1985; Tian, 1986). To investigate the effects of density stratification due to salinity gradient in both the horizontal and vertical directions on the flow pattern and sediment transport, a 3-D model is required. This is the subject of the following chapter.

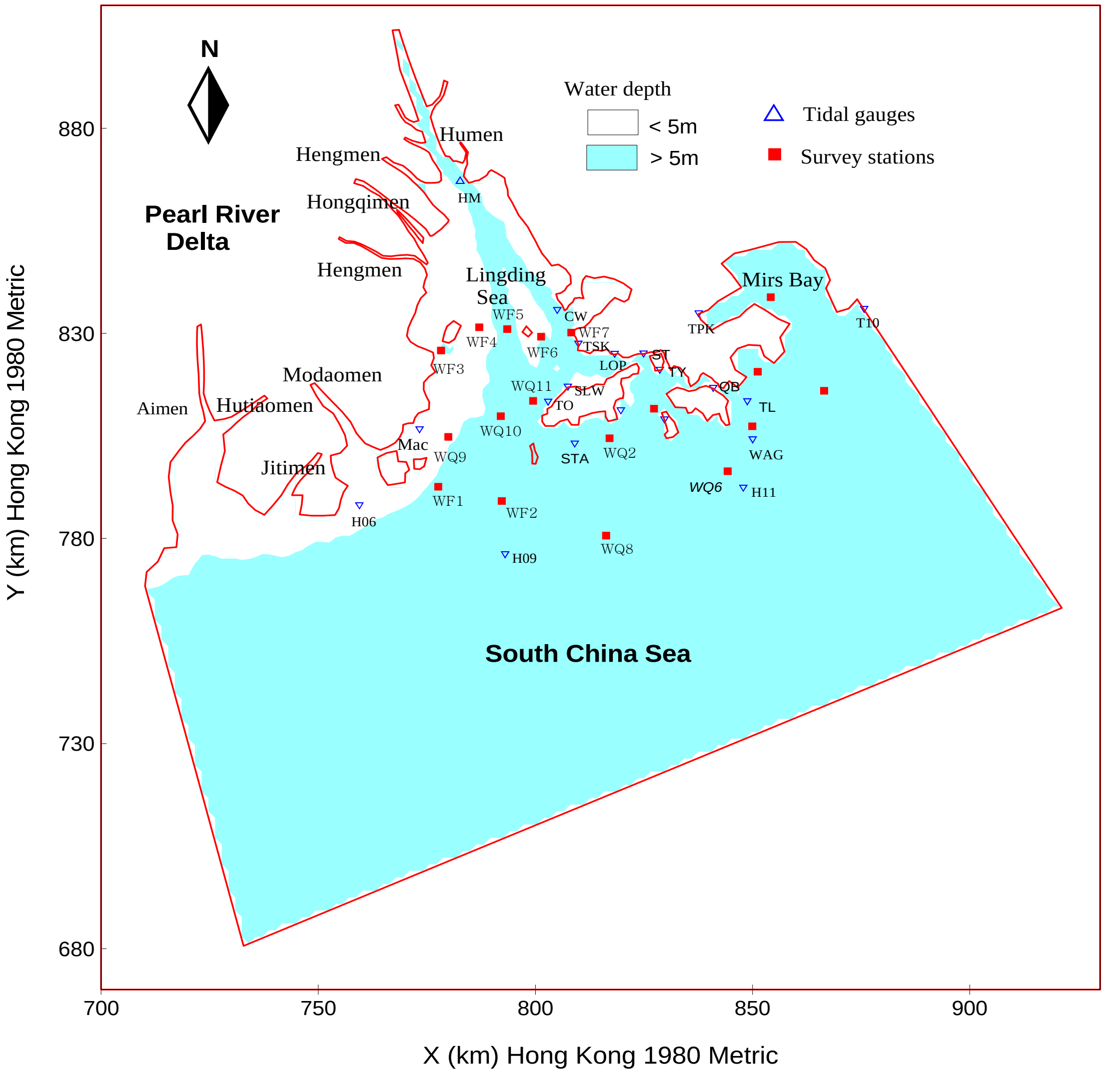

Fig. 4.1 Computational domain, tidal gauges and survey stations

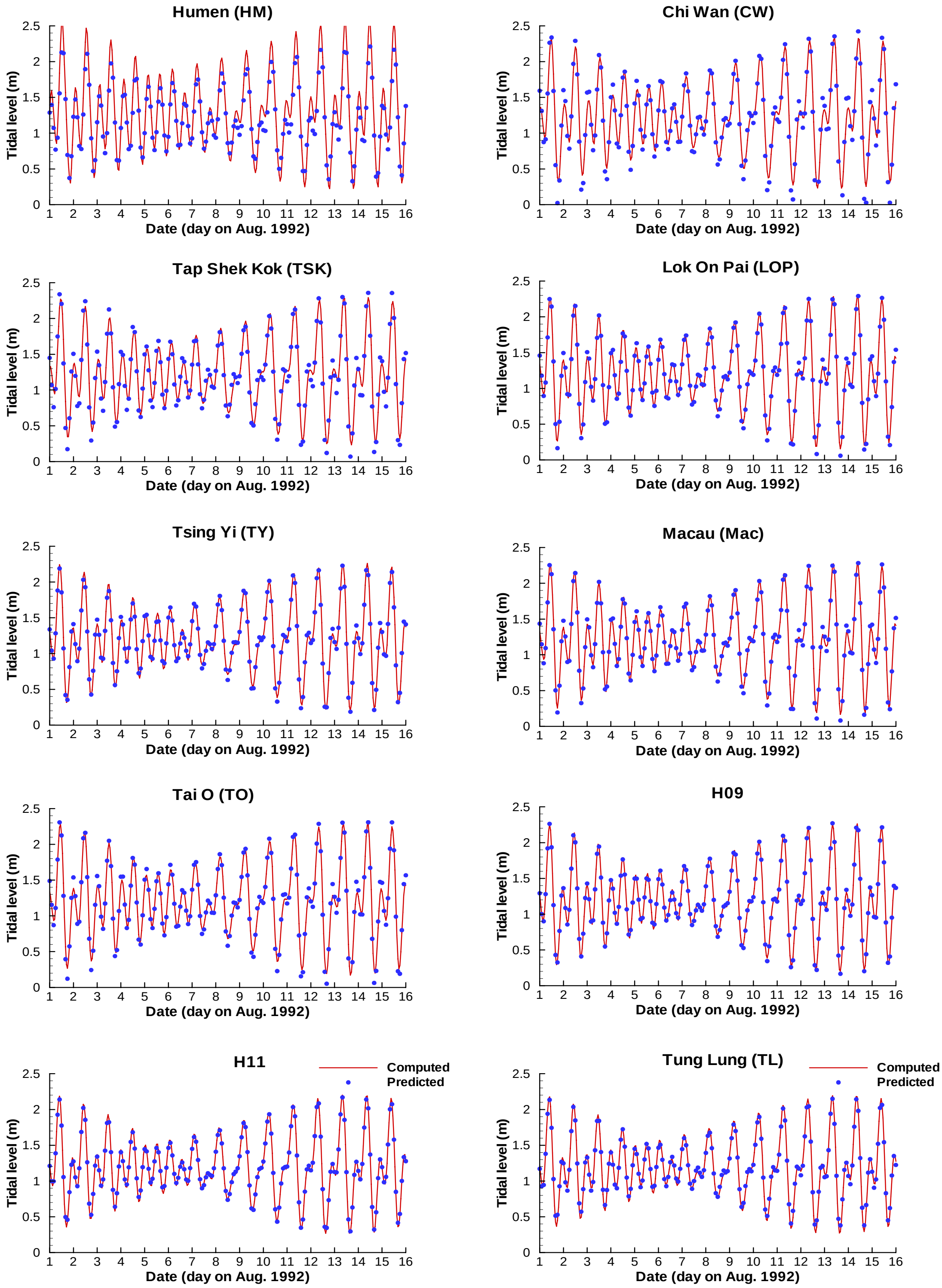

Fig. 4.2 Comparison of computed and predicted tidal levels

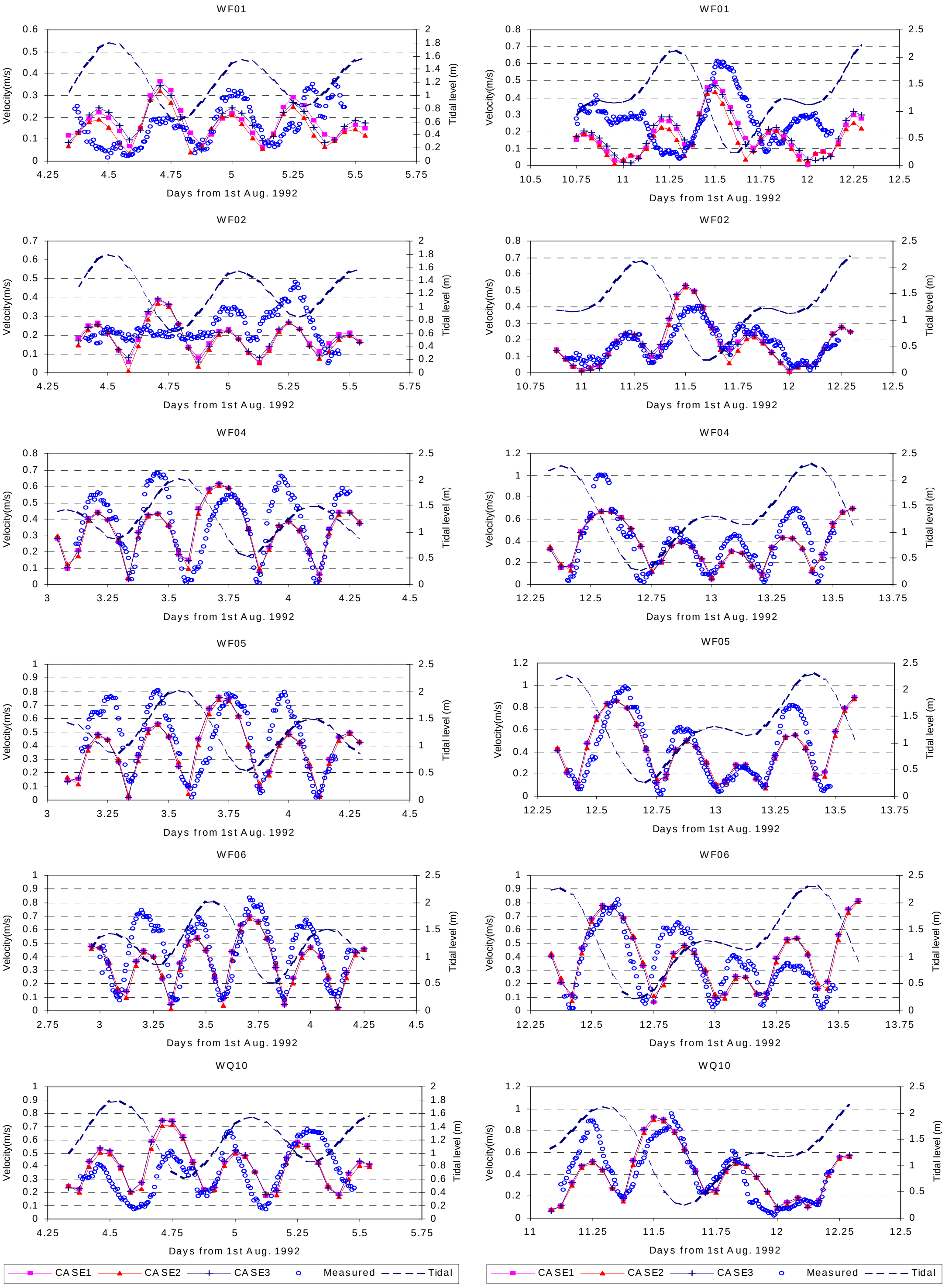

(a) Neap tide

(b) Spring tide

Fig. 4.3 Comparison of computed and measured current in the wet season (August 1992):Case1--with Coriolis but without wind; Case2--neither Coriolis nor wind; Case3--both Coriolis and wind

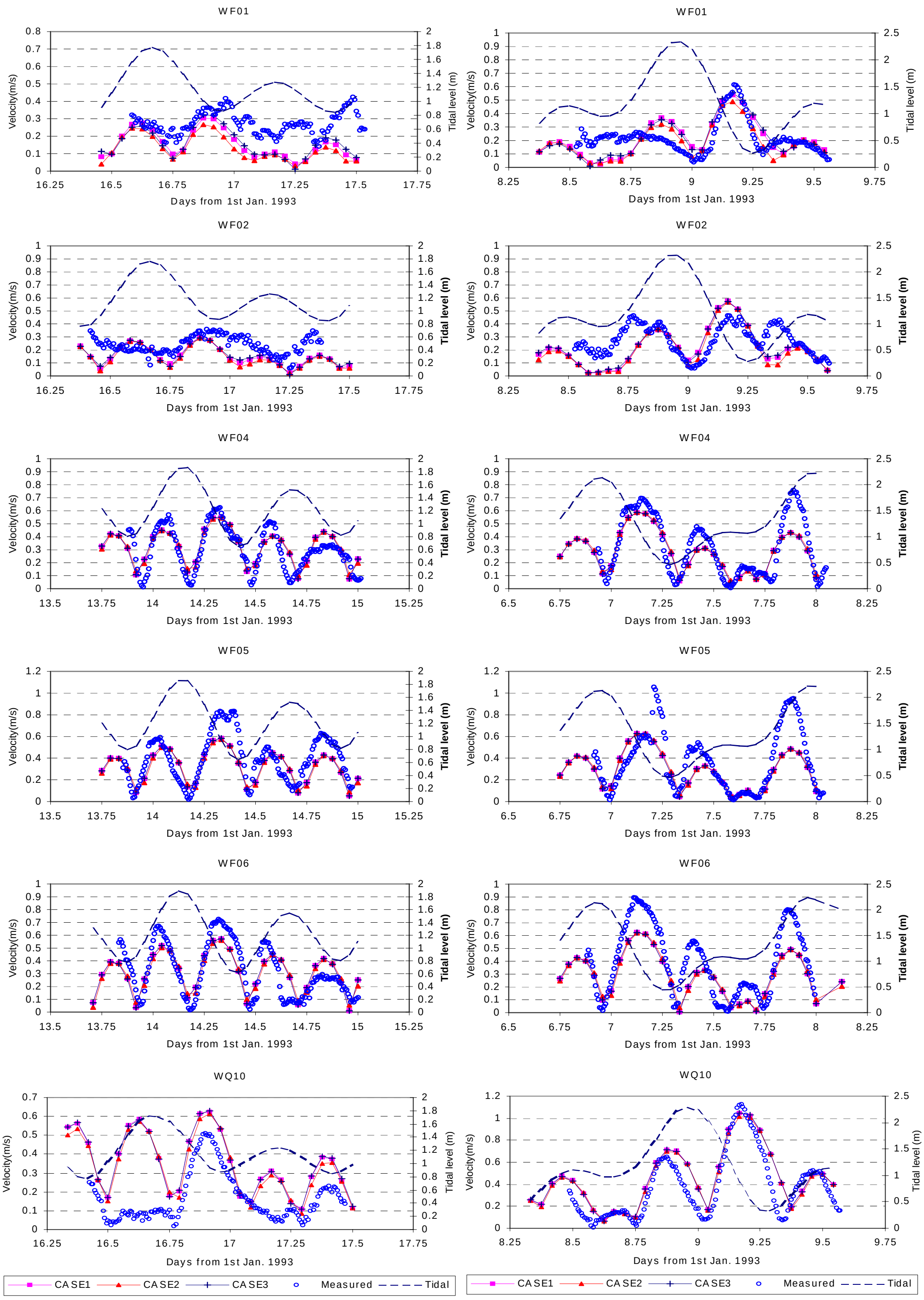

(Neap tide) (Spring tide)

Fig. 4.4 Comparison of computed and measured current in the dry season (January 1993): Case1--with Coriolis but without wind; Case2--neither Coriolis nor wind; Case3--both Coriolis and wind.

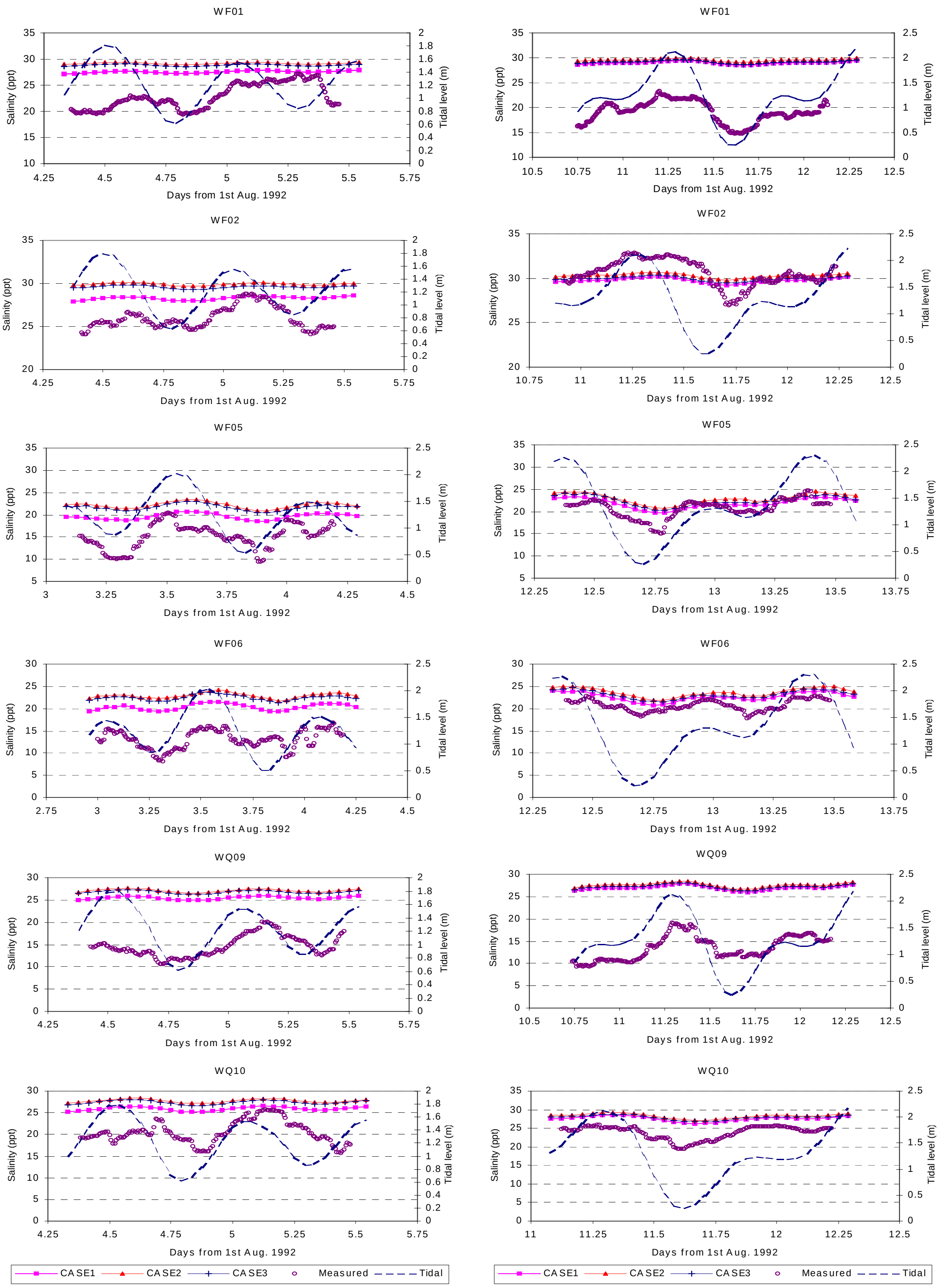

(Neap tide) (Spring tide)

Fig. 4.5 Comparison of computed and measured salinity in the wet season (August 1992): Case1--with Coriolis but without wind; Case2--neither Coriolis nor wind; Case3--both Coriolis and wind.

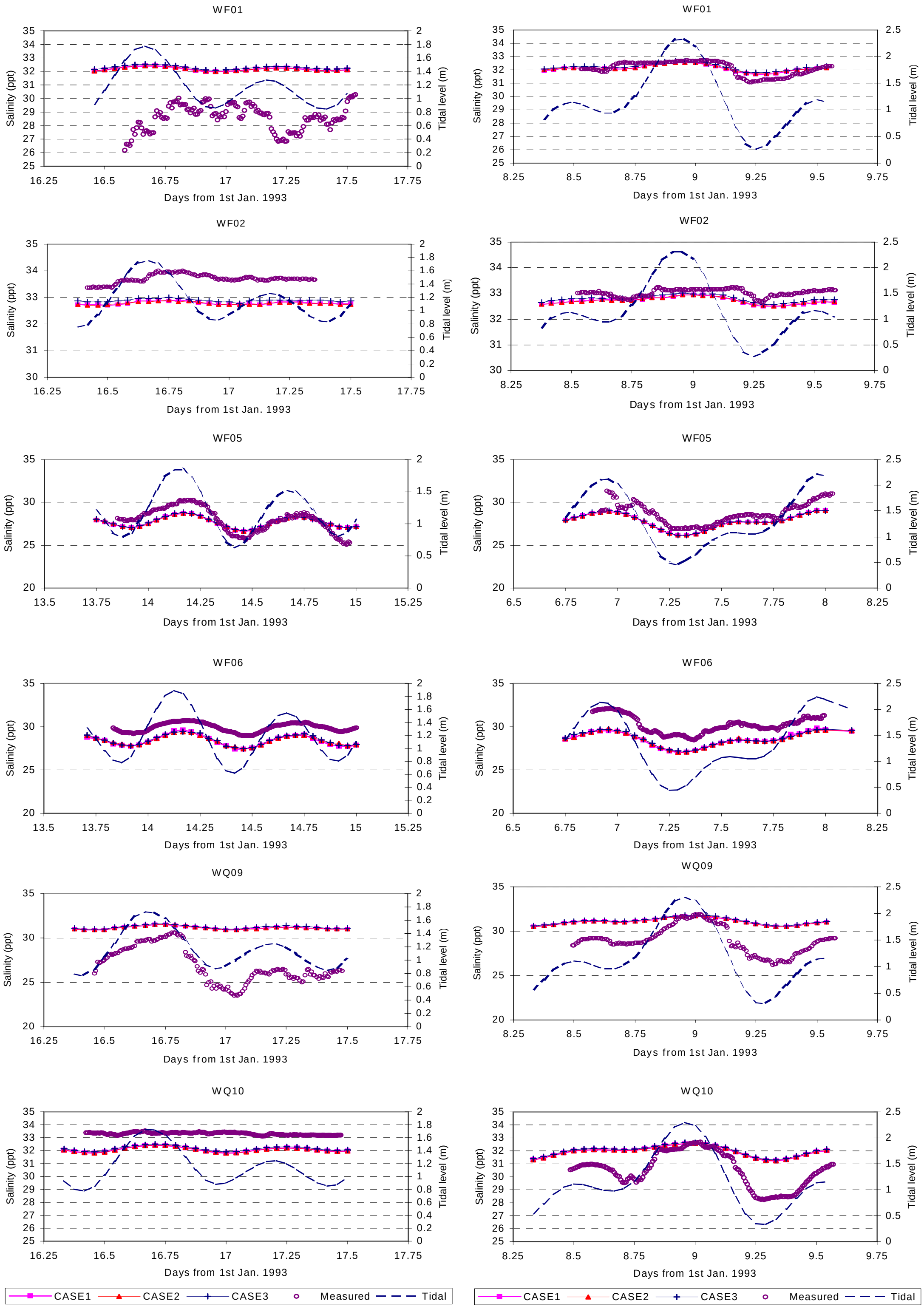

(neap tide) (Spring tide)

Fig. 4.6 Comparison of computed and measured salinity in the dry season (January 1993): Case1--with Coriolis but without wind; Case2--neither Coriolis nor wind; Case3--both Coriolis and wind.

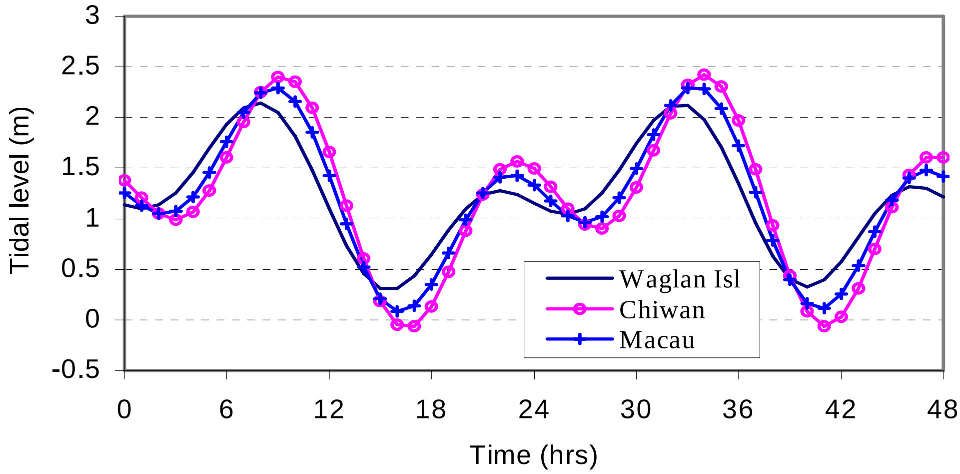

Fig. 4.7 Tidal propagation in the PRE

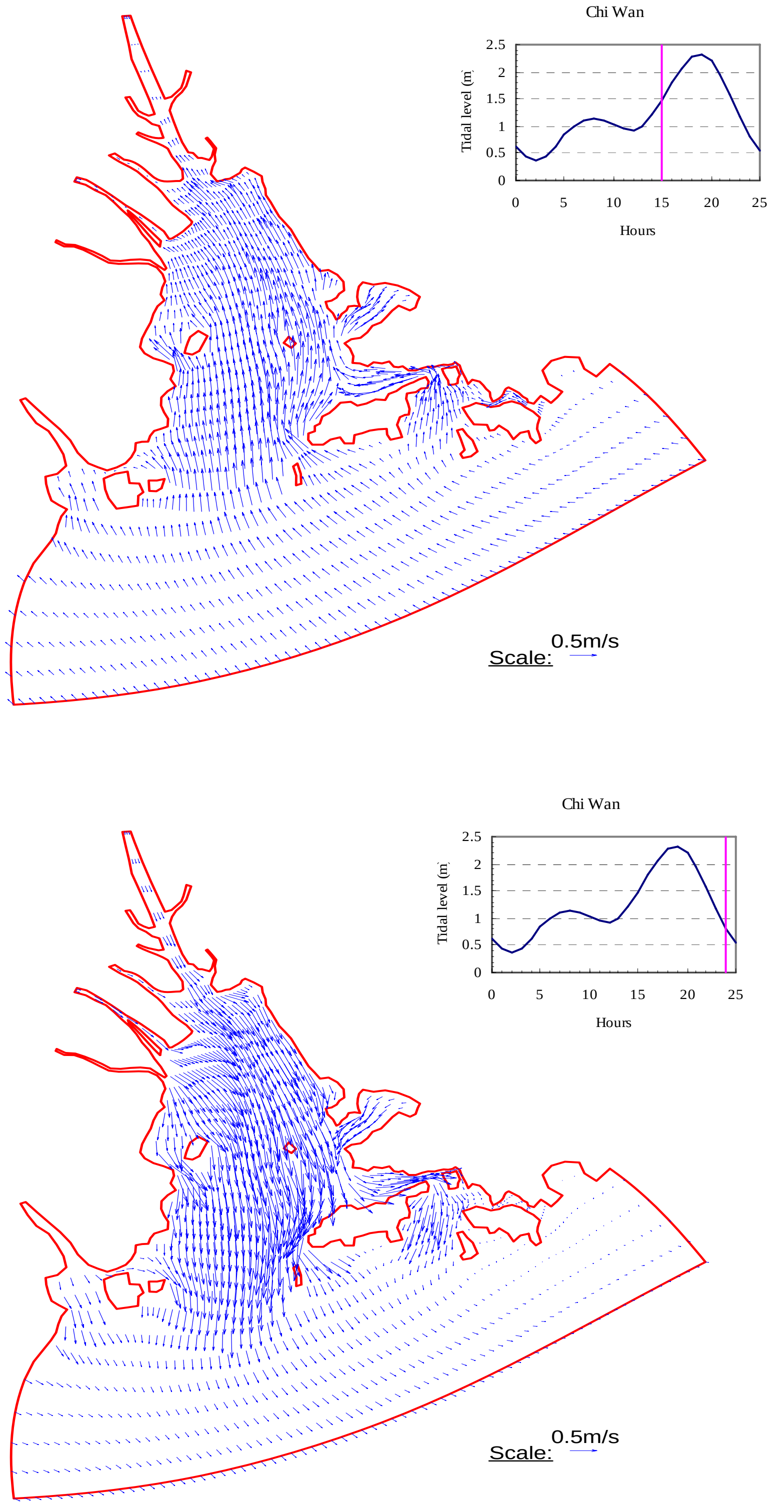

Fig. 4.8a Computed flow patterns during flooding and ebbing of a spring tide
in the dry season (January 1993)

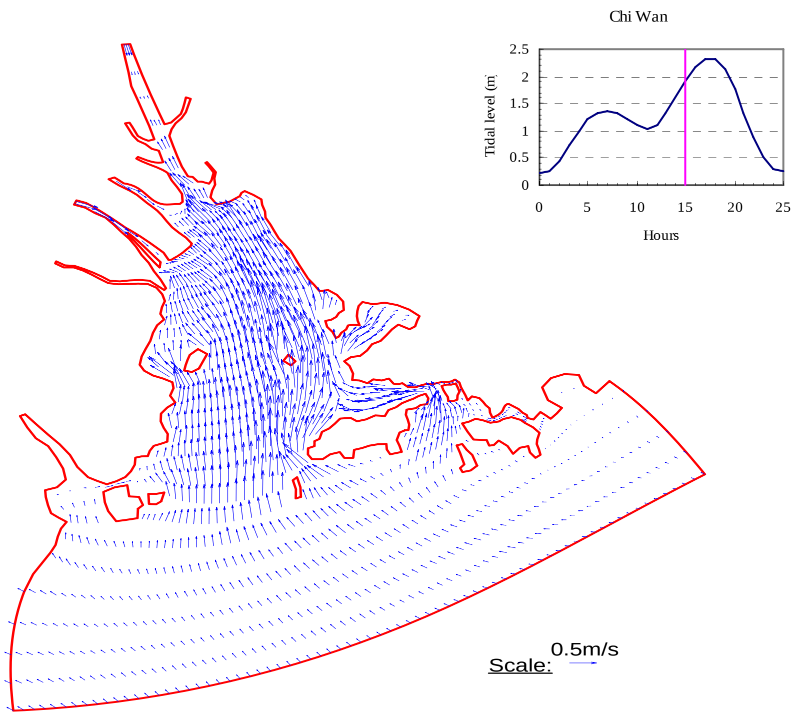

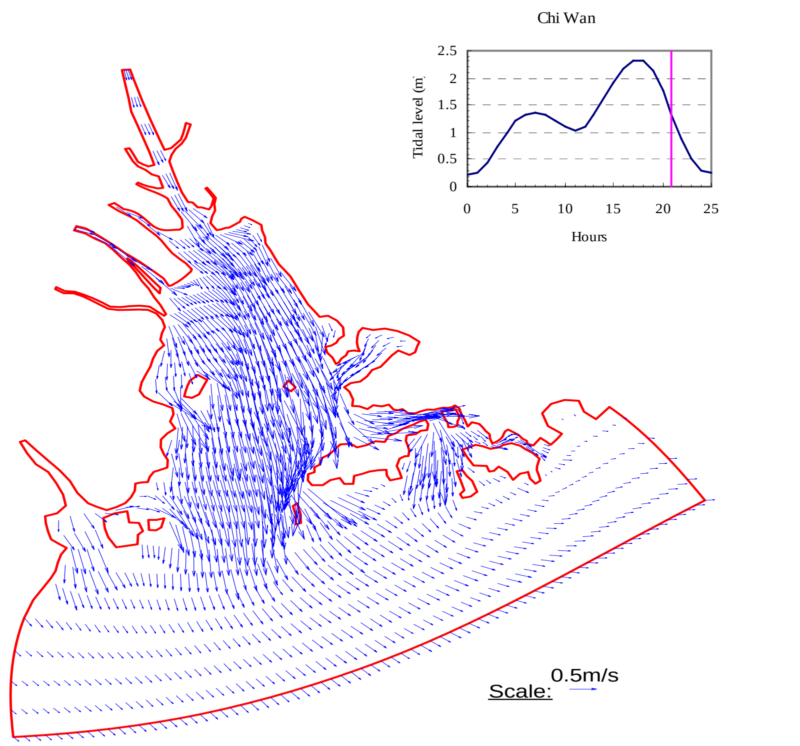

Fig. 4.8b Computed flow patterns during flooding and ebbing of a spring tide in the wet season (August 1992)

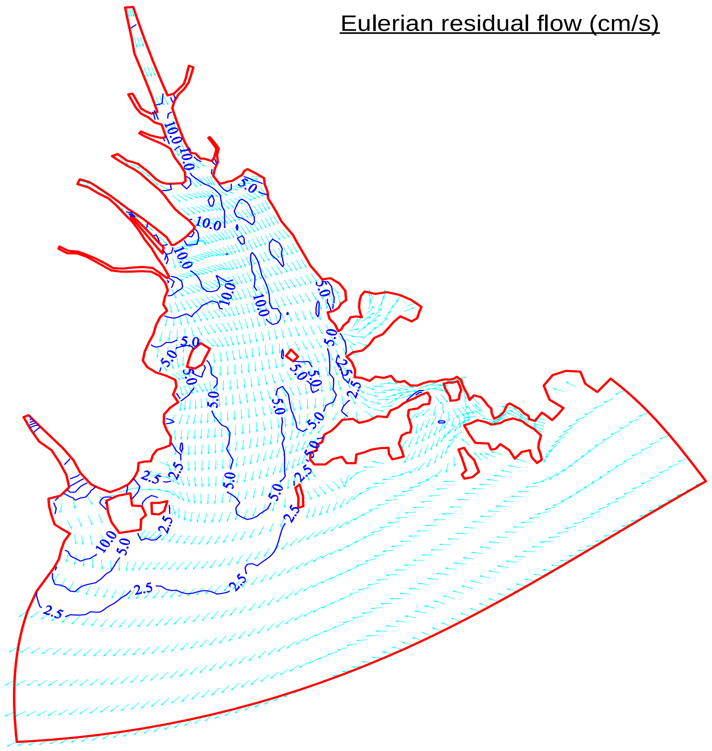

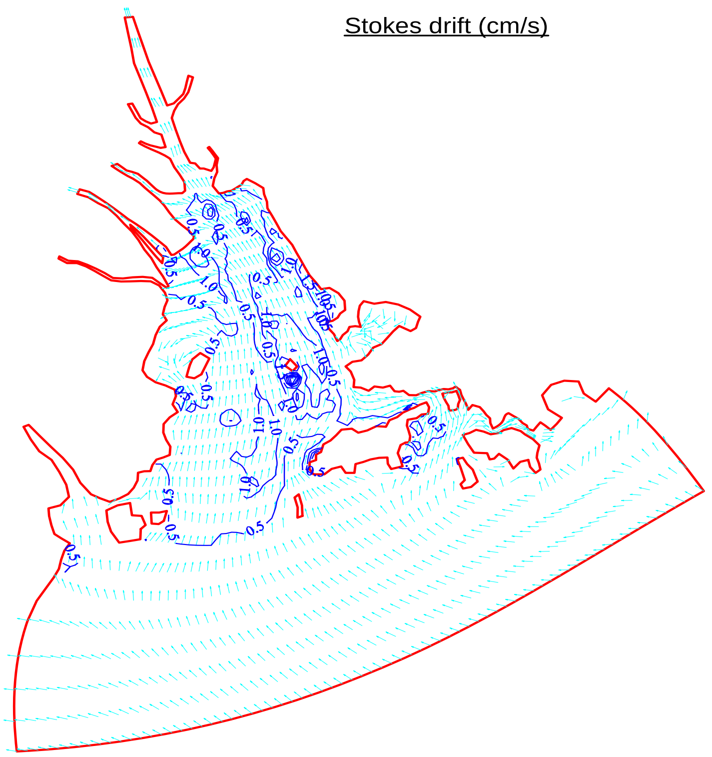

Fig. 4.9a Computed Eulerian residual flow and Stokes drifts of a neap tide in the wet season (August 1992): Contour lines represent the magnitude and arrows represent the direction.

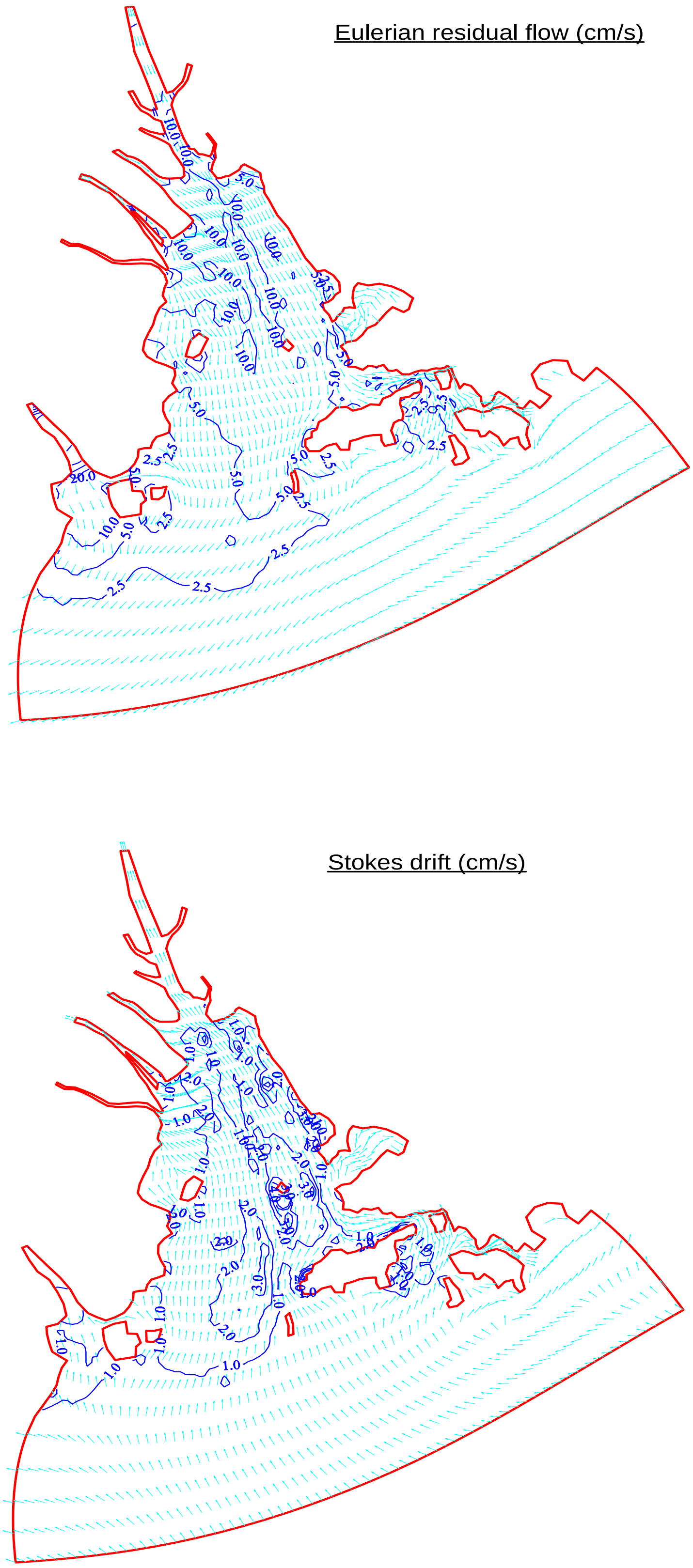

Fig. 4.9b Computed Eulerian residual flow and Stokes drifts of a spring tide in the wet season (August 1992): Contour lines represent the magnitude and arrows represent the direction.

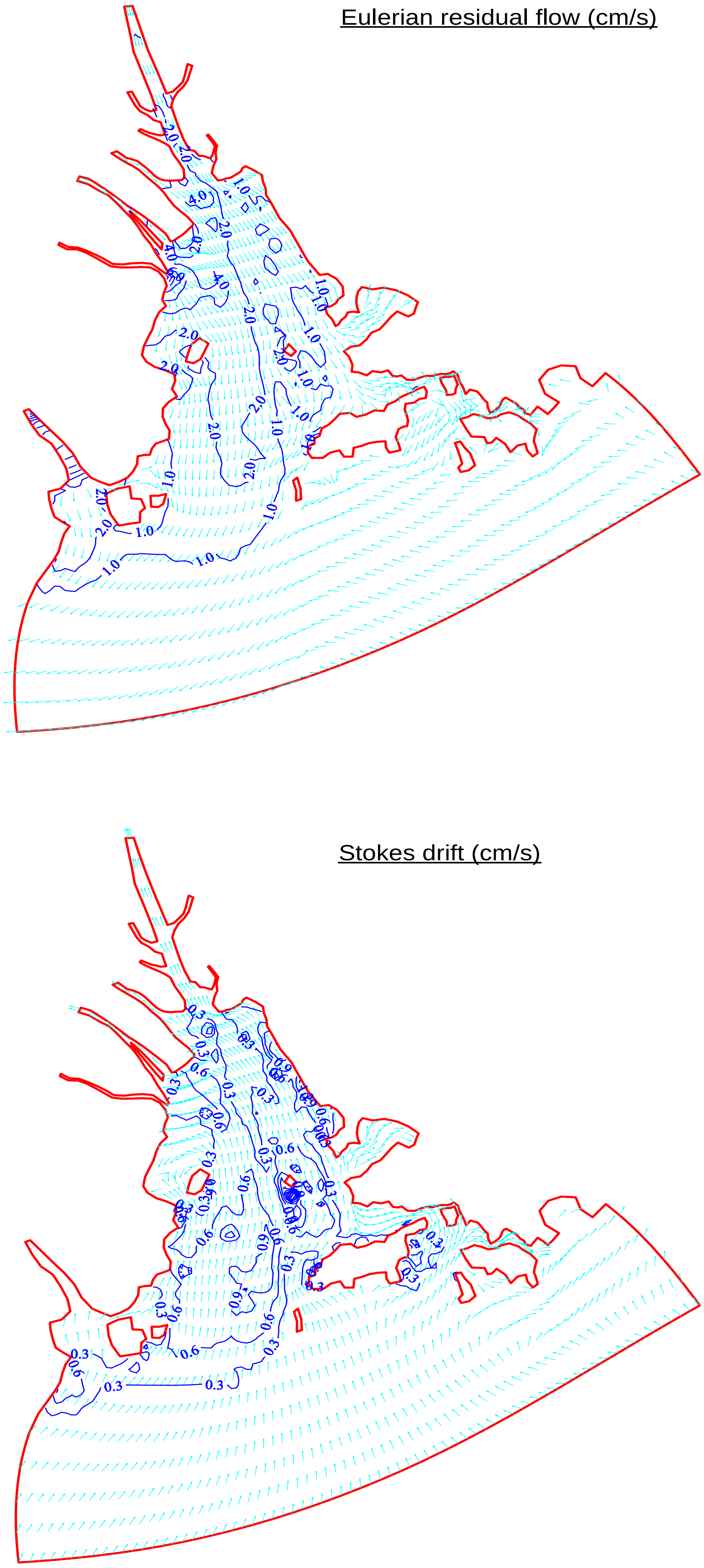

Fig. 4.10a Computed Eulerian residual flow and Stokes drifts of a neap tide in the dry season (January 1993): Contour lines represent the magnitude and arrows represent the direction.

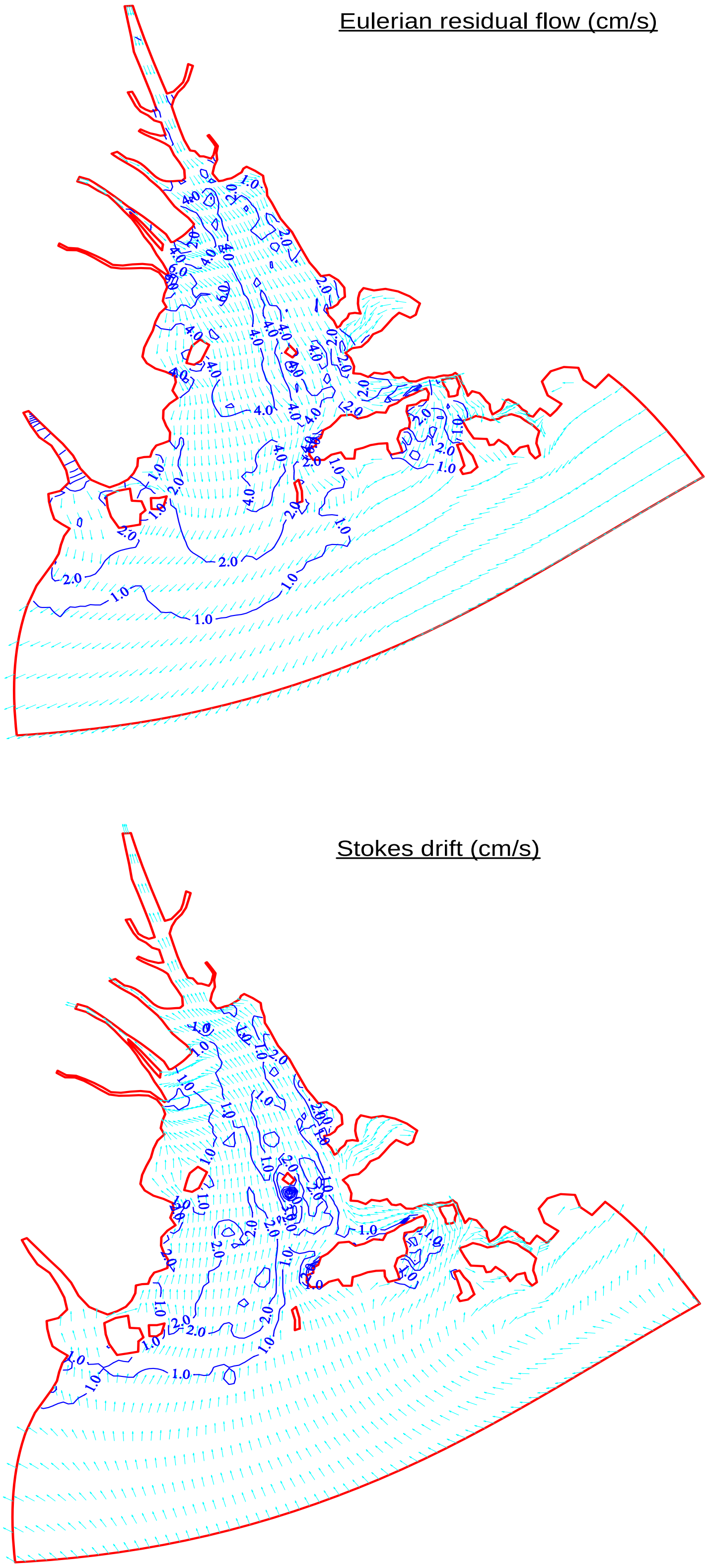

Fig. 4.10b Computed Eulerian residual flow and Stokes drifts under a spring tide in the dry season (January 1993): Contour lines represent the magnitude and arrows represent the direction.

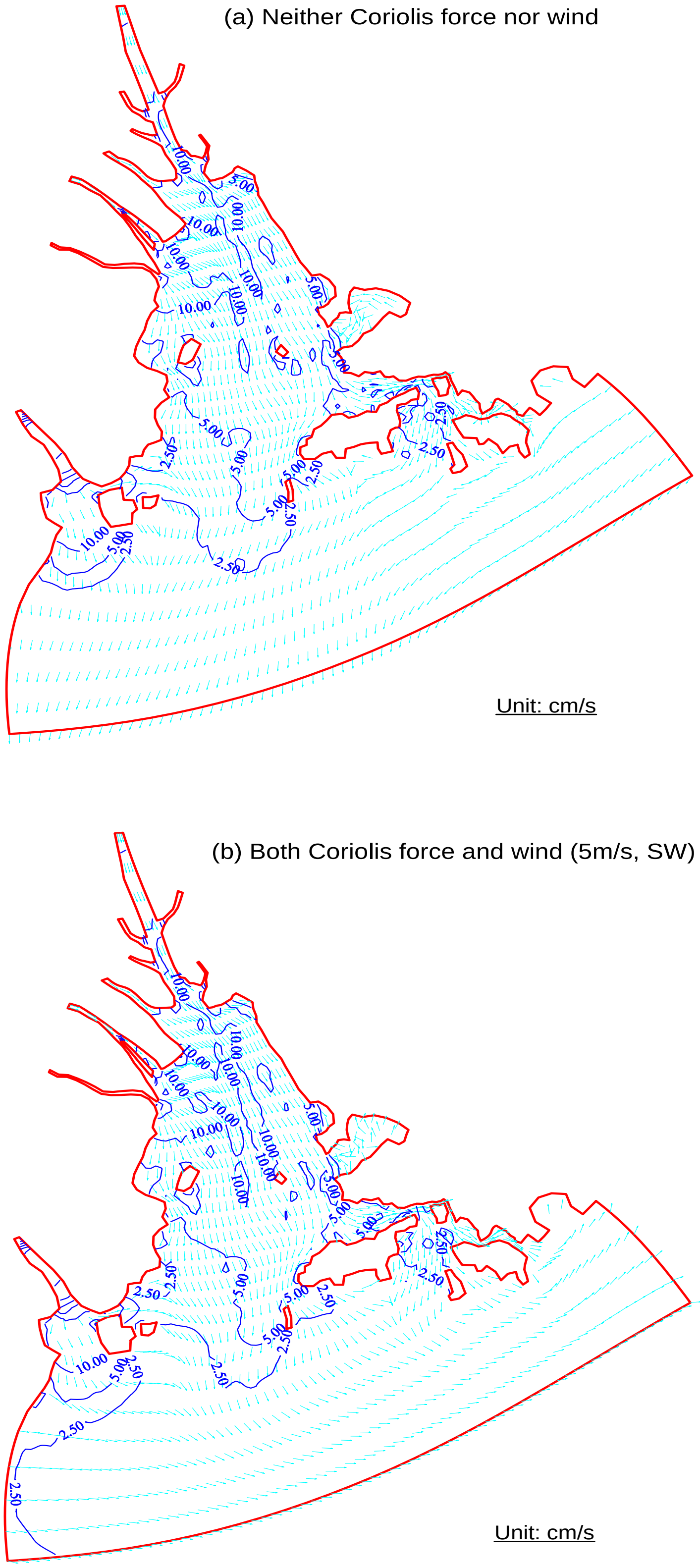

Fig. 4.11 Computed Eulerian residual flow during a spring tide in the wet season (August 1992)): Contour lines represent the magnitude and arrows represent the direction.

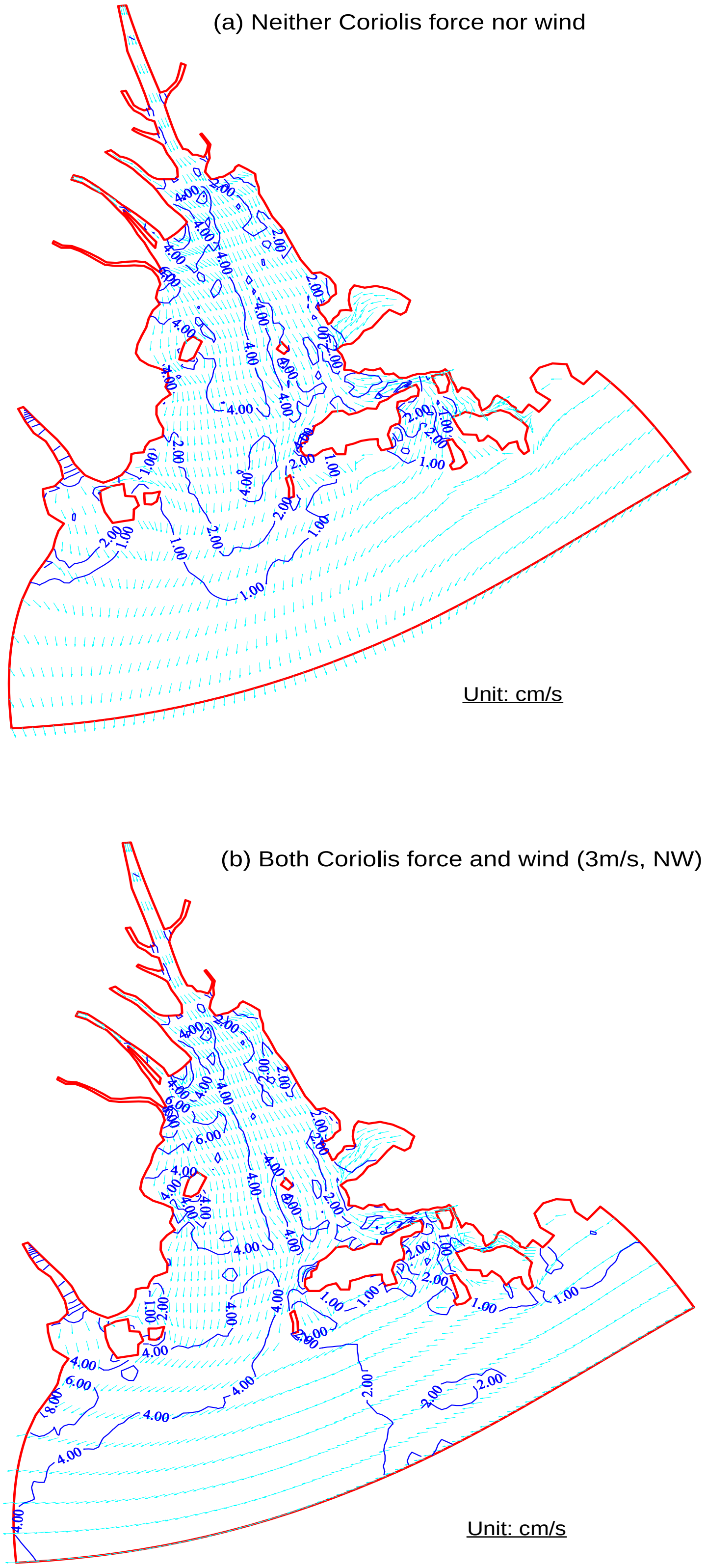

Fig. 4.12 Computed Eulerian residual flow during a spring tide in the dry season (January 1993) : Contour lines represent the magnitude and arrows represent the direction.

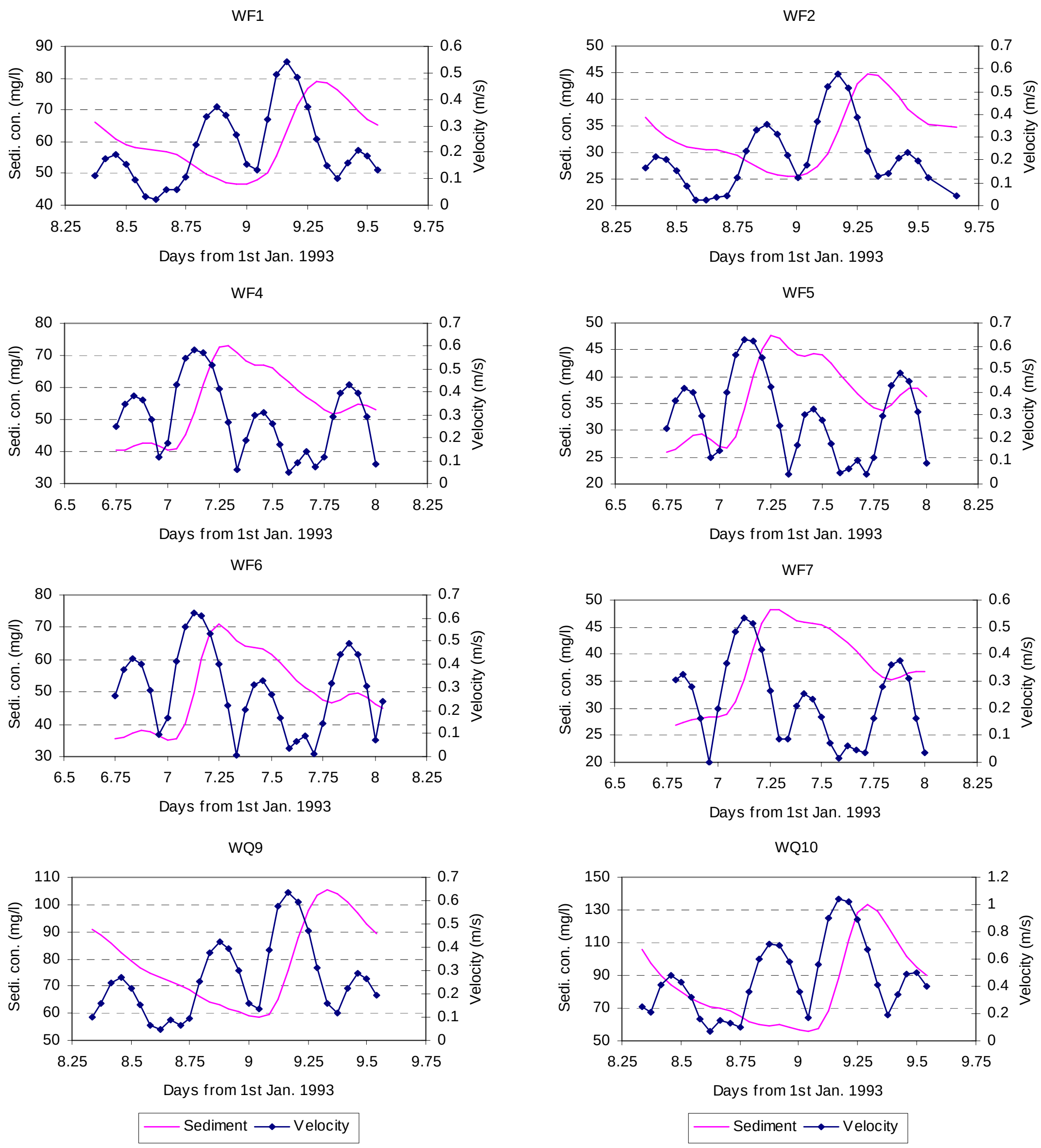

Fig. 4.13 Computed sediment concentration during a spring tide in the dry season (January 1993)

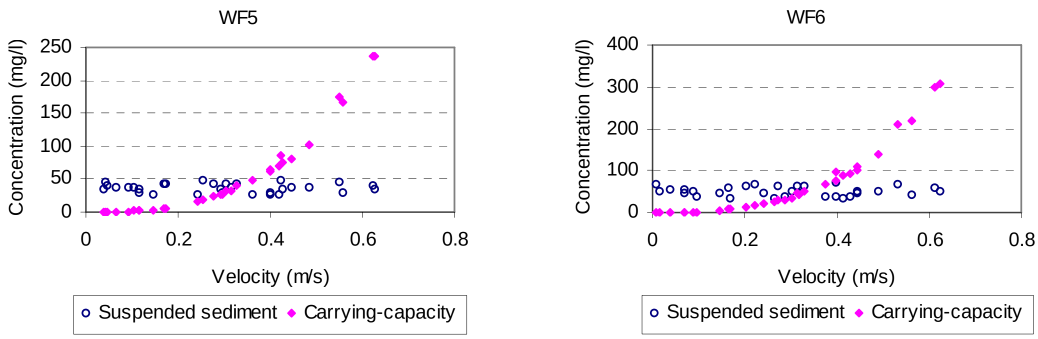

Fig. 4.14 Relationships of sediment concentration and sediment-carrying capacity with velocity.

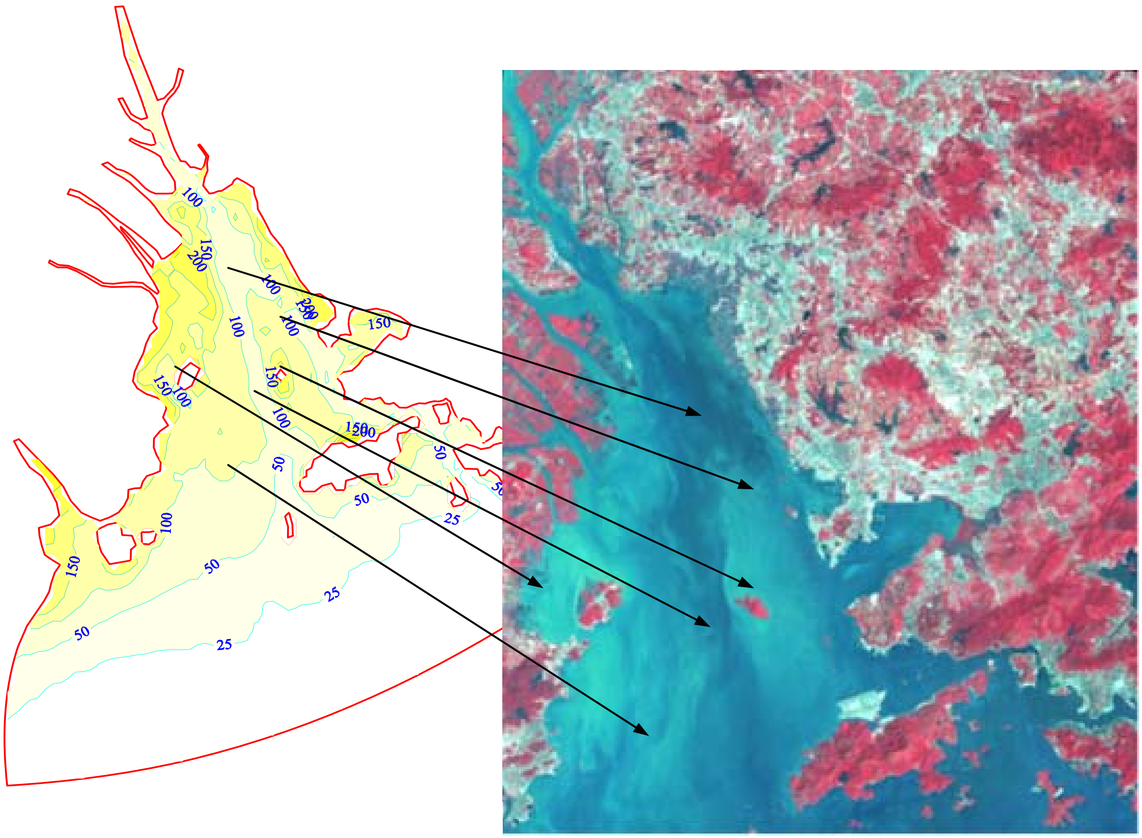

Fig. 4.15 Comparison of computed sediment concentration pattern during an ebbing neap tide in August 1992, with a satellite picture taken on September 4, 1997.

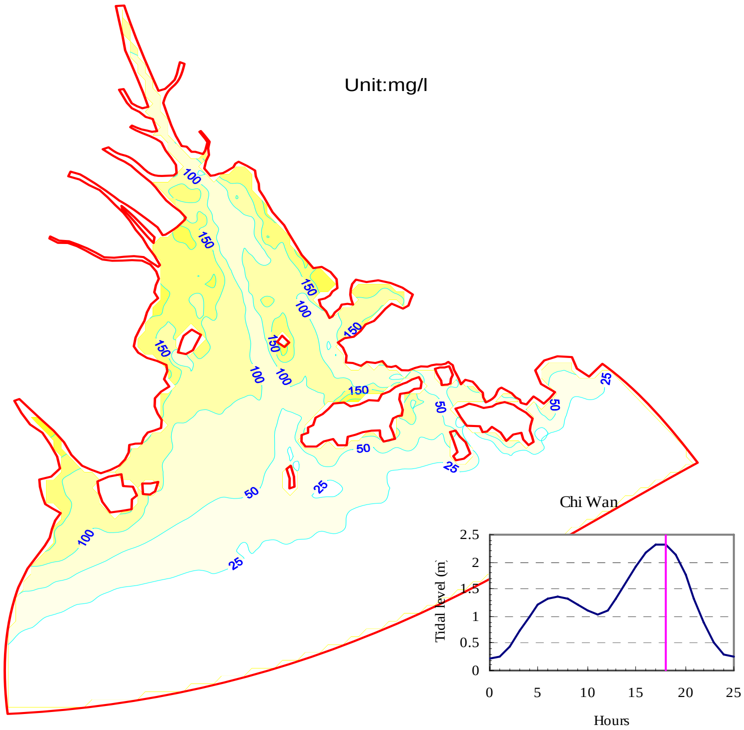

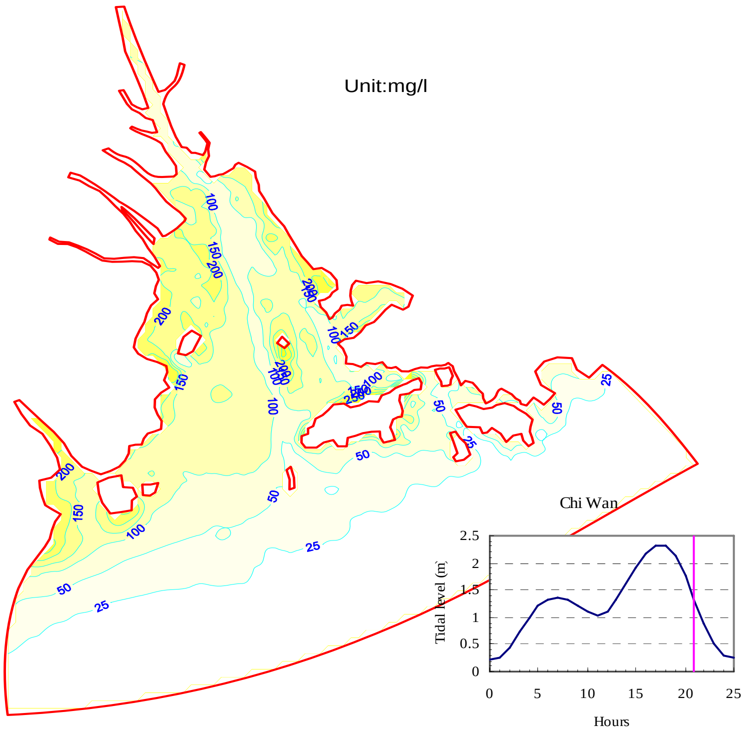

Fig. 4.16a Computed sediment concentration patterns during high slack and ebbing of a spring tide in the wet season (August 1992)

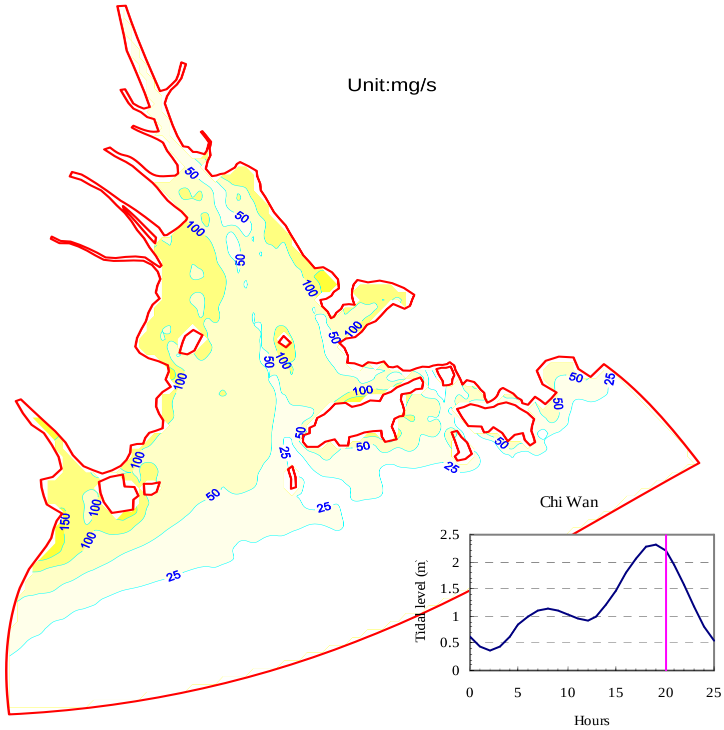

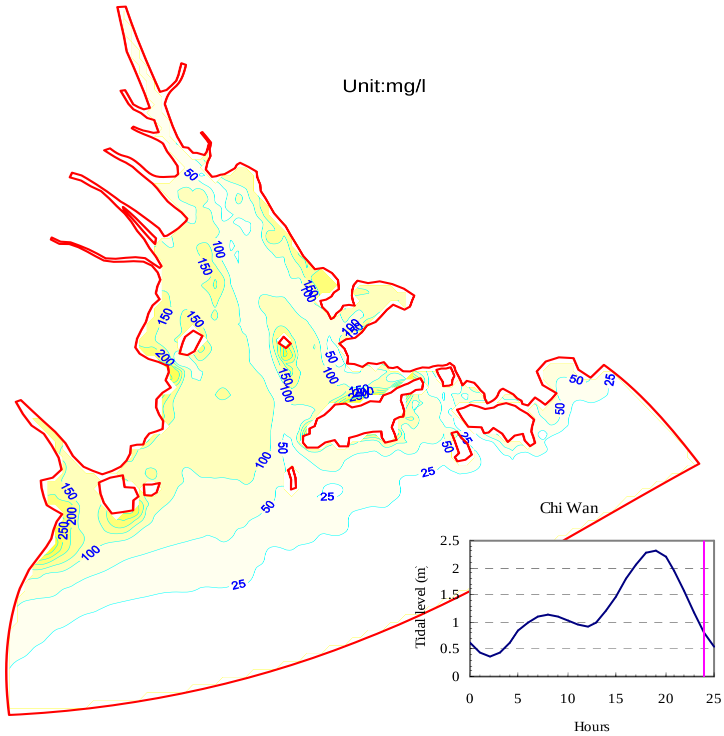

Fig. 4.16b Computed sediment concentration patterns during shortly after high slack and ebbing of a spring tide in the dry season (Jan. 1993)

CHAPTER 5

THREE-DIMENSIONAL HYDRODYNAMICS AND MASS TRANSPORT MODELLING

5.1 General remarks

In the previous chapter, the horizontal characteristics of hydrodynamics and sediment transport have been studied by a vertically integrated two-dimensional model. The simulated results provide the background knowledge on horizontal flow pattern, residual flow, sediment transport characteristics, and the effect of Coriolis force and wind in the Pearl River Estuary. However, the turbidity maximum (TM) in estuaries is a very complicated physical phenomenon, as has been reviewed in Chapter 2. TM is always related to saltwater intrusion and gravitational circulation of reversed net flow in the upper layer and lower layer near the head of the saltwater wedge is generally an important force for sediment convergence in TM. Vertically integrated 2D model is incapable of revealing the vertical structure of flow and salinity intrusion. It is necessary to use a three-dimensional mass transport model to study such features.

A three-dimensional model for simulating hydrodynamics and sediment transport processes in coastal and estuarine regions was developed by Lu (1997). In this model, an efficient operator-splitting scheme of Eulerian-Lagrangian method, finite element method and finite difference method was adopted to solve the horizontal advection terms, horizontal diffusive terms and vertical diffusion terms of the governing equations of hydrodynamics and mass transport respectively, which can render the model unconditionally stable (Lu, 1997; Wai and Lu, 1998, 1999). The model used a Gauss-Jacobian iteration method (GJ) to solve the set of unsymmetrical linear equations, which is efficient enough when the number of meshes in the domain of interest is not too large. However, the efficiency will decrease sharply when the number of computational meshes further increases. Usually, due to the scarcity of measurement data, the open boundary should be set far enough to minimize the effect from inaccurate boundary conditions, resulting in a large computational domain. Also salinity is one of the important factors in estuarine and coastal flows, which must be taken into account. The intrusion of salinity from the open sea results in the change of sediment particle size, settling velocity and stratification, which significantly affect the hydrodynamics, and sediment erosion and deposition consequently.

In an estuary or coastal area where freshwater and seawater meet, the freshwater, being less dense than seawater, tends to mix slowly with the seawater initially forming a brackish surface layer overlying the dense oceanic water. The stable density gradients between the water surface and seabed then tend to reduce the turbulent mixing and this factor needs to be addressed when computer models are applied to simulate stratified or partially stratified flows. In the said model, the parabolic or parabolic-constant profile of vertical eddy viscosity, which is only related to the friction velocity, was used. It is obviously impossible to give a detailed description of the complicated turbulence generation and dissipation processes, especially in the wedge of saltwater intrusion.

This chapter describes the further development of the said 3D model, and model validation compared with field data. The improvement on the said model comprises the following.

- Improvement of the efficiency of the model by using the conjugate residual method (CRM) instead of the Gauss-Jacobian method for solving the large, sparse, unsymmetrical, linear equation system.

- Coupling of the salinity transport process by considering the baroclinic term due to the horizontal density gradient to enable the model to represent the highly stratified flow.

- Coupling of the Level 2.5 turbulence closure with the Navier-Stokes equations to obtain a more elaborated vertical turbulent structure, which is not only affected by the flow pattern, but also is influenced by the vertical density gradient due to sediment concentration and salinity.

- Calculation of the horizontal eddy viscosity by the Smagorinsky formula to overcome the problem of under-estimated horizontal diffusivity from turbulence closure, or the unreasonable use of a constant diffusion coefficient in the existing model.

In the following sections, the details of the upgraded 3D hydrodynamics and mass transport model are presented, and then the turbulence closure is introduced. After that, the model is applied to the Pearl River Estuary, and hydrodynamics, salinity and sediment concentration during spring and neap tides are validated by field data measured in the wet season (August) and dry season (March), in 1998.

5.2 Model description

5.2.1 Governing equations

5.2.1.1 Hydrodynamics

The hydrodynamics model predicts the water surface elevations and horizontal and vertical velocities by solving the governing equations of fluid flow. Generally, the flow in estuaries and coastal area can be assumed to be isothermal and the vertical acceleration is small compared to the gravitational acceleration, yielding a hydrostatic pressure distribution (Liu *et al*., 2002). The Boussinesq approximation describes the way the density variations enter into equations of motion. Boussinesq approximation can be introduced by assuming that the basic state of the fluid is the state of no motion, defined by pressure P_0 and density ρ_0. Motion will arise due to the variations of pressure and density from the basic state (Balas and Özhan, 2002). The Navier-Stokes equations under the assumption of hydrostatic pressure and Boussinesq approximation after Reynolds averaging in the Cartesian coordinate are used in this model with the salinity gradient in the horizontal direction and the baroclinic term taken into account.

5.2.1.1.1 Basic equations

Continuity equation

$$\frac{\partial u}{\partial x}+\frac{\partial v}{\partial y}+\frac{\partial w}{\partial z}=0 \tag{5.1}$$

Momentum equation

$$\frac{\partial u}{\partial t}+u\frac{\partial u}{\partial x}+v\frac{\partial u}{\partial y}+w\frac{\partial u}{\partial z}=-g\frac{\partial \zeta}{\partial x}-\frac{g}{\rho_0}\frac{\partial}{\partial x}\left(\int_z^{\zeta}\rho' dz'\right)$$
$$+\frac{\partial}{\partial x}\left(\varepsilon_h\frac{\partial u}{\partial x}\right)+\frac{\partial}{\partial y}\left(\varepsilon_h\frac{\partial u}{\partial y}\right)+\frac{\partial}{\partial z}\left(\varepsilon_z\frac{\partial u}{\partial z}\right)+fv \tag{5.2}$$

$$\frac{\partial v}{\partial t}+u\frac{\partial v}{\partial x}+v\frac{\partial v}{\partial y}+w\frac{\partial v}{\partial z}=-g\frac{\partial \zeta}{\partial y}-\frac{g}{\rho_0}\frac{\partial}{\partial y}\left(\int_z^{\zeta}\rho' dz'\right)$$
$$+\frac{\partial}{\partial x}\left(\varepsilon_h\frac{\partial v}{\partial x}\right)+\frac{\partial}{\partial y}\left(\varepsilon_h\frac{\partial v}{\partial y}\right)+\frac{\partial}{\partial z}\left(\varepsilon_z\frac{\partial v}{\partial z}\right)-fu \tag{5.3}$$

$$\frac{\partial P}{\partial z}=-\rho g \tag{5.4}$$

where t is time; u, v and w are the velocity components in the x, y and z directions, respectively in the Cartesian coordinate system; ζ is the tidal level; z is the vertical coordinate increasing upward with z =0 located at the undisturbed sea surface, and positive upward, z' is an independent variable; ρ_0 is the constant reference density of water, ρ' is the local variation from the reference density; P is the pressure; g is the gravitational acceleration; $f=2\Omega\sin\varphi$ is the Coriolis parameter, Ω is the earth's rotation speed, φ is the latitude; and ε_h and ε_z are the eddy viscosity of turbulent flow in the horizontal and vertical directions, respectively.

The state equation of density ρ is a function of temperature, salinity and sediment concentration,

$$\rho=1000+1.4555Cl-0.0065(T-4+0.4Cl)^2+0.623c \tag{5.5}$$

in which T is the temperature; c is the suspended sediment concentration; and Cl is the chlorinity, which relates to salinity by

$$Cl = (s - 0.03)/1.805 \tag{5.6}$$

in which s is the salinity of sea water.

5.2.1.1.2 Boundary conditions

The dynamic boundary conditions for Eq. 5.1 to Eq. 5.4, specifying the stresses and vertical velocity at the water surface ($z = \zeta$), are

$$\rho\varepsilon_z\left(\frac{\partial u}{\partial z}, \frac{\partial v}{\partial z}\right) = \left(\tau_{s,x}, \tau_{s,y}\right) \tag{5.7}$$

$$w = \frac{\partial \zeta}{\partial t} + u\frac{\partial \zeta}{\partial x} + v\frac{\partial \zeta}{\partial y} \tag{5.8}$$

where $\tau_s = \{\tau_{s,x}, \tau_{s,y}\}$ is the wind-induced water surface stress components in the x and y directions, respectively, which can be expressed as:

$$\tau_s = \{\tau_{s,x}, \tau_{s,y}\} = \rho_a C_d^w \{u^w, v^w\}\sqrt{u^{w2} + v^{w2}} \tag{5.9}$$

where ρ_a is the density of air (=1.25 g/l); u^w and v^w are the wind velocity components in the x and y directions, respectively; C_d^w is the drag coefficient of air. If the wind speed is less than 11 m/s, the drag coefficient is 0.0012 (Large and Pond, 1981).

The seabed boundary conditions for Eq. 5.1 to Eq. 5.4, evaluated at $z = -h$, are

$$\rho\varepsilon_z\left(\frac{\partial u}{\partial z},\frac{\partial v}{\partial z}\right)=\left(\tau_{b,x},\tau_{b,y}\right) \tag{5.10}$$

$$w=-u\frac{\partial h}{\partial x}-v\frac{\partial h}{\partial y} \tag{5.11}$$

where $\tau_b = \{\tau_{b,x}, \tau_{b,y}\}$ is the current-induced shear stress at seabed in the x, y directions, respectively. In the three-dimensional model, the bottom friction is deduced from the logarithmic approximation of the velocity profile. A quadratic bottom stress formulation is applied at the bottom boundary as follows:

$$\tau_b = \{\tau_{b,x}, \tau_{b,y}\} = \rho C_d \{u_b, v_b\}\sqrt{u_b^2 + v_b^2} \tag{5.12}$$

where ρ is the density of sea water; u_b and v_b are the horizontal velocity components near seabed in the x and y directions, respectively and; C_d is the bottom drag coefficient of flow, which is specified to match the law of the wall in the bottom logarithmic layer where the water is neutrally stratified:

$$C_d = \left[\frac{1}{\kappa}\ln\left(\frac{H+z_b}{z_0}\right)\right]^{-2} \tag{5.13}$$

where κ is the von Kármán constant; H is the total water depth; z_0 is the bottom roughness, set equal to 0.001 m for the clay bottom and; z_b is the distance from seabed to the first grid nearest the bottom.

The open boundary conditions are either known from field data or interpolation values based on measurement near the boundaries. Usually, the open boundary conditions are the known tidal level or current velocities.

On the closed boundaries, the normal velocity is set to zero,

$$u_{\vec{n}} = 0 \tag{5.14}$$

where $\vec{n}$ is the unit normal of the closed boundary.

5.2.1.2 Salinity conservation

5.2.1.2.1 Basic equation

The basic conservation equation of salinity is

$$\frac{\partial s}{\partial t} + u\frac{\partial s}{\partial x} + v\frac{\partial s}{\partial y} + w\frac{\partial s}{\partial z} = \frac{\partial}{\partial x}\left(\varepsilon_{s,h}\frac{\partial s}{\partial x}\right) + \frac{\partial}{\partial y}\left(\varepsilon_{s,h}\frac{\partial s}{\partial y}\right) + \frac{\partial}{\partial z}\left(\varepsilon_{s,z}\frac{\partial s}{\partial z}\right) \tag{5.15}$$

where s is the salinity; $\varepsilon_{s,h}$ and $\varepsilon_{s,z}$ are the horizontal and vertical diffusivities of salinity (and sediment), respectively.

5.2.1.2.2 Boundary conditions

No salinity exchange occurs at the water surface and the seabed,

$$\left.\frac{\partial s}{\partial z}\right|_{z=-h,\ z=\zeta} = 0 \tag{5.16}$$

At the closed boundary, the salinity gradient in the normal direction is set to zero.

$$\frac{\partial s}{\partial \vec{n}} = 0 \tag{5.17}$$

At the open boundaries, salinity condition can be set either by measurement, or determined by

$$\frac{\partial s}{\partial t} + u_{\vec{n}} \frac{\partial s}{\partial \vec{n}} = 0 \tag{5.18}$$

5.2.1.3 Sediment transport and bed deformation

5.2.1.3.1 Basic equations

The relevant sediment transport processes are: (a) the convection of the sediment particles by the horizontal and vertical fluid velocities; (b) the diffusion or mixing of the sediment particles due to current-related mixing processes; (c) the settling of sediment particles due to gravity; and (d) the erosion of sediment particles from the bed by flow. The governing equation for the suspended sediment transport, which can be derived from the law of mass conservation, is as follows:

$$\frac{\partial c}{\partial t} + u\frac{\partial c}{\partial x} + v\frac{\partial c}{\partial y} + w\frac{\partial c}{\partial z} - \frac{\partial \omega_s c}{\partial z} = \frac{\partial}{\partial x}\left(\varepsilon_{s,h}\frac{\partial c}{\partial x}\right) + \frac{\partial}{\partial y}\left(\varepsilon_{s,h}\frac{\partial c}{\partial y}\right) + \frac{\partial}{\partial z}\left(\varepsilon_{s,z}\frac{\partial c}{\partial z}\right) \tag{5.19}$$

where c is the suspended sediment concentration; and ω_s is the hydrodynamic settling velocity of sediment particles.

According to the principle of mass conservation in the seabed during the sediment deposition and suspension process, the evolution of seabed level may be calculated by the equation (Dou *et al*., 1995) given below

$$\Delta Z_b = \frac{\alpha_d \omega_s}{\gamma'}\left(c - \beta c_a\right)\Delta t \tag{5.20}$$

in which ΔZ_b is the evolution of seabed level; γ' is the dry-bulk density of sediment; α_d is the probability of the sediment settling to the seabed with the range of 0 to 1; and β is a suspension probability of sediment particles, defined as

$$\beta = \begin{cases} 1 & (c > c_a) \\ 1 & (c \le c_a \text{ and } \tau_b > \tau_{b,cr}) \\ c/c_a & (c \le c_a \text{ and } \tau_b \le \tau_{b,cr}) \end{cases} \tag{5.21}$$

where $\tau_{b,cr}$ is the critical shear stress for erosion and c_a is the near bed reference sediment concentration.

5.2.1.3.2 Boundary conditions

To solve the Eq. 5-19, the boundary conditions and some physical parameters associated with the sediment dynamics must be specified.

At the open boundary, the suspended sediment concentrations can be prescribed using field measurements. At the closed boundaries, the sediment flux is set to zero as for the salinity and there is also no sediment particle exchange at the water surface.

However, due to sediment particles settling to and erosion from the seabed, there is sediment particles exchange along the water column. The vertical sediment exchange flux, denoted by q_s, can be derived under the principle of mass balance,

$$q_s = \omega_s c + \varepsilon_{s,z} \frac{\partial c}{\partial z} \tag{5.22}$$

This equation represents the net sediment flux in the vertical direction, expressed as the difference of the downward sediment flux, $D = \omega_s c$, and the upward sediment flux, $E = -\varepsilon_{s,z} \frac{\partial c}{\partial z}$, that is

$$q_s = D - E \tag{5.23}$$

The net vertical sediment flux at an internal interface can be calculated by Eq. 5.22 or Eq. 5.23. The condition q_s = 0 means that there is no net sediment exchange, or settling sediment particles are balanced by upward moving sediment particles due to vertical diffusion. The condition $\omega_s C = \varepsilon_z \frac{\partial C}{\partial z} = 0$ means that there is neither settling sediment particle flux nor upward moving sediment particle flux. The net sediment flux at the water surface can be assumed to be zero, resulting in the condition q_s = 0. The net vertical sediment flux at the seabed is considered as the difference of the deposition to the bed, denoted by D_1, and the sediment entrainment from the bed, denoted by E_1.

For uniform sediment particles, the deposition rate is proportional to the sediment concentrations and can be expressed as the product of settling velocity and sediment settling probability that takes account of the turbulent effect.

$$D_1 = \alpha_d \omega_s c \tag{5.24}$$

The entrainment rate from seabed is more complicated and is in general assumed to be a function of flow parameters, physical features of bed sediments at a specific height above the mean bed level and the bed shear stress.

$$E_1 = \begin{cases} 0 & (\tau_b \le \tau_{b,cr}) \\ -\left(\varepsilon_{s,z} \dfrac{\partial c}{\partial z}\right)_{z=a} = \alpha_s \omega_s c_a & (\tau_b > \tau_{b,cr}) \end{cases} \tag{5.25}$$

where c_a is the near-bed equilibrium reference concentration; a is the bed reference level above mean seabed; α_s is the suspension probability of sediment particles, $\alpha_s = \beta\alpha_d$; τ_b is the bed shear stress; and $\tau_{b,cr}$ is the critical bed erosion shear stress.

This approach is attractive because the bed sediment concentration or sediment flux may be represented by its equilibrium value assuming that there is an almost instantaneous adjustment to equilibrium conditions close to the bed (van Rijn, 1986a).

5.2.1.3.3 Important sediment parameters

In order to have an accurate simulation of sediment transport, the sediment settling velocity of fine cohesive particles, critical shear stress for threshold of sediment motion and the near bed reference sediment concentration must be treated carefully in the model to include the effects of sediment flocculation, and the deposition and resuspension processes.

(1) Settling velocity

The settling velocity of a particle can be found by balancing the submerged particle weight with the fluid drag force on the particle. The sediment settling velocity in the water-sediment mixture is a function of particle size and density, water temperature, salinity, flow condition and sediment concentration. The settling velocity of a single particle in still water can be determined by the following formula obtained from experiments (Yalin, 1972; and van Rijn, 1990). It is suitable for single particles with no flocculation.

$$\omega_s = \begin{cases} \dfrac{(s_d - 1)gd^2}{18\upsilon} & (0.001mm < d < 0.1mm) \\ \dfrac{10\upsilon}{d}\left[\sqrt{1 + \dfrac{0.01(s_d - 1)gd^3}{\upsilon^2}} - 1\right] & (0.1mm < d < 1.0mm) \\ 1.1\sqrt{(s_d - 1)gd} & (d > 1.0mm) \end{cases} \tag{5.26}$$

where s_d is the relative density, $= \rho_s / \rho$, ρ_s is the density of sediment particle; d is the size of sediment particle; and υ is the kinematic viscosity of water.

Water temperature has an effect on the kinematic viscosity, which changes with water temperature as follows

$$\upsilon = 1.792 \times 10^{-6} e^{-0.042T^{0.87}} \qquad \left(0^\circ < T \le 30^\circ C\right) \tag{5.27}$$

where T is the water temperature.

The suspended sediment particles in estuaries are in general fine and cohesive. Flocculation occurs widely when fine sediment particles are transported in salt water. The settling velocity of flocs is much larger than that of the individual particles in the dispersed state. In the study of sediment transport in estuaries, it is obviously necessary to consider the sediment flocculation process. The settling velocity of flocs is related to the size of flocs, sediment concentration, water qualities and turbulent fluctuations. Migniot (1968) and Huang (1989) carried out experiments on sediment settling, and found that the critical particle size was about 27 to 30 μm. If the particles are coarser than the critical size, flocculation is not remarkable. The settling velocity of flocs increases with increasing sediment concentrations when the sediment concentration is smaller than 15 g/l. The settling velocity decreases when sediment concentration exceeds 15 g/l. Salinity is also a very important medium. It provides numerous ions for sediment particle aggregation. There exists a limiting salinity, below which the settling velocity increases with increasing salinity. If the salinity is larger than the limiting value, the settling velocity of flocs no long increases, but decreases or approaches a constant value. Experimental studies and field investigations showed that the limiting salinity for flocculation in Bohai bay and Changjiang estuary in China is about 10 to 15 ppt when the sediment concentration was less than 1.0 g/l.

Turbulent fluctuations may increase the chance of particle collisions, leading to stronger flocculation and hence larger particle settling velocity. However, very strong turbulent fluctuation may generate high shear stress, resulting in the collapse of the flocculation structure and thus reducing the settling velocity of flocs. It can be seen that flocculation is a very complicated process and the best approach to estimate the settling velocity is to have a relationship with turbulence, sediment concentration, salinity, particle size, and other relevant parameters. Winterwerp and Kranenburg (1997a, b) studied the dynamics of flocculation, taking into account the collision rate, aggregation and floc breakup, and proposed a simple one-dimensional vertical transport (1DV) model to simulate the generation and breakup of flocs and establish the relationship between the size of flocs and turbulence and sediment concentration. Jiang (2003) expanded this 1DV model to a 3D model and coupled it with the hydrodynamics model to study the sediment transport in the Pearl River Estuary. However, because of the lack of systematic data, the effect of turbulent fluctuation on flocculation and the settling velocity of sediment particles have not been studied quantitatively. For simplicity, some empirical relationships of dynamic settling velocity and flocculation were adopted in this model.

The smaller the sediment particle size is, the stronger the flocculation effect will be. Migniot (1968) used a factor F to express the effect of flocculation on settling velocity,

$$F = \omega_{F50} \big/ \omega_{D_{50}} \tag{5.28}$$

where ω_{F50} is the flocculation limited setting velocity; ω_{D50} is the basic sand particle settling velocity without flocculation; and D_{50} is the median diameter of sediment of which 50% by weight is finer.

Huang (1989) derived a function for the sediment settling velocity, which depends on the water temperature, the settling distance, the particle size and the sediment concentration,

$$F_{\max} = \frac{\omega_{F50}}{\omega_{D50}} = 7.25 \times 10^{-4} \cdot D_{50}^{-2} \tag{5.29}$$

where the unit of D_{50} is mm.

However, as described above, the flocculation process is directly related to the salinity. The empirical relationship between settling velocity, salinity and concentration is used in this model as depicted in Fig. 5.1 (Chien and Wan, 1999). It can be seen that the sediment settling velocity increases with both salinity and sediment concentration. There exists a limiting salinity for a particular sediment concentration and salinity exceeding the limiting value will hardly influence the settling velocity. The higher the sediment concentration is, the lower is the limiting value. The relationship between the settling velocity and salinity can be empirically stated as follows.

$$F = \begin{cases} F(s) & \text{Salinity is less than limiting value} \\ F_{\max} & \text{Salinity is larger than limiting value} \end{cases} \tag{5.30}$$

Since the flocculation mechanism of cohesive sediment is rather complicated, it should be further investigated. Under the usual sediment concentrations at muddy beaches (around 1.0 g/l or smaller), the settling velocity of flocs is normally in the range of 0.01 to 0.06 cm/s and its equivalent particle diameter is about 15 to 30 μm. That is to say, for cohesive sediment in seawater, no matter how small the diameters of dispersed particles are, the equivalent particle diameters after flocculation are all within the range of 15 to 30 μm. This provides a useful range of values of sediment settling velocity for solving coastal engineering problems.

In the following real application in the PRE, the settling velocity of a single sediment particle is calculated by Eq. 5.26. The suspended sediment concentration in the PRE is relatively low, thus its effect on settling velocity can be neglected. However, the effect of flocculation of fine cohesive sediment particles in the PRE on the floc settling velocity should be considered, which is described by the flocculation factor in Eq. 5.28. Because of the scarcity of experimental data on the floc settling velocity in the PRE, the floc settling velocity given in Fig. 5.1 is used and the limiting salinity is taken as 12 ppt. If the salinity exceeds the limiting value, the flocculation factor for floc settling velocity is set to the maximum value described by Eq. 5.29. The flocculation factor is linearly-interpolated from zero to the maximum value according to the ratio of local salinity to the limiting salinity if the local salinity is less than the limiting salinity.

(2) Critical shear stress

Particle movement will occur when the hydraulic forces on particles are larger than a critical value. In general, the bed shear stress for the threshold of particle motion, also called the critical erosion shear stress, can be used to describe the critical hydraulic force. Through many experiments related to a flat bed with various particle sizes, Shields (1936) obtained the curve describing the relation of critical erosion shear stress and the particle size, the famous Shields' curve (Shields, 1936; Chien and Wan, 1999) as depicted in Fig. 5.2. Using the dimensionless parameter θ_{cr} and the particle parameter D_*, the Shields' curve is given by the following expressions (Yalin, 1972):

$$\theta_{cr} = \begin{cases} 0.24D_*^{-1} & (D_* \le 4) \\ 0.14D_*^{-0.64} & (4 < D_* \le 10) \\ 0.04D_*^{-0.10} & (10 < D_* \le 20) \\ 0.013D_*^{0.29} & (20 < D_* \le 150) \\ 0.055 & (D_* > 150) \end{cases} \tag{5.31}$$

in which $\theta_{cr} = \dfrac{\tau_{b,cr}}{(\rho_s - \rho)gD_{50}}$; D_* is a dimensionless particle parameter, and $D_* = D_{50}\left[\dfrac{(\rho_s/\rho - 1)g}{\upsilon^2}\right]^{1/3}$.

Shields' curve is well known and used widely. However, the curve is only suitable for non-cohesive sediment particles (Chien and Wan, 1999). However, the sediment critical shear stress or threshold flow velocity should ideally cover both non-cohesive and cohesive sediment particle. Tang (1963)'s formula on settling velocity is introduced in this model.

Based on the data of more than 1200 test points, which included field measurement and physical model tests, Tang (1963) derived a function of threshold current velocity. The range of sand size is 0.001~125 mm. In the function, the viscosity forces between sediments are considered.

$$u_{b,cr} = \theta \bar{u}_{b,cr} = \left[3.2\left(\frac{\rho_s - \rho}{\rho}\right) g D_{50} + \left(\frac{\rho_b}{\rho_{b0}}\right)^{10} \frac{\xi}{\rho'' D_{50}} \right]^{1/2} \tag{5.32}$$

in which, $u_{b,cr}$ is the critical bottom threshold current velocity; $\bar{u}_{b,cr}$ is the vertically averaged critical threshold current velocity; $\theta = \frac{m+1}{m} \Big/ \left(\frac{h}{D_{50}}\right)^{1/m}$; $m = 4.7\left(\frac{h}{D_{50}}\right)^{0.06}$, for rivers m=6; ξ is a coefficient which is related to viscosity forces, $\xi = 2.9 \times 10^{-5}$ kg/m; ρ'' =102 kg.s^2/m^4; ρ_b is the density of porous sediment on seabed and ρ_{b0} is the density of consolidated sediment on seabed.

According to Eq. 5.32, when $D_{50} \geq 1.0$ mm, gravity forces will obstruct sand movement; when $D_{50} \leq 0.01$ mm, viscosity forces will obstruct sand movement; and when $0.01 \leq D_{50} \leq 1.0$ mm, both gravity and viscosity should be considered.

Critical shear stress can be derived from Eq. 5.32, and its expression is as follows (Tang, 1963).

$$\tau_{b,cr} = \frac{g}{77.5}\left[3.2\left(\rho_s - \rho\right)D_{50} + \left(\frac{\rho_b}{\rho_{b0}}\right)^{10}\frac{\xi}{D_{50}}\right] \tag{5.33}$$

The distinguishing feature of the formula is that the relative consolidation of the sediment on the bed is included in the term for cohesive sediments (Chien and Wan, 1999). Undoubtedly, such a relationship is correct qualitatively. Fig. 5.2 compares Shields' relation with Tang (1963)'s relation for seabed sediment density ρ_b =1200 kg/m^3. It can be seen that Shields' curve is suitable for non-cohesive sediment only, while Tang's relationship is suitable for both non-cohesive and cohesive sediment. The shear stress for threshold motion has a minimum value corresponding to a particle size of about 80 μm. For the threshold motion of coarser sediment particles, the gravity force is dominant. However, for the threshold motion of finer sediment particles, the shear stress must be large enough to overcome the cohesive force between sediment particles. The smaller the grain size is, the larger the cohesive force and hence the larger the critical bed shear stress is for erosion.

(3) Reference concentration at seabed

In the computation of suspended sediment transport, the reference concentration is commonly used as the bed boundary condition.

In Chapter 4, the near bed reference sediment concentration is used to solve the sediment carrying capacity, and the 2D model gives a reasonable sediment concentration pattern in the PRE. The sediment carrying capacity is closely related to the near bed sediment concentration. Both the sediment carrying capacity and near bed reference sediment concentration increase in same phase with the flow intensity. However, the sediment carrying capacity is a vertically averaged value and the sediment concentration will be overestimated if the reference sediment concentration is replaced by the sediment carrying capacity in the 3D model. Hence, the near bed reference sediment concentration is determined directly based on the flow condition and sediment properties to give the deposition rate and erosion rate of sediment using Eq. 5.24 and Eq. 5.25, respectively.

Based on both theoretical and experimental work at equilibrium conditions, van Rijn (1984) proposed the following bed-concentration function. It is valid for sand particle size in the range of 0.1 to 0.5 mm.

$$c_{a,c,w} = 0.015\,\frac{D_{50}}{a}\,\frac{T_*^{1.5}}{D_*^{0.3}}\cdot\rho_s \tag{5.34}$$

in which $c_{a,c,w}$ is the bed-boundary concentration by waves and currents, at the reference level above bed a ; and T_* is the bed shear stress parameter, $T_* = \left(\tau_b - \tau_{b,cr}\right)/\tau_{b,cr}$.

Eq. 5.34 is based on the calibration by using flume and field data with flow velocities in the range of 0.4 to 1.6 m/s, and water depth in the range of 0.1 to 25 m.

van Rijn (1984) also suggested the following reference level

$$a = \max(\frac{1}{2}\Delta, 0.01h) \tag{5.35}$$

or

$$a = \max(k_s, 0.01h) \tag{5.36}$$

where Δ is the bed-form height, k_s is the bed roughness height, and h is water depth.

5.2.1.4 Turbulence closure

In the above hydrodynamics and mass transport governing equations, there is a very important coefficient, the vertical eddy viscosity or diffusion coefficient, which is influenced by and also affects the flow structure, and salinity and sediment concentration distributions.

Turbulence is mainly generated by friction on the bed and other external forces like wind, stirring by vessels and other obstacles. Predictions of the 3D models are quite sensitive to the representation of turbulence. There are different turbulence models in 3D modelling studies of estuarine and coastal transport processes. Some of the models use a constant eddy viscosity for the whole flow field, whose value is found from experiments or from trial and error calculations to match the observations. In some models, variations in the vertical eddy viscosity are described in algebraic forms with different mixing length formulations proposed for applications to estuarine flows (Bloss *et al.*, 1988; Lin and Falconer, 1997). Stability functions or damping functions, which are parameterized in terms of the Richardson number, are used to characterize the estuarine stratification. However, the application of mixing length models is limited since the mixing length distribution is often case dependent (Balas and Özhan, 2000, 2001 and 2002). To overcome the limitations of the mixing length hypothesis, turbulence models were developed and applied to the modelling of estuarine and coastal transport processes (Mellor and Yamada, 1982; Rodi, 1993; Xing and Davies, 1996; Gross *et al*., 1999).

In the 3D model developed by Lu (1997), the following vertical eddy viscosity in parabolic-constant form suggested by van Rijn (1986) is used,

$$\varepsilon_z = \begin{cases} 0.25\kappa u_* h & \dfrac{z}{h} \geq 0.5 \\ \kappa u_* z\left(1-\dfrac{z}{h}\right) & \dfrac{z}{h} < 0.5 \end{cases} \tag{5.37}$$

Using this vertical eddy viscosity distribution, sound results had been obtained for flows in the Pearl River Estuary without salinity intrusion and stratification (Lu , 1997; Wai and Lu, 1998, 1999; Chen *et al*., 1999). Although the parabolic-constant eddy viscosity profile is simple in form and efficient computationally, it is not applicable in cases with density stratification.

In the present model, the Level 2.5 Mellor-Yamada turbulence closure model (Mellor and Yamada, 1982), together with a prognostic equation (Mellor *et al*., 1998) for the turbulence macroscale, are adopted to upgrade the parabolic-constant vertical eddy viscosity expression. The Level 2.5 Mellor-Yamada turbulence closure uses two partial differential equations to compute the turbulent kinetic energy ($q^2/2$) and a turbulence macroscale (l). The equation for the turbulent kinetic energy is

$$\frac{\partial q^2}{\partial t}+u\frac{\partial q^2}{\partial x}+v\frac{\partial q^2}{\partial y}+w\frac{\partial q^2}{\partial z}$$
$$=\frac{\partial}{\partial x}\left(\varepsilon_q\frac{\partial q^2}{\partial x}\right)+\frac{\partial}{\partial y}\left(\varepsilon_q\frac{\partial q^2}{\partial y}\right)+\frac{\partial}{\partial z}\left(\varepsilon_q\frac{\partial q^2}{\partial z}\right)+2\left[P_s+P_b-\frac{q^3}{B_1 l}\right] \tag{5.38}$$

where the shear production is

$$P_s=\varepsilon_z\left(\frac{\partial u}{\partial z}\right)^2+\varepsilon_z\left(\frac{\partial v}{\partial z}\right)^2 \tag{5.39}$$

and the buoyant production is

$$P_b=\frac{g}{\rho_0}\varepsilon_{s,z}\frac{\partial\rho}{\partial z} \tag{5.40}$$

and $q^3/B_1 l$ is the turbulent dissipation. Thus the turbulent kinetic energy is governed by local production, dissipation, horizontal transport and vertical diffusion within each water column. The governing equation of the turbulent macroscale is

$$\frac{\partial q^2 l}{\partial t}+u\frac{\partial q^2 l}{\partial x}+v\frac{\partial q^2 l}{\partial y}+w\frac{\partial q^2 l}{\partial z}$$
$$=\frac{\partial}{\partial x}\left(\varepsilon_q\frac{\partial q^2 l}{\partial x}\right)+\frac{\partial}{\partial y}\left(\varepsilon_q\frac{\partial q^2 l}{\partial y}\right)+\frac{\partial}{\partial z}\left(\varepsilon_q\frac{\partial q^2 l}{\partial z}\right) \tag{5.41}$$
$$+lE_1\left[P_s+P_b\right]+lE_1E_3\frac{g}{\rho_0}\left(\frac{\partial\rho}{\partial z}-\frac{1}{{v_s}^2}\frac{\partial p}{\partial z}\right)-\frac{q^3}{B_1}\left[1+E_2\left(\frac{l}{\kappa L}\right)^2\right]$$

where $L=\left[(\zeta-z)^{-1}+(H-z)^{-1}\right]$; $\varepsilon_q=qlS_q$ is the eddy diffusion coefficients for turbulence energy; p is water pressure; v_s is sound speed; and k is the von Kármán constant. The last term in the equation accounts for the effects of solid walls and the free surfaces on the length scale.

The boundary conditions applied at the top and bottom boundaries, respectively (Blumberg and Mellor, 1987), are

$$q^2 = B_1^{2/3} u_*^2, \qquad q^2 l = 0 \tag{5.42}$$

The length scale l, is computed as $l = q^2 l / q^2$ with the following length scale limiter proposed by Blumberg *et al*. (1992):

$$l \le \frac{0.53q}{N} \tag{5.43}$$

where $N =$ buoyancy frequency, defined as

$$N = \left(\frac{-g}{\rho_0} \frac{\partial \rho}{\partial z} \right)^{1/2} \tag{5.44}$$

The vertical eddy viscosity and diffusion coefficients ε_z and $\varepsilon_{s,z}$ are defined according to

$$\varepsilon_z = qlS_z \tag{5.45}$$

$$\varepsilon_{s,z} = qlS_s \tag{5.46}$$

The coefficients S_z and S_s are stability functions related to the Richardson number, and are given by

$$S_z = \frac{A_2 \left(1 - 6 A_1 / B_1\right)}{1 - \left(3A_2 B_2 + 18 A_1 A_2\right) G_H} \tag{5-47}$$

$$S_s = \frac{A_1 \left(1 - 3C_1 - 6 A_1 / B_1\right) + S_z \left(18 A_1^2 + 9 A_1 A_2\right) G_H}{1 - 9 A_1 A_2 G_H} \tag{5-48}$$

where G_H is defined as

$$G_H = -\frac{l^2}{q^2}\frac{g}{\rho_0}\left(\frac{\partial\rho}{\partial z} - \frac{1}{v_s^2}\frac{\partial p}{\partial z}\right) \tag{5.49}$$

The constants used in these equations are A_1 =0.92, A_2 =0.74, $B_1 = 16.6$, $B_2 = 10.1$, C_1=0.08, $E_1 = 1.8$, E_2 =1.33, E_3=0.25-1.0, and S_q =0.2 (Blumberg *et al*. 1992).

The vertical eddy viscosity and diffusion coefficients can be computed by equations Eq. 5.45 and Eq. 5.46, respectively. In general, the Mellor-Yamada level 2.5 turbulence model underpredicts the horizontal momentum fluxes in the presence of stratification. In the processes of mass advection and diffusion, although the horizontal diffusion is less important in relation to horizontal advection and the vertical mixing, the horizontal eddy viscosity and diffusion coefficients are also very important for modelling the transport of particles and mass of the recirculation zone (Chen, 2001). The constant horizontal eddy viscosity and diffusion coefficients are usually employed in estuarine and coastal mass transport simulations and the values are in the range of 0.1 and 1.0 m^2/s (van Rijn, 1987, 1990). In the present model, the Smagorinsky formula is introduced to compute the horizontal eddy viscosity and diffusion coefficients according to the horizontal velocity gradient and the size of the computational meshes,

$$\varepsilon_h, \varepsilon_{s,h} = \frac{1}{2}CA\left[\left(\frac{\partial u}{\partial x}\right)^2 + \frac{1}{2}\left(\frac{\partial u}{\partial y} + \frac{\partial v}{\partial x}\right)^2 + \left(\frac{\partial v}{\partial y}\right)^2\right]^{1/2} \tag{5.50}$$

where the constant C is in the range of 0.1-0.2 (Oey *et al.*, 1985a, b, c). A is the area of the quadrilateral or triangular element. The advantages of this formula are that the value of the eddy viscosity and diffusion coefficients will decrease when the element is finer, and will also be small if the velocity gradient is small (Jiang, 2003).

5.3 Numerical methods

5.3.1 The $\sigma-$coordinate transformation

To deal with the free surface and simplify the numerical formulation consequently, the $\sigma-$coordinate system is applied to transform temporally and spatially varying water depth into a uniform depth. The relationships between independent variables in the $\sigma-$coordinate system and in Cartesian coordinate are

$$t_\sigma = t\,;\; x_\sigma = x\,;\; y_\sigma = y\,;\; \sigma = \frac{z+h}{H} \tag{5.51}$$

After coordinate transformation based on the derivative chain-rule, and neglecting the high-order derivatives, the corresponding governing equations of hydrodynamics in the $\sigma-$coordinate system are as follows,

$$\frac{\partial \zeta}{\partial t} + \frac{\partial Hu}{\partial x} + \frac{\partial Hv}{\partial y} + \frac{\partial Hw_\sigma}{\partial \sigma} = 0 \tag{5.52}$$

$$\begin{aligned} \frac{\partial u}{\partial t} + u\frac{\partial u}{\partial x} + v\frac{\partial u}{\partial y} + w_\sigma \frac{\partial u}{\partial \sigma} &= -g\frac{\partial \zeta}{\partial x} - \frac{g}{\rho_0}\frac{\partial}{\partial x}\left(\int_\sigma^1 H\rho' d\sigma'\right) \\ &+ \frac{\partial}{\partial x}\left(\varepsilon_h \frac{\partial u}{\partial x}\right) + \frac{\partial}{\partial y}\left(\varepsilon_h \frac{\partial u}{\partial y}\right) + \frac{\partial}{\partial \sigma}\left(\varepsilon_\sigma \frac{\partial u}{\partial \sigma}\right) + fv \end{aligned} \tag{5.53}$$

$$\frac{\partial v}{\partial t}+u\frac{\partial v}{\partial x}+v\frac{\partial v}{\partial y}+w_\sigma\frac{\partial v}{\partial z}=-g\frac{\partial \zeta}{\partial y}-\frac{g}{\rho_0}\frac{\partial}{\partial y}\left(\int_\sigma^1 H\rho' d\sigma'\right)$$
$$+\frac{\partial}{\partial x}\left(\varepsilon_h\frac{\partial v}{\partial x}\right)+\frac{\partial}{\partial y}\left(\varepsilon_h\frac{\partial v}{\partial y}\right)+\frac{\partial}{\partial \sigma}\left(\varepsilon_\sigma\frac{\partial v}{\partial \sigma}\right)-fu \tag{5.54}$$

$$\frac{\partial P}{\partial \sigma}=-\rho g H \tag{5.55}$$

where $\varepsilon_\sigma=\frac{\varepsilon_z}{H^2}$, is the vertical eddy viscosity in $\sigma-$coordinate; w_σ is the vertical velocity in $\sigma-$coordinate, and its relation to the vertical velocity in Cartesian coordinate is

$$w_\sigma=\frac{1}{H}\left[w-\sigma\frac{\partial \zeta}{\partial t}+\left(u\frac{\partial h}{\partial x}+v\frac{\partial h}{\partial y}\right)-\sigma\left(u\frac{\partial H}{\partial x}+v\frac{\partial H}{\partial x}\right)\right] \tag{5.56}$$

The salinity conservation equation in the $\sigma-$coordinate is as follows.

$$\frac{\partial s}{\partial t}+u\frac{\partial s}{\partial x}+v\frac{\partial s}{\partial y}+w_\sigma\frac{\partial s}{\partial \sigma}=\frac{\partial}{\partial x}\left(\varepsilon_{s,h}\frac{\partial s}{\partial x}\right)+\frac{\partial}{\partial y}\left(\varepsilon_{s,h}\frac{\partial s}{\partial y}\right)+\frac{\partial}{\partial \sigma}\left(\varepsilon_{s,\sigma}\frac{\partial s}{\partial \sigma}\right) \tag{5.57}$$

The sediment transport equation in the $\sigma-$coordinate is given below.

$$\frac{\partial c}{\partial t}+u\frac{\partial c}{\partial x}+v\frac{\partial c}{\partial y}+w_\sigma\frac{\partial c}{\partial \sigma}-\frac{1}{H}\frac{\partial \omega_s c}{\partial \sigma}$$
$$=\frac{\partial}{\partial x}\left(\varepsilon_{s,h}\frac{\partial c}{\partial x}\right)+\frac{\partial}{\partial y}\left(\varepsilon_{s,h}\frac{\partial c}{\partial y}\right)+\frac{\partial}{\partial \sigma}\left(\varepsilon_{s,\sigma}\frac{\partial c}{\partial \sigma}\right) \tag{5.58}$$

in which the vertical diffusion coefficient in the $\sigma-$coordinate $\varepsilon_{s,\sigma}=\frac{\varepsilon_{s,z}}{H^2}$.

The turbulence kinetic energy and macroscale equations in the $\sigma-$coordinate are

$$\frac{\partial q^2}{\partial t}+u\frac{\partial q^2}{\partial x}+v\frac{\partial q^2}{\partial y}+w_\sigma\frac{\partial q^2}{\partial \sigma}$$
$$=\frac{\partial}{\partial x}\left(\varepsilon_q\frac{\partial q^2}{\partial x}\right)+\frac{\partial}{\partial y}\left(\varepsilon_q\frac{\partial q^2}{\partial y}\right)+\frac{\partial}{\partial \sigma}\left(\varepsilon_{q,\sigma}\frac{\partial q^2}{\partial \sigma}\right)+2\left[P_s+P_b-\frac{q^3}{B_1 l}\right] \tag{5.59}$$

where $\varepsilon_{q,\sigma}=\frac{\varepsilon_q}{H^2}$, and the shear production is

$$P_s=\varepsilon_\sigma\left(\frac{\partial u}{\partial \sigma}\right)^2+\varepsilon_\sigma\left(\frac{\partial v}{\partial \sigma}\right)^2 \tag{5.60}$$

The buoyant production is

$$P_b=\frac{gH}{\rho_0}\varepsilon_{s,\sigma}\frac{\partial \rho}{\partial \sigma} \tag{5.61}$$

$$\frac{\partial q^2 l}{\partial t}+u\frac{\partial q^2 l}{\partial x}+v\frac{\partial q^2 l}{\partial y}+w_\sigma\frac{\partial q^2 l}{\partial \sigma}$$
$$=\frac{\partial}{\partial x}\left(\varepsilon_q\frac{\partial q^2 l}{\partial x}\right)+\frac{\partial}{\partial y}\left(\varepsilon_q\frac{\partial q^2 l}{\partial y}\right)+\frac{\partial}{\partial \sigma}\left(\varepsilon_{q,\sigma}\frac{\partial q^2 l}{\partial \sigma}\right) \tag{5.62}$$
$$+lE_1\left[P_s+P_b\right]+lE_1E_3\frac{g}{H\rho_0}\left(\frac{\partial \rho}{\partial \sigma}-\frac{1}{v_s{}^2}\frac{\partial p}{\partial \sigma}\right)-\frac{q^3}{B_1}\left[1+E_2\left(\frac{l}{\kappa L}\right)^2\right]$$

5.3.2 Splitting method and temporal difference scheme

5.3.2.1 Temporal difference scheme for flow momentum and mass transport equations

In this model, an efficient splitting method, which was developed by Wai and Lu (1998) and has been confirmed as a stable and effective approach by Chen *et al.* (1999), Chen (2001) and Jiang (2003), is used to split the complicated physical phenomenon into several simple processes. The hydrodynamics equations and mass conservation and transport equations are solved in three sub-steps.

In the first step, the advection terms and Coriolis force terms in momentum equations Eq. 5.53 and Eq. 5.54, and pure advection terms of scalar variables of salinity, sediment transport and kinetic energy of turbulence and macroscale of turbulence in Eq.5.57 to Eq. 5.59, and Eq.5.62 are solved,

$$\frac{u^{n+\frac{1}{3}}-u^n}{\Delta t}+u^n\frac{\partial u^n}{\partial x}+v^n\frac{\partial u^n}{\partial y}+w_\sigma^n\frac{\partial u^n}{\partial \sigma}-fv^{n+\frac{1}{3}}+P_x^*=0 \tag{5.63}$$

$$\frac{v^{n+\frac{1}{3}}-v^n}{\Delta t}+u^n\frac{\partial v^n}{\partial x}+v^n\frac{\partial v^n}{\partial y}+w_\sigma^n\frac{\partial v^n}{\partial \sigma}+fu^{n+\frac{1}{3}}+P_y^*=0 \tag{5.64}$$

$$\frac{\mathbf{S}^{n+\frac{1}{3}}-\mathbf{S}^n}{\Delta t}+u^n\frac{\partial \mathbf{S}^n}{\partial x}+v^n\frac{\partial \mathbf{S}^n}{\partial y}+w_\sigma^n\frac{\partial \mathbf{S}^n}{\partial \sigma}=0 \tag{5.65}$$

in which $P_x^*=\frac{g}{\rho_0}\frac{\partial}{\partial x}\left(\int_\sigma^1 H\rho' d\sigma'\right)$, $P_y^*=\frac{g}{\rho_0}\frac{\partial}{\partial y}\left(\int_\sigma^1 H\rho' d\sigma'\right)$, $\mathbf{S}=\{s, c, q^2, q^2 l\}^T$, and n is the time steps.

In the second sub-step, the horizontal diffusion terms in vector and scalar equations are solved as follows.

For vectors,

$$\frac{\mathbf{V}^{n+\frac{2}{3}}-\mathbf{V}^{n+\frac{1}{3}}}{\Delta t}=\frac{\partial}{\partial x}\left(\varepsilon_h\frac{\partial \mathbf{V}^{n+\frac{2}{3}}}{\partial x}\right)+\frac{\partial}{\partial y}\left(\varepsilon_h\frac{\partial \mathbf{V}^{n+\frac{2}{3}}}{\partial y}\right) \tag{5.66}$$

in which $\mathbf{V}=\{u, v\}^T$.

For scalars,

$$\frac{\mathbf{S}^{n+\frac{2}{3}} - \mathbf{S}^{n+\frac{1}{3}}}{\Delta t} = \frac{\partial}{\partial x}\left(\boldsymbol{\varepsilon}_{\mathbf{s,h}} \frac{\partial \mathbf{S}^{n+\frac{2}{3}}}{\partial x} \right) + \frac{\partial}{\partial y}\left(\boldsymbol{\varepsilon}_{\mathbf{s,h}} \frac{\partial \mathbf{S}^{n+\frac{2}{3}}}{\partial y} \right) \tag{5.67}$$

in which $\boldsymbol{\varepsilon}_{\mathbf{s,h}} = \left\{ \varepsilon_{s,h}, \varepsilon_{s,h}, \varepsilon_q, \varepsilon_q \right\}^T$.

The vertical diffusion terms and pressure terms in the momentum equations, and the vertical dispersion terms and source-sink terms in the scalar transport equations are solved in the third sub-step as follows:

For flow momentum terms,

$$\frac{\mathbf{V}^{n+1} - \mathbf{V}^{n+\frac{2}{3}}}{\Delta t} = \frac{\partial}{\partial \sigma}\left(\varepsilon_\sigma \frac{\partial \mathbf{V}^{n+1}}{\partial \sigma} \right) + \mathbf{RV}^{n+1} \tag{5.68}$$

where $\mathbf{RV} = \left\{ -g\frac{\partial \zeta}{\partial x}, -g\frac{\partial \zeta}{\partial y} \right\}$

For scalars,

$$\frac{\mathbf{S}^{n+1} - \mathbf{S}^{n+\frac{2}{3}}}{\Delta t} = \frac{\partial}{\partial \sigma}\left(\boldsymbol{\varepsilon}_{\mathbf{s,\sigma}} \frac{\partial \mathbf{S}^{n+1}}{\partial \sigma} \right) + \mathbf{RS}^{n+1} \tag{5.69}$$

in which $\boldsymbol{\varepsilon}_{\mathbf{s,\sigma}} = \left\{ \varepsilon_{s.,\sigma}, \varepsilon_{s,\sigma}, \varepsilon_{q,\sigma}, \varepsilon_{q,\sigma} \right\}^T$, and

$$\mathbf{RS} = \left\{ 0, \frac{1}{H}\frac{\partial \omega_s c}{\partial \sigma}, 2\left(P_s + P_b - \frac{q^3}{B_{1l}} \right), \right.$$
$$\left. lE_1\left[P_s + P_b \right] + lE_1 E_3 \frac{g}{H\rho_0}\left(\frac{\partial \rho}{\partial \sigma} - \frac{1}{v_s^{\,2}}\frac{\partial p}{\partial \sigma} \right) - \frac{q^3}{B_1}\left[1 + E_2\left(\frac{l}{\kappa L} \right)^2 \right] \right\}$$

5.3.2.2 Temporal difference scheme for flow continuity and vertical velocity

By integrating Eq.5.52 from the seabed to the water surface and employing the corresponding boundary conditions Eq. 5.8 and Eq. 5.11, the continuity equation becomes

$$\frac{\partial \zeta}{\partial t} + \frac{\partial}{\partial x}\left(H \cdot \int_0^1 u d\sigma \right) + \frac{\partial}{\partial y}\left(H \cdot \int_0^1 v d\sigma \right) = 0 \tag{5.70}$$

In order to maintain mass conservation in a time step, the above continuity equation should be implicitly solved,

$$\frac{\xi^{n+1} - \zeta^{n}}{\Delta t} + \frac{\partial}{\partial x}\left(H \cdot \int_0^1 u^{n+1} d\sigma \right) + \frac{\partial}{\partial y}\left(H \cdot \int_0^1 v^{n+1} d\sigma \right) = 0 \tag{5.71}$$

The equation for solving the vertical velocity at any height above the seabed can be derived by the integration of the continuity equation from the bottom to σ,

$$w_{\sigma} = \frac{1}{H}\left[-\sigma \frac{\partial \zeta}{\partial t} - \frac{\partial}{\partial x}\left(H \cdot \int_0^{\sigma} u^{n+1} d\sigma' \right) - \frac{\partial}{\partial y}\left(H \cdot \int_0^{\sigma} v^{n+1} d\sigma' \right) \right] \tag{5.72}$$

5.3.3 Numerical schemes for solving spatial differences

5.3.3.1 Explicit Eulerian-Lagrangian method for advection

Eulerian-Lagrangian method (ELM) is based on the assumption that a particle in a specified point is transported directly from a location along a streamline within a short time period. So the values of the physical parameters associated with the particle at that position can be estimated from the corresponding values of the particle traced back along the streamline. In the first temporal fractional step, an explicit Eulerian-Lagrangian method is employed to solve Eq. 5.63 to Eq. 5.65 by

$$u^{n+\frac{1}{3}} = \left(u_P^n + \Delta t \cdot f \cdot v_P^n - P_x^* - \Delta t \cdot f \cdot P_y^*\right) / \left[1 + \left(\Delta t \cdot f\right)^2\right] \tag{5.73}$$

$$v^{n+\frac{1}{3}} = \left(v_P^n - \Delta t \cdot f \cdot u_P^n - P_y^* + \Delta t \cdot f \cdot P_x^*\right) / \left[1 + \left(\Delta t \cdot f\right)^2\right] \tag{5.74}$$

$$\mathbf{S}^{n+\frac{1}{3}} = \mathbf{S}_p^n \tag{5.75}$$

In the above equations, once the previous position p of the particle is determined, the unknown variables can be solved directly. The position of point p can be found easily by tracing back along the streamline as follows.

$$x_p = x - \Delta t \cdot u\,, \quad y_p = y - \Delta t \cdot v\,, \quad \sigma_p = \sigma - \Delta t \cdot w_\sigma \tag{5.76}$$

5.3.3.2 Implicit Finite Element method for horizontal diffusion

In the second time step, the standard Galerkin finite element method (FEM), with second-order 9-node quadrilateral isoparametric finite elements are used to approximate the vector and scalar variables in Eq. 5.66 and Eq. 5.67 in each layer as follows,

For vectors,

$$\left[D\right]\left\{\mathbf{V}_i^{n+\frac{2}{3}}\right\} = \left[M\right]\left\{\mathbf{V}_i^{n+\frac{1}{3}}\right\} \tag{5.77}$$

For scalars,

$$\left[\mathbf{D}_{\boldsymbol{\varepsilon}}\right]\left\{\mathbf{S}_i^{\,n+\frac{2}{3}}\right\} = \left[M\right]\left\{\mathbf{S}_i^{\,n+\frac{1}{3}}\right\} \tag{5.78}$$

where $\mathbf{V}_i = [V_1, V_2, \cdots, V_N]^T$, $\mathbf{S}_i = [S_1, S_2, \cdots, S_N]^T$, N is the number of nodes in the domain of interest, and the matrices are given below.

$$\left[D\right] = \sum_{e=1}^{M}\left\{S_{1\,jl}^{\ \ (e)} + \Delta t \cdot \varepsilon_h \cdot S_{2\,jl}^{\ \ (e)}\right\} \tag{5.79}$$

$$\left[\mathbf{D}_{\boldsymbol{\varepsilon}}\right] = \sum_{e=1}^{M}\left\{S_{1\,jl}^{\ \ (e)} + \Delta t \cdot \boldsymbol{\varepsilon}_{\mathbf{s},\mathbf{h}} \cdot S_{2\,jl}^{\ \ (e)}\right\} \tag{5.80}$$

$$\left[M\right] = \sum_{e=1}^{M} S_{1\,jl}^{\ \ (e)} \tag{5.81}$$

$$S_{1\,jl}^{\ \ (e)} = \iint_{\Omega^e} \phi_j \phi_l \left|\mathbf{J}\right| d\xi d\eta \tag{5.82}$$

$$S_{2\,jl}^{\ \ (e)} = \iint_{\Omega^e} Q_j Q_l \frac{1}{\left|\mathbf{J}\right|} d\xi d\eta + \iint_{\Omega^e} R_j R_l \frac{1}{\left|\mathbf{J}\right|} d\xi d\eta - \oint_{\Gamma} \frac{\partial \phi_k}{\partial n} \phi_j d\Gamma \tag{5.83}$$

$$Q_j = \frac{\partial y}{\partial \eta}\frac{\partial \phi_j}{\partial \xi} - \frac{\partial y}{\partial \xi}\frac{\partial \phi_j}{\partial \eta} \tag{5.84}$$

$$R_j = -\frac{\partial x}{\partial \eta}\frac{\partial \phi_j}{\partial \xi} + \frac{\partial x}{\partial \xi}\frac{\partial \phi_j}{\partial \eta} \tag{5.85}$$

$$\mathbf{J} = \begin{Bmatrix} \dfrac{\partial x}{\partial \xi} & \dfrac{\partial y}{\partial \xi} \\ \dfrac{\partial x}{\partial \eta} & \dfrac{\partial y}{\partial \eta} \end{Bmatrix} \tag{5.86}$$

where Ω is the domain of interest; Γ is the boundary around the domain; $\frac{\partial}{\partial n}$ is the derivative normal to the boundary; $\mathbf{J}$ is Jacobian matrix; ϕ is the shape function; e is an element; ξ, η are local element coordinates; and $j, l = 1, 2, \cdots, 9$ are the node numbers in an element.

In Eq. 5.77 and Eq. 5.78, the coefficient matrix $[M]$ is only related to the structure of the elements. So once the computational domain is meshed, it can be calculated in advance as a constant matrix. However, the coefficient matrices $[D]$ and $[\mathbf{D}_{\boldsymbol{\varepsilon}}]$ vary with the horizontal eddy viscosity or diffusion/dispersion coefficient and their inverse matrices should be solved at each time step. Hence it is necessary for a large computational domain to choose an efficient algorithm to avoid excessive computational time. In this model, the Pre-conditional Conjugate Residual (PCR) method is introduced to solve the above equations. The procedures are as follows: firstly, lay aside the boundary terms and transform the coefficient matrices $[D]$ and $[\mathbf{D}_{\boldsymbol{\varepsilon}}]$ from non-positive, asymmetric ones to positive and symmetric matrices; secondly, use PCR to solve efficiently the large, sparse matrices; and finally, set the boundary condition $\left.\frac{\partial}{\partial n}\right|_{\Gamma} = 0$.

5.3.3.3 Implicit Finite Difference method for vertical diffusion

An implicit finite difference method (FDM) is used to discretize Eq. 5.68 and Eq. 5.69, resulting in the following set of non-linear equations,

$$[B]\left\{\Xi_i^{n+1}\right\} = [F_i] \tag{5.87}$$

where $\Xi_i = \{u, v, s, c, q^2, q^2 l\}$, $F_i = [F_1, F_2, ..., F_L]^T$; L is the number of vertical layers; B is a triangular coefficient matrix and F is a known vector,

$$B = \begin{bmatrix} b_{1,2} & b_{1,3} & & & & & \\ b_{2,1} & b_{2,2} & b_{2,3} & & & & \\ & \ddots & & & & & \\ & & b_{l,1} & b_{l,2} & b_{l,3} & & \\ & & & \ddots & & & \\ & & & b_{L-1,1} & b_{L-1,2} & b_{L-1,3} & \\ & & & & b_{L,1} & b_{L,2} & \end{bmatrix} \tag{5.88}$$

Coupling with the boundary conditions at the water surface and seabed, Eq. 5.87 can be efficiently solved using the double sweep method in each column. The coefficient matrix and known vector are defined below.

For the vertical diffusion of flow and salinity, at bottom layer $l = 1$,

$$\begin{cases} b_{1,2} = \left[1 + \dfrac{\Delta t}{\Delta\sigma^2}\left(\upsilon_{\sigma 2} + \upsilon_{\sigma 1}\right)\right] \\ b_{1,3} = -\dfrac{\Delta t}{\Delta\sigma^2}\left(\upsilon_{\sigma 2} + \upsilon_{\sigma 1}\right) \\ F_{u,1} = u_1^{n+\frac{2}{3}} - \Delta t g \dfrac{\partial\zeta}{\partial x} - \dfrac{2\Delta t}{\Delta\sigma}\dfrac{\tau_{b,x}}{H} \\ F_{v,1} = v_1^{n+\frac{2}{3}} - \Delta t g \dfrac{\partial\zeta}{\partial y} - \dfrac{2\Delta t}{\Delta\sigma}\dfrac{\tau_{b,y}}{H} \\ F_{s,1} = s_1^{n+\frac{2}{3}} \end{cases} \tag{5.89}$$

In the interior layers $l = 2,3,\ldots,L-1$

$$\begin{cases} b_{l,1} = -\dfrac{\Delta t}{2\Delta\sigma^2}\left(\upsilon_{\sigma\, l} + \upsilon_{\sigma\, l-1}\right) \\ b_{l,2} = 1 + \dfrac{\Delta t}{2\Delta\sigma^2}\left(\upsilon_{\sigma\, l+1} + 2\upsilon_{\sigma l} + \upsilon_{\sigma\, l-1}\right) \\ b_{l,3} = -\dfrac{\Delta t}{2\Delta\sigma^2}\left(\upsilon_{\sigma\, l+1} + \upsilon_{\sigma\, l}\right) \\ F_{u,1} = u_l^{n+\frac{2}{3}} - \Delta t g \dfrac{\partial\zeta}{\partial x} \\ F_{v,1} = v_l^{n+\frac{2}{3}} - \Delta t g \dfrac{\partial\zeta}{\partial y} \\ F_{s,l} = s_l^{n+\frac{2}{3}} \end{cases} \tag{5.90}$$

At the surface layer $l = L$

$$\begin{cases} b_{L-1,1} = -\dfrac{\Delta t}{\Delta\sigma^2}\left(\upsilon_{\sigma\, L} + \upsilon_{\sigma\, L-1}\right) \\ b_{L,2} = 1 + \dfrac{\Delta t}{\Delta\sigma^2}\left(\upsilon_{\sigma\, L=1} + \upsilon_{\sigma\, L}\right) \\ F_{u,L} = u_L^{n+\frac{2}{3}} - \Delta t g \dfrac{\partial\zeta}{\partial x} + \dfrac{2\Delta t}{\Delta\sigma}\dfrac{\tau_{s,x}}{H} \\ F_{v,L} = v_L^{n+\frac{2}{3}} - \Delta t g \dfrac{\partial\zeta}{\partial y} + \dfrac{2\Delta t}{\Delta\sigma}\dfrac{\tau_{s,y}}{H} \\ F_{s,L} = s_L^{n+\frac{2}{3}} \end{cases} \tag{5.91}$$

In Eq. 5.89 to Eq. 5.91, υ_σ denotes the vertical eddy viscosity ε_σ for flow and vertical diffusion coefficient and $\varepsilon_{s,\sigma}$ for salinity in σ-coordinate.

For the vertical diffusion of sediment, at surface layer $l = 1$,

$$\begin{cases} b_{1,2} = 1 + \dfrac{\Delta t}{\Delta\sigma^2}\varepsilon_{s,\sigma,2} \\ b_{1,3} = -\dfrac{\Delta t}{\Delta\sigma^2}\left(\varepsilon_{s,\sigma\,2} + \dfrac{\Delta\sigma}{H}\omega_{s,2}\right) \\ F_{c,1} = c_1^{n+\frac{2}{3}} - \dfrac{\Delta t}{\Delta\sigma}\dfrac{q_{s,b}}{H} \end{cases} \tag{5.92}$$

In the interior layers $l = 2, 3, \ldots, L-1$

$$\begin{cases} b_{l,1} = \dfrac{\Delta t}{2\Delta\sigma^2}\left(\dfrac{\Delta\sigma}{H}\omega_{s,l-1} - \varepsilon_{s.\sigma,l} - \varepsilon_{s,\sigma,l-1}\right) \\ b_{l,2} = 1 + \dfrac{\Delta t}{2\Delta\sigma^2}\left(\varepsilon_{s,\sigma,l+1} + 2\varepsilon_{s,\sigma,l} + \varepsilon_{s,\sigma\,l-1}\right) \\ b_{l,3} = \dfrac{\Delta t}{2\Delta\sigma^2}\left(\dfrac{\Delta\sigma}{H}\omega_{s,l+1} + \varepsilon_{s.\sigma,l+1} + \varepsilon_{s,\sigma,l}\right) \\ F_{c,l} = c_l^{n+\frac{2}{3}} \end{cases} \tag{5.93}$$

At the surface layer $l = L$

$$\begin{cases} b_{L,1} = \dfrac{\Delta t}{\Delta\sigma^2}\left(\dfrac{\Delta\sigma}{H}\omega_{s,L-1} - \varepsilon_{s,\sigma\,L-1}\right) \\ b_{L,3} = 1 + \dfrac{\Delta t}{\Delta\sigma^2}\varepsilon_{s,\sigma,2} \\ F_{c,L} = c_L^{n+\frac{2}{3}} \end{cases} \tag{5.94}$$

The vertical differential equations of turbulence energy and its macroscale describe in Eq. 5.69 can be solved using the same approach. In order to keep the model stable, the dissipation term should be discretized implicitly (Gross, *et al.*, 1999).

5.3.3.4 Approximations of the continuity equation for tidal level

By integrating the vertical diffusion equation of flow, Eq. 5.68, from the bottom to the surface and coupling with the boundary conditions given by Eq. 5.7 and Eq. 5.10, we can get:

$$\int_0^1 u^{n+1} d\sigma = \int_0^1 u^{n+\frac{2}{3}} d\sigma - g\cdot\Delta t\frac{\partial\zeta}{\partial x} + \frac{\Delta t}{H}\left(\tau_{s,x} - \tau_{b,x}\right) \tag{5.95}$$

$$\int_0^1 v^{n+1} d\sigma = \int_0^1 v^{n+\frac{2}{3}} d\sigma - g \cdot \Delta t \frac{\partial \zeta}{\partial y} + \frac{\Delta t}{H}\left(\tau_{s,y} - \tau_{b,y}\right) \tag{5.96}$$

Substituting Eq. 5.95 and Eq. 5.96 into the continuity equation, Eq. 5.71, the tidal level can be solved from the following equation.

$$\begin{aligned} \frac{\zeta^{n+1} - \zeta^{n}}{\Delta t} &+ \frac{\partial}{\partial x}\left(H^{n+1} \cdot \bar{u}^{n+\frac{2}{3}}\right) + \frac{\partial}{\partial y}\left(H^{n+1} \cdot \bar{v}^{n+\frac{2}{3}}\right) \\ &- \Delta t \cdot g\left[\frac{\partial}{\partial x}\left(H^{n+1} \cdot \frac{\partial \zeta^{n+1}}{\partial x}\right) + \frac{\partial}{\partial y}\left(H^{n+1} \cdot \frac{\partial \zeta^{n+1}}{\partial y}\right)\right] \\ &+ \Delta t\left[\frac{\partial}{\partial x}\left(\tau_{s,x} - \tau_{b,x}\right) + \frac{\partial}{\partial y}\left(\tau_{s,y} - \tau_{b,y}\right)\right] = 0 \end{aligned} \tag{5.97}$$

where $\bar{u} = \int_0^1 u d\sigma, \bar{v} = \int_0^1 v d\sigma$.

Eq. 5.97 is non-linear and an iterative method is applied to compute the tidal level. A first-order FEM using four-node polynomial interpolation functions for both the tidal level and water depth are introduced to discretize the equation (Lu, 1997). Applying the standard Galerkin method, the resulting matrix equation is as follows:

$$[D]\left\{\zeta_i^{n+1}\right\} = [Z] \tag{5.98}$$

where

$$[D] = \sum_{e=1}^{M}\left\{S1_{jk}^{(e)} - \Delta t \cdot \left[S2_{jkl}^{(e)} \cdot \bar{u}_l^{(e)} + S3_{jkl}^{(e)} \cdot \bar{v}_l^{(e)}\right] + \Delta t^2 \cdot g \cdot S4_{jkl}^{(e)} \cdot H_l^{(e)}\right\} \tag{5.99}$$

$$\begin{aligned} [Z] = \sum_{e=1}^{M} S1_{jk}^{(e)} \cdot \zeta_k^{n(e)} &+ \Delta t \cdot \left[S2_{jkl}^{(e)} \cdot \bar{u}_l^{(e)} + S3_{jkl}^{(e)} \cdot \bar{v}_l^{(e)}\right] \cdot h_k^{(e)} \\ &- \Delta t^2 \cdot \left[S5_{jk}^{(e)}\left(\tau_{s,x,k} - \tau_{b,x,k}\right) + S6_{jk}^{(e)}\left(\tau_{s,y,k} - \tau_{b,y,k}\right)\right]\} \end{aligned} \tag{5.100}$$

and

$$S1_{jk}^{(e)} = \iint_{\Omega^e} \phi_j \varphi_k \left|J\right| d\xi \, d\eta \tag{5.101}$$

$$S2_{jkl}^{(e)} = \iint_{\Omega^e} Q_j \varphi_k \phi_l d\xi d\eta - \int_{\Gamma} \phi_j \varphi_k \phi_l y_{\xi} d\xi - \int_{\Gamma} \phi_j \varphi_k \phi_l y_{\eta} d\eta \tag{5.102}$$

$$S3_{jkl}^{(e)} = \iint_{\Omega^e} R_j \varphi_k \phi_l d\xi d\eta + \int_{\Gamma} \phi_j \varphi_k \phi_l x_{\xi} d\xi + \int_{\Gamma} \phi_j \varphi_k \phi_l x_{\eta} d\eta \tag{5.103}$$

$$\begin{aligned} S4_{jkl}^{(e)} = & \iint_{\Omega^e} \frac{Q_j Q_k' \varphi_l}{\left|J\right|} d\xi d\eta + \iint_{\Omega^e} \frac{R_j R_k' \varphi_l}{\left|J\right|} d\xi d\eta \\ & - \int_{\Gamma} \phi_j \left(\frac{R_k'}{\left|J\right|} x_{\xi} - \frac{Q_k'}{\left|J\right|} y_{\xi} \right) \varphi_l d\xi - \int_{\Gamma} \phi_j \left(\frac{R_k'}{\left|J\right|} x_{\eta} - \frac{Q_k'}{\left|J\right|} y_{\eta} \right) \varphi_l d\eta \end{aligned} \tag{5.104}$$

$$S5_{jk}^{(e)} = \iint_{\Omega^e} \phi_j Q_k d\xi d\eta \tag{5.105}$$

$$S6_{jk}^{(e)} = \iint_{\Omega^e} \phi_j R_k d\xi d\eta \tag{5.106}$$

$$Q_j' = \frac{\partial y}{\partial \eta} \frac{\partial \varphi_j}{\partial \xi} - \frac{\partial y}{\partial \xi} \frac{\partial \varphi_j}{\partial \eta} \tag{5.107}$$

$$R_j' = \frac{\partial x}{\partial \eta} \frac{\partial \varphi_j}{\partial \xi} + \frac{\partial x}{\partial \xi} \frac{\partial \varphi_j}{\partial \eta} \tag{5.108}$$

φ_j is the four-node isoparametric shape functions.

5.4 Model validation

Before the application of the model described above, it should be calibrated and validated extensively, not only by some simple cases with analytical solutions or experimental data as had been done by Wai and Lu (1998), Chen (2001) and

Jiang (2003), but also by field data. Here, the model was verified by the measurements carried out in the Pearl River Estuary during the dry season (March) and the wet season (August) in 1998.

5.4.1 Measurement data

In 1998, two hydrographic and water quality surveys during the dry season (March) and the wet season (July) were carried out by the Civil Engineering Department of the Hong Kong Government. The hydrographic survey included the measurement of water level, current velocity, temperature, and wind speed and wave characteristics. Monitoring stations were set up at several locations throughout the Pearl River Estuary. The locations of the monitoring stations for the dry and wet season surveys are shown in Fig. 5.3. Each seasonal hydrographic survey consisted of a 30-day continuous survey on water level variation at 5 specified stations from February 25 to March 27 during dry season, and from June 20 to July 20 during wet season; a 15-day fixed station continuous measurement on current and depth at specified stations from March 9 to 24 during dry season, and from July 1 to 16 during wet season; a 28-hour ship-based measurement on profiles of CTD; and a 28-hour simultaneous water quality sampling at the specified stations and laboratory testing on a variety of water quality parameters during spring tide (March 12 to 13) and neap tide (March 19 to 20) in the dry season, and during neap tide (July 4 to 5) and spring tide (July 9 to 10) in the wet season.

The marine water was monitored for specific parameters including suspended solids, temperature, salinity and heavy metals. All water quality samplings were carried out at least 72 hours after commencement of fixed station survey. Water samples and on-site water quality measurements were conducted for a neap tide and a spring tide in both the wet season and the dry season. Each sampling period covered 28 hours. The sampling intervals were 3 to 3.5 hours giving a total of 8 samples for each sampling station in a 28-hour period. For in-situ hydrographic parameters, measurements were made at 1 m interval from surface to sea bottom to provide profile distribution and water samples were collected at 3 depths (1 m below sea surface, mid-depth and 1 m above seabed) during the dry season survey and at 5 depths (at equal vertical intervals from surface to seabed) during the wet season survey. In addition, hourly measurement of water depth and current speed and direction were carried out at specified stations to confirm the hydrodynamic conditions under which the sample had been collected.

Wave measurement was carried out at station 7 only in the wet season where rough wave climate might occur during a tropical storm or a typhoon event.

5.4.2 Model establishment and boundary conditions

To simulate tidal current, salinity intrusion and sediment transport in the PRE, a large coastal area was selected to be the computational domain, which covers the entire the PRE as depicted in Fig. 5.4. The computational area is 203 km × 188 km in size, with a total sea area of about 18500 km^2. The coastal area to be simulated was divided into 1404 nine-node elements and the total number of nodes was 6036. The area of each element varied from 0.3 km^2 in the Hong Kong Waters to 63 km^2 near the open sea boundary. Mesh size zooming in the Lingding Bay (see Fig. 5.4), which was of most interest in this study, was around 1.5 km × 2.0 km. The water column was divided into 10 layers equally from the seabed to water surface at each node.

There are eleven open boundaries in the numerical model, of which eight are the Pearl River outlets. These eight outlets are the waterways that discharge freshwater and sediment into the PRE and the other three are the open sea boundaries.

The same boundary conditions used in the 2D modelling described in Chapter 4 were also applied in this 3D modelling. Tidal elevations and flow rates at the boundaries drive the model. At river outlets, due to the lack of data synchronous with the field measurement in 1998, the mean seasonal flow rates and sediment concentration at each outlet were used. Their values are listed in Table 4-1. The salinity at these boundaries was assumed to be zero, i.e., it was assumed that salt water can not cross the boundaries of river outlets. The open sea boundaries were set far away from the coastline. No tidal gauges or survey stations can be found along the open sea boundaries exactly and the tidal elevations at these boundaries were extrapolated from the tidal records at the nearest tidal gauges using the M2, S2, O1 and K1 harmonic tide components (see Fig. 4.1). The constant sediment concentration and salinity in different seasons as listed in Table 4-2 were imposed as the open sea boundary conditions.

In the present modelling, the model ran from 0:00 March 10 to 0:00 March 21 during the dry season, and from 0:00 July 1 to 0:00 July 11 during the wet season. The duration of each model run covers both a spring tide and a neap tide. A five-day simulation was done before the commencement of the actual simulation period to generate the initial conditions. The time step of the simulation is 180 s.

For the sediment transport, the modelling only considered the suspended sediment and bed materials with a uniform sediment particle size of 10 μm, which is the most abundant sediment fraction in the PRE.

The following results are based on the parameters listed in Table 5.1.

Table 5.1 Parameters used in the 3D modelling

Symbols	Values	Physical meanings
a	0.01H	Reference height above seabed (H is total water depth)
C	0.1	Coefficient for horizontal eddy viscosity
D_{50}	10	Median diameter of sediment particle
E_3	0.25	Coefficient in turbulence module
g	9.81 m/s^2	Gravity acceleration
T	20 ℃	Water temperature
α_d	1	Deposition probability of sediment settling to the seabed
α_s	1	Erosion probability of sediment from seabed
γ'	1200 kg/m^3	Dry-bulk density of sediment
κ	0.4	von Kármán constant
φ	22.5°	Latitude of computational domain
ρ_0	1000 kg/m^3	Constant reference density of water
ρ_{b0}	1600 kg/m^3	Density of consolidated sediment on seabed
ρ_s	2650 kg/m^3	Density of sediment particle

5.4.3 Model validation

The model was verified on tidal level, current (speed and direction) and flow pattern, salinity profile and sediment concentration at specified stations with neap and spring tides during dry and wet seasons.

5.4.3.1 Tidal level

The comparisons of the computed and observed tidal levels at stations 1, 3, 11 to 13 during neap and spring tides in the dry and wet seasons are shown in Fig. 5.5a to Fig.5.5d. Generally, considering only four tidal harmonic components driving the model, both the computed amplitude and phase of tidal levels can be seen in good agreement with the observed ones. The mean errors of computed tidal level are listed in Table 5.2. It can be seen that most of the mean errors are less than 0.15 m, and generally the tidal errors at the river outlet (station 1) are larger than those at other stations, and errors in the wet season are larger than those in the dry season. That may be caused by the uncertainties in the boundary conditions.

Table 5.2 Mean errors between computed tidal levels and observed ones

Station No.	Mean errors of tidal level (m)			
	Dry season		Wet Season	
	Neap tide	Spring tide	Neap tide	Spring tide
1	0.136	0.146	0.168	0.266
3	0.101	0.142	0.142	0.187
11	0.124	0.135	0.112	0.113
12	0.074	0.081	0.141	0.137
13	0.078	0.093	0.148	0.139

Due to the bottom friction and the topography, the tidal range increases from open sea to Humen when tidal current propagates upstream. Freshwater runoffs from river outlets affect not only the tidal current, but also the tidal level, especially in the region near the outlets.

5.4.3.2 Tidal current and flow patterns

Tidal current in the PRE is not only affected by the tides from open sea, but also strongly affected by the strong runoff discharging from the Pearl River through the eight outlets. The velocity during ebbing is larger than that during flooding, and the duration of ebbing is also longer (Xu, *et al*., 1985). The computed velocity at five stations 3, 6, 8, 15, and 16 are compared with the observed ones. Station 3 is located near the Neilingding Island, at the middle of the Lingding bay. Stations 6 and 8 are located at the end of the East Channel and the West Channel, respectively. Stations 15 and 16 are situated near the outlets of Hongqimen and Jiaomen, respectively.

Fig. 5.6 compares the computed current speed and direction with measured ones at three layers, namely bottom layer (0.9H), middle layer (0.5H) and surface layer (0.1H) during spring tide in the dry season. Fig. 5.7 to Fig. 5.9 show the comparison of computed tidal current with measurements during neap tide in the dry season, during spring tide in the wet season and during neap tide in the wet season, respectively. Basically, it can be seen that both the magnitude of computed velocity and its direction at different layers are in good agreement with the measurements at each station in all the three cases. This indicates that the model can simulate tidal current well under different hydrodynamic conditions. Stations 6 and 8 are located far away from the outlets and hence the effect of freshwater runoff on the current is weaker, with the duration of flooding and ebbing flow nearly equal. Flows are mainly along the deep channels and the model captures these flow characteristics well. At station 3, which is located near Neilingding Island, the flow is affected by the tidal forcing, freshwater runoff, intrusion of salt water at the bottom layer, and the circumfluence around the Neilingding Island. The complicated hydrodynamic conditions, the particular geographical location and to a lesser extent the insufficiently refined mesh size contribute to the relative inaccuracy of the computed results in that station. The current speed at the surface layer is smaller than the measured values. This may be mainly due to the inaccuracy in the specification of runoffs at river outlets. Stations 15 and 16 are strongly affected by the runoff from Hongqimen and Jiaomen, respectively. The duration of ebbing is much longer than that of flooding. The phase of the computed flow agrees well with measurements at both stations. The computed current speed at station 15 is also reasonably good. However, the current speed at station 16 is under predicted. That is possibly due to the combined result of an underestimated runoff from Jiaomen and the tidal flats near the outlets.

The flow patterns when flooding, high slack ebbing and low slack during a spring tide in the wet season in the PRE are shown in Fig. 5.10a to Fig. 5.10d, respectively. Generally, the model can simulate the complex flow patterns well. Even with the complicated irregular land boundaries, the simulated results can capture the main features of water flowing mainly along the deep channels and the lag between tide and current.

The current speed in the PRE decreases when the tide comes to the low level at Chiwan station. At low slack, the flow between Neilingding Island and Macau to the Hong Kong Waters is very small, especially in the bottom layer. However, it can be seen that there exist seaward flows near the western outlets and along the East and West channels from bottom to the water surface. At that time, flooding commences through the Victoria Channel and Ma Wan Strait in the whole water column, which suggests the flooding process propagating from east to west in the open sea. There is a flow reversal from the bottom, which flows upstream, to the water surface, which flows seaward along Urmston Channel indicating the intrusion of salt water. The region downstream of Neilingding Island is the main area where the salt water goes back and forth in each tidal cycle in the wet season. The greater horizontal density gradient drives the salt water intrusion riverward in the bottom layer. The issue of saltwater intrusion is discussed in the following section in detail.

When the tide turns to flooding, the flows at the surface layer and bottom layer are basically in the same direction, with the flow propagating from the southeastern open sea. The flow mainly goes through the deep channels around Lantau Island. It then partly goes directly to Humen through the East Channel and the West Channel and partly turns west to the western outlets after entering Lingding bay. When the tide level reaches high slack in the PRE, the current at the outer part of the PRE begins to ebb, while that at Lingding Bay is still in the flood stage. Under the action of strong freshwater outflow, the current outside Hengmen and Hongqimen begins to flow seaward at that time. Due to the different phase lags between current and tide at different stations, the flow pattern at high slack is complicated. Some large scale vortices flowing clockwise can be found at the entrance of Deep Bay and in the waters at the west of Hong Kong International Airport, while some vortices flowing anticlockwise exist in the middle of the Lingding Bay.

During ebbing, the flow discharges downstream partly to the southeastern Lingding Bay, driven by the strong freshwater runoff from the three west outlets. The Lantau Island separates the flow into two parts. One part flows to the east into Victoria Harbor through the channel at the north of the Lantau Island, where the maximum velocity reaches around 2.0 m/s during spring tide in the wet season. The other part of the ebbing water flows to the south through the west channel of Lantau Island. The directions of ebbing flow at the surface layer and bottom layer are nearly the same. Compared to the magnitude of the maximum flooding velocity, ebbing flow not only has larger magnitude, but also has longer duration.

Fig. 5.11 shows the computed distribution of bottom shear stress during flooding and ebbing in a spring tide in 1998. It can be seen that, during flooding and ebbing in the spring tide, bottom shear stresses increase from downstream of the PRE, reach the maximum values in the middle reach, and then decrease landward again. The maximum bottom shear stress is about 2.0 N/m^2, which is located around Qi'ao Island, and larger shear stresses of 1.0-2.0 N/m^2 can be found in the Middle Shoal around Neilingding Island and the seaward end of the sand bars in the East and West channels. This implies that bed materials can be easily resuspended in these regions during flooding and ebbing in a spring tide. Shear stresses in other parts of the PRE are between 0.25 and 0.75 N/m^2. Bottom shear stresses vary during tidal cycles. Fig. 5.12 shows the time series of bottom shear stress at stations 2, 3 and 14 within a spring tide, with the corresponding maximum values of 1.33, 1.23 and 0.97 N/m^2, respectively.

Fig. 5.13 shows the distribution of vertically averaged horizontal eddy viscosity during flooding in a spring tide. It can be seen that the effect of land boundaries on the horizontal eddy viscosity is significant. Its value is about 8-10 m^2/s near land boundaries and lower than 4 m^2/s in most region during flooding in the spring tide. Fig. 5.14 shows the time series of vertically averaged horizontal eddy viscosity in the spring tide at stations 2 and 14. Its values vary during tidal cycles, increasing during flooding and ebbing and decreasing during tidal slacks.

Fig. 5.15 shows the variation of vertical eddy viscosity in the middle layer during a spring tidal cycle. The vertical eddy viscosity is smaller than the horizontal eddy viscosity. The maximum values in the middle layer at stations 2, 3 and 14 are 0.023, 0.015 and 0.018 m^2/s, respectively.

5.4.3.3 Salinity

Density gradient both in the horizontal and along water column due to the salinity distribution is one of the main hydrodynamic forces as in most shallow estuaries. The effect of temperature is usually very small. The salinity distribution also affects the strength of the turbulence. Salinity induced stratification will suppress the flow turbulence. Saltwater intrusion is directly related to the turbidity maximum in an estuary. Therefore, salinity is an essential parameter in estuarine modelling. However, saltwater intrusion is difficult to be simulated well because it is affected by both the tides and freshwater runoff. The salinity distribution in an estuary generally varies during different tidal cycles and between seasons.

In the dry season, the salinity at east and south boundaries was set to 35 ppt over the entire water column. Salinity at the northwestern corner of the west open boundary was 25 and 33 ppt at the surface and bottom layer, respectively. At other open boundary grid nodes and intermediate heights in the water column, the specified salinity was based on linear interpolation of the values at corners. Due to insufficient measurement data, the salinity at the boundaries of river outlets was set to zero, resulting in salt water not able to cross these boundaries. The comparisons of the time series of salinity of the surface layer, middle layer and bottom layer at stations 2, 4, 6 and 8 during spring tide and neap tide in the dry season (March 1998) are shown in Fig. 5.16 and Fig. 5.17. Generally, the salinity during neap tide and spring tide at these stations in the dry season is reproduced by the model with a maximum difference of 10% in the tidally averaged values when compared with measurements. At station 2, the model captures the strong intratidal transport of salinity with a maximum difference of computed salinity of about 23 ppt between flooding and ebbing. This indicates that the specified boundary conditions of salinity at open sea are reasonable and the imposed seasonally averaged flow rates at river boundaries basically match the real flow, especially at Humen. Away from the river outlets, the effect of freshwater runoff on the salinity intrusion becomes weaker. The variation of intratidal salinity becomes smaller with a maximum difference of computed salinity of about 15 ppt at station 4 and of about 7 ppt at station 6 at the surface layer along the East Channel. At station 8, which is located at the main ebbing waterway, salinity at the middle and bottom layer has little variation between tidal flooding and ebbing in the dry season. At the surface layer, the intratidal variation of salinity reaches a maximum value of 15 ppt. The computed result at this station during neap tide is good, but the model slightly underpredicts the salinity at the surface layer during spring tide.

In the wet season, the salinity at east and south boundaries was set to 33 ppt over the entire water column. Salinity at the northwestern corner of the west open boundary was 15 and 25 ppt at the surface and bottom layer, respectively. At other boundary grid nodes and intermediate heights in the water column, the specified salinity was also based on linear interpolation of the values at corners. Salinity at the boundaries of river outlets is also set to zero. Fig. 5.18 and Fig. 5.19 show the time series of computed and measured salinity of the bottom layer, middle layer and surface layer at stations 2, 6, 8 and 10 during neap tide (July 4 to 5) and spring tide (July 9 to 10) in the wet season (July, 1998), respectively. It can be seen that the computed salinity at different layers are in agreement with the measured ones at different stations generally, especially during the period of spring tide, which implies that the model can be used to simulate the advection and diffusion of conservative substances and the boundary conditions imposed at the Pearl River outlets correspond with the real situations basically.

During the neap tide, the model underpredicts slightly the variation of salinity during the whole tidal cycle in the bottom layer. But in a large part of the tidal cycle, the model over-predicts the salinity by about 3 to 5 ppt in the middle layer and bottom layer at station 2. These were partly related to the specified seasonal mean flow rate at Humen and partly to the accuracy of the vertical diffusion coefficient generated by the turbulence model. Station 2 is located at the head of the saltwater intrusion and the flow is fully stratified during the neap tide in the wet season, resulting in the suppression of turbulence. This is a very complicated hydrodynamic phenomenon which cannot be modelled very accurately. The model also over-predicts the surface salinity at stations 8 and 10 by about 2 and 5 ppt.

The salinity profiles at stations 2, 6, 8 and 10 during spring tide and neap tide in the wet season are shown in Fig. 5.20 and Fig. 5.21, respectively. Although there exist some differences between computed and observed profiles at these stations, the computed salinity during spring tide matches the field data quit well. During the neap tide in the wet season, the freshwater runoff from the Pearl River outlets dominates the hydrodynamics in the Lingding bay and the computed salinity at stations 2 and 6 are greater than measurements along the entire water column during a large part of the tidal cycle. It indicates that the seasonal mean flow rate at Humen was slightly smaller than the actual flow rate on that day.

Saltwater intrusion in the Pearl River Estuary is a very complicated phenomenon, which is not only strongly affected by the tidal flow and freshwater runoff, but also closely related to the complex bathymetry. The pattern of salinity intrusion in the PRE varies semi-diurnally, fortnightly and seasonally with the tidal flooding and ebbing changing from spring tide to neap tide and with the daily fluctuation in river runoff.

Fig. 5.22 and Fig. 5.23 show the computed salinity patterns at the surface and bottom layers during high and low slacks of a typical spring tide in the wet season (July, 1998), respectively. From these figures, we can see the tidal excursion of salt water in the wet season under the effect of seasonally averaged freshwater runoff from the Pearl River. Comparing these two figures, several characteristics of saltwater intrusion in the Pearl River Estuary could be discerned: a) Tidal level is one of the key factors that affect the intrusion of salt water, the higher the tidal level, the further upstream the salt water intrusion. During the high slack, the salt water wedge is closer to the river outlets than during the lower slack. b) Under the action of horizontal pressure gradient resulting from the salinity of the seawater, the effect of tidal level on the excursion of the salt water at the bottom layer is weaker than that at the surface layer. c) The salinity pattern at the bottom layer shows some consistency with the bathymetry of the Pearl River Estuary. The salt water is easier to intrude along the channels. d) In the wet season, the freshwater runoff from the Pearl River affects strongly the intrusion of the salt water, especially in the surface layer, where the influence of runoff could reach the open sea boundary. This implies that a large computational domain is necessary to give an accurate salinity pattern during the wet season in the PRE. Fig. 5.24 clearly shows the changes of salinity during the high slack and the lower slack in the wet season in the Lingding bay. It could be seen that: a) the maximum difference of salinity within a tidal cycle could reach 15 ppt in the surface layer, and to 25 ppt at the bottom layer; and b) the locations of the sharp changing zone are on the seaward side of sand bars in the East and West channels, where tidal flow begins to dominate the flow pattern instead of the river flow. Downstream of this zone, the salt water could easily intrude in the absence of the opposing river flow.

5.4.3.4 Sediment transport

Fig. 5.25 compares the profiles of computed sediment concentrations with measurements at stations 2, 6, 8 and 14 during a spring tide (July 9 to 10) in the wet season (July, 1998). Fig. 5.26 compares the time series of sediment concentrations at stations 2, 3 4 and 14 with measurements during a spring tide in the dry season (March, 1998). The computed sediment concentrations are in good agreement with measurements generally. The model results reveal that resuspension occurs during tidal flooding and ebbing, and deposition occurs during tidal slack periods. During flooding and ebbing, the sediment particles are resuspended from the seabed, with the sediment concentration near bottom increasing quickly from nearly 0 to 30-50 mg/l at these three stations. The differences of sediment concentration between the bottom layer and surface layer are also simulated well by the model.

Due to the existence of several river outlets, the sediment transport in the PRE is very complex. It is not only strongly affected by the freshwater runoff from the Pearl River, but also by tidal pumping, local resuspension, and flocculation. Fig. 5.27 to Fig. 5.29 show the suspended sediment concentration distribution at high slack, ebbing and low slack during a spring tide, respectively. Generally, the suspended sediment concentrations in channels are less than that on shoals. The concentration in the East Channel is less than that in the West Channel, because the latter is strongly affected by the input from the west outlets. The sediment concentration near Humen is lower. In the Hong Kong Waters, sediment concentration is low. Sediment particles depositing at high slack period will be resuspended during tidal ebbing, when a belt of high sediment concentration can be found extending from Hongqimen to the east of Qi'ao Island. A small amount of sediment particles passing through the main channels can reach the Hong Kong Waters.

Fig. 5.30 to Fig. 5.32 show the patterns of suspended sediment concentration at lower slack, during flooding and at high slack in the dry season in 1998. The quantity of sediment input from the Pearl River is small in the dry season, resulting in lower sediment concentration in the dry season. The sediment concentration in the channels is lower than 10 mg/l generally. In the shoals, during tidal flooding and ebbing, sediment particles can be resuspended from the seabed and sediment concentration in the bottom layer would reach 20-30 mg/l, and even more than 30 mg/l near the western river outlets.

5.5 Summary

In this chapter, a three-dimensional hydrodynamics and sediment mass transport model is developed and applied to study the sediment transport in the Pearl River Estuary. Based on the above study, the following conclusions can be drawn.

(1) The operator-splitting method applied to approximate and solve the governing equations is stable and effective. The model is improved in accuracy by considering the baroclinic term and coupling with the level 2.5 turbulence closure model of Mellor-Yamada.

(2) The model was extensively validated by measurement data obtained in July 1998. The computed results of tidal level, flow velocity, salinity and sediment concentration are in good agreement with the measurements, generally. The model can be used to simulate the fine cohesive sediment transport in a partially-mixed and high stratification estuary, and it could also be a useful tool to study the formation and development of turbidity maximum in the Pearl River Estuary.

(3) Salt water intrudes along deep channels. The range of the salt water wedge movement is 10 to15 km. The head of the wedges can reach the middle reach of

the East Channel and to the upstream of Nelingding Island in the West Channel during spring tide in the wet season. Most of the Pearl River Estuary region is affected by salt water in the dry season, and the salt water can intrude into the Humen channel.

(4) The maximum difference of salinity within a tidal cycle could reach 15 ppt at the surface layer, and 25 ppt at the bottom layer. The location of the sharp changing zone is on the seaward side of sand bars in the East and West channels.

(5) It can be seen from the horizontal distribution of suspended sediment concentration that the turbid zones are located near the three western outlets and at the middle shoal around Neilingding Island. Both sediment particles from the Pearl River, especially through the three western outlets, and from the deposition and resuspension within tidal cycles contribute to the sediment concentration and sediment transport in the Pearl River. Generally, the suspended sediment concentration in the Pearl River Estuary is lower in channels than in shoals. It is also lower in the East Channel than in the West Channel, and is lower during dry seasons than during wet seasons.

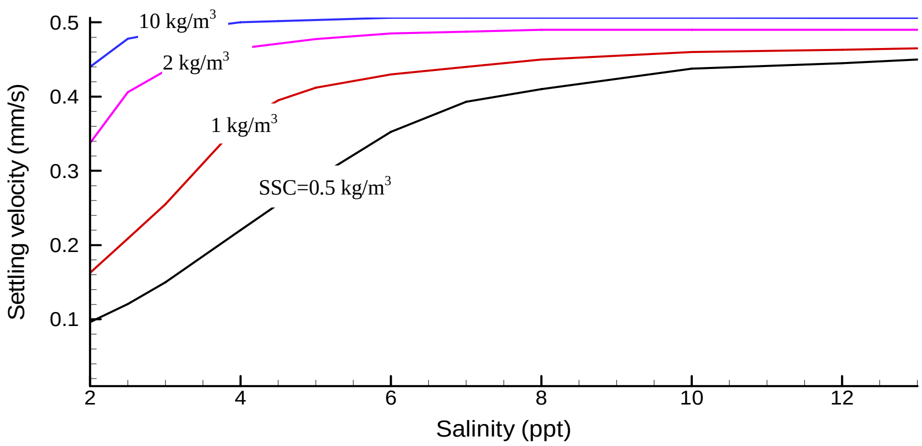

Fig. 5.1 Diagram of the relationship between settling velocity, salinity and concentration (Chien and Wan, 1999)

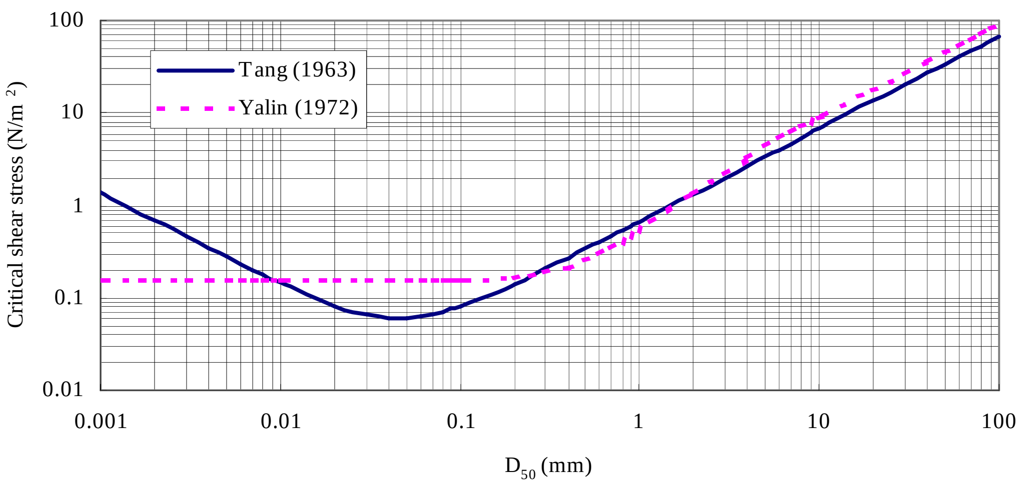

Fig. 5.2 Critical shear stress for fine sediment particles

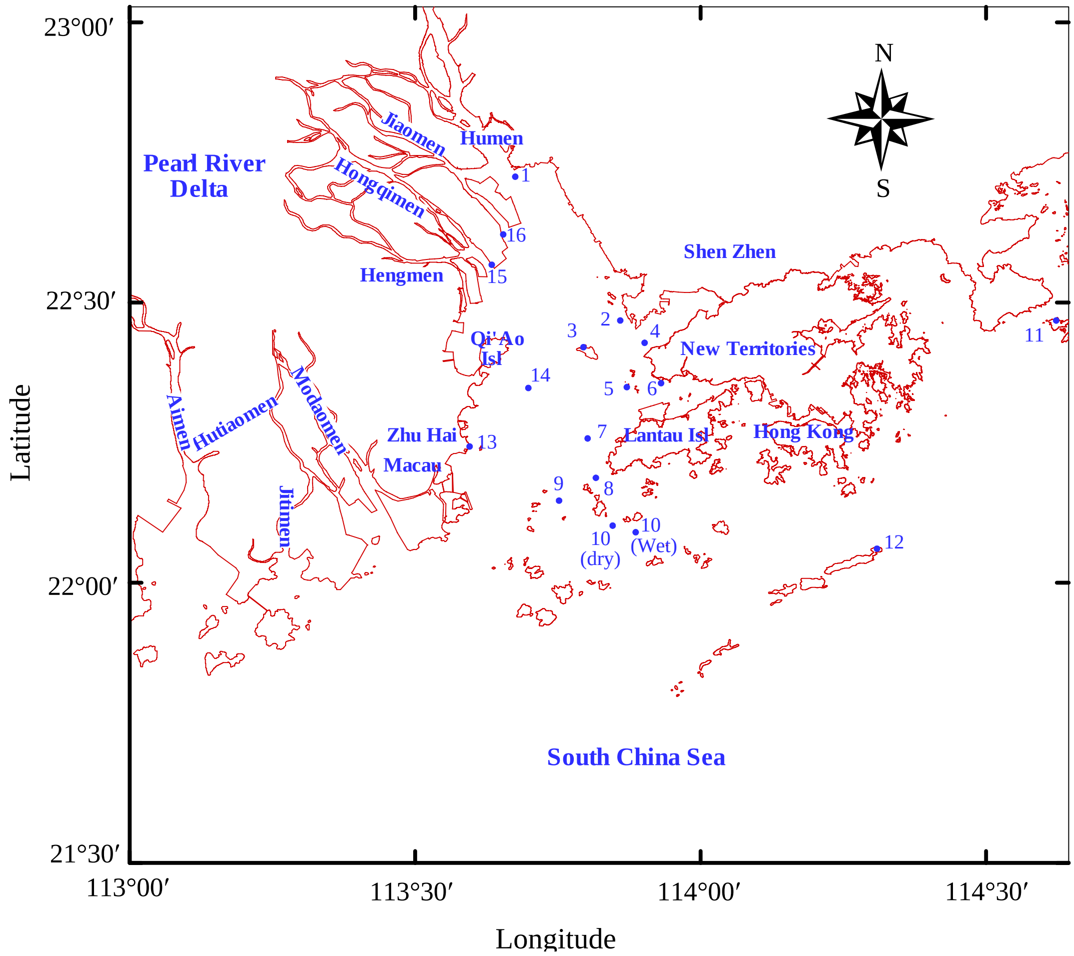

Fig. 5.3 Monitoring stations for hydrographic and water survey in 1998: stations 1 and 5 are the ADCP stations; 1,3, and 11 to13 are the tidal level stations; 3,6,8,15, and 16 are the stations for current; 7 is the wave record station; 1 to 10 and14 to 16 are the stations for water quality survey.

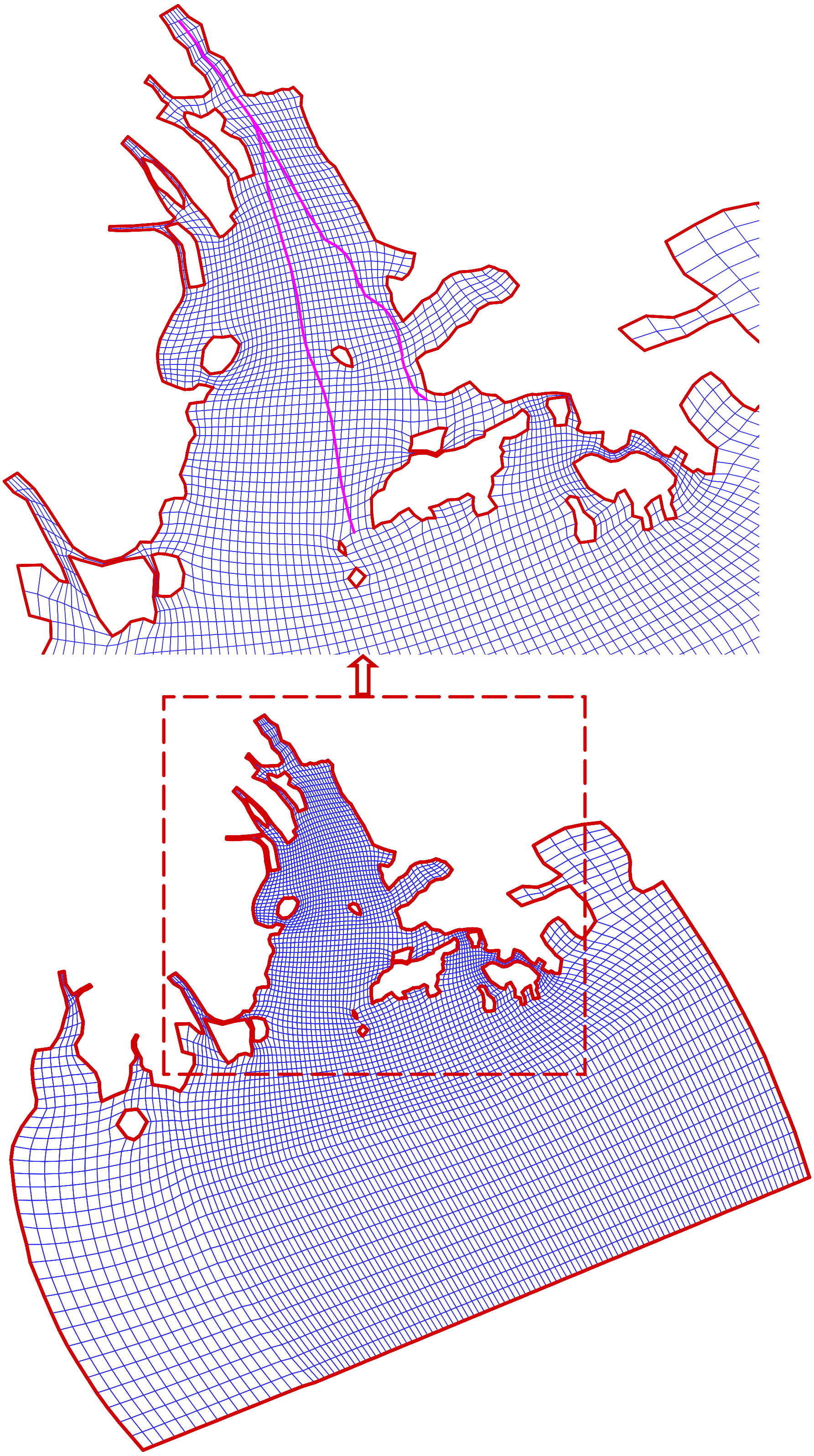

Fig. 5.4 Computational domain for 3D modelling

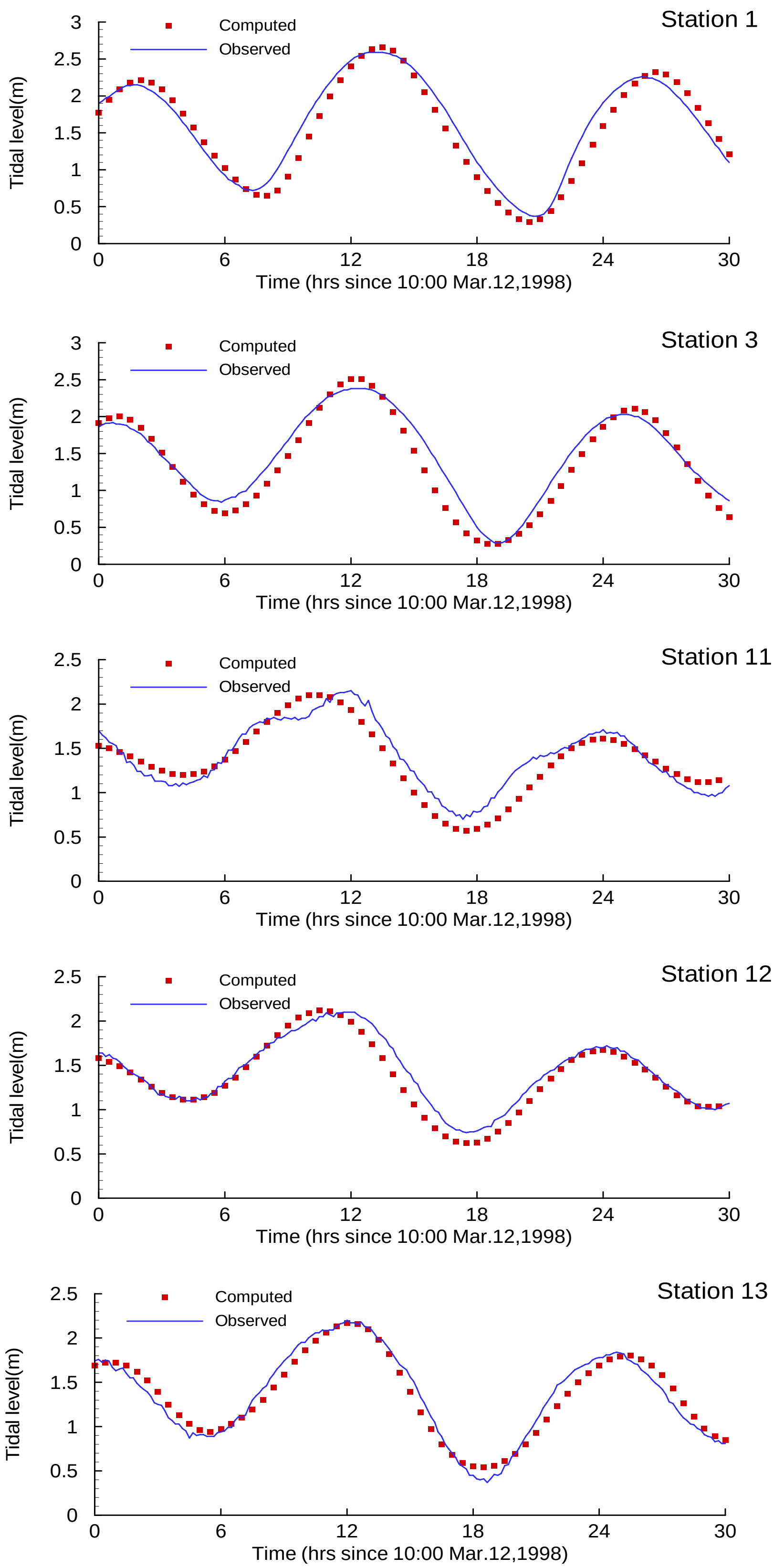

Fig. 5.5a Comparisons of computed and observed tidal level during a spring tide in the dry season (March 1998)

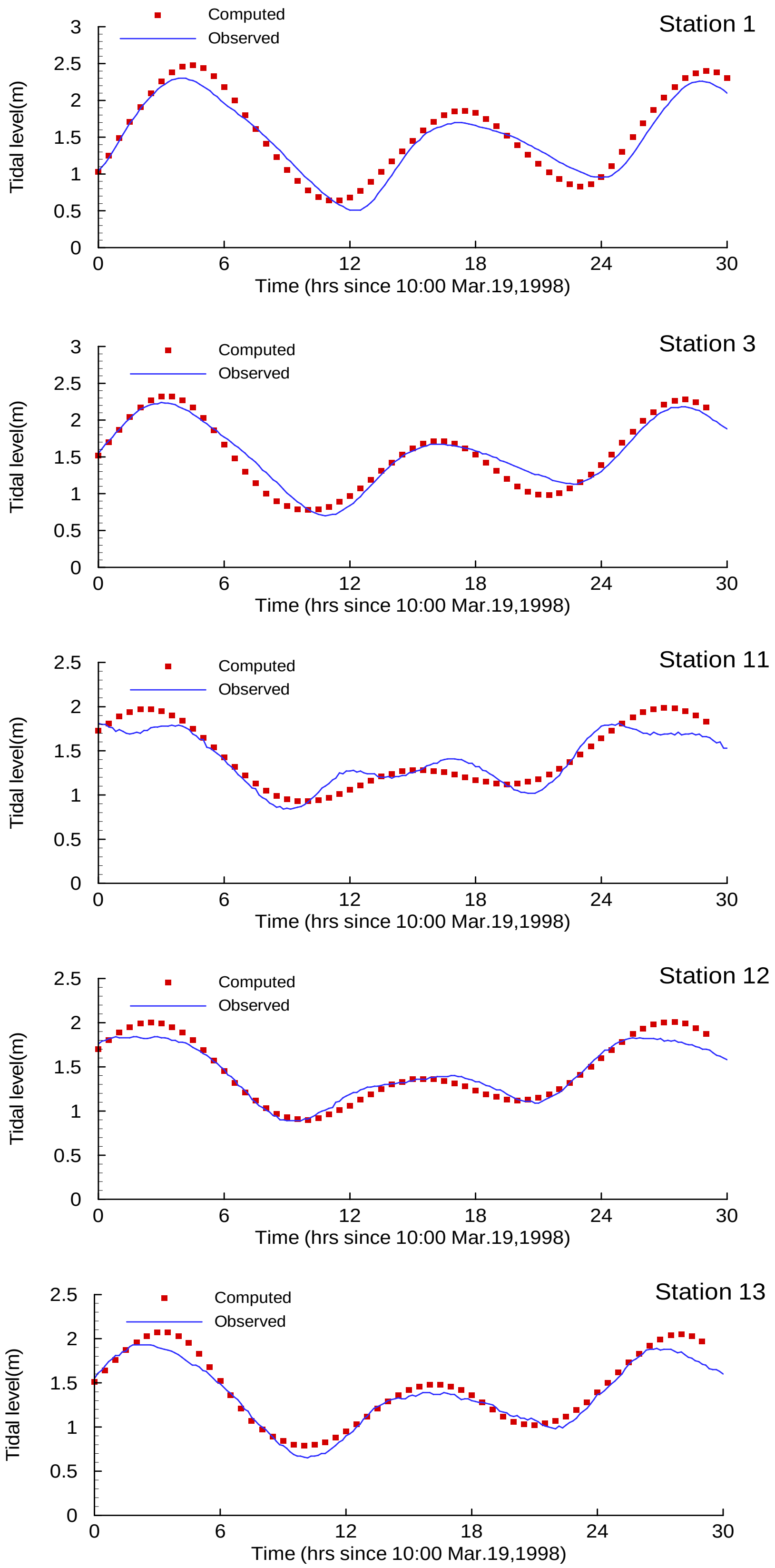

Fig. 5.5b Comparisons of computed and observed tidal level during a neap tide in the dry season (March 1998)

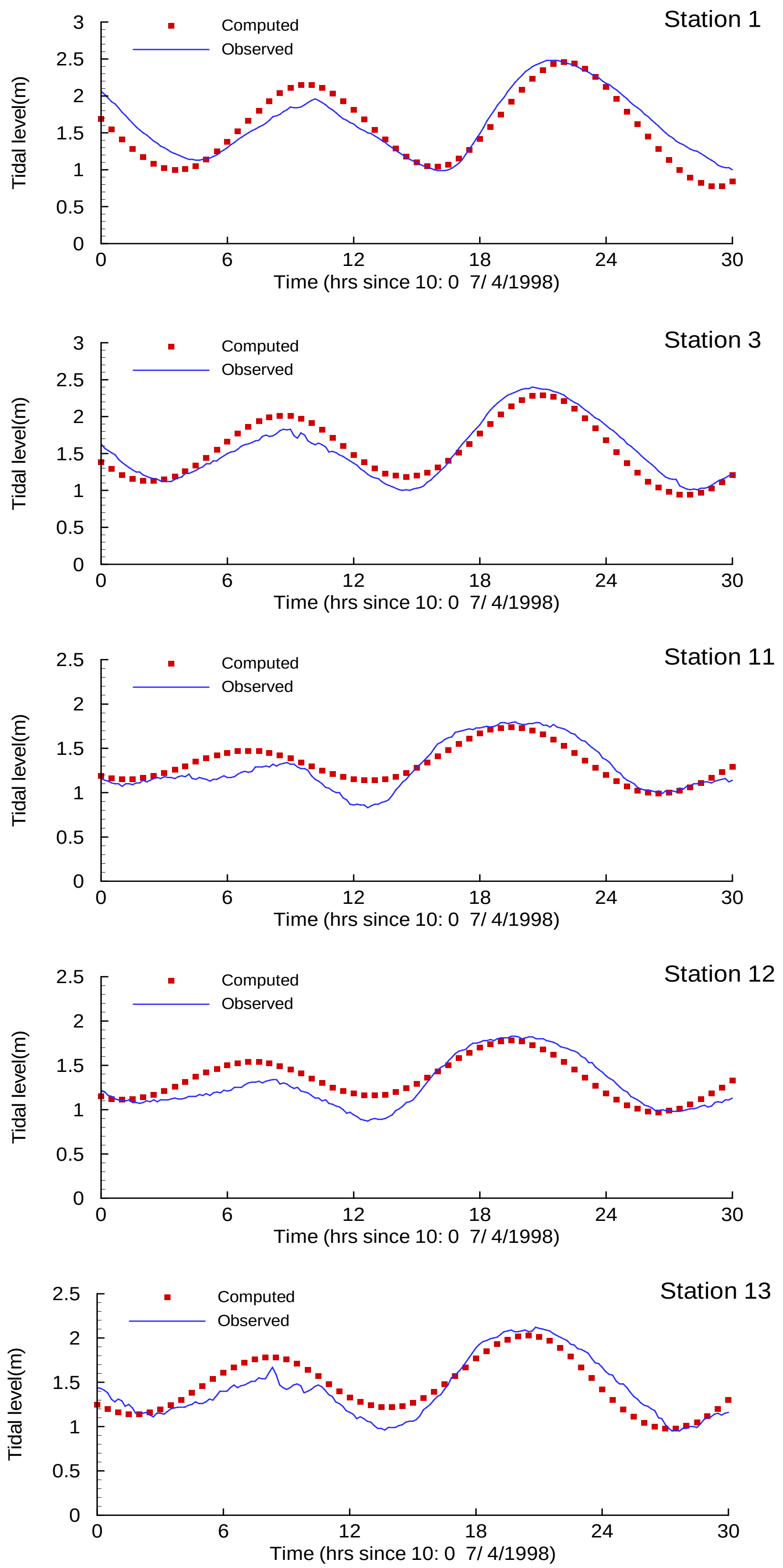

Fig. 5.5c Comparisons of computed and observed tidal level during a neap tide in the wet season (July 1998)

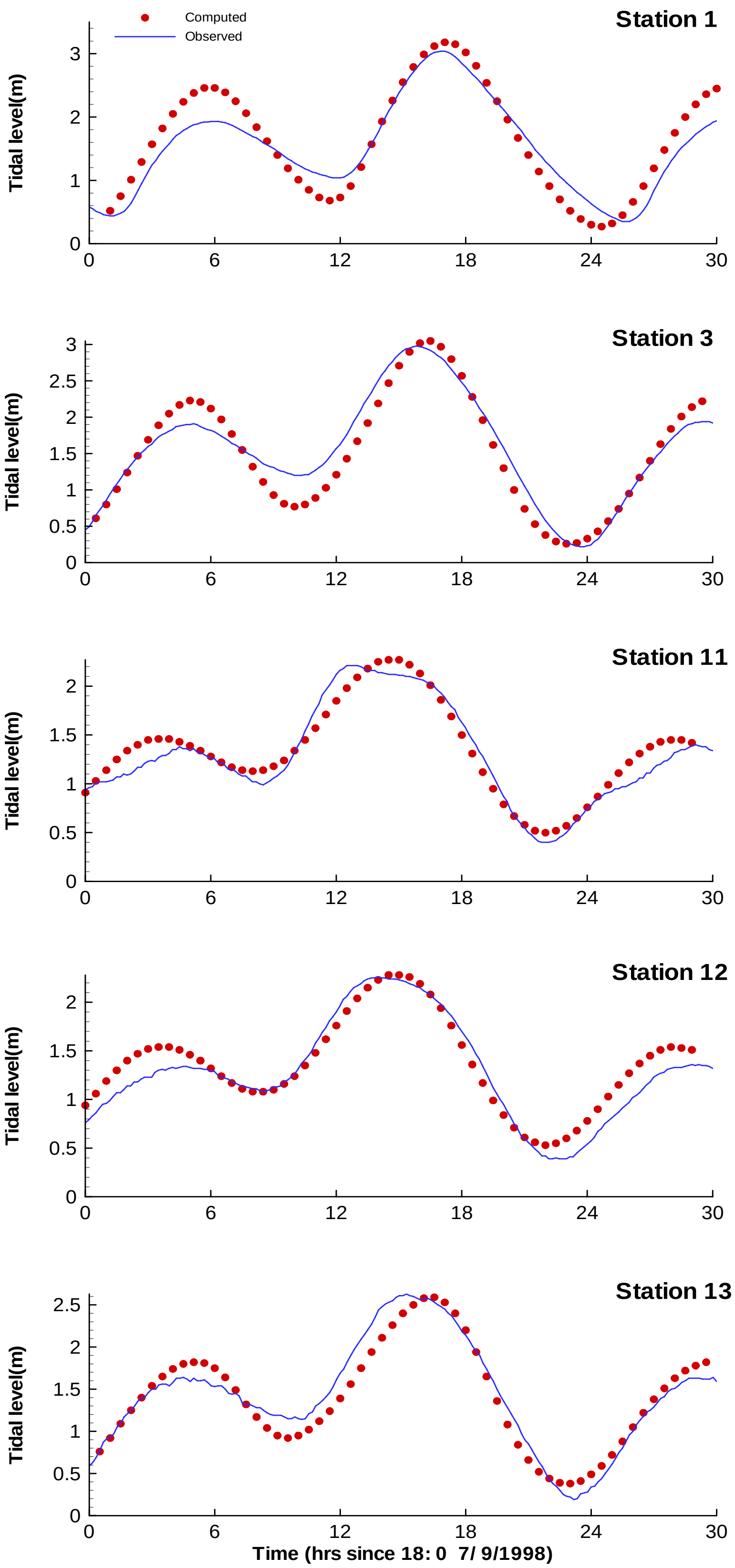

Fig. 5.5d Comparisons of computed and observed tidal level during a spring tide in the wet season (July 1998)

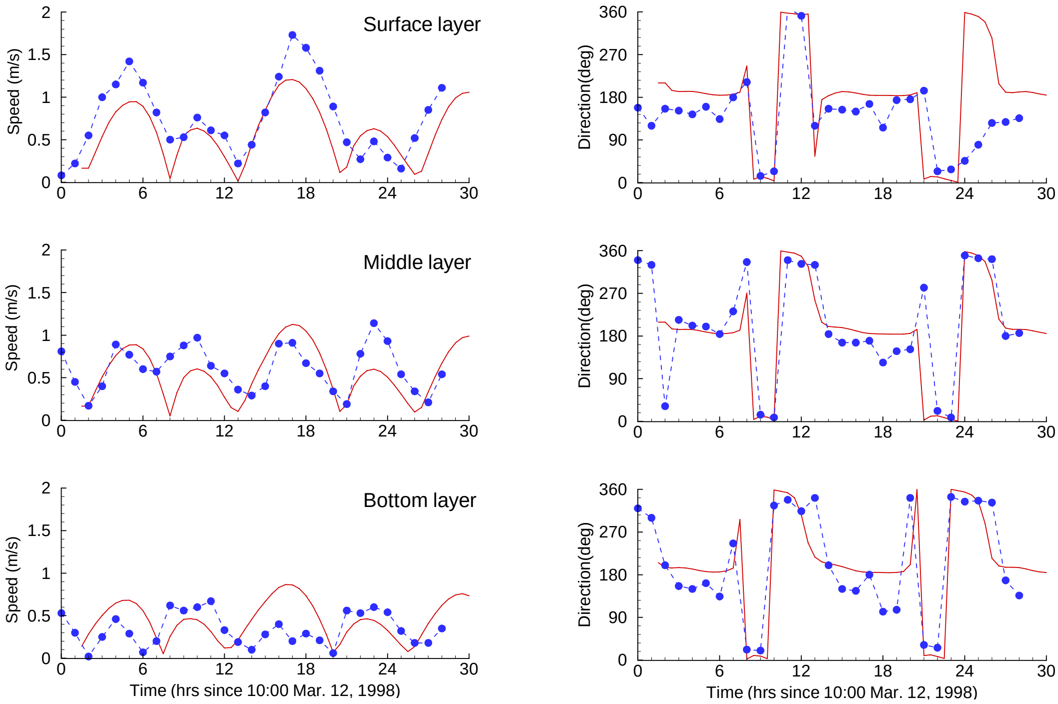

Fig. 5.6a Comparisons of current speed and direction (clockwise from north) at station 3 during a spring tide in the dry season: Solid lines represent computed results and dash lines denote the measurements.

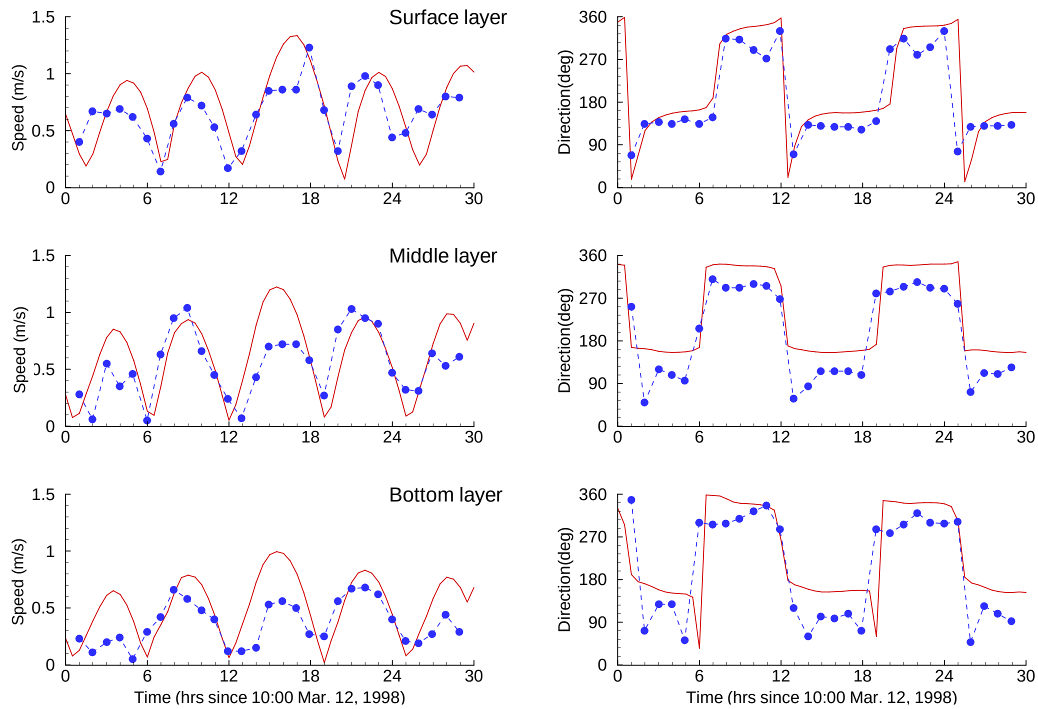

Fig. 5.6b Comparisons of current speed and direction (clockwise from north) at station 6 during a spring tide in the dry season: Solid lines represent computed results and dash lines denote the measurements.

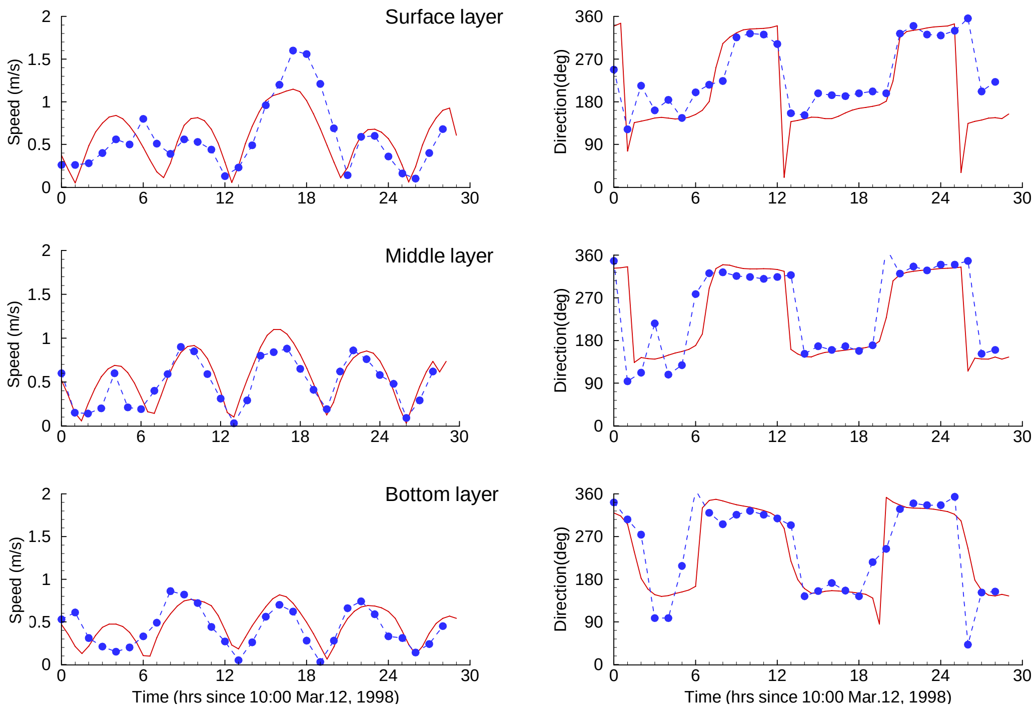

Fig. 5.6c Comparisons of current speed and direction (clockwise from north) at station 8 during a spring tide in the dry season: Solid lines represent computed results and dash lines denote the measurements.

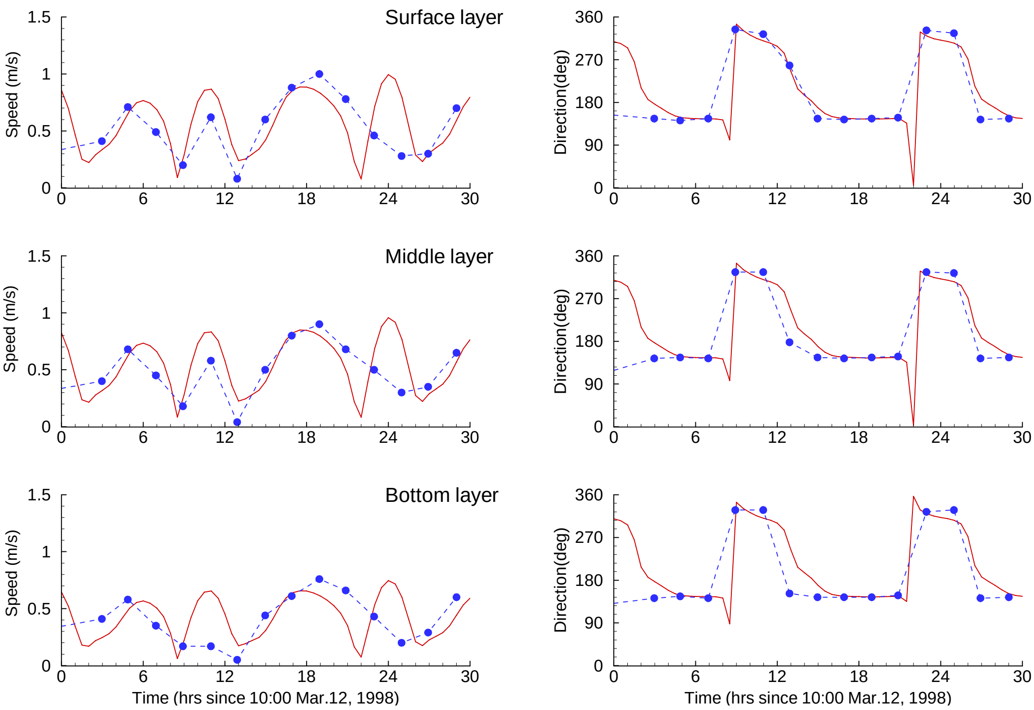

Fig. 5.6d Comparisons of current speed and direction (clockwise from north) at station 15 during a spring tide in the dry season: Solid lines represent computed results and dash lines denote the measurements.

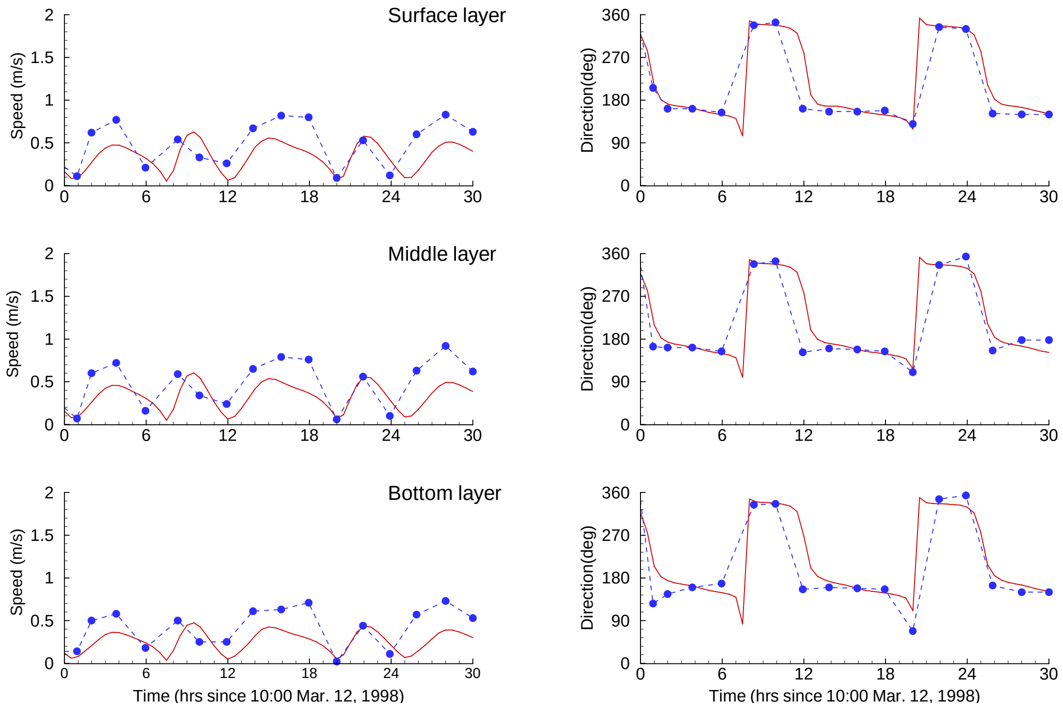

Fig. 5.6e Comparisons of current speed and direction (clockwise from north) at station 16 during a spring tide in the dry season: Solid lines represent computed results and dash lines denote the measurements.

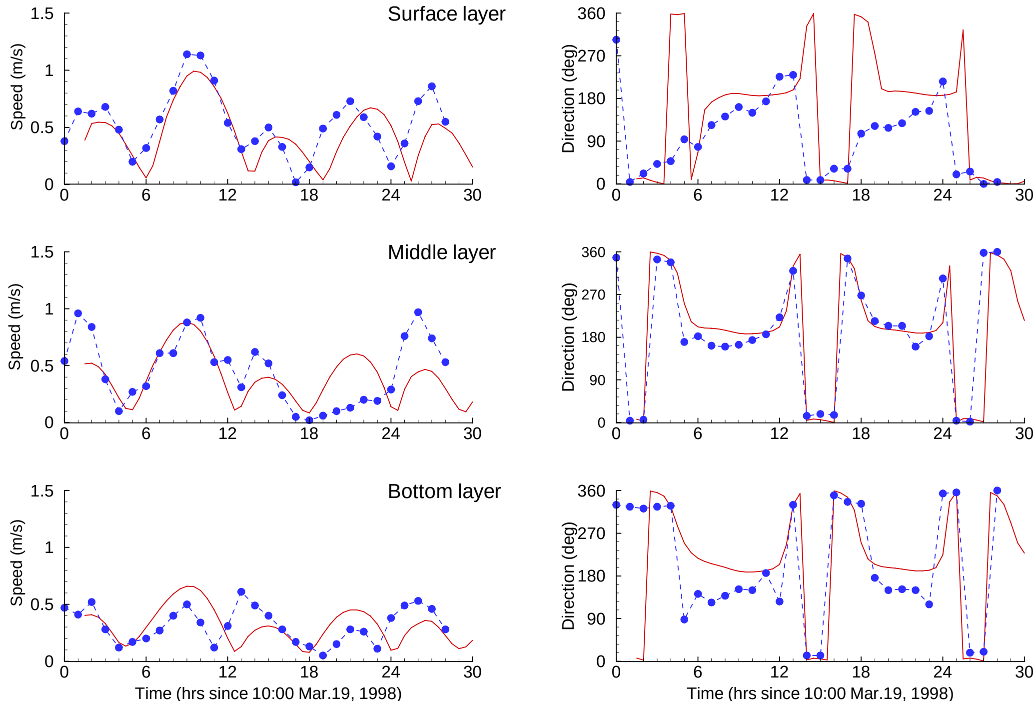

Fig. 5.7a Comparisons of current speed and direction (clockwise from north) at station 3 during a neap tide in the dry season: Solid lines represent computed results and dash lines denote the measurements.

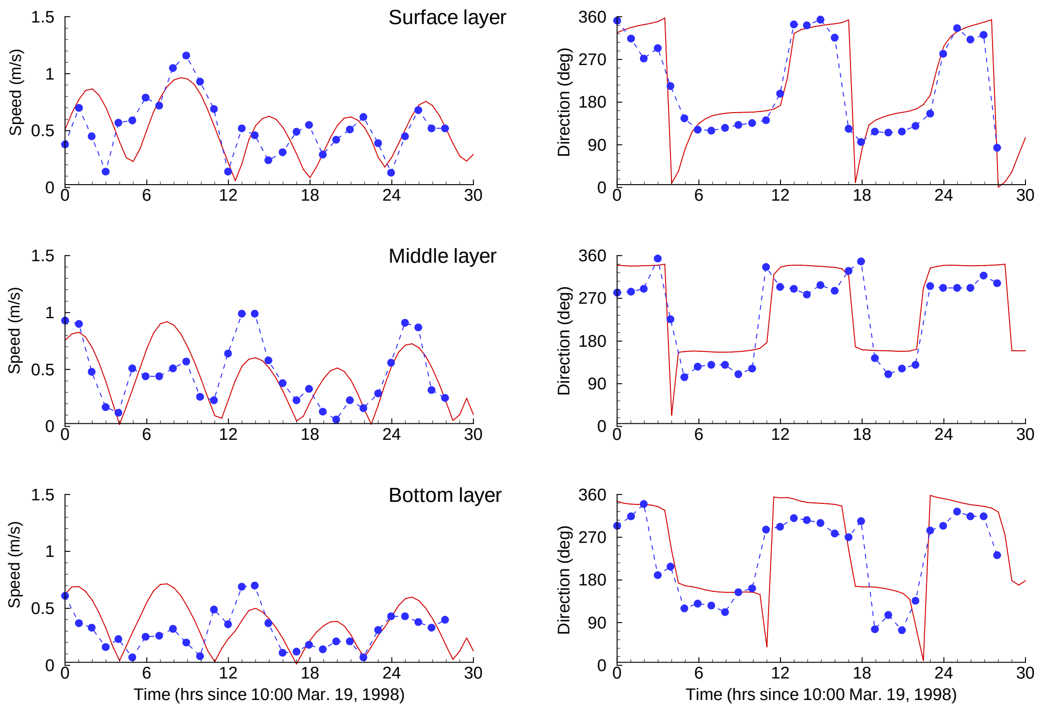

Fig. 5.7b Comparisons of current speed and direction (clockwise from north) at station 6 during a neap tide in the dry season: Solid lines represent computed results and dash lines denote the measurements.

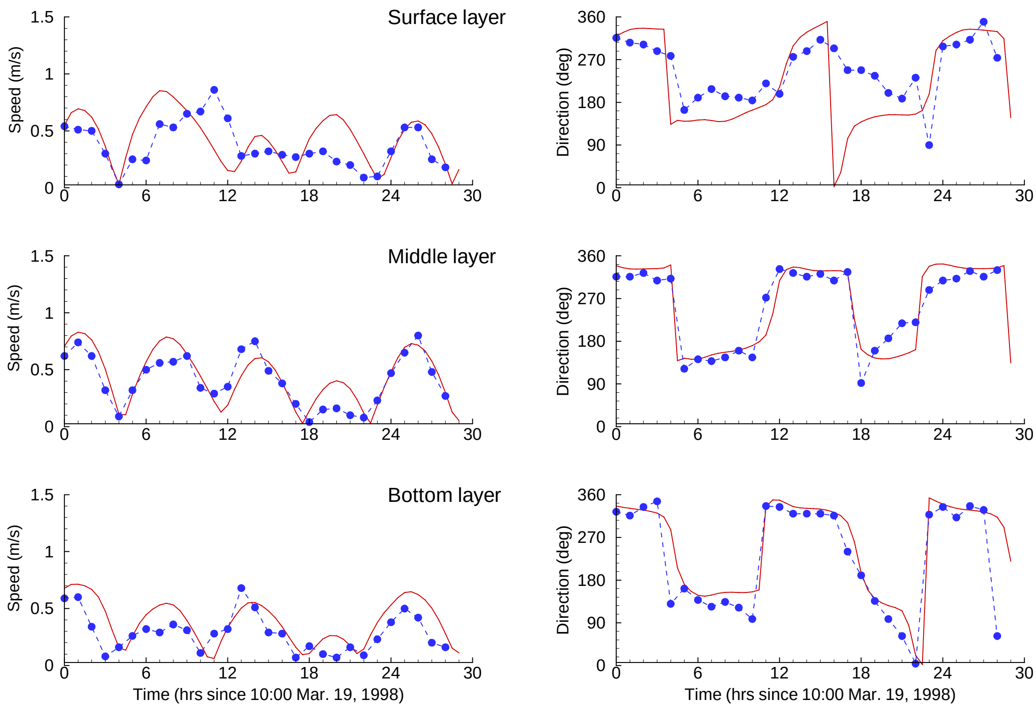

Fig. 5.7c Comparisons of current speed and direction (clockwise from north) at station 8 during neap tide in the dry season: Solid lines represent computed results and dash lines denote the measurements.

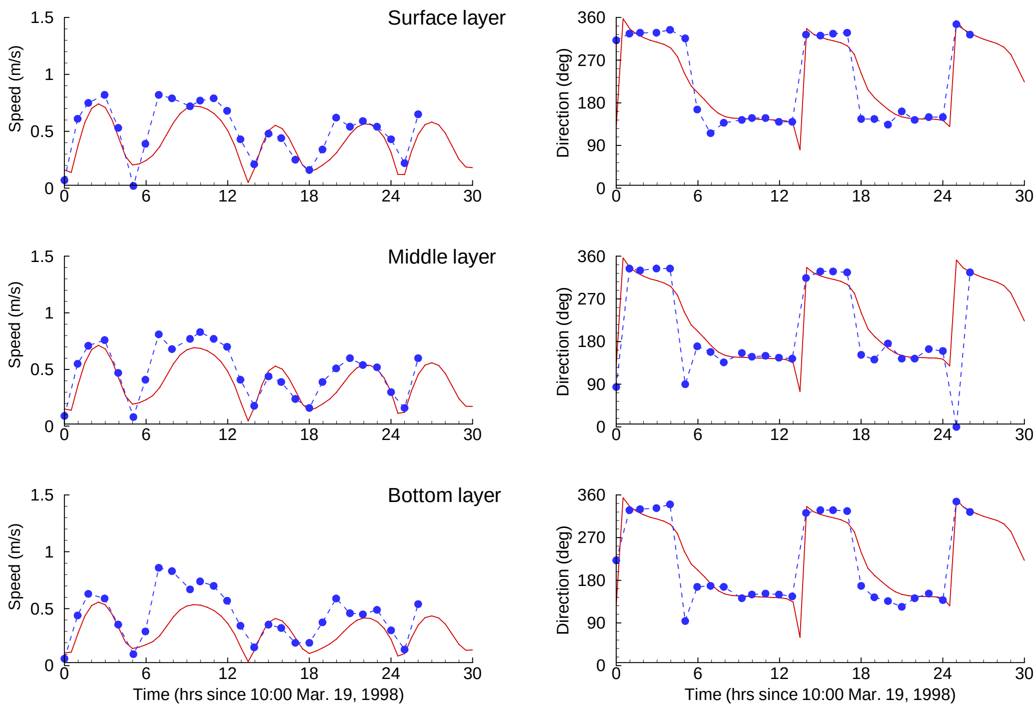

Fig. 5.7d Comparisons of current speed and direction (clockwise from north) at station 15 during a neap tide in the dry season: Solid lines represent computed results and dash lines denote the measurements.

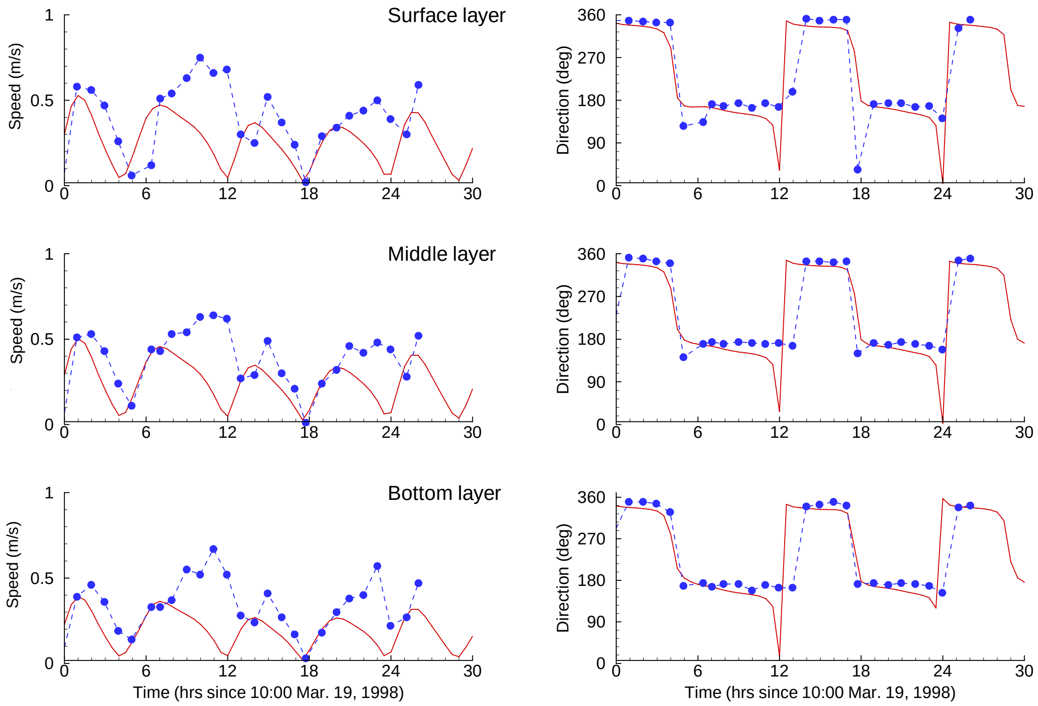

Fig. 5.7e Comparisons of current speed and direction (clockwise from north) at station 16 during a neap tide in the dry season: Solid lines represent computed results and dash lines denote the measurements.

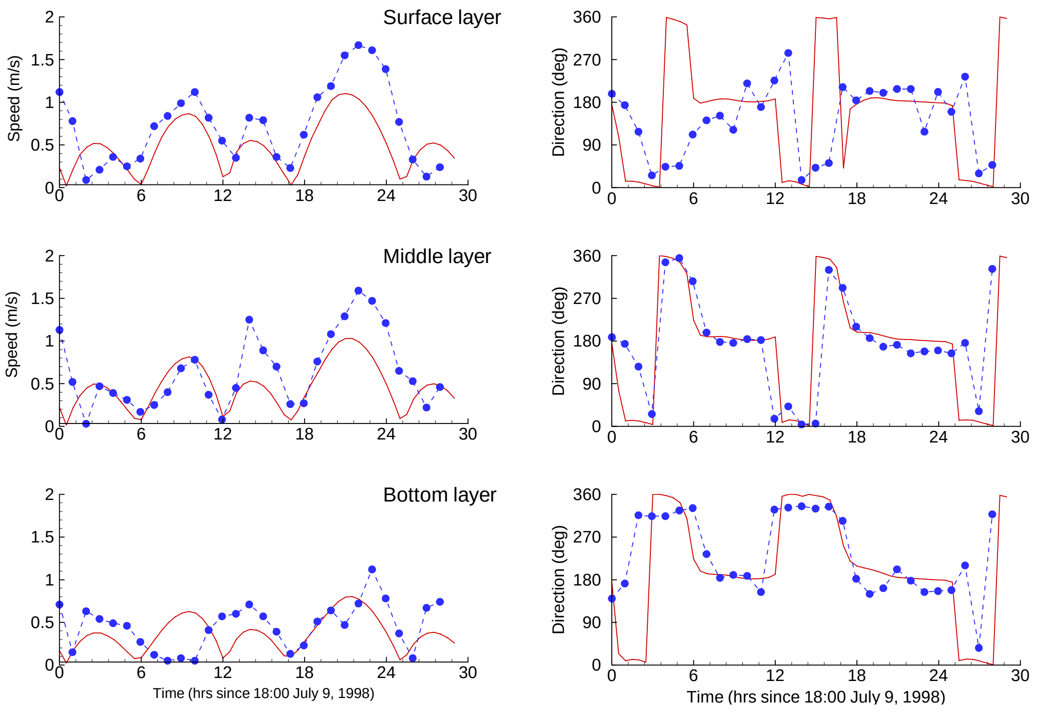

Fig. 5.8a Comparisons of current speed and direction (clockwise from north) at station 3 during a spring tide in the wet season: Solid lines represent computed results and dash lines denote the measurements.

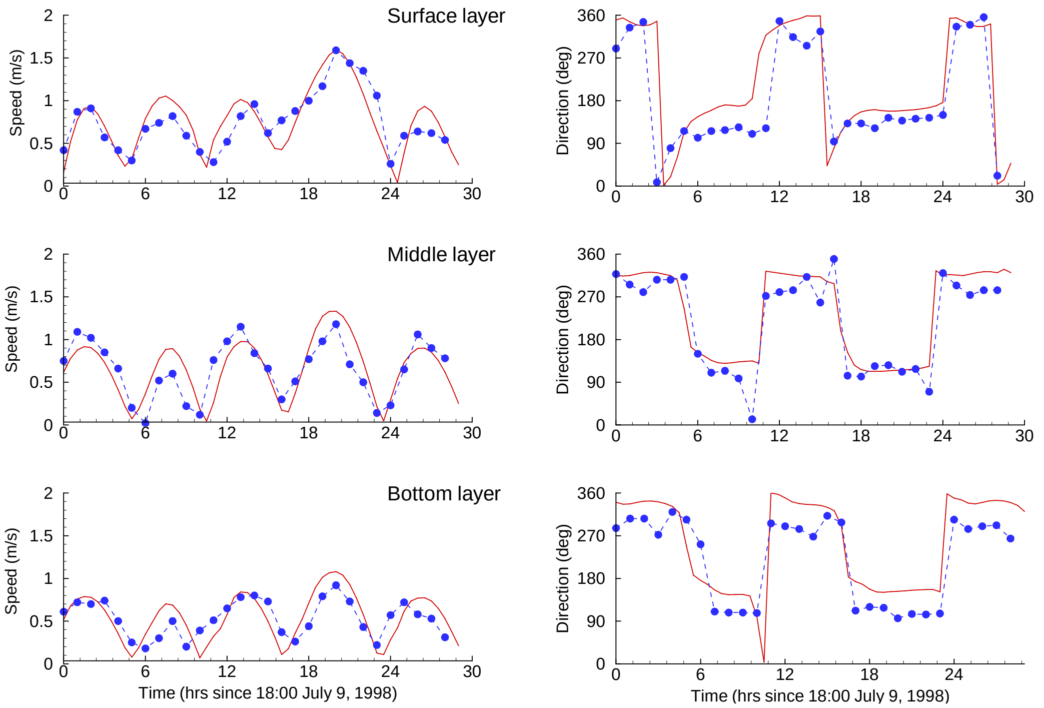

Fig. 5.8b Comparisons of current speed and direction (clockwise from north) at station 6 during a spring tide in the wet season: Solid lines represent computed results and dash lines denote the measurements.

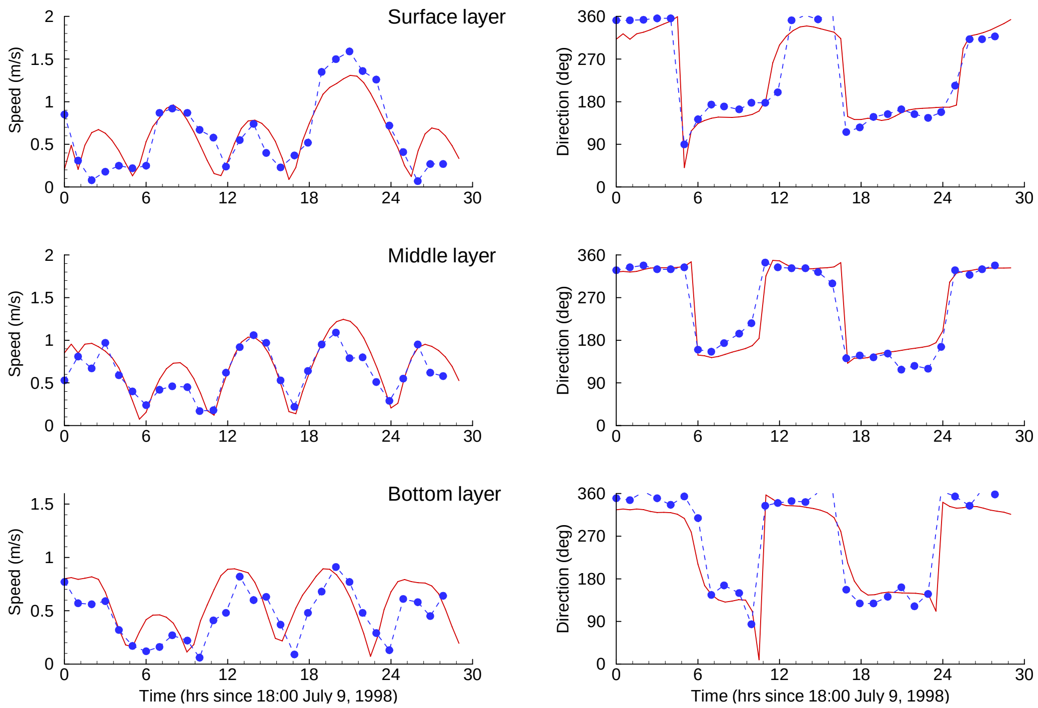

Fig. 5.8c Comparisons of current speed and direction (clockwise from north) at station 8 during a spring tide in the wet season: Solid lines represent computed results and dash lines denote the measurements.

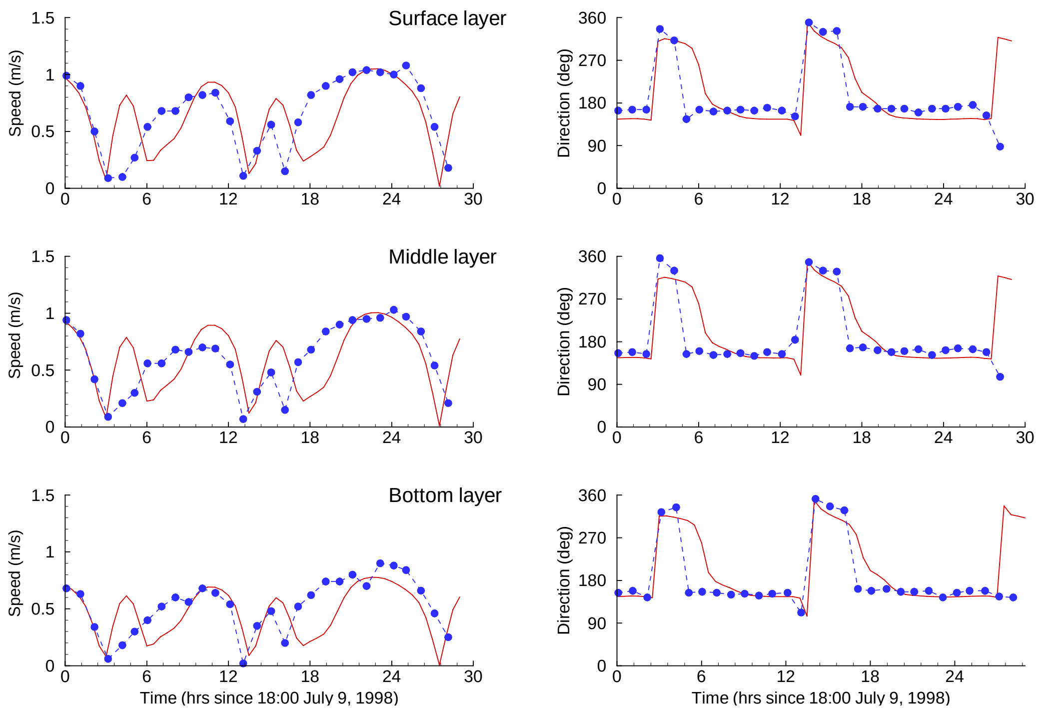

Fig. 5.8d Comparisons of current speed and direction (clockwise from north) at station 15 during a spring tide in the wet season: Solid lines represent computed results and dash lines denote the measurements.

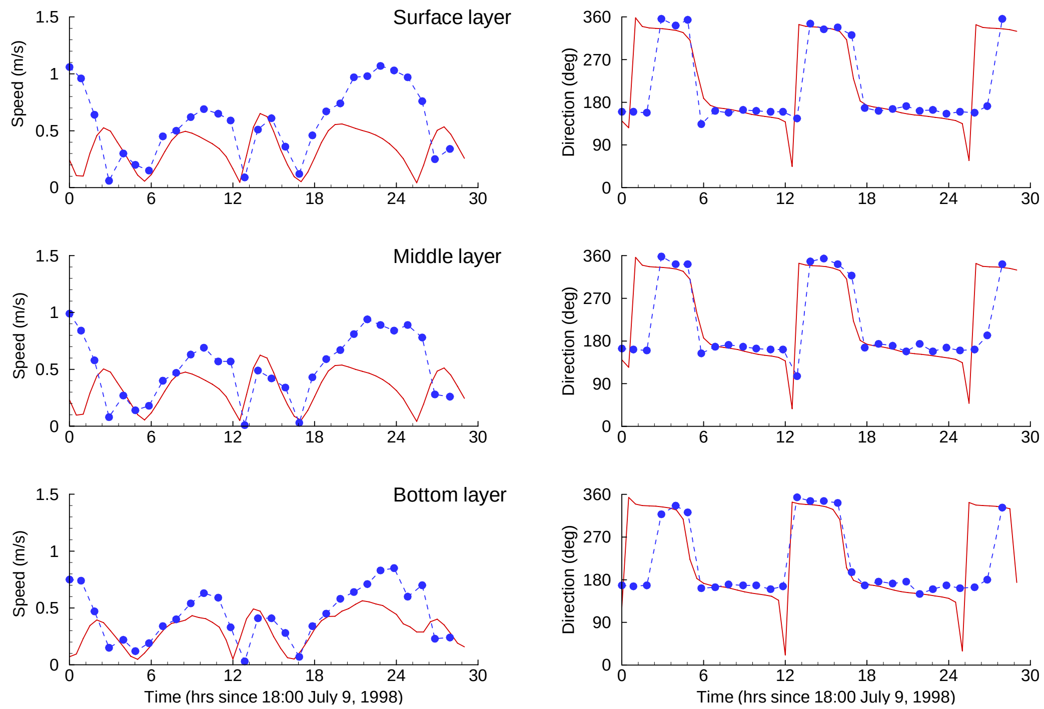

Fig. 5.8e Comparisons of current speed and direction (clockwise from north) at station 16 during a spring tide in the wet season: Solid lines represent computed results and dash lines denote the measurements.

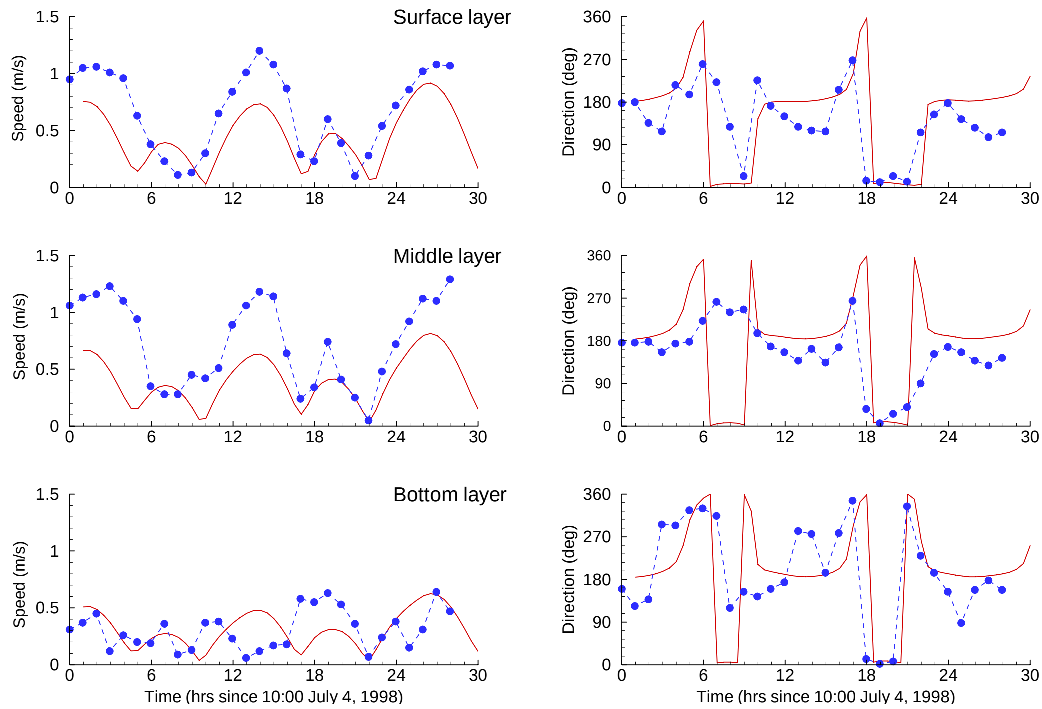

Fig. 5.9a Comparisons of current speed and direction (clockwise from north) at station 3 during a neap tide in the wet season: Solid lines represent computed results and dash lines denote the measurements.

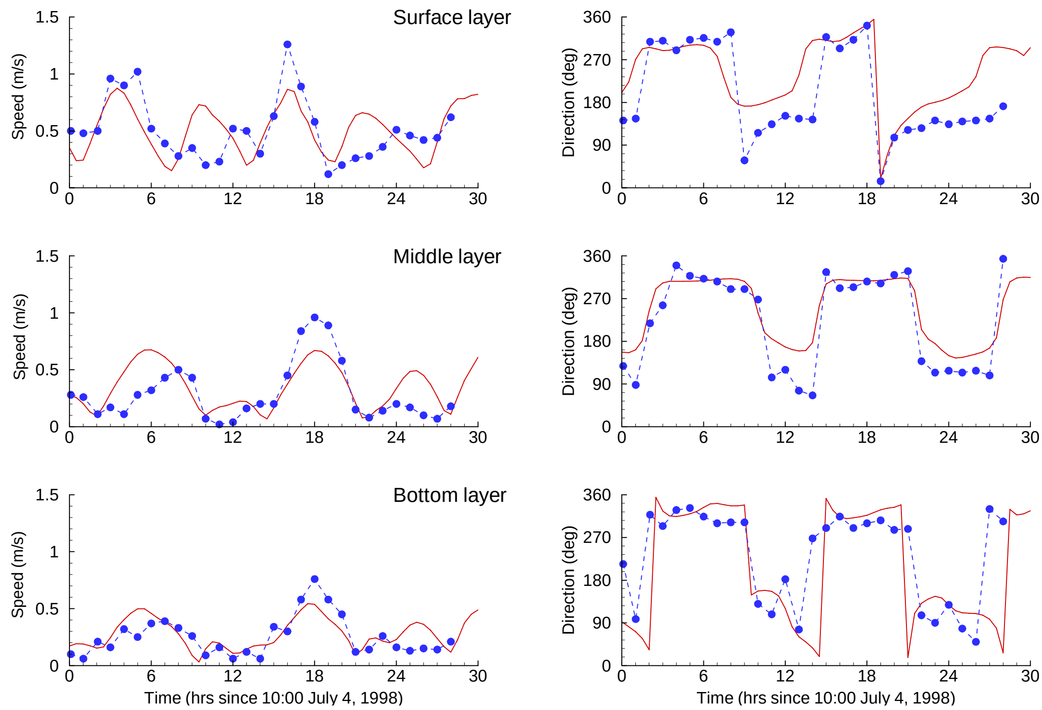

Fig. 5.9b Comparisons of current speed and direction (clockwise from north) at station 6 during a neap tide in the wet season: Solid lines represent computed results and dash lines denote the measurements.

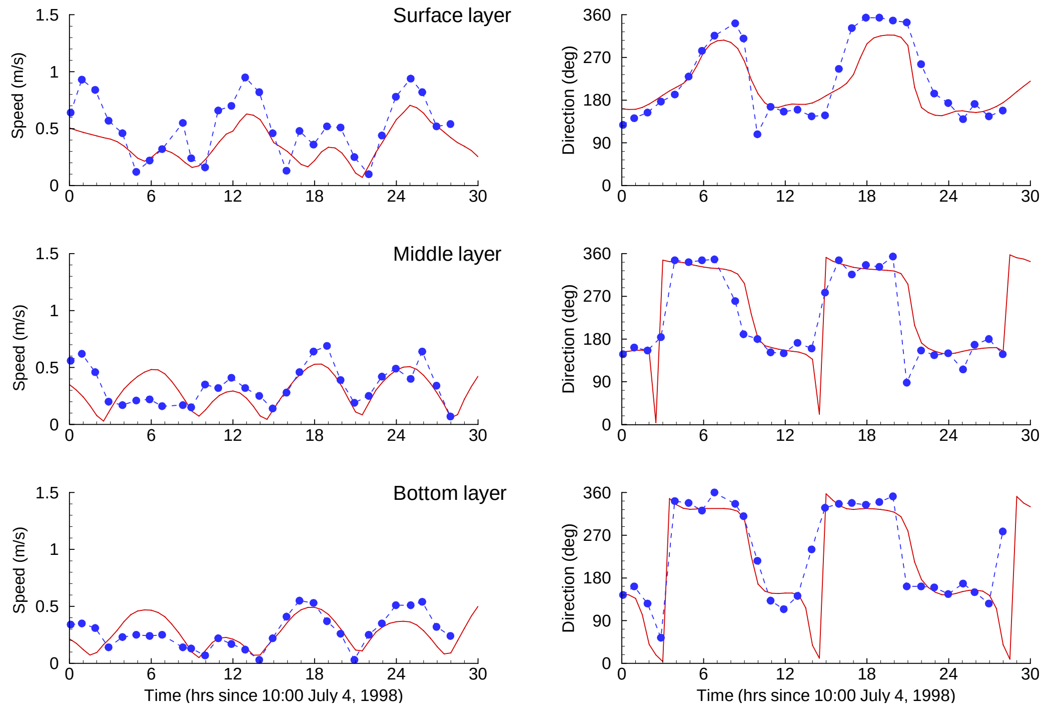

Fig. 5.9c Comparisons of current speed and direction (clockwise from north) at station 8 during a neap tide in the wet season: Solid lines represent computed results and dash lines denote the measurements.

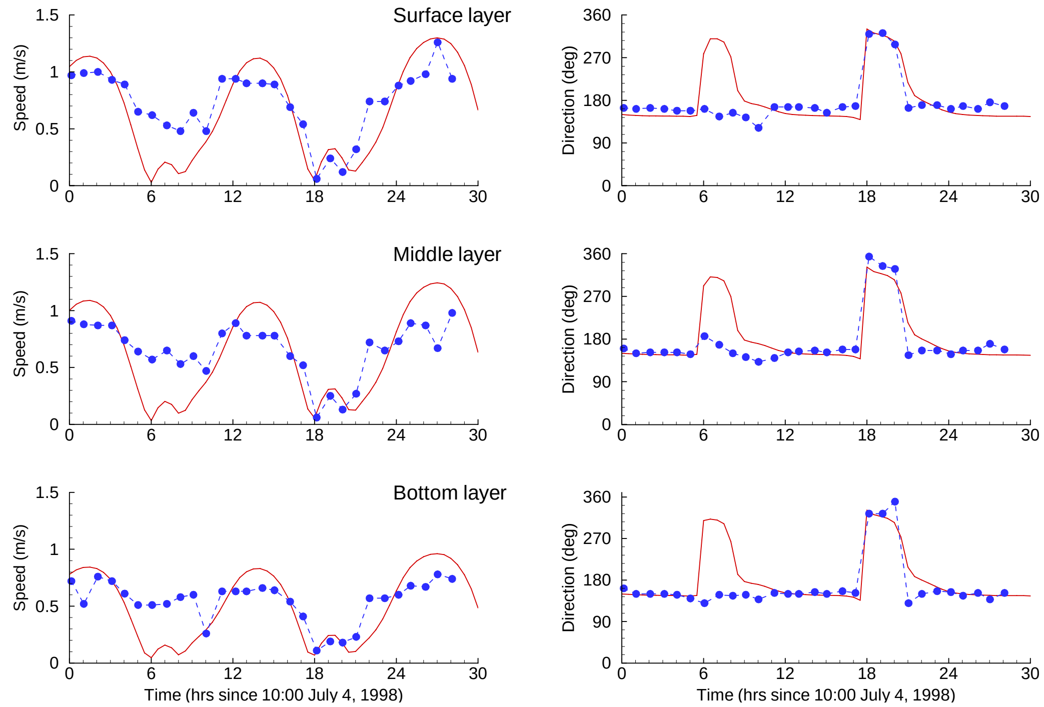

Fig. 5.9d Comparisons of current speed and direction (clockwise from north) at station 15 during a neap tide in the wet season: Solid lines represent computed results and dash lines denote the measurements.

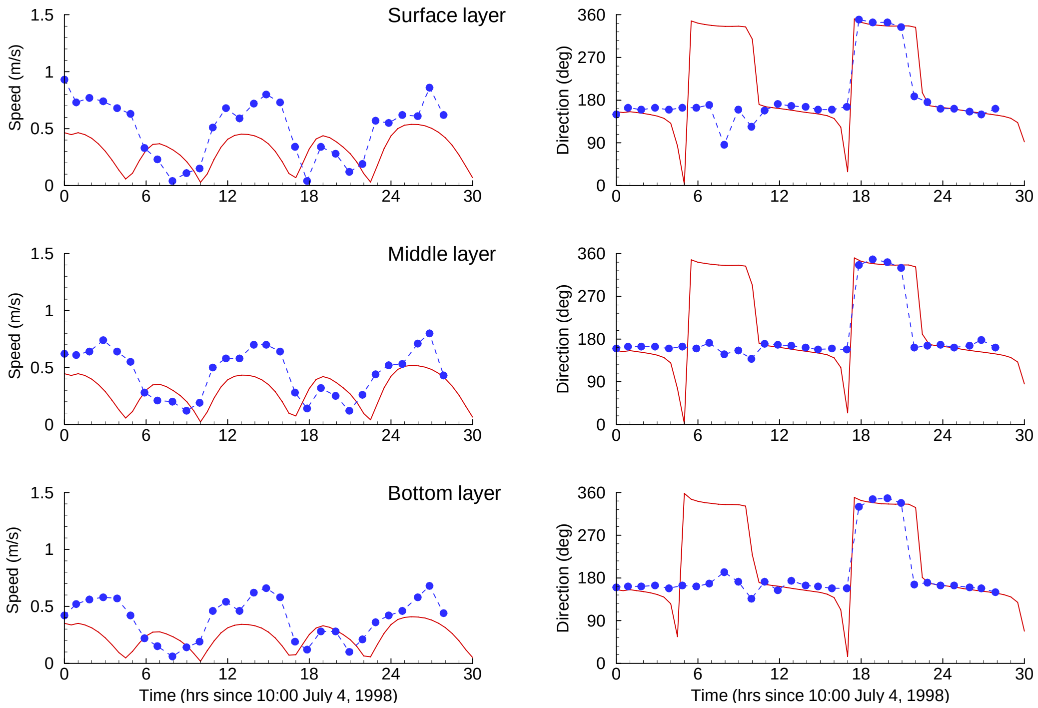

Fig. 5.9e Comparisons of current speed and direction (clockwise from north) at station 16 during a neap tide in the wet season: Solid lines represent computed results and dash lines denote the measurements.

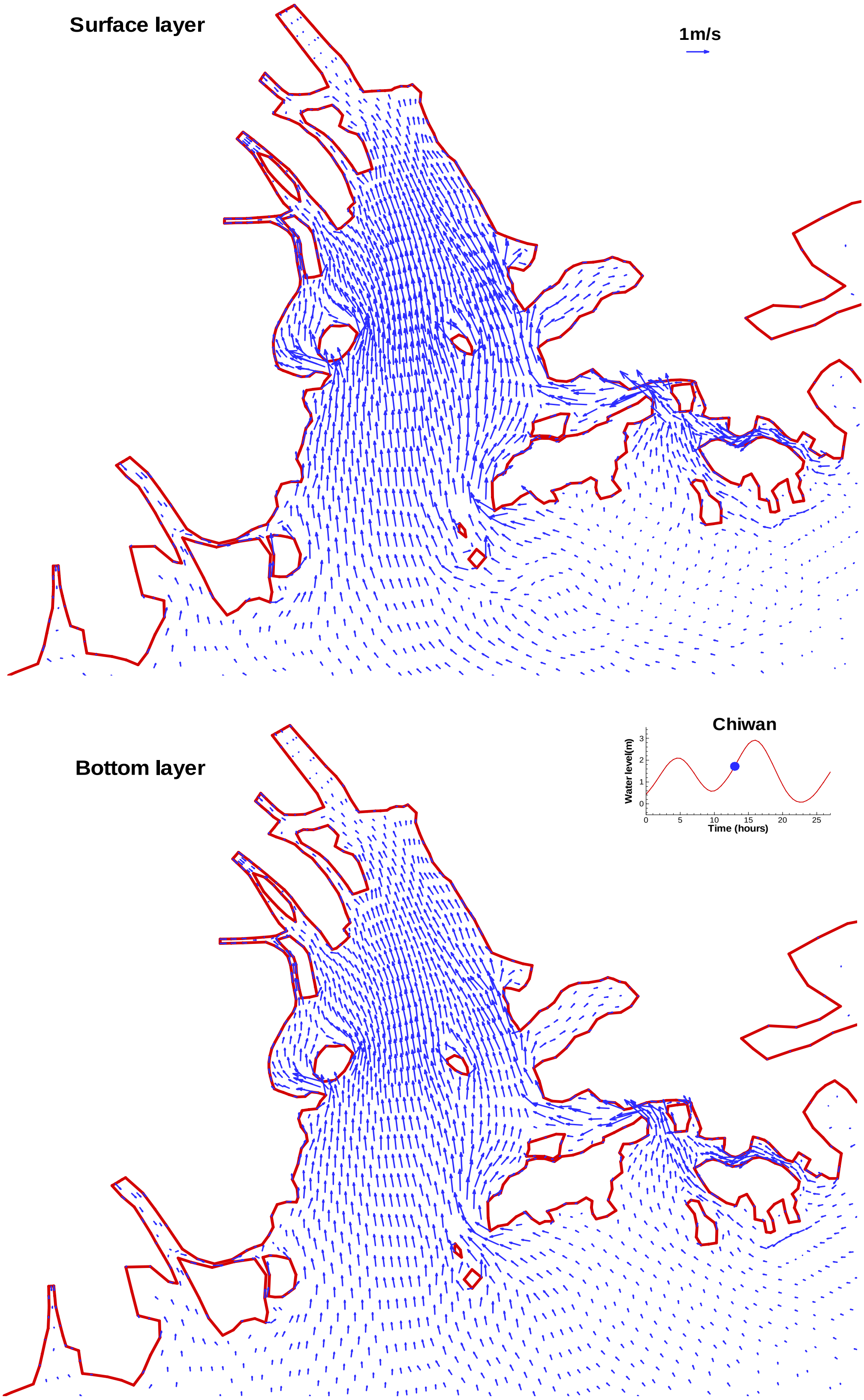

Fig. 5.10a Flow patterns during a flooding spring tide in the wet season (July 1998)

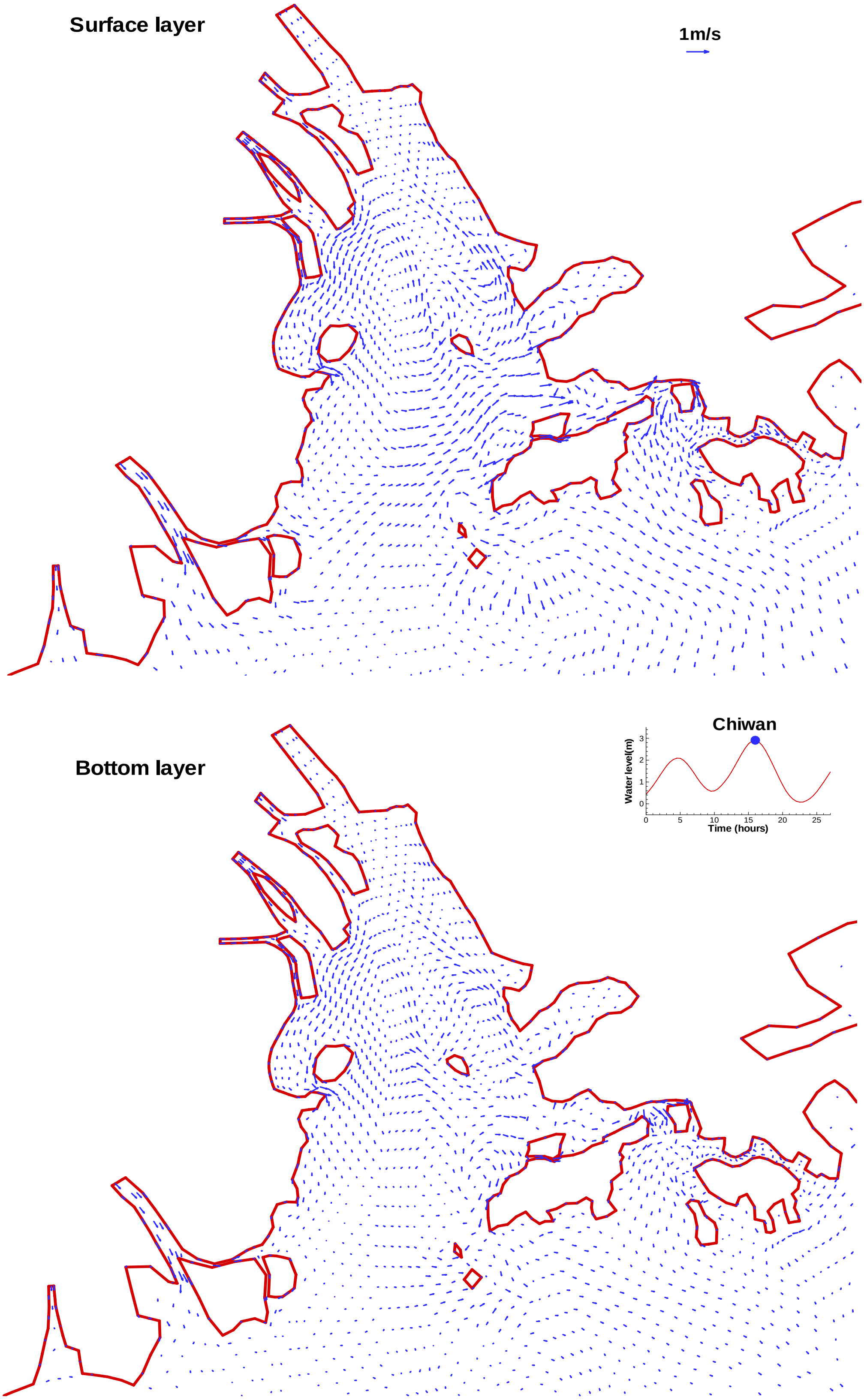

Fig. 5.10b Flow patterns at high slack during a spring tide in the wet season (July 1998)

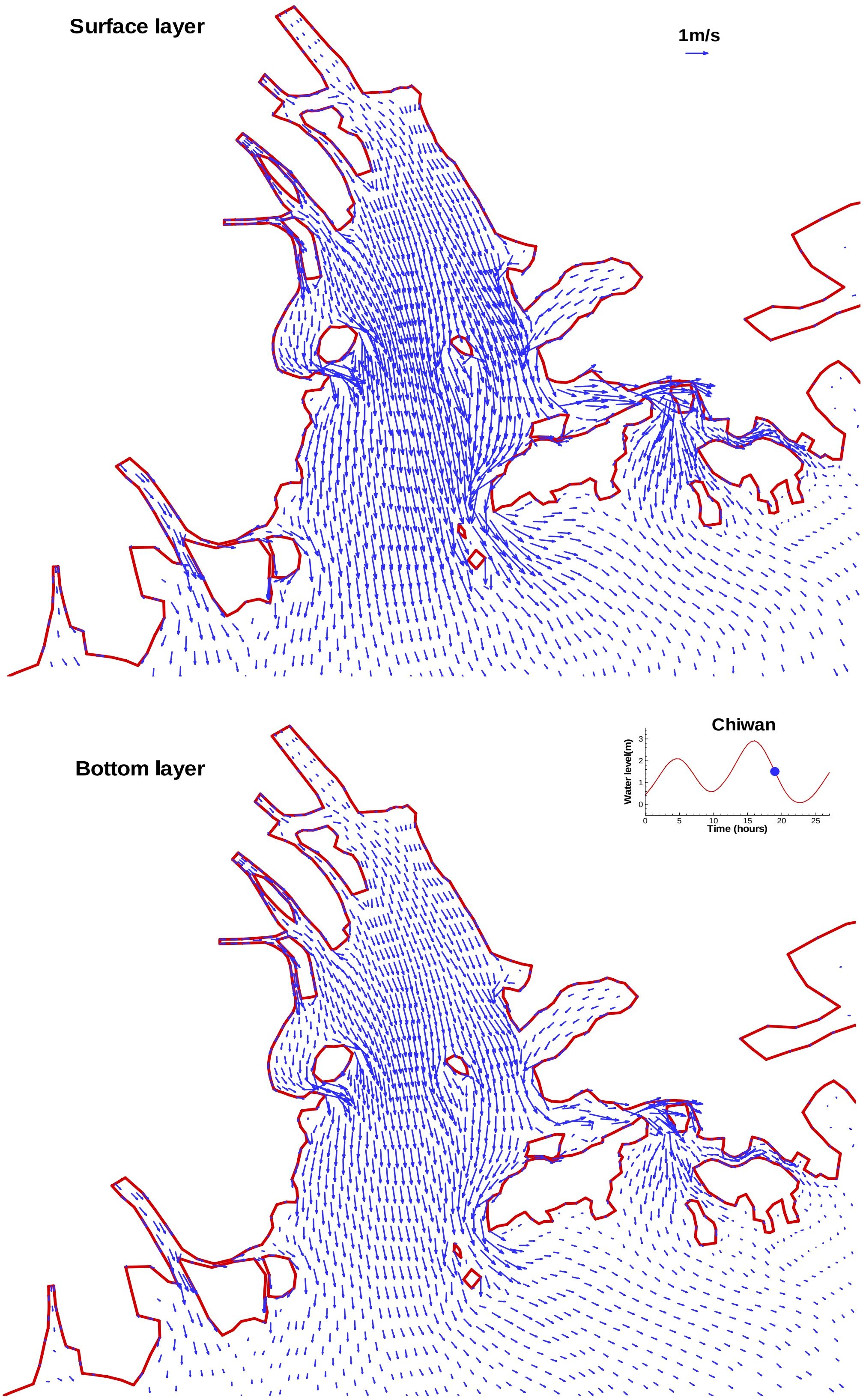

Fig. 5.10c Flow patterns during an ebbing spring tide in the wet season (July 1998)

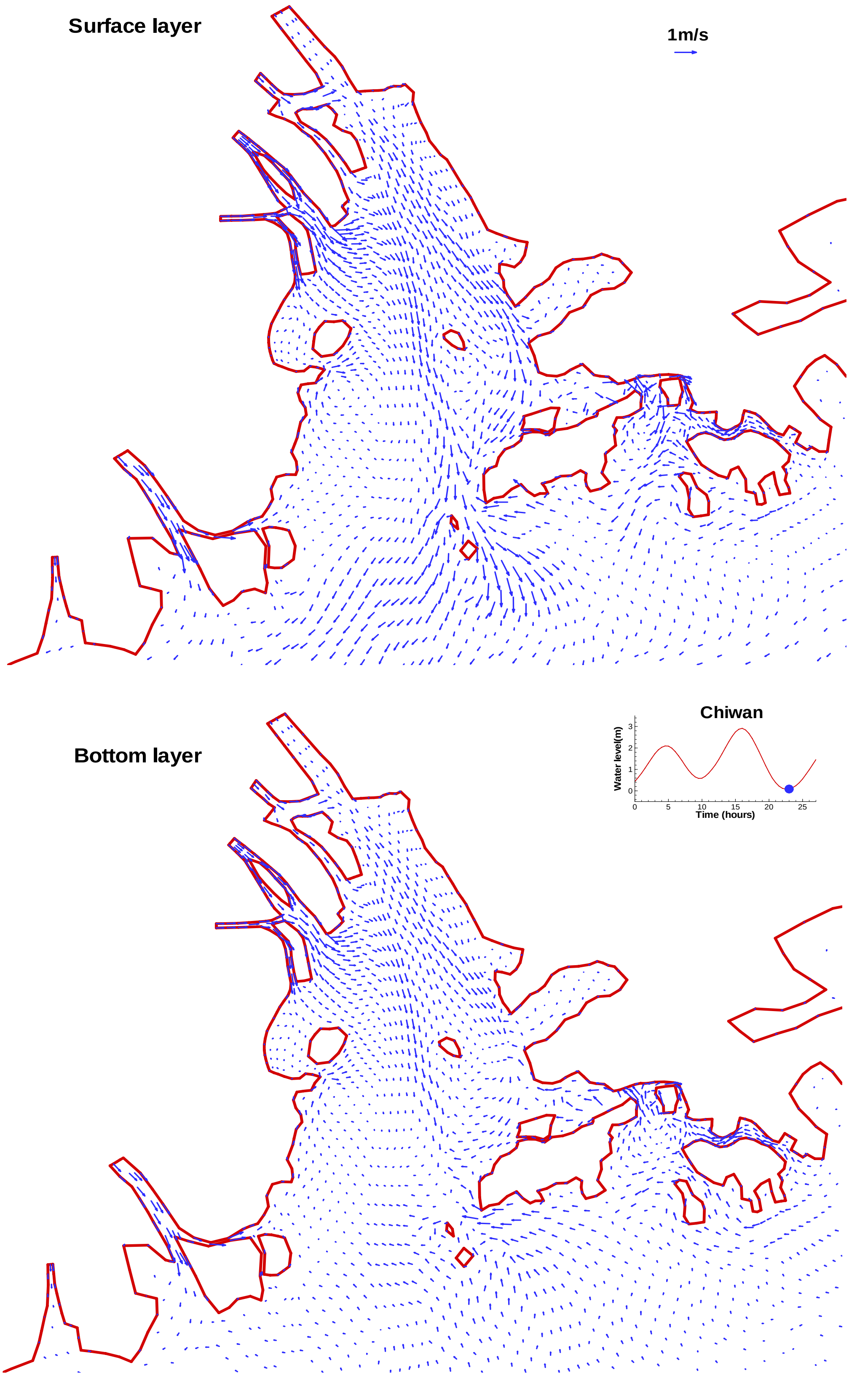

Fig. 5.10d Flow patterns at low slack during a spring tide in the wet season (July 1998)

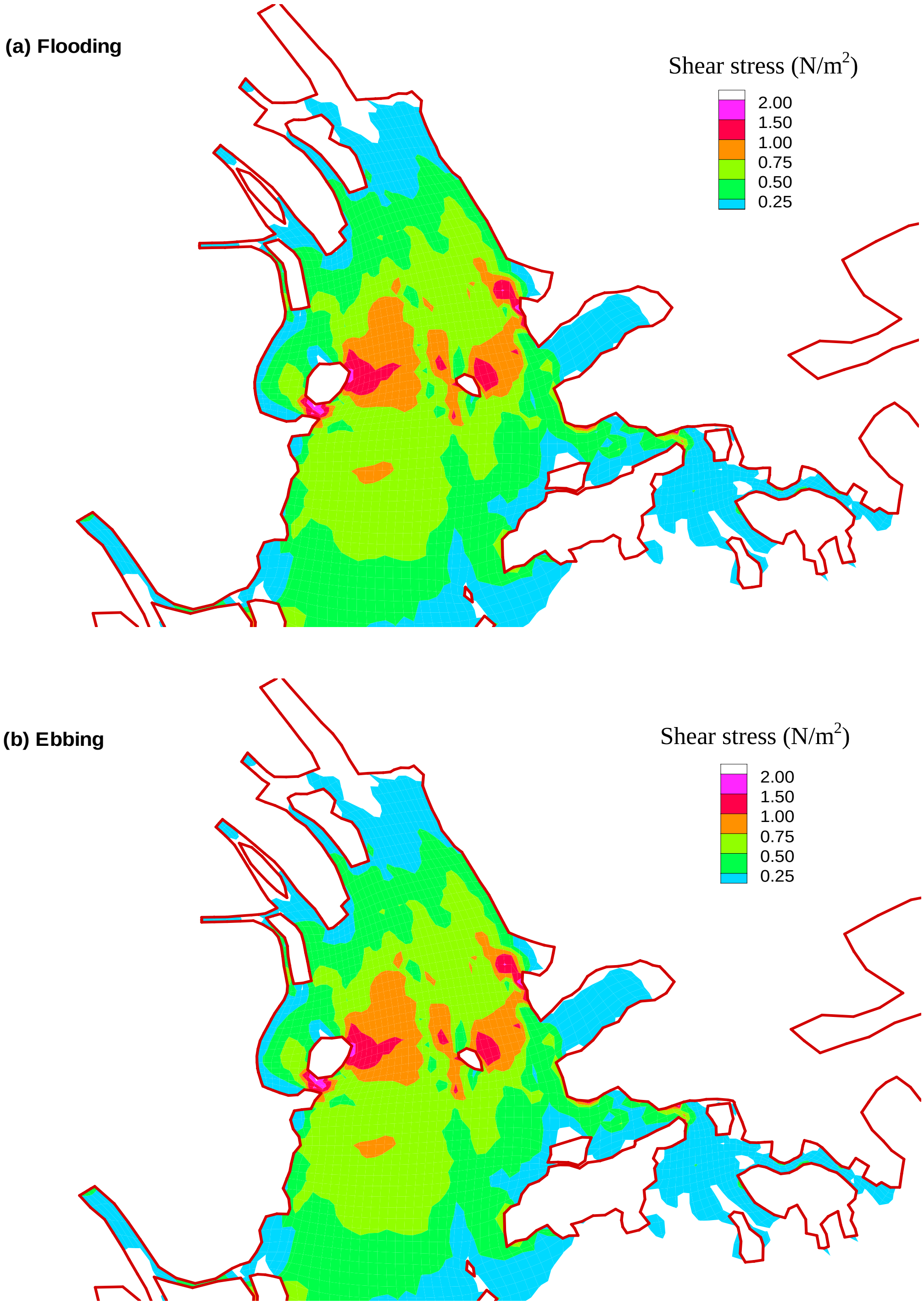

Fig. 5.11 Distribution of bottom shear stress during (a) flooding and (b) ebbing in a spring tide

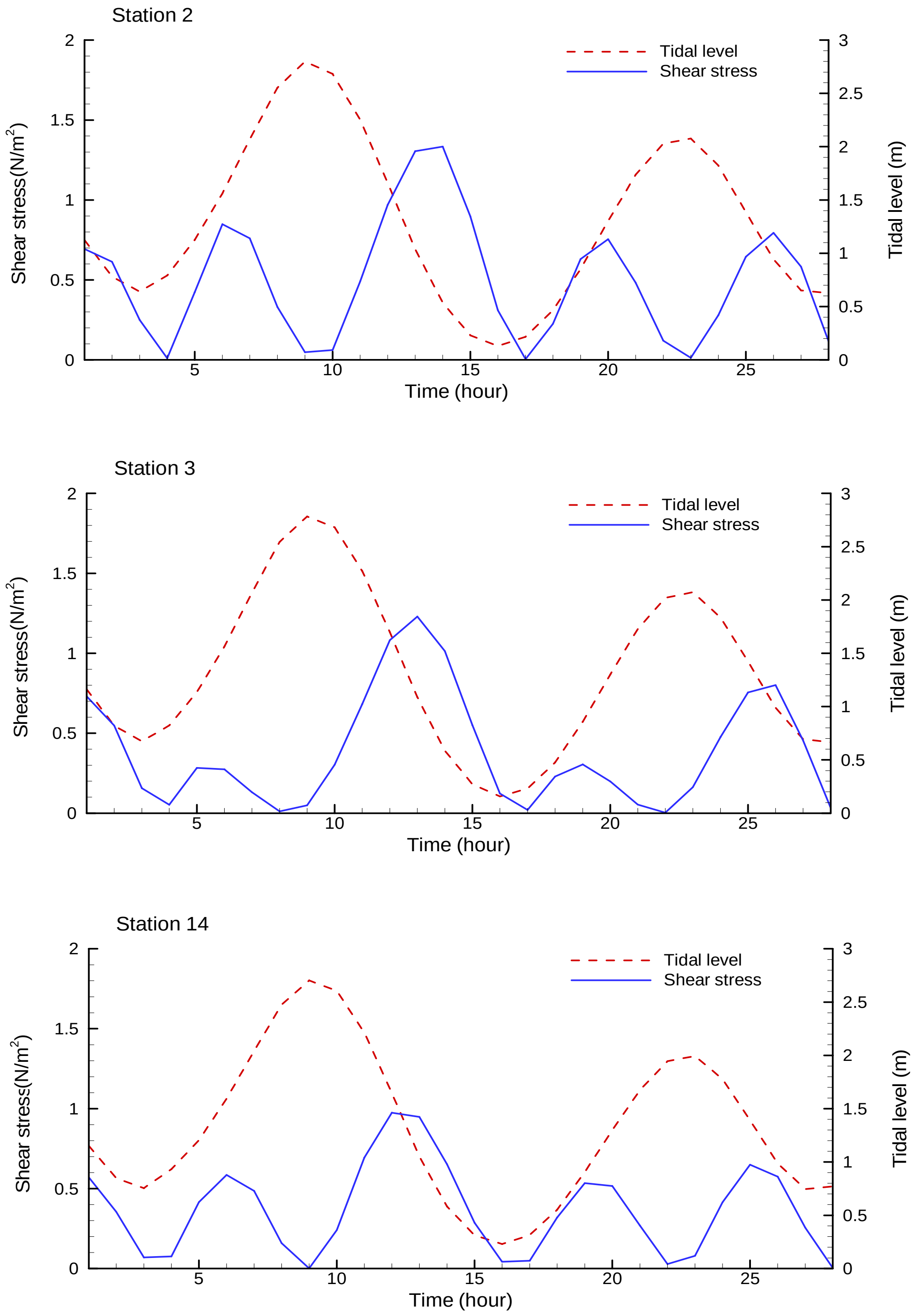

Fig. 5.12 Time series of bottom shear stress at stations 2, 3 and 14 in a spring tide

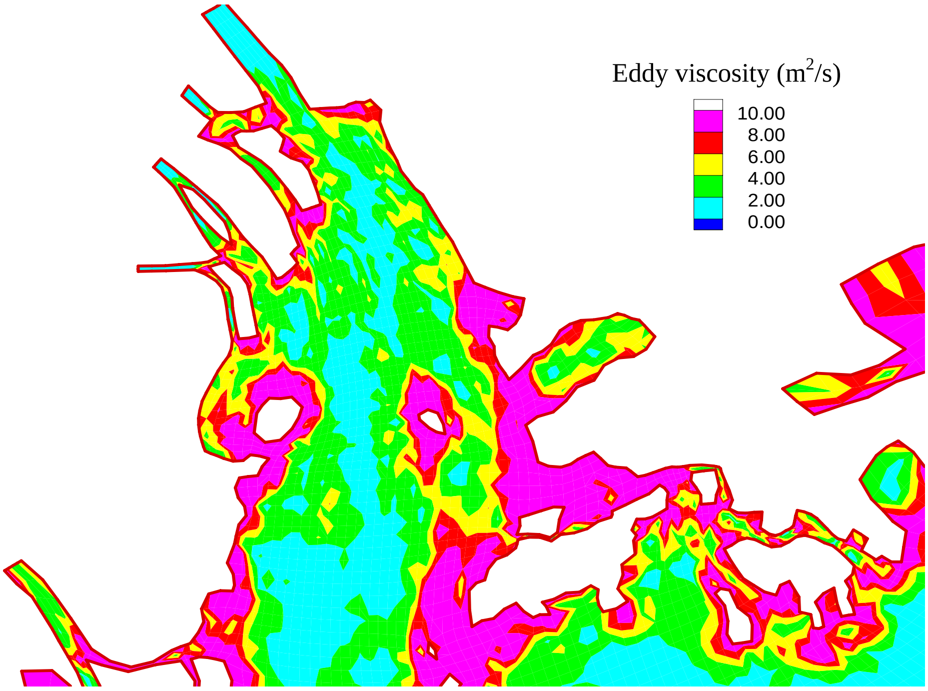

Fig. 5.13 Distribution of vertically averaged horizontal eddy viscosity during flooding in a spring tide

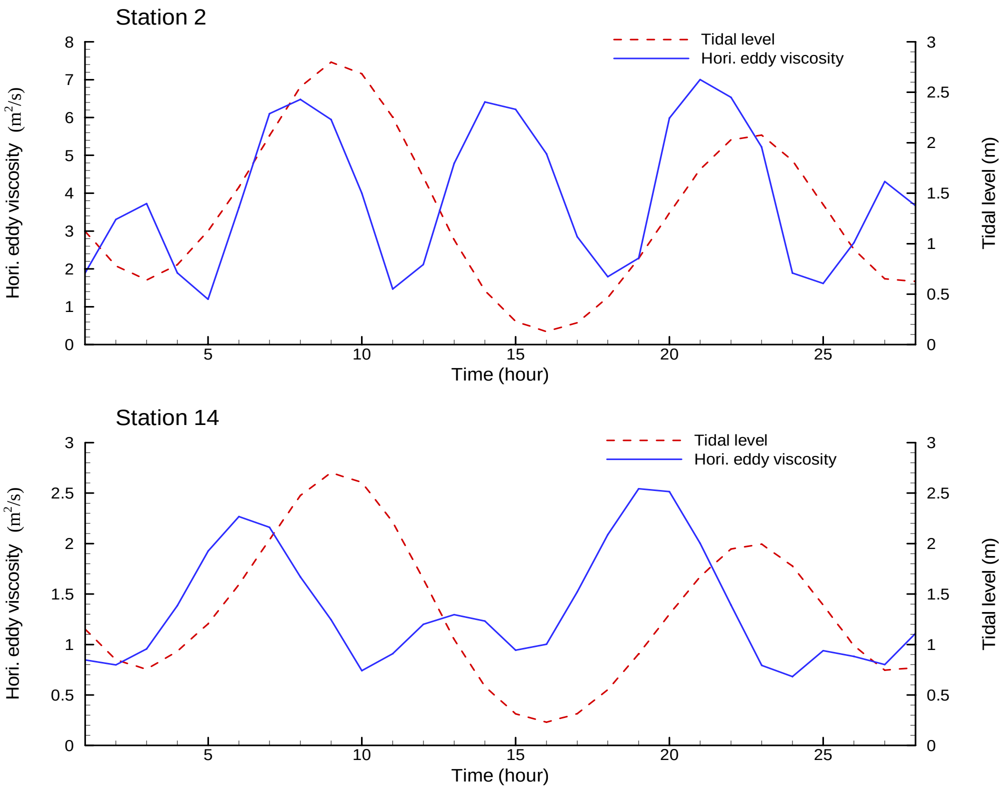

Fig. 5.14 Time series of vertically averaged horizontal eddy viscosity in a spring tide at stations 2 and 14

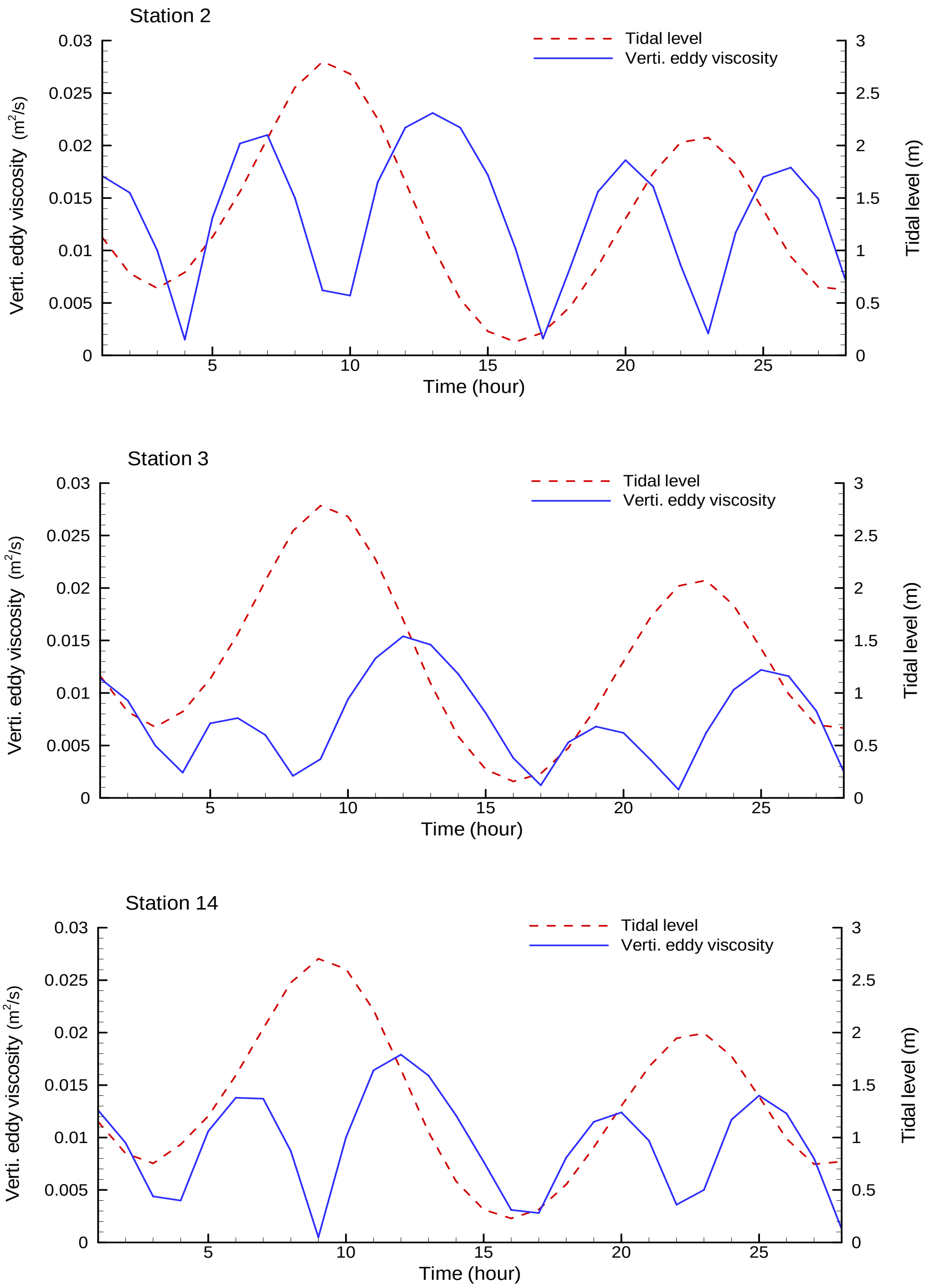

Fig. 5.15 Time series of vertical eddy viscosity in the middle layer in a spring tide at stations 2, 3 and 14

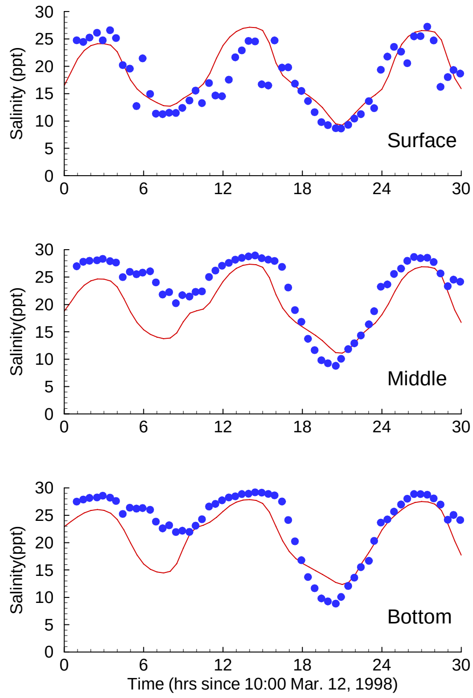

(a) Station 2

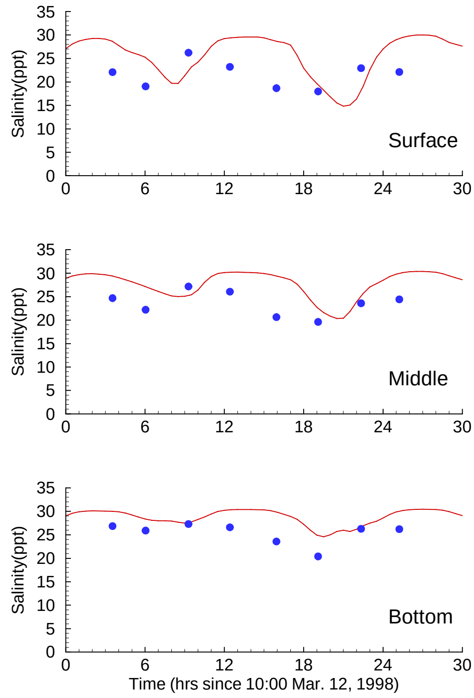

(b) Station 4

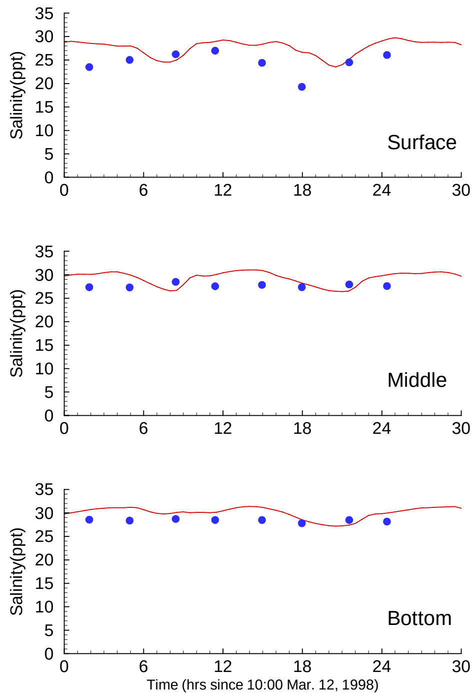

(c) Station 6

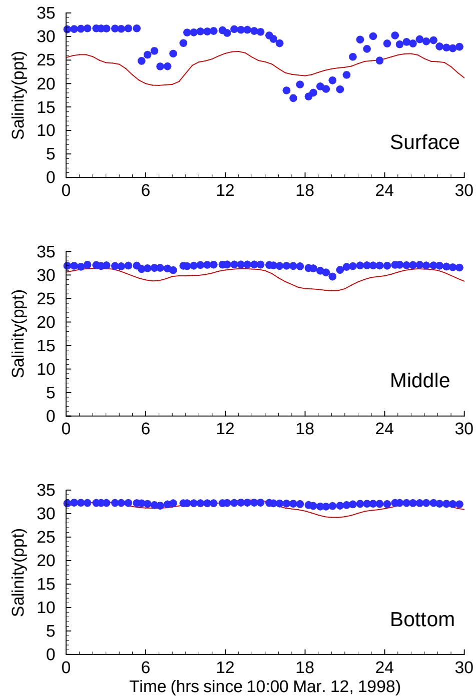

(d) Station 8

Fig. 5.16 Comparisons of computed and measured salinity during a spring tide in the dry season (March 1998): Solid line represents computed salinity and dots denote the measurements.

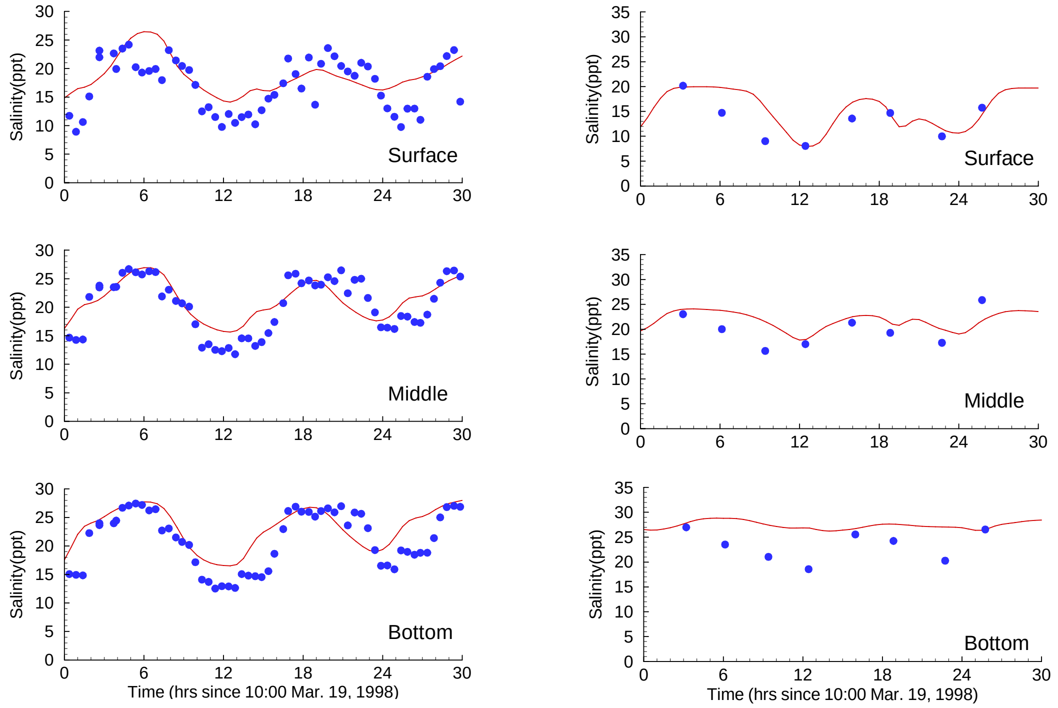

(a) Station 2

(b) Station 4

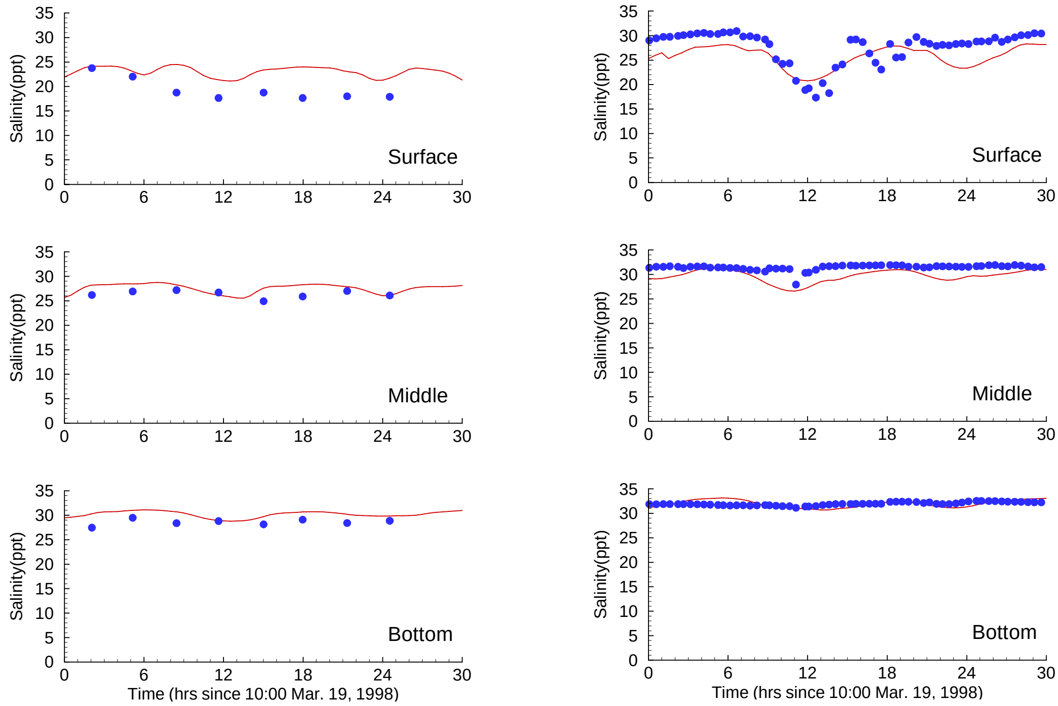

(c) Station 6

(d) Station 8

Fig. 5.17 Comparisons of computed and measured salinity during a neap tide in the dry season (March 1998): Solid lines represent computed salinity and dots denote the measurements.

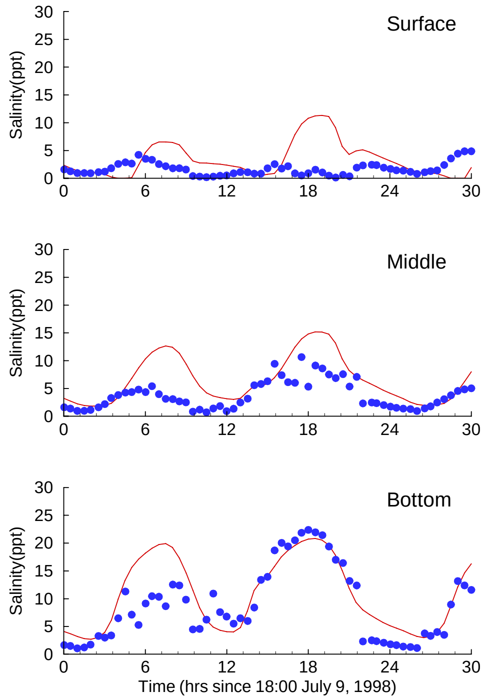

(a) Station 2

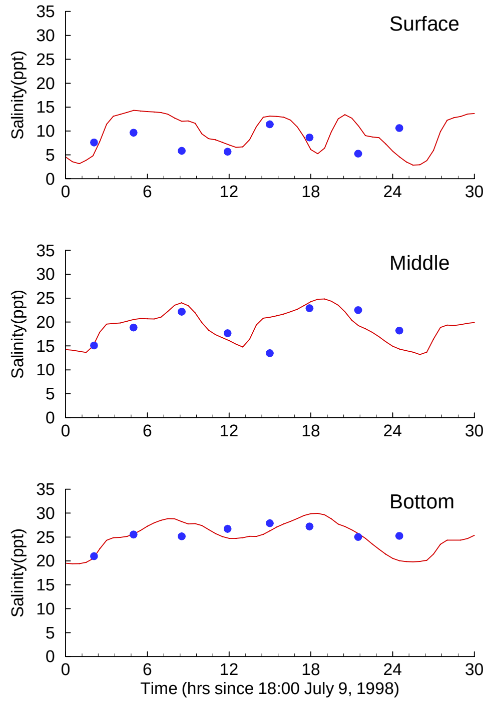

(b) Station 6

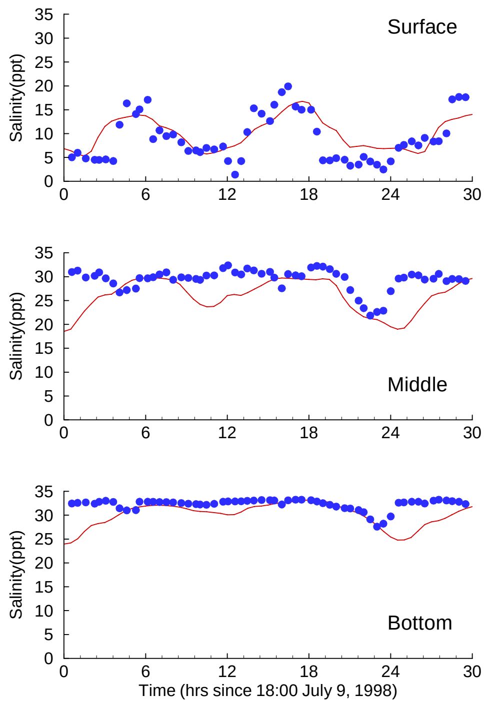

(c) Station 8

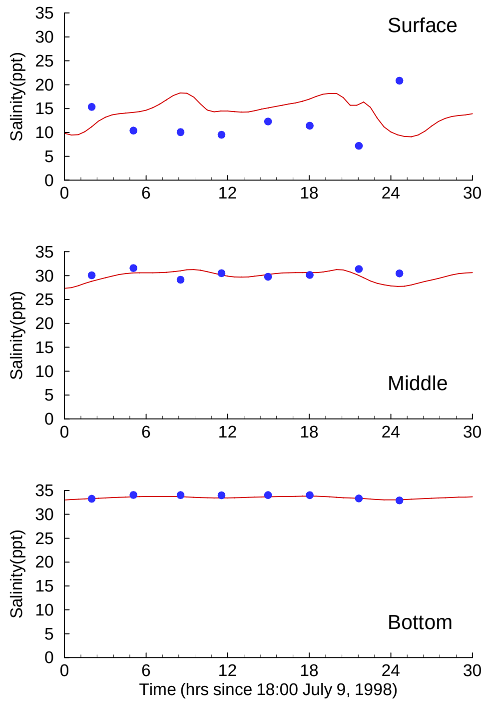

(d) Station 10

Fig. 5.18 Comparisons of computed and measured salinity during a spring tide in the wet season (July 1998): Solid lines represent computed salinity and dots denote the measurements.

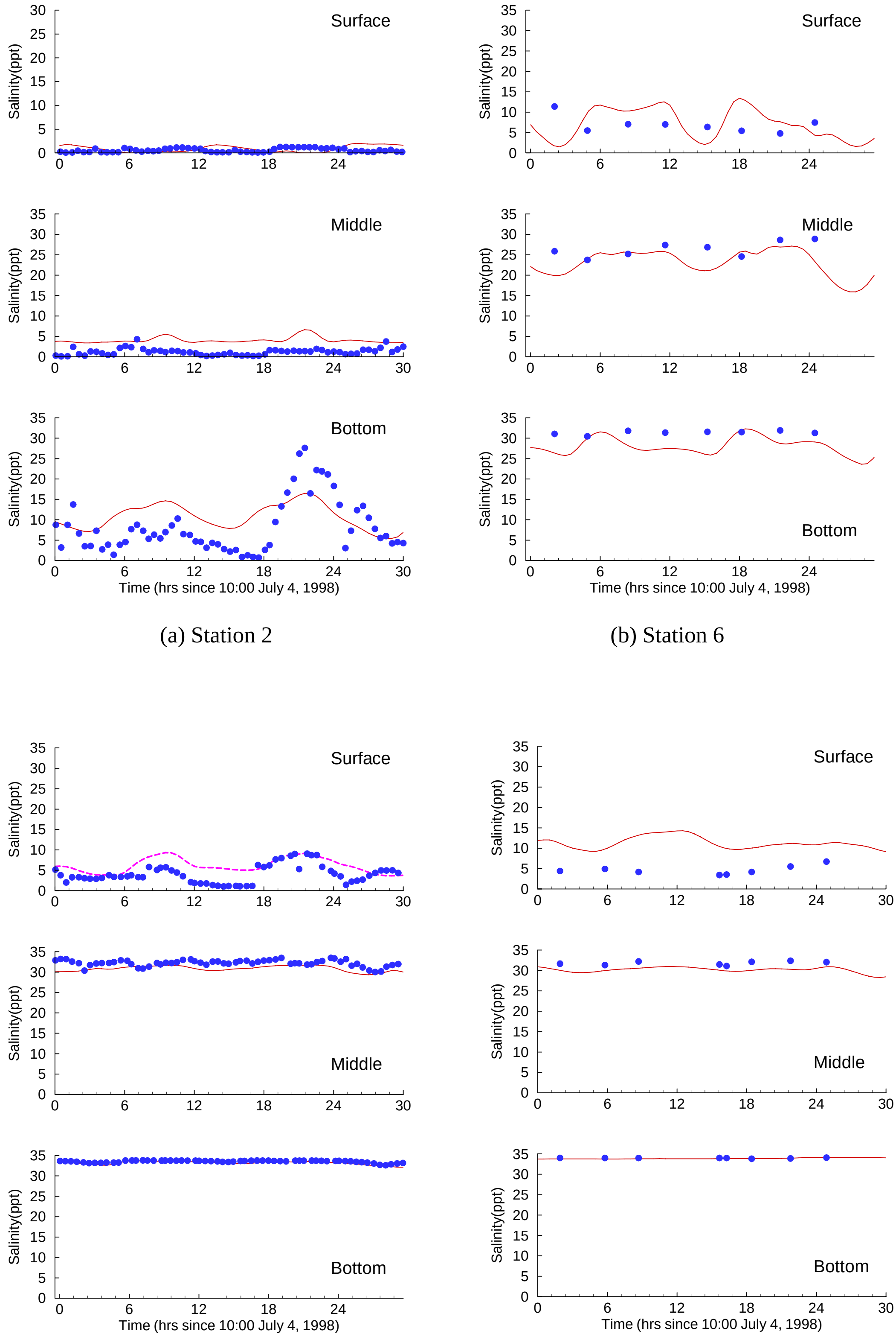

(a) Station 2 (b) Station 6

(c) Station 8 (d) Station 10

Fig. 5.19 Comparisons of computed and measured salinity during a neap tide in the wet season (July 1998): Solid line represents computed salinity and dots denote the measurements.

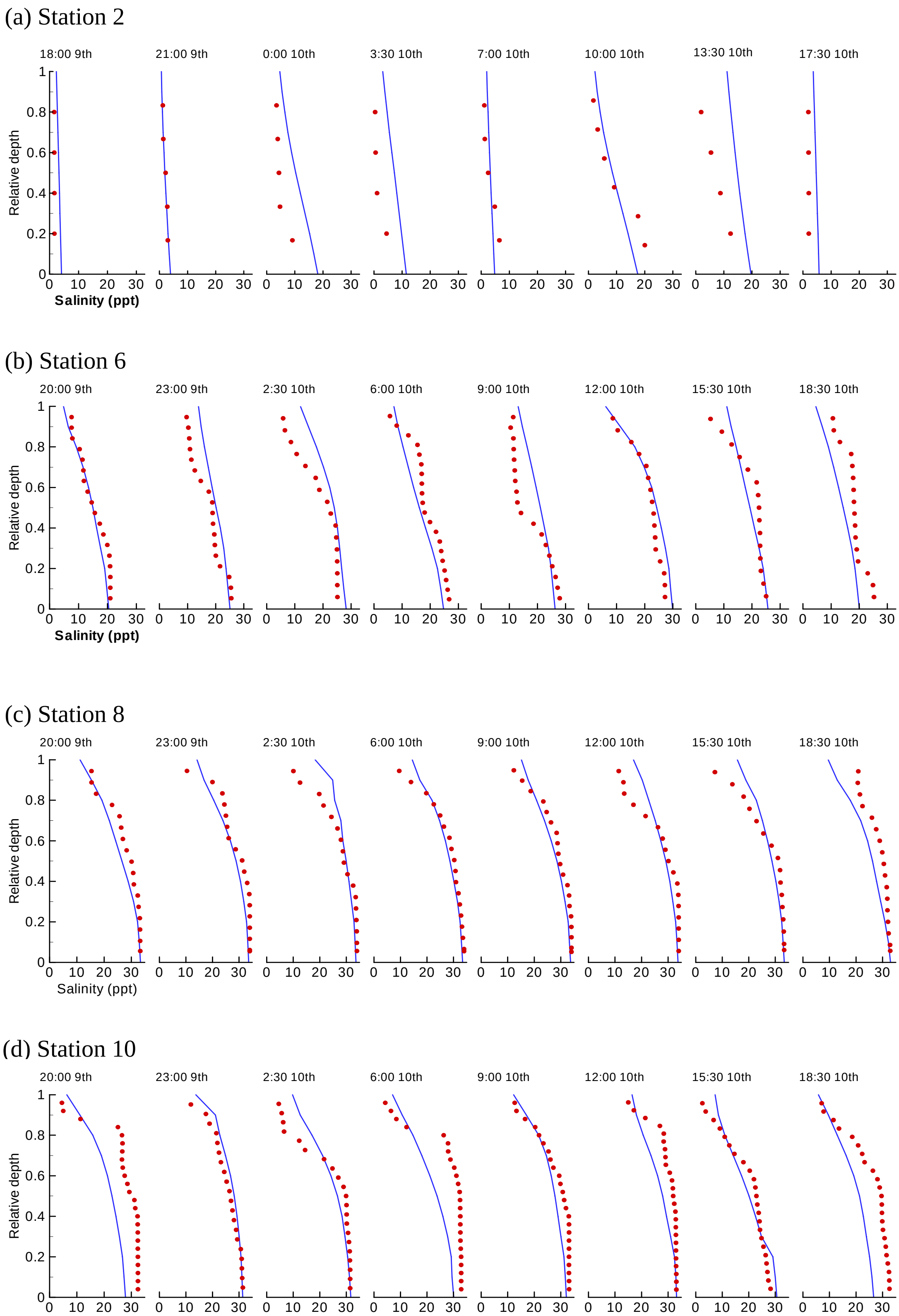

Fig. 5.20 Comparisons of computed and measured salinity profiles during a spring tide in the wet season (July 1998): Solid lines represent computed salinity and dots denote measurements.

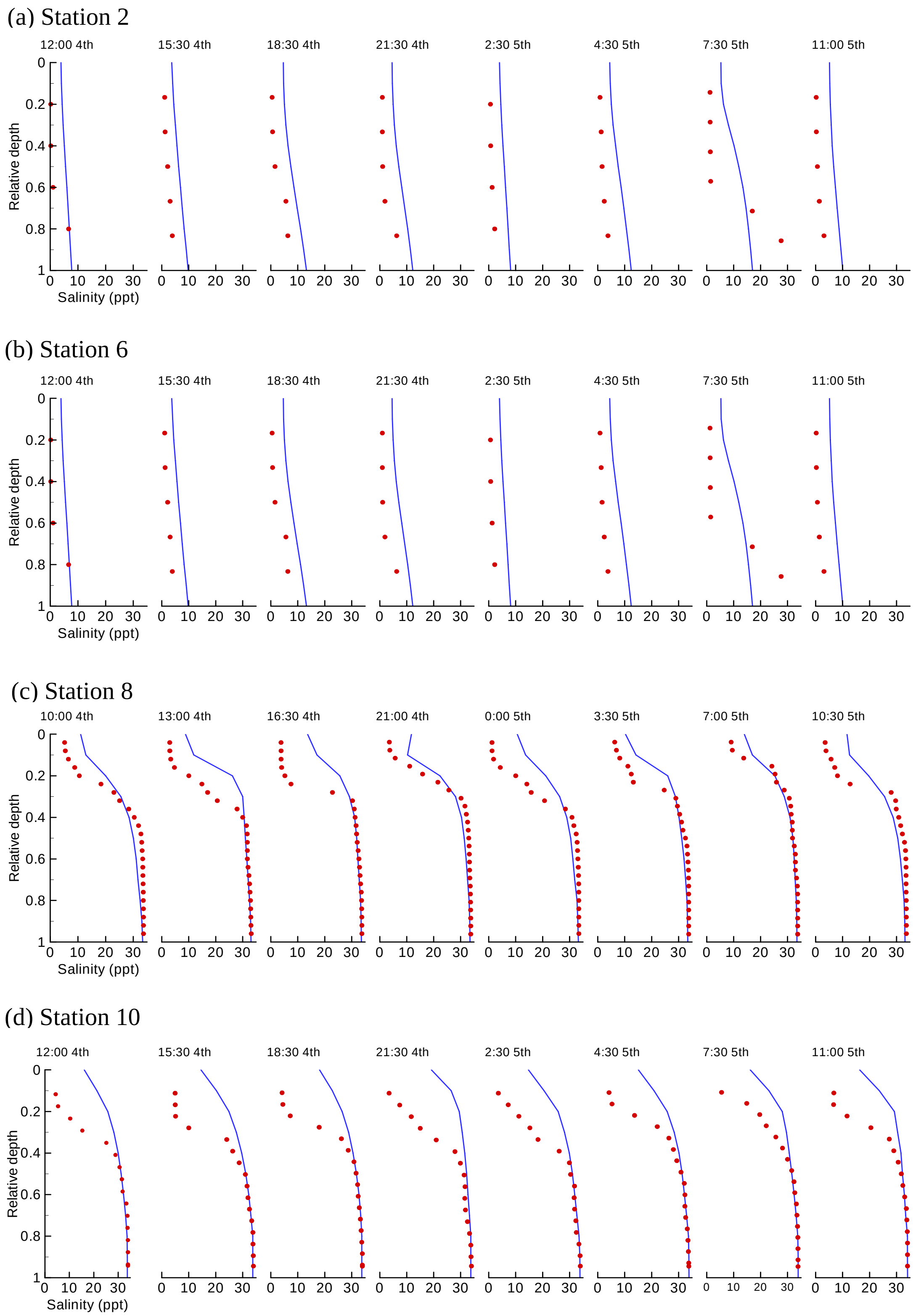

Fig. 5.21 Comparisons of computed and measured salinity profiles during a neap tide in the wet season (July 1998): Solid lines represent computed salinity and dots denote measurements.

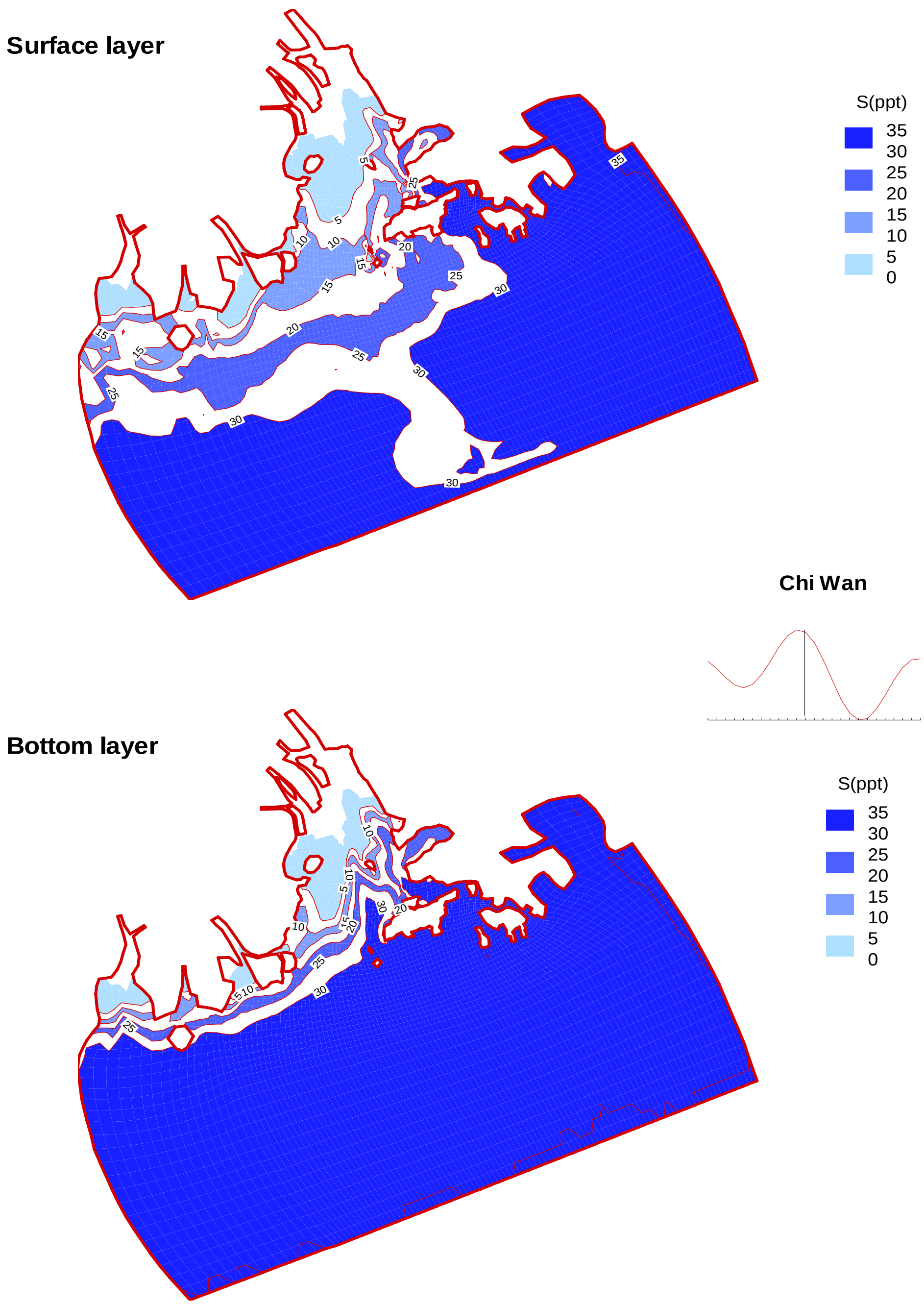

Fig. 5.22 Computed salinity patterns at high slack during a spring tide in the wet season (July 1998)

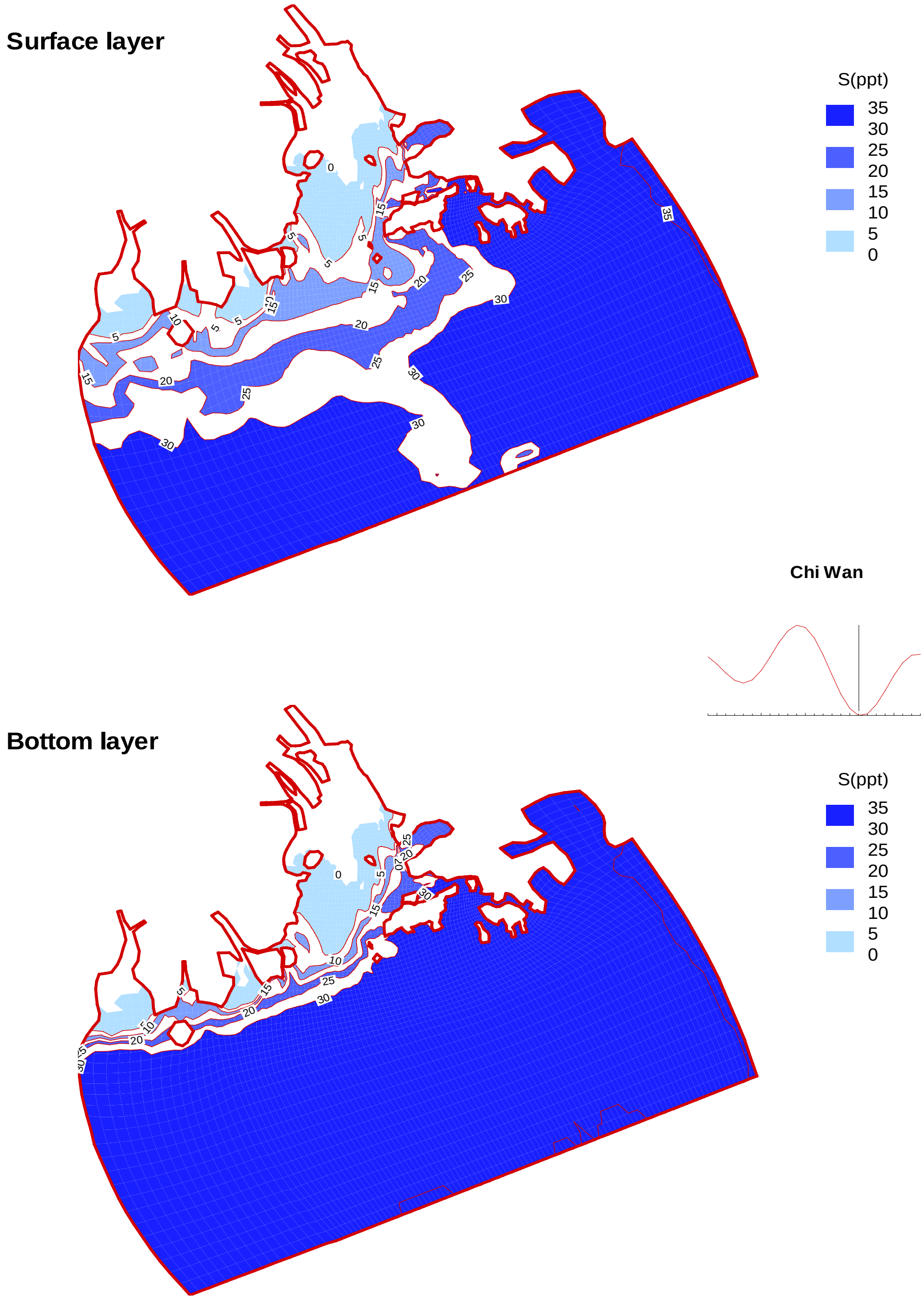

Fig. 5.23 Computed salinity patterns at low slack during a spring tide in the wet season (July 1998)

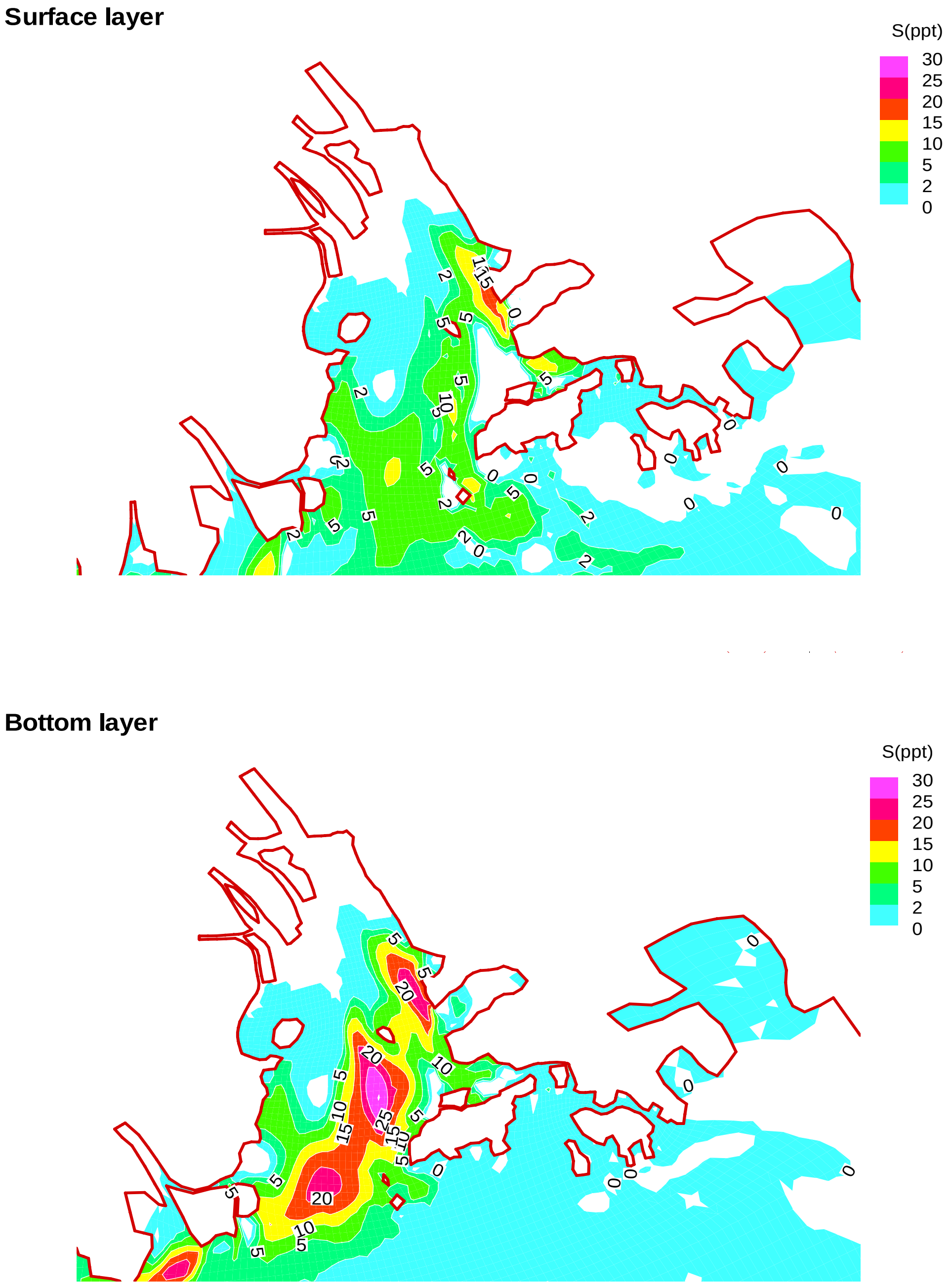

Fig. 5.24 Variations of salinity between high slack and lower slack during a spring tide in the wet season (July 1998)

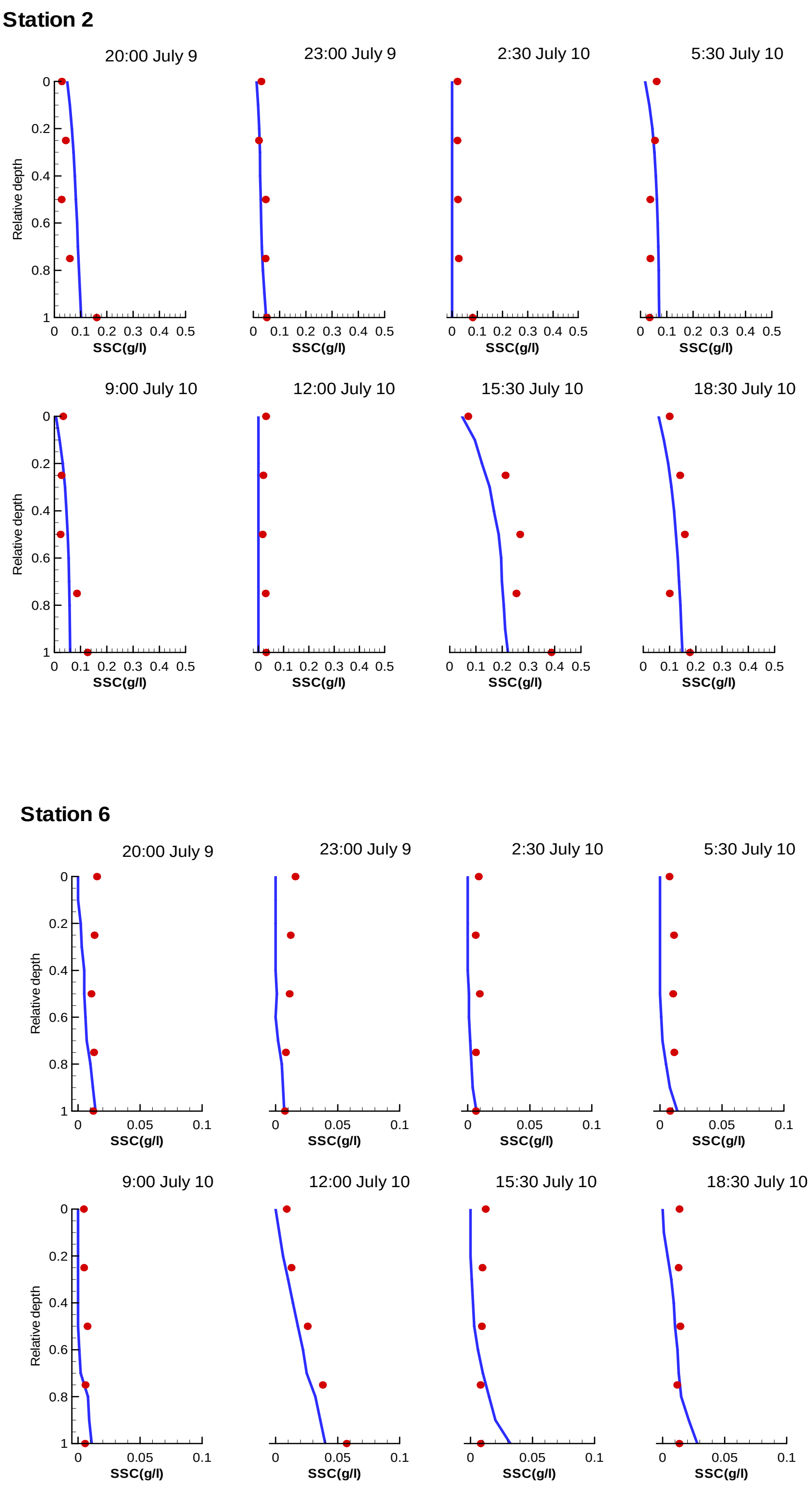

Fig. 5.25a Comparisons of computed and measured sediment concentration at stations 2 and 6 during a spring tide in the wet season (July 1998): Solid lines represent computed concentration and dots denote measurements.

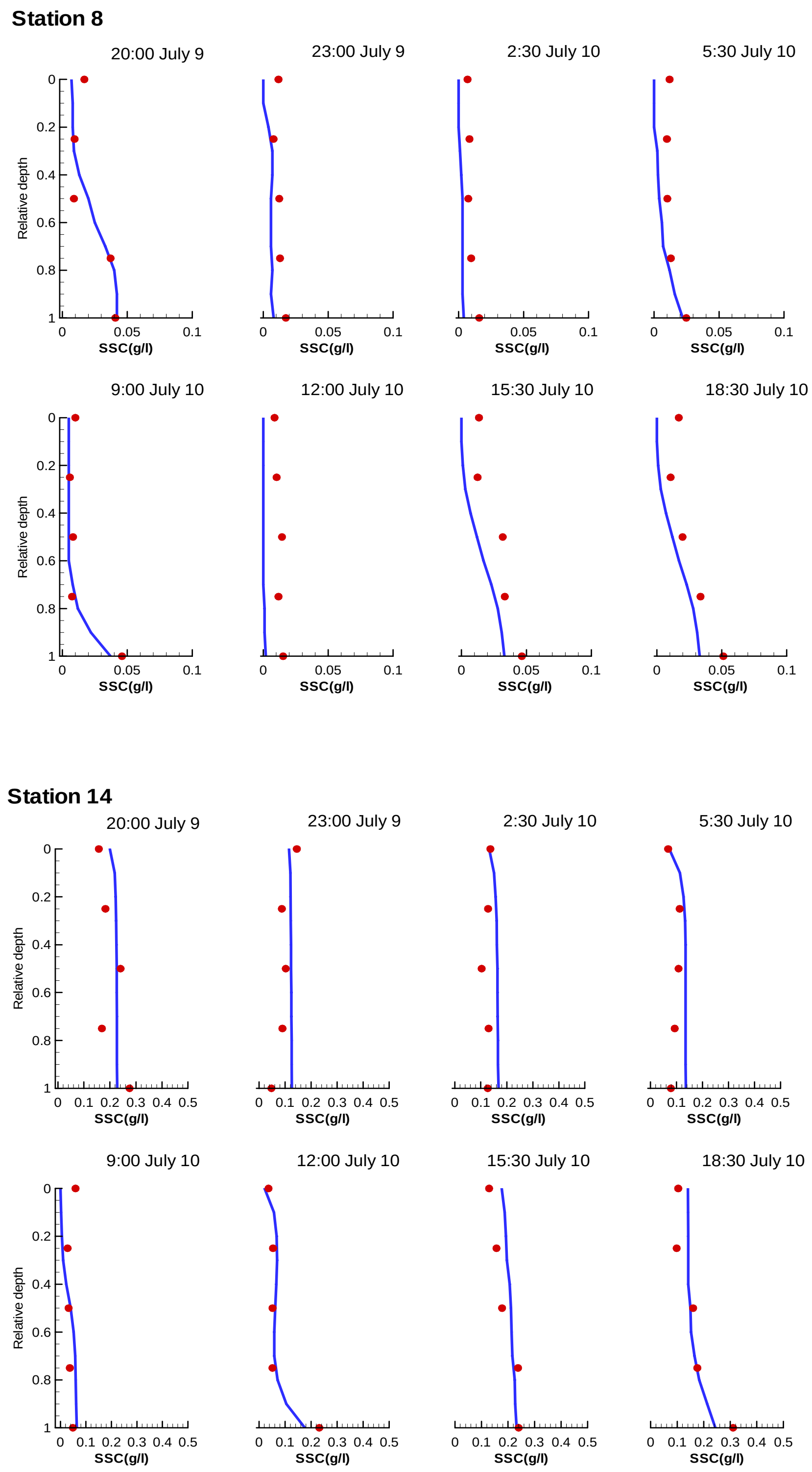

Fig. 5.25b Comparisons of computed and measured sediment concentration at stations 8 and 14 during a spring tide in the wet season (July 1998): Solid lines represent computed concentration and dots denote measurements.

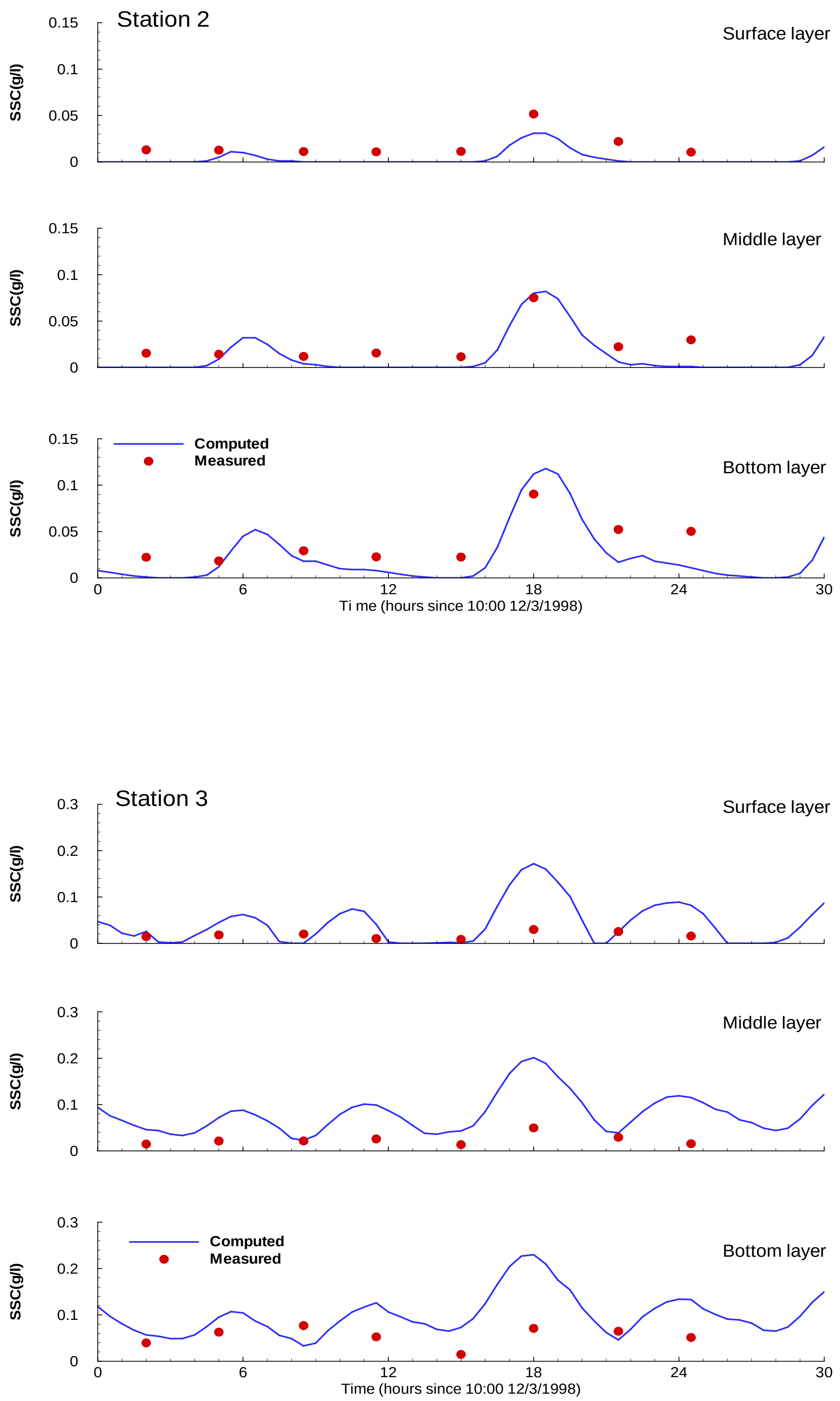

Fig. 5.26a Comparisons of computed and measured sediment concentration at stations 2 and 3 during a spring tide in the dry season (March 1998)

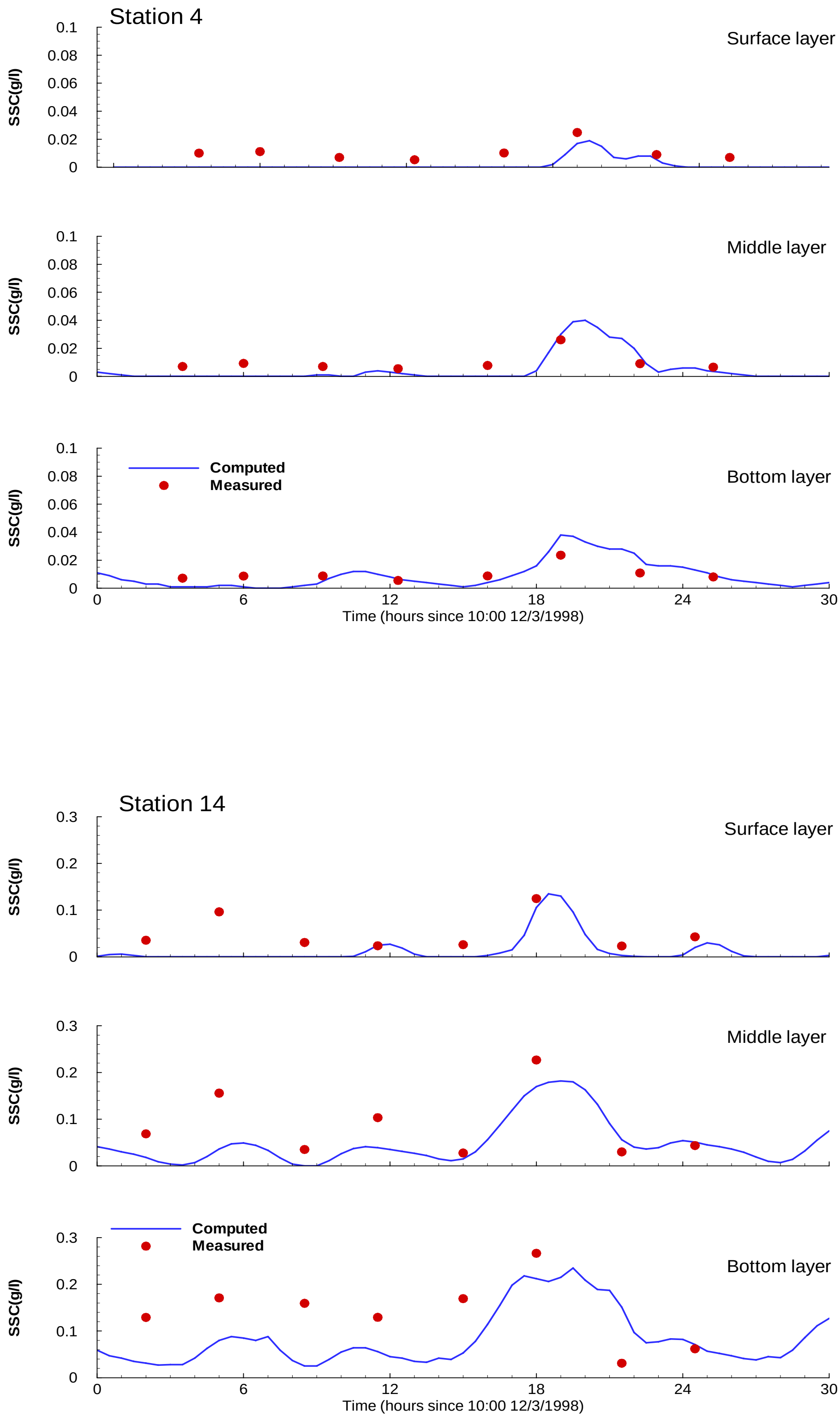

Fig. 5.26b Comparisons of computed and measured sediment concentration at stations 4 and 14 during a spring tide in the dry season (March 1998)

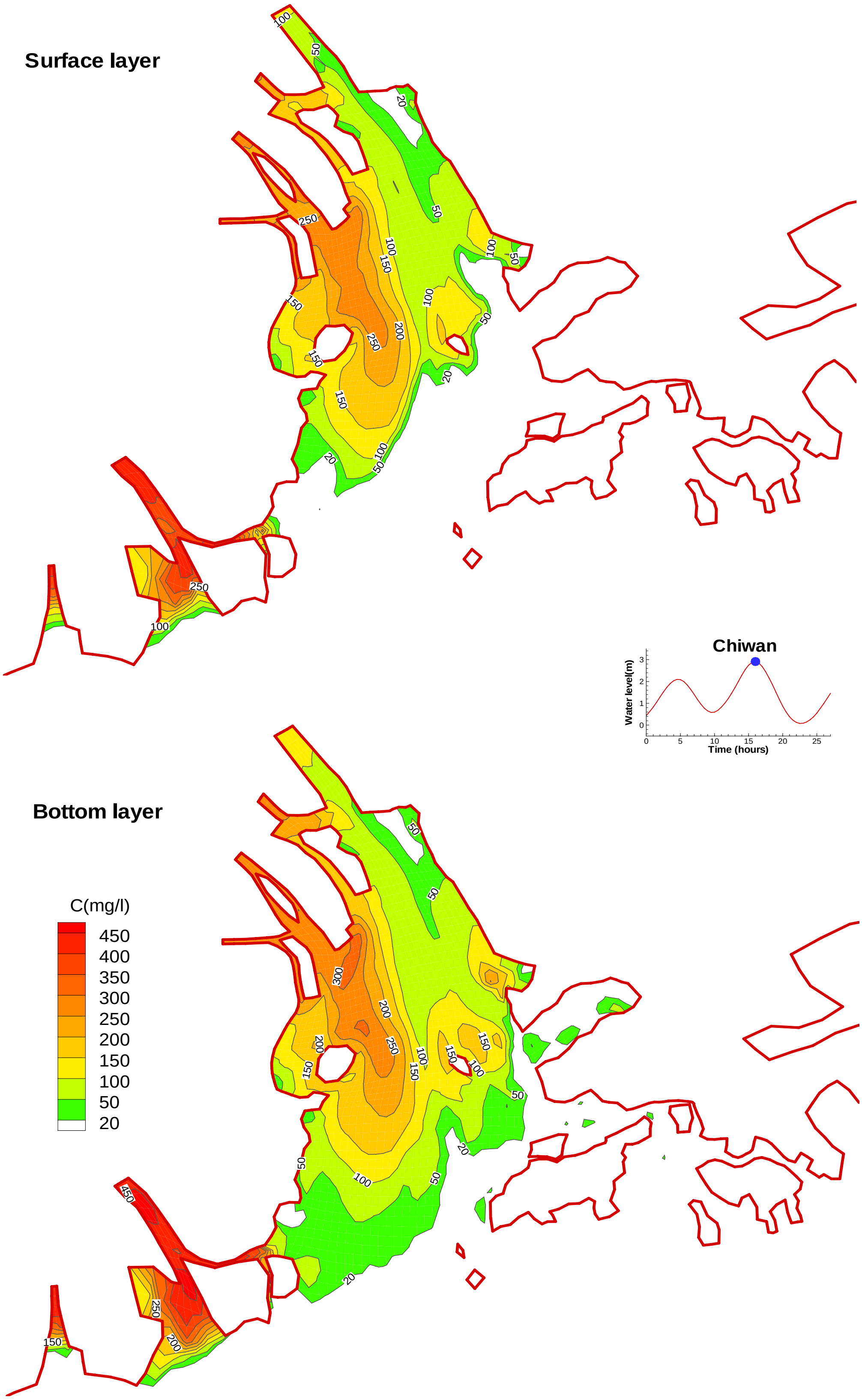

Fig. 5.27 Computed sediment concentration patterns at high slack during a spring tide in the wet season (July 1998)

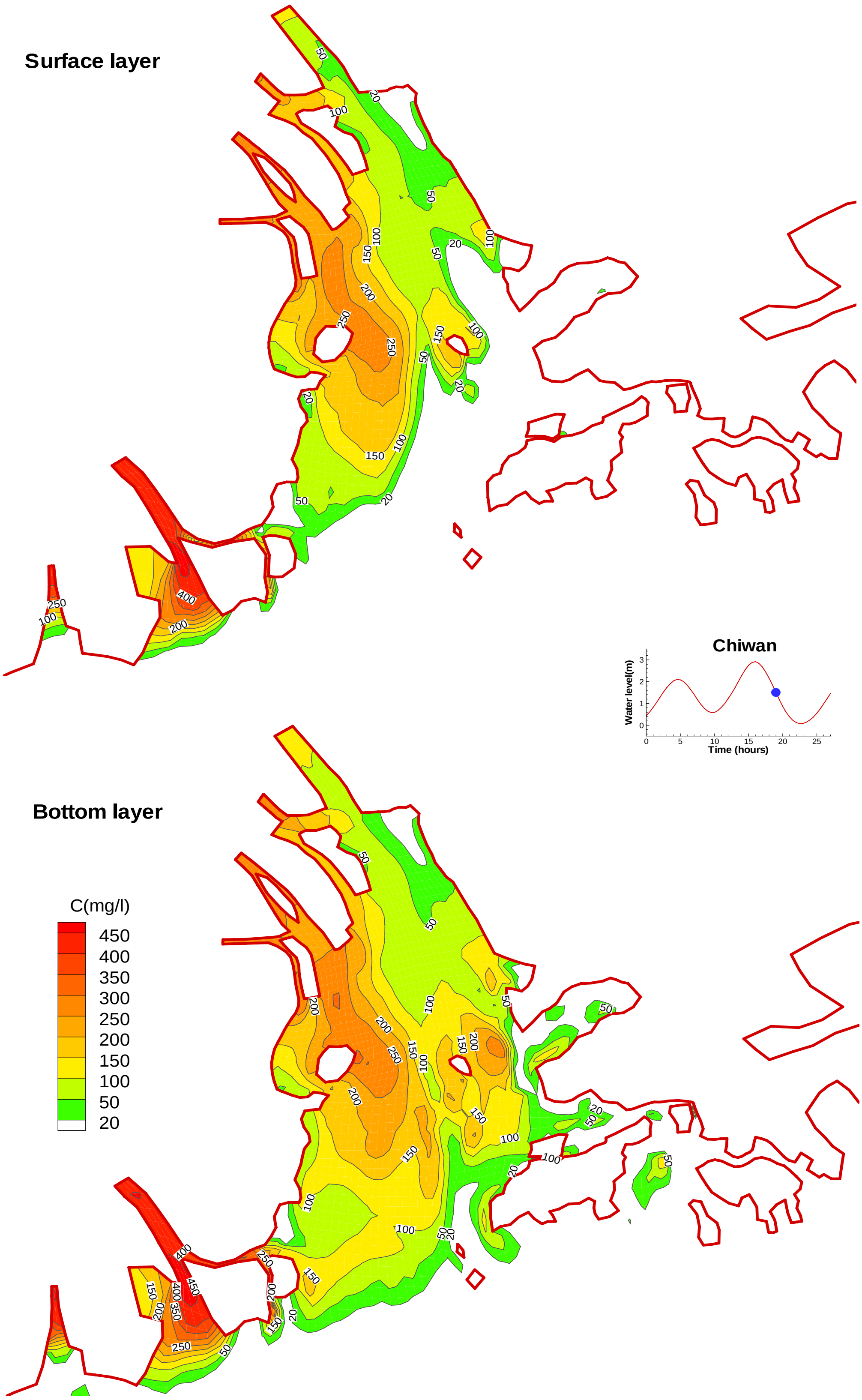

Fig. 5.28 Computed sediment concentration patterns during an ebbing spring tide in the wet season (July 1998)

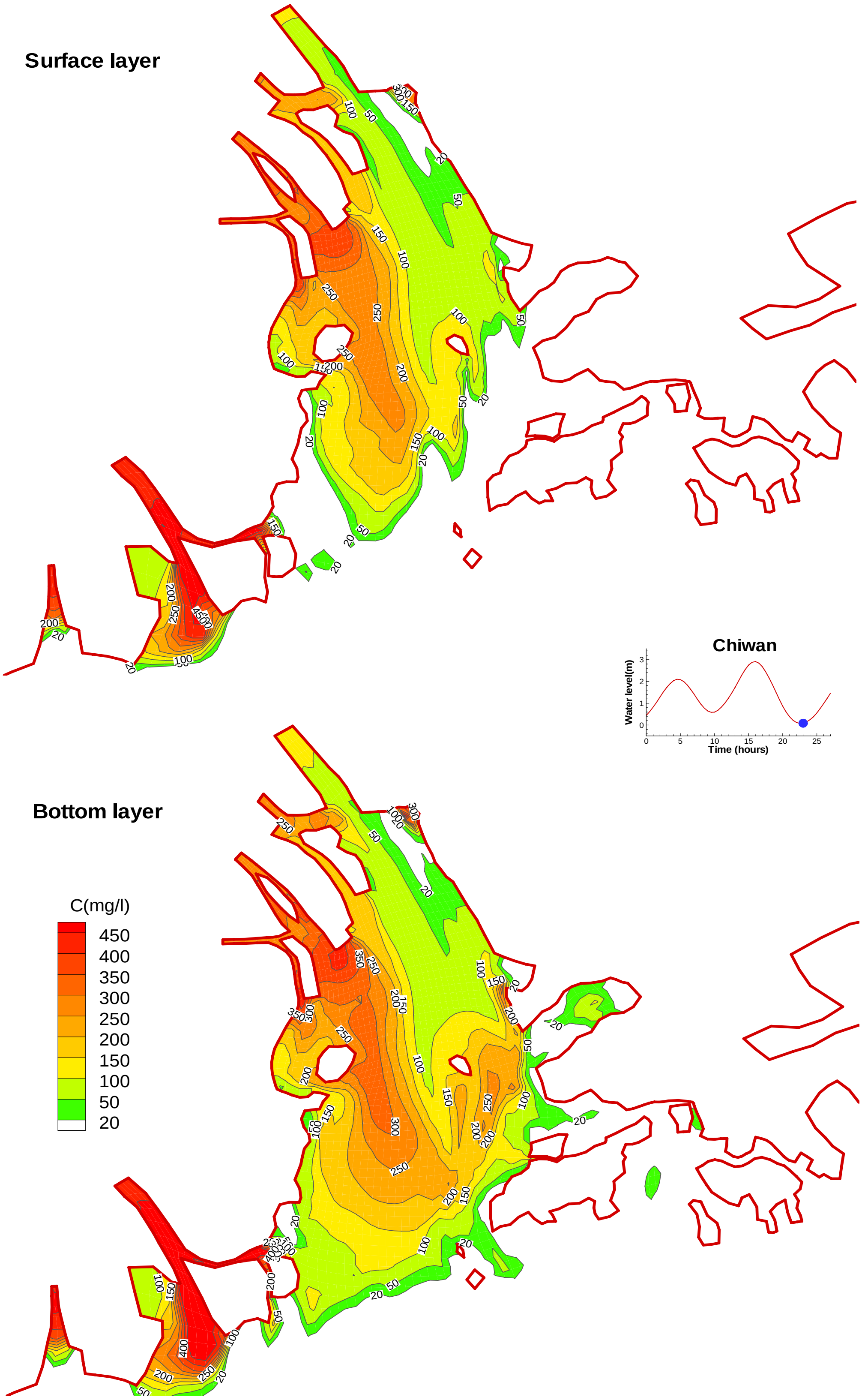

Fig. 5.29 Computed sediment concentration patterns at low slack during a spring tide in the wet season (July 1998)

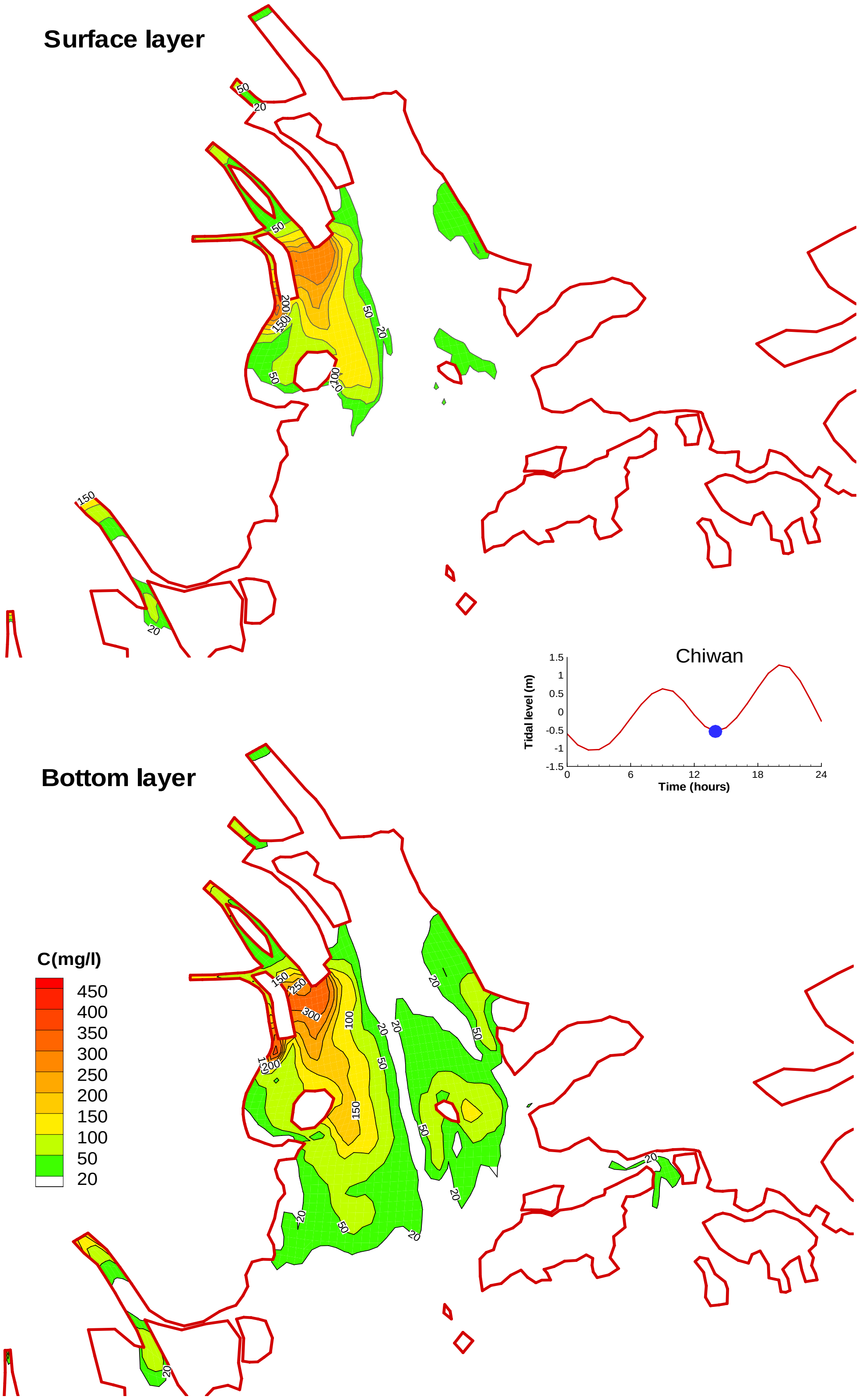

Fig. 5.30 Computed sediment concentration patterns at low slack during a spring tide in the dry season (March 1998)

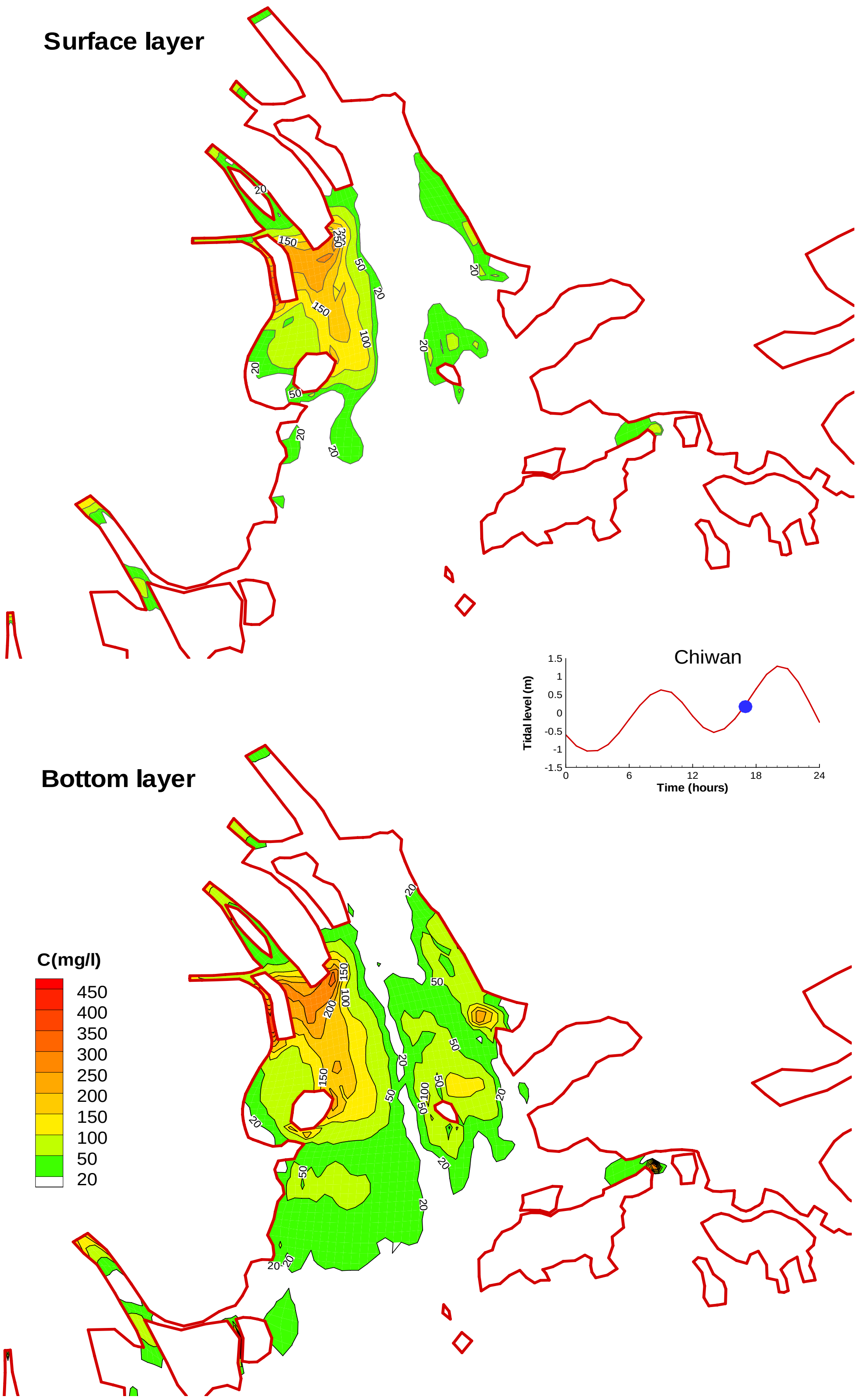

Fig. 5.31 Computed sediment concentration patterns during a flooding spring tide in the dry season (March 1998)

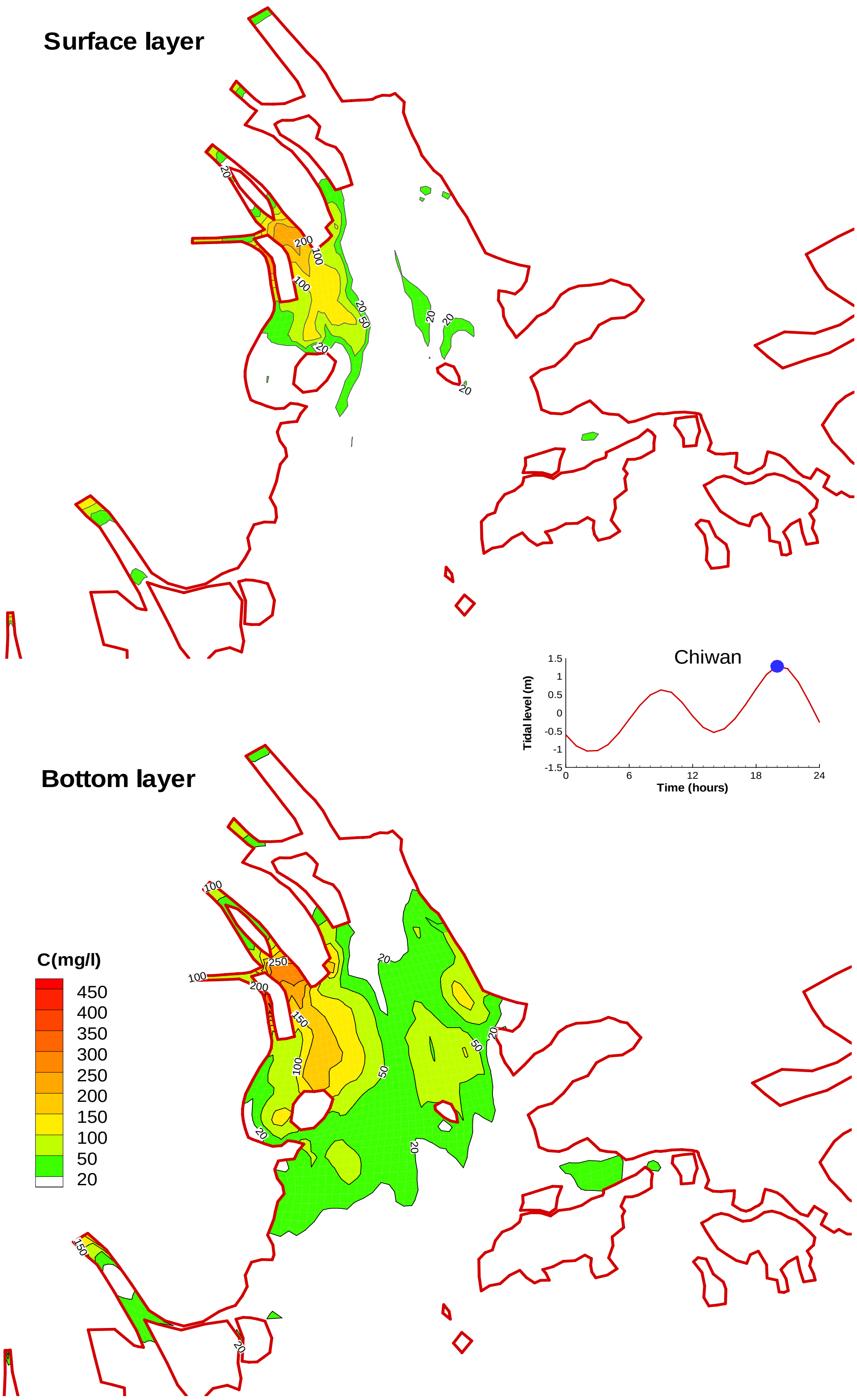

Fig. 5.32 Computed sediment concentration patterns at high slack during a spring tide in the dry season (March 1998)

CHAPTER 6

MODELLING OF CURRENT INDUCED TURBIDITY MAXIMUM IN THE PEARL RIVER ESTUARY

6.1 General remarks

In Chapter 3, the formation mechanism of the turbidity maximum in the Pearl River Estuary was analyzed based on numerous measurement data. Although the turbidity maximum is ubiquitous, it is a complex phenomenon in partially-mixed estuaries. To study the formation of turbidity maximum, the analysis of synchronous measurement data is a useful and effective way. However, generally, many measurement stations covering the entire zone of turbidity maximum should be set up, and the physical parameters of tidal level, water depth, velocity, suspended sediment concentration and salinity should be measured synchronously. So it is a challenging and expensive task to collect enough field data for studying the turbidity maximum. Therefore, numerical modelling has been used extensively to study the turbidity maximum in an estuary.

In Chapter 5, a three-dimensional hydrodynamics and sediment transport model is proposed and validated by measurements. The modelling results have shown that the turbidity maxima in the Pearl River Estuary (PRE) are generally located on shoals and the transitional regions between the river outlets and the main channels. The turbidity maximum always results in the sedimentation in the waterway, and consequently regular dredging has to be carried out to maintain sufficient water depth for navigation. In this chapter, the developed 3D numerical model is used to study the turbidity maximum along the main channels of the Pearl River Estuary. The objectives of the study are as follows.

1) To reveal the locations of the turbidity maxima in the Pearl River Estuary;

2) To study the relationship between turbidity maximum, salt water intrusion and the stagnant points of flow in the Pearl River Estuary.

3) To study the development process and variation of the locations of turbidity maxima and the dependence of the suspended sediment concentration in the turbidity maximum on the freshwater runoff from the Pearl River and tidal level.

4) To study the impact of wind on turbidity maximum in the Pearl River Estuary.

6.2 Turbidity maximum in the PRE

The turbidity maximum is a ubiquitous phenomenon in a partially-mixed estuary, where the concentration of suspended sediment is much higher than that in either the river or the sea. Its occurrence is related to the intrusion of salt water and the vertical water density gradient due to the salinity stratification. Generally, the turbidity maximum develops fully in the wet season when the input freshwater flow rate is strong, resulting in strong stratification near the head of salt water intrusion. In the following, the formation and development of turbidity maximum in the wet season during a spring tidal cycle in the Pearl River Estuary will be expounded.

Fig. 6.1 and Fig. 6.2 show the profiles of flow, salinity and suspended sediment concentration during flooding, high slack, ebbing and low slack within a spring tide in the wet season along the West Channel. From these two figures, we can see the formation and development (evolution) of the turbidity maximum along the West Channel. A clear front of SSC can be observed in the West Channel and it moves back and forth within the tidal cycle. Around 5 to 10 km upstream of this front, there is a turbidity maximum which always occurs in the West Channel in a spring tidal cycle. It develops with increasing flow intensity during flooding and ebbing time and the sediment concentration in the turbidity maximum generally reaches the maximum of above 200 mg/l at the height of ebbing. The uppermost location of the turbidity maximum is about 43 km downstream of the start point of the profile in Humen Channel, which was located at about 12 km upstream of Humen outlet (Dahu). Hence, the uppermost location during high slack of a spring tide in the wet season is about 31 km downstream of the Humen outlet. The lowermost location during low slack is about 65 km from the start point of the profile, or 53 km from the Humen outlet. Therefore, the cruising range of the turbidity maximum in the spring tide is about 22 km. By comparing the turbidity maximum with the flow structure and the salt water intrusion processes, it can also be concluded that during flooding and ebbing, the turbidity maximum correlates with the velocity of flow. The sediment particles are resuspended from the seabed, resulting in the increase of sediment concentration with the increasing flow intensity. It is a fast adjustment process. The sediment particles congregate at the upstream limit of the head of the salt wedge intrusion during flooding in a highly stratified flow, and form the turbidity maximum a little downstream of the head of the salt wedge intrusion. During tidal slacks, the location of turbidity maximum is always at the upstream limit of the head of the intrusion saltwater wedge, where flow velocity is small.

Fig. 6.3 and Fig. 6.4 show the profiles of flow, salinity and suspended sediment concentration during flooding, high slack, ebbing and low slack within a spring tide in the wet season along the East Channel. Due to the weak freshwater input from Humen, tidal flow is dominant in the East Channel and fewer sediment particles can penetrate into the East Channel from the three western outlets. The situation is different in the West Channel where the strong freshwater input is dominant. Consequently, the East Channel shows the character of a partially-mixed estuary in the wet season, with different flow structure and development process compared with the West Channel. Within the spring tidal cycle, the turbidity maximum in the East Channel forms about 2-3 hours later than the high and low slack due to the time lag between flow and sediment erosion/deposition.

Fig. 6.3 shows the existence of a turbidity maximum with sediment concentration of about 70 mg/l during flooding, which is located at the reach about 28 km downstream of the Humen outlet. During the high slack, the head of the salt water intrusion is basically well mixed. Although a turbidity maximum near the head of salt water intrusion could also be found, the sediment concentration in the turbidity maximum is relatively lower, only about 60 mg/l. The vertical distribution of the sediment concentration is uniform at that location. That implies it is difficult for sediment particles to congregate at the upstream limit of the head of the intrusion wedge of salt water in the East Channel due to the relatively well-mixed condition.

Another interesting phenomenon in the East Channel should also be mentioned. Because of the freshwater input from the west outlets, which passes through the West Channel and flows to the East Channel, the flow downstream of the East Channel is stratified in the wet season. Hence, locally resuspended sediment particles and sediment particles penetrating the head of the salt water wedge will be captured there, resulting in the formation of a turbidity maximum. This phenomenon can be found during flooding at a location of 36 km and during high slack at a location of 34.8 km downstream of the Humen outlet, both with a lower sediment concentration than other turbidity maxima. This phenomenon can be seen clearly during ebbing in Fig. 6.4. A turbidity maximum with a sediment concentration of more than 130 mg/l can be found in the bottom layer downstream of the salt wedge head where density stratification occurs, about 38 km downstream from the Humen outlet.

During the low slack, the turbidity maximum moves seaward to a location about 42 km downstream of the Humen outlet. Meanwhile, the sediment concentration decreases with the weakening flow intensity and the turbidity maximum grows upward along the water column with well-mixed flow near the turbidity maximum.

The cruising range of the turbidity maximum in the East Channel in a spring tide in the wet season is about 22 km, which is same as that in the West Channel.

To reveal the relationship between the formation of turbidity maximum with flow and the intrusion of salt water, tidally-averaged profiles along the West Channel and the East Channel are shown in Fig. 6.5 and Fig. 6.6, respectively. From these two figures, we can see the gravitational circulation flow structure.

Net seaward flow occurs at the upper layer, while net landward flow occurs at the lower layer, with the stagnant points located at the end of the sand bars. This is caused by the stratification of flow due to the intrusion of salt water. The high stratification along the West Channel is due to the stronger freshwater input with maximum seaward and landward residual flows of about 25.3 cm/s and 5.23 cm/s, respectively. The stratification along the East Channel is weak due to the relatively dominant tidal flow, with maximum seaward and landward residual flows of about 15.0 cm/s and 5.74 cm/s, respectively. Based on field data, the formation mechanism of turbidity maximum in the Pearl River Estuary is analyzed in Chapter 3. Both gravitational circulation and tidal pumping are identified as the main causes of the turbidity maximum in PRE. The residual flow confirms that the gravitational circulation in the West Channel is the main force causing the turbidity maximum. However, tidal pumping of the resuspended sediment particle is the dominant force for the turbidity maximum in the East Channel.

Fig. 6.5 and Fig. 6.6 also show the computed turbidity maxima in the Pearl River Estuary, their locations corresponding with the stagnant points and the heads of salt water intrusion. Particularly, due to the complicated bathymetry in the Pearl River Estuary, four turbidity maxima can be found along the West Channel. The upstream three turbidity maxima are obviously formed by local convergence of sediment particles coming from the western outlets. The fourth one, located at about 36 km downstream of the Humen outlet, is a typical turbidity maximum in a partially mixed estuary, which occurs at the upstream limit of the head of the salt water intrusion. In the East Channel, tidally-averaged profile of sediment concentration also shows four turbidity maxima, with the downstream one a typical turbidity maximum. One special feature is that there are two peaks of sediment concentration in the turbidity maximum. One peak is located near the head of the salt water intrusion, which is mainly caused by the tidal pumping. The downstream one is caused by fresh water input from the western outlets, where gravitational circulation plays an important role in its formation.

Particularly, the locations of the typical turbidity maxima in Fig. 6.5 and Fig. 6.6 are not observably difference from the field measurement in Fig. 3.11, which confirms that the measurements conducted in 1978 and 1979 for analyzing the formation mechanisms of turbidity maximum in the PRE are still valid for the present situation.

6.3 Fortnightly variation of turbidity maximum

In the last section, the formation and development of turbidity maximum during a spring tide in the wet season has been analyzed. Generally, the tidal level will go through a cycle of spring tide and neap tide every two weeks in the Pearl River Estuary, which is a semi-diurnal estuary. Hence the turbidity maximum will also vary with the tidal level within half a month. It is therefore necessary to study the formation of the turbidity maximum during a neap tide to complete the investigation.

Fig. 6.7 and Fig. 6.8 show the tidally-averaged velocity, salinity and suspended sediment concentration within a neap tide in the wet season along the West and East Channels, respectively. It can be seen that the flow is highly stratified due to the weak tidal flow from the open sea. The maximum landward residual flow is about 6.91 cm/s in the West Channel, which is larger than that during a spring tide. Although the gravitational circulations still exist along the two main channels, except one turbidity maximum located at about 20 km from the start of the profiles due to the input sediment particles from Jiaomen, the typical turbidity maximum near the head of the wedge of salt water intrusion does not occur. That means sediment particles in the turbidity maximum in the Pearl River Estuary mainly come from local resuspension from the seabed. During the neap tide, although the gravitational circulation would tend to drive sediments to congregate to form a turbidity maximum, the weak tidal flow is unable to erode the seabed to supply enough sediment particles to form one.

6.4 Seasonal variation of turbidity maximum

The model was also used to simulate the sediment concentration during a spring tide and a neap tide in the dry season to study the seasonal variation of turbidity maximum in the Pearl River Estuary. Fig. 6.9 and Fig. 6.10 show the tidally-averaged velocity, salinity and suspended sediment concentration within a spring tide (from 10:00 March 12 to 11:00 March 13, 1998) in the dry season along the West Channel and the East Channel, respectively. Fig. 6.11 and Fig. 6.12 show the tidally-averaged velocity, salinity and suspended sediment concentration within a neap tide (from 10:00 March 19 to 11:00 March 20, 1998) in the dry season along the West Channel and the East Channel, respectively.

In the dry season, the fresh water input from the Pearl River is small. Since tidal flow is dominant, salt water could penetrate into the Humen Channel. The salinity difference along a water column on the sand bar in the main channels is less than 3 ppt, generally. However, there is more than 9 ppt vertical salinity difference at the downstream end of the sand bar in the West Channel. The landward residual flow, which covers most of the water body along the main channels, especially at the lower layer, will transport the fine sediment particles into the Pearl River Estuary from the open sea. The strong landward residual flow corresponds with the 6 to 9 ppt vertical salinity difference mentioned above. From the sediment concentration profile shown in Fig. 6.9 and Fig. 6.10, we could find the existence of turbidity maximum in the main channels. The turbidity maximum in the dry season along the main channels has the following characteristics: 1) the sediment concentration in the core of turbidity maximum is low, not more than 70 mg/l during a spring tide, and not more than 20 mg/l during a neap tide; 2) turbidity maximum in the West Channel covers a long longitudinal distance, with the core located at the middle to end of the reach of the sand bars; 3) Turbidity maximum in the dry season is mainly caused by the resuspension of sediment during the spring tide. Once the sediment particles are resuspended, they tend to remain in suspension until the tide changes from a spring tide to a neap one.

6.5 Impact of runoff on turbidity maximum

The location and development of turbidity maximum in the PRE is not only related to the type of tide, but also closely related to the freshwater and sediment input from the Pearl River. Here, a scenario with 1.5 times mean seasonal flow rates with double sediment concentration during a spring tide in the wet season was also simulated to study the impact of runoff on the turbidity maximum in the PRE. Fig. 6.13 shows the tidally averaged horizontal patterns of suspended sediment concentration with the river boundary conditions of increased mean seasonal flow rates. It can be seen that strong freshwater flow drives more sediment particles to the open sea, with the increased flow rates resulting in the increase of sediment concentration in the PRE. West Shoal of the PRE is becoming more turbid. However, this impact is mainly limited to the West Shoal. It seems that even stronger runoff is needed to transport more sediment particles across to the West Channel because of the Coriolis force and landward residual flow due to the intrusion of saltwater.

Fig. 6.14 shows impacts of increased flow rate on the profiles of longitudinal net flow, tidally averaged salinity and sediment concentration along the main channels. It can be seen that the landward density induced net flow decreases, and stagnant points and the heads of the wedge of the intrusion saltwater move 1-1.5 km downstream along the main channels. The change of the locations of turbidity maxima in the main channels due to 50% increase in freshwater flow is not significant. However, because more sediment particles are transported from the Pearl River outlets, sediment concentrations in the turbidity maximum zones in the main channels increase both longitudinally and vertically. Consequently, the turbidity maxima elongate longitudinally and thicken vertically. The sediment concentrations in the centers of the turbidity maxima in the West and East channels are 94 mg/l and 77 mg/l, increases of about 7 mg/l and 5 mg/l compared with the values resulting from the mean seasonal flow rates, respectively.

6.6 Impact of wind on turbidity maximum

The effects of wind on current and sediment concentration have been studied in Chapter 4 qualitatively. The results show that wind stress affects the residual flow in both magnitude and direction, which would result in the change of the fate of sediment in the PRE in the long term. In this chapter, numerical modelling with two wind speeds of 5 m/s and 10 m/s, which are considered as moderate and fresh winds by the Hong Kong Observatory, respectively, from the south in a spring tide in the wet season, was also carried out to study the impacts of wind on the turbidity maximum in the PRE quantitatively. Fig. 6.15 and Fig.6.16 show the horizontal distribution of tidally averaged suspended sediment concentration and profiles of current, salinity and sediment concentration along the main channels with and without a moderate south wind of speed of 5 m/s, respectively. Fig. 6.17 and Fig. 6.18 show the effect of a fresh south wind of 10 m/s. It can be seen that the moderate wind only slightly increases the sediment concentration, but to a slight degree, generally. However, the sediment concentration increases significantly with the blowing of the fresh wind. Because the wind direction is opposite to the ebbing flow, the wind induced flow will prevent sediment from transporting into the open sea and the contours of sediment concentration incline to the east due to increased sediment resuspension under the effect of wind stress. Consequently, the sediment distribution in the vertical is much more uniform under the fresh wind. These could be seen clearly in Fig. 6.18.

The wind stress mixes the flow better in the main channels, where the water depth is relatively shallow compared with that in the open sea, and the south wind also increases the flow rate in the lower layer of the water column. As a result, the head of saltwater intrusion and the locations of turbidity maxima move about 1-2 km and 5-7 km downstream under winds of 5 m/s and 10 m/s, respectively. The sediment concentrations in the centers of the turbidity maxima also increase with the blowing of the fresh wind.

6.7 Summary

In this chapter, the tidally, fortnightly and seasonal development processes of turbidity maximum in the main channels in the Pearl River Estuary are simulated by a three-dimensional hydrodynamics and sediment transport model. After analyzing the modelling results, the following conclusions could be drawn:

1) Turbidity maximum exists in the main channels of the Pearl River Estuary. It occurs during spring tides and disappears during neap tides no matter in the wet season or in the dry season.

2) With a sufficient supply of fine sediment particles from the Pearl River in the wet season and resuspension within a spring tide, the turbidity maximum fully develops during ebbing.

3) In the wet season, the West Channel shows full stratification. The turbidity maximum there is located at the upstream limit of the wedge head of salt water intrusion. Tidal flow dominates in the wedge of salt water intrusion and the freshwater from the three western outlets stratifies the flow downstream of the wedge. Turbidity maximum in the East Channel has two peaks of sediment concentration.

4) Turbidity maximum moves back and forth in the middle and downstream reach of the sand bars in the main channels within a tidal cycle. The cruising range is about 22 km in the wet season. The sediment concentration in the turbidity maximum is higher, and subsequent sediment particle deposition will affect the navigation course.

5) Gravitational circulation, tidal pumping and resuspension are the main factors in the formation of turbidity maximum in the Pearl River Estuary. Gravitational circulation and tidal pumping provide the favorable hydrodynamic condition for sediment particles to congregate. Local sediment resuspension is the main sediment source for the development of turbidity maximum. In the wet season, all the three factors play important role in the formation of turbidity maximum in the West Channel. For the turbidity maximum in the East Channel, tidal pumping and gravitational circulation dominate the upstream and downstream peaks of sediment concentration, respectively. However, local resuspension is the main cause for the formation of turbidity maximum in the dry season.

6) An increase in 50% of the mean seasonal freshwater flow rates makes the West Shoal more turbid. However, its impacts on turbidity maxima in the main channels are limited.

7) Under the influence of a southerly wind, the flow mixes better and the heads of intrusion saltwater and the locations of turbidity maxima in the main channels move downstream. Sediment concentrations in the turbidity maxima increase significantly if the wind is fresh to strong.

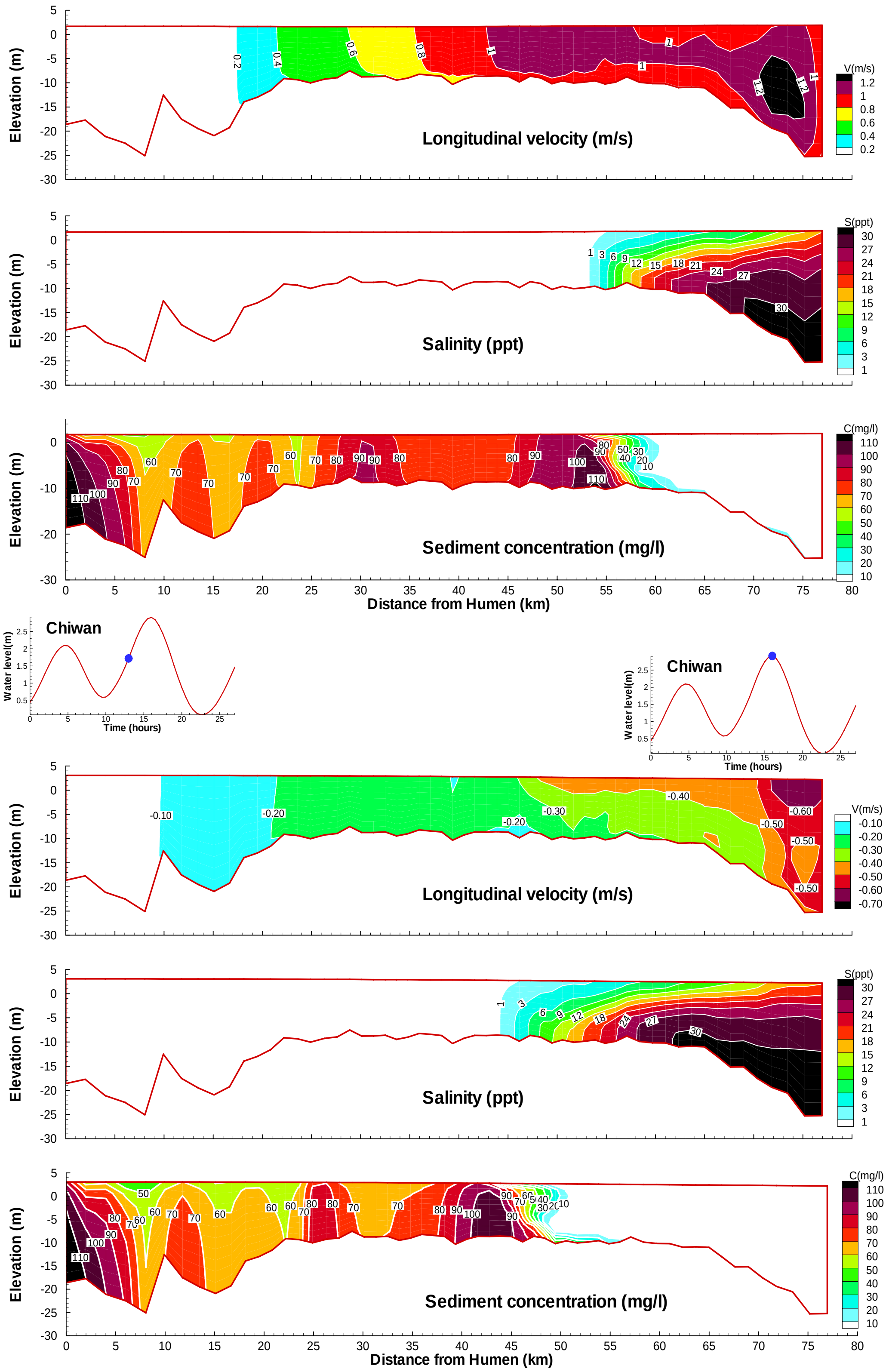

Fig. 6.1 Profiles of flow, salinity and sediment concentration during flooding and high slack of a spring tide in the wet season along the West Channel

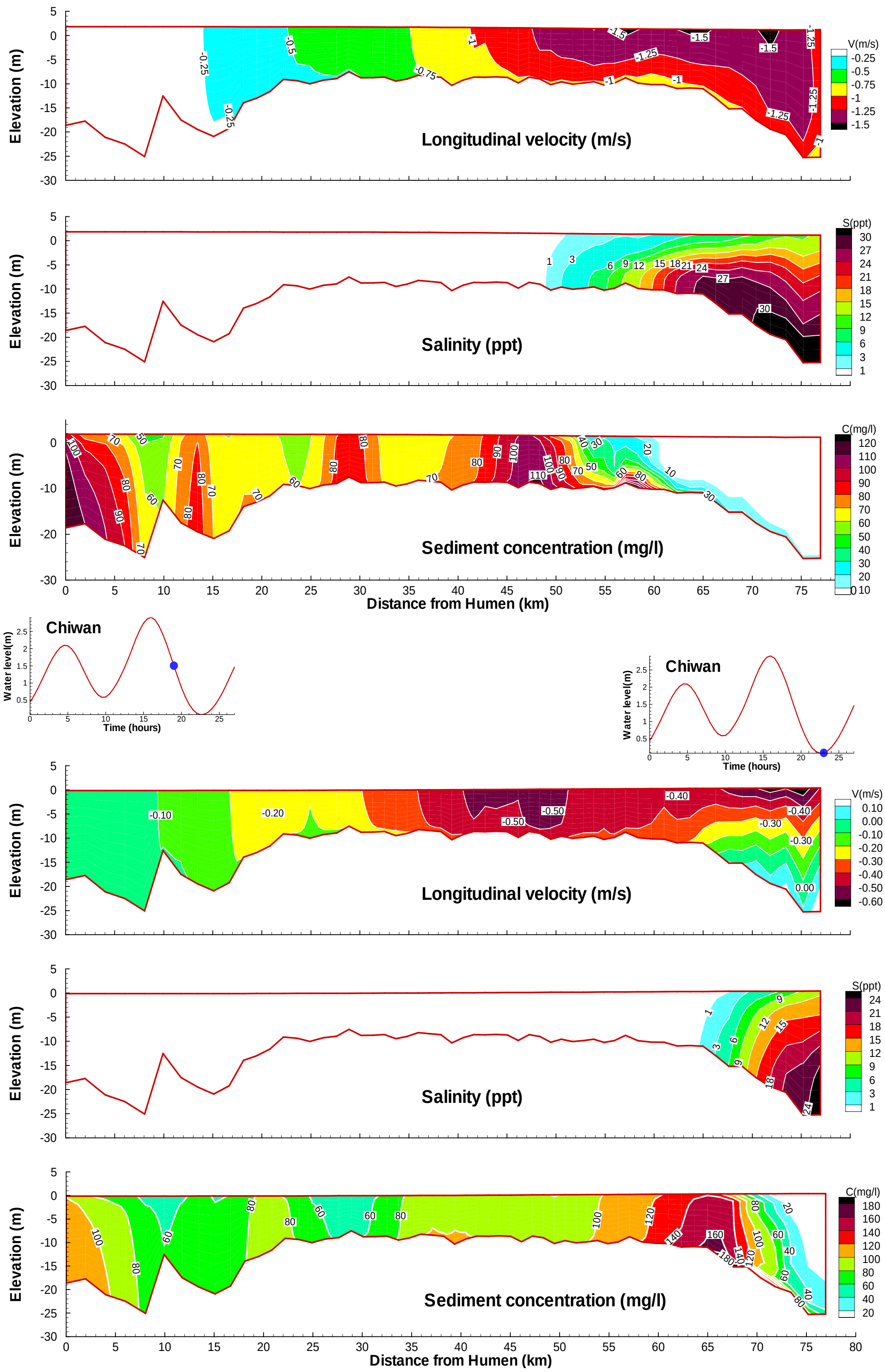

Fig. 6.2 Profiles of flow, salinity and sediment concentration during ebbing and low slack of a spring tide in the wet season along the West Channel

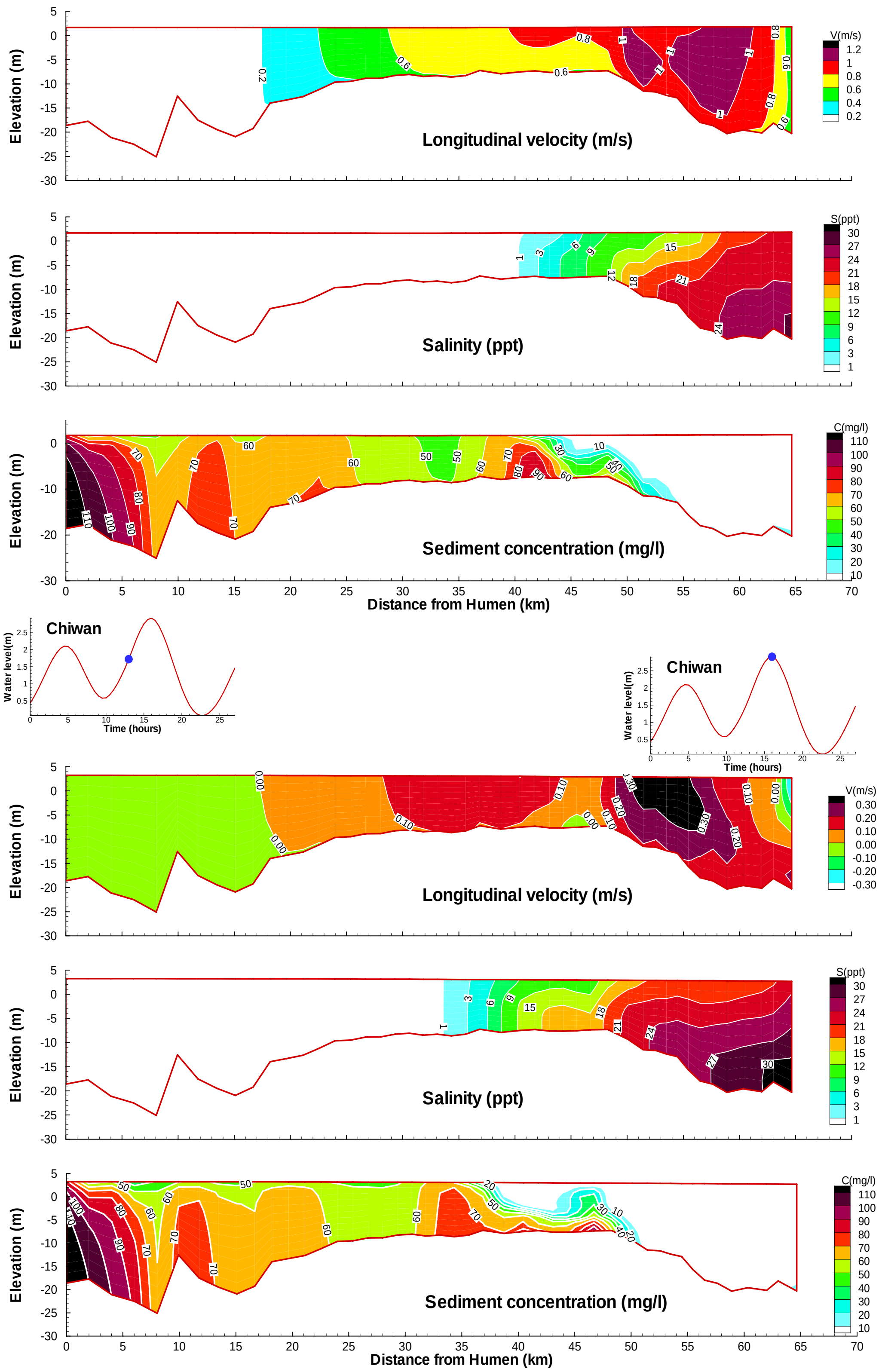

Fig. 6.3 Profiles of flow, salinity and sediment concentration during flooding and high slack of a spring tide in the wet season along the East Channel

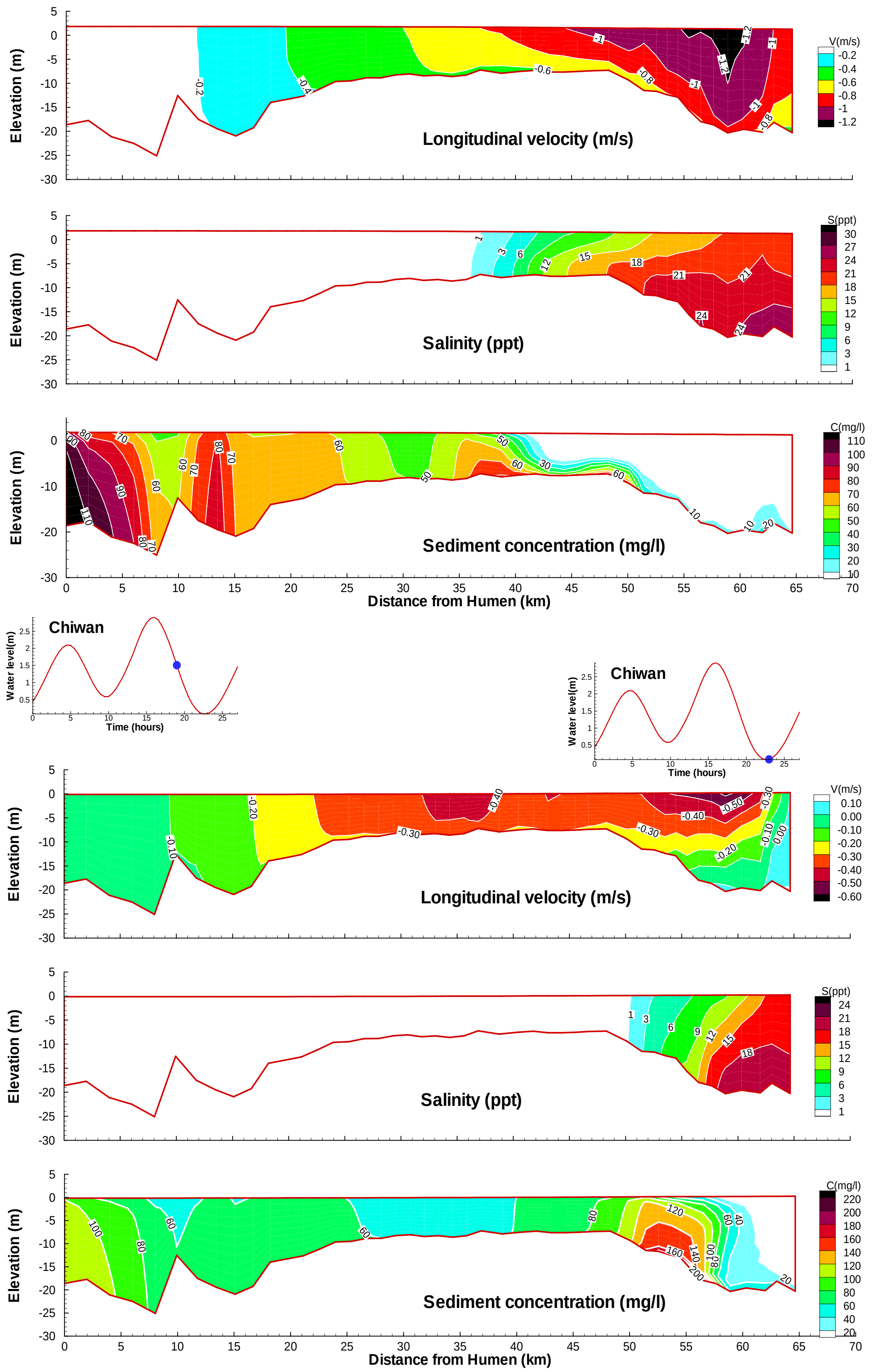

Fig. 6.4 Profiles of flow, salinity and sediment concentration during ebbing and low slack of a spring tide in the wet season along the East Channel

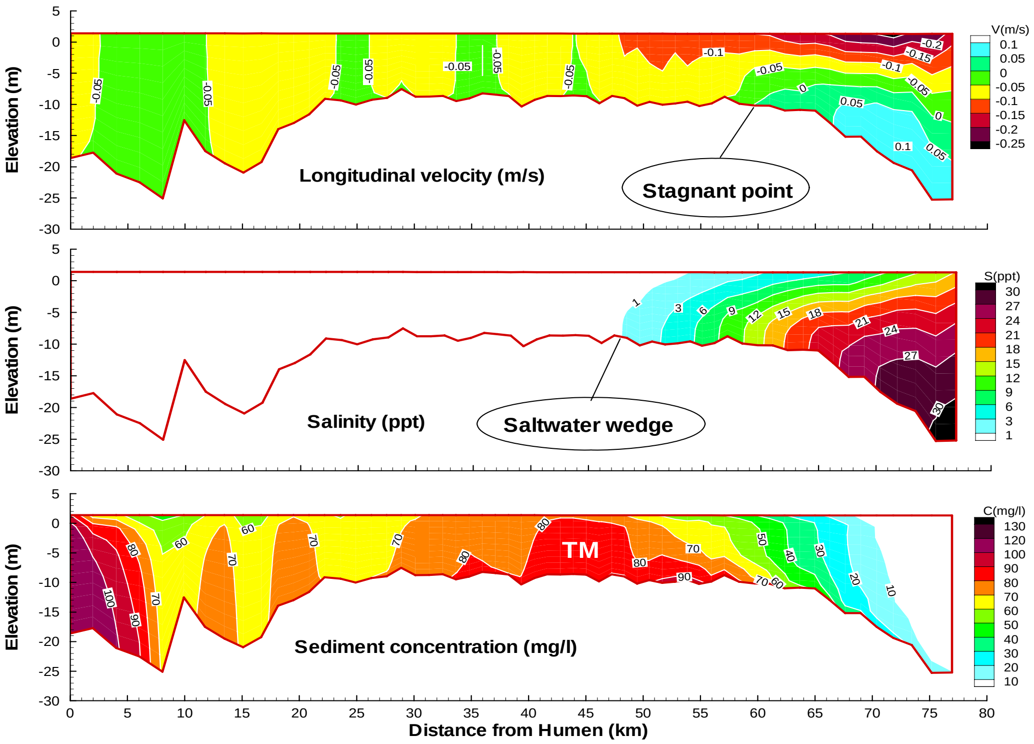

Fig. 6.5 Tidally-averaged profiles of flow, salinity and sediment concentration along the West Channel within a spring tide in the wet season

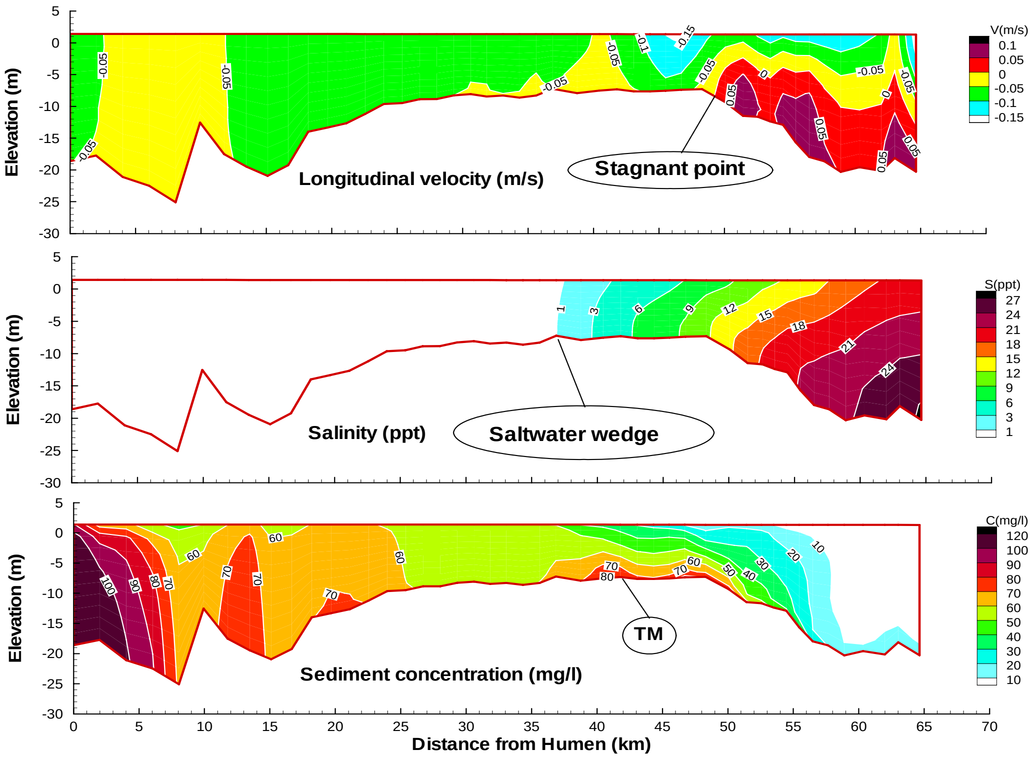

Fig. 6.6 Tidally-averaged profiles of flow, salinity and sediment concentration along the East Channel within a spring tide in the wet season

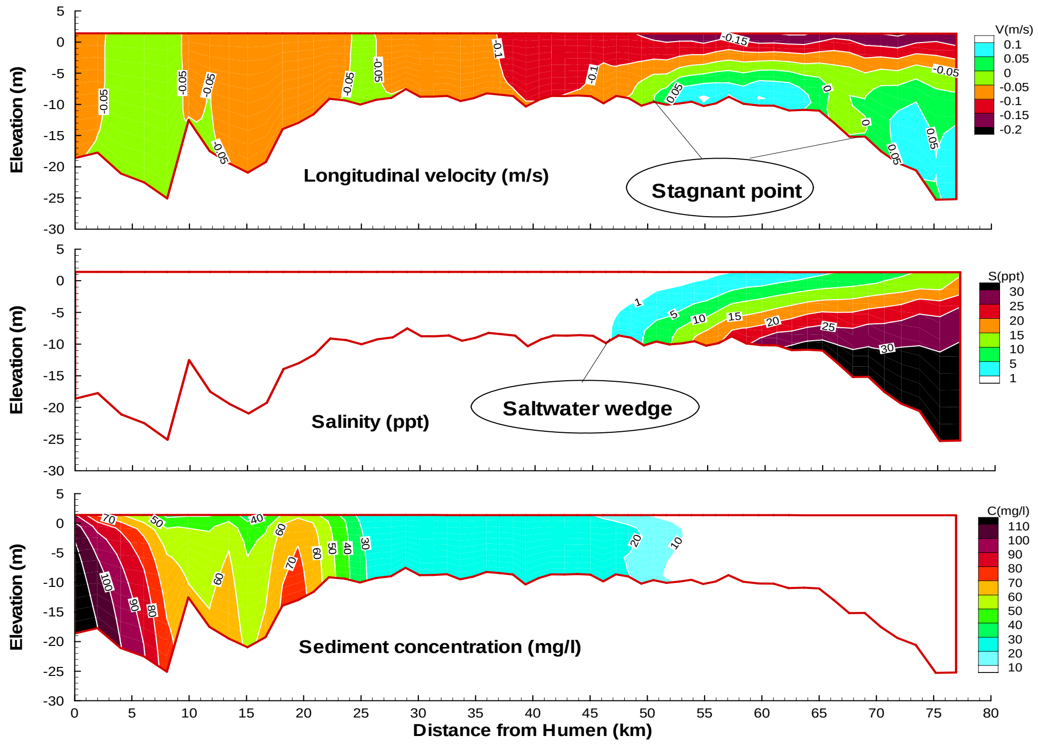

Fig. 6.7 Tidally-averaged profiles of flow, salinity and sediment concentration along the West Channel within a neap tide in the wet season

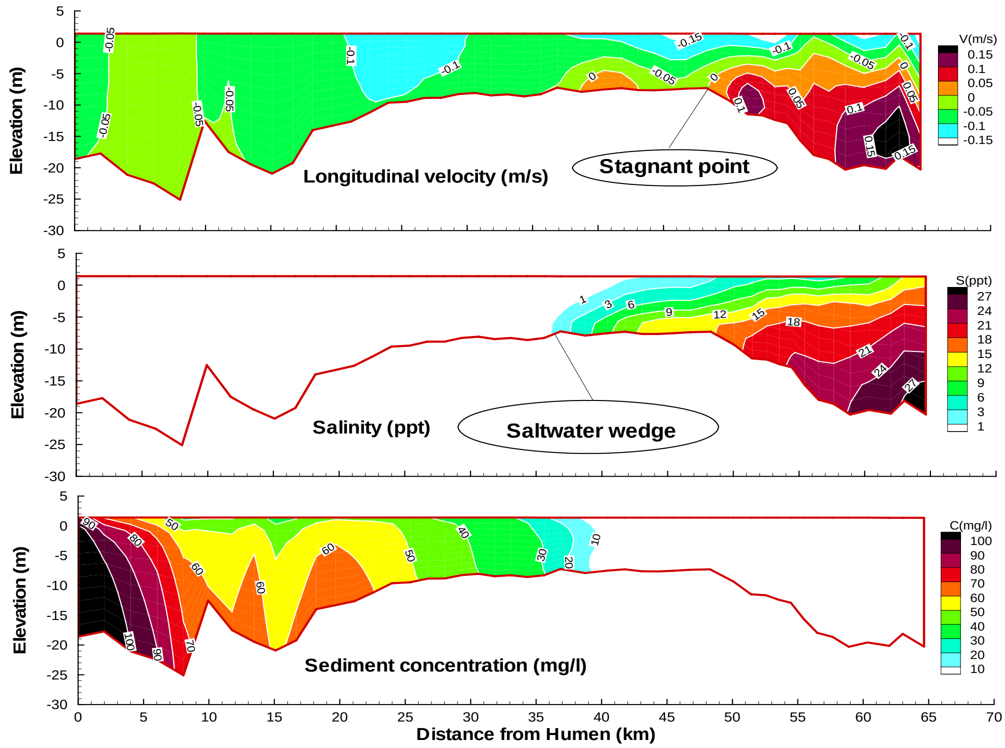

Fig. 6.8 Tidally-averaged profiles of flow, salinity and sediment concentration along the East Channel within a neap tide in the wet season

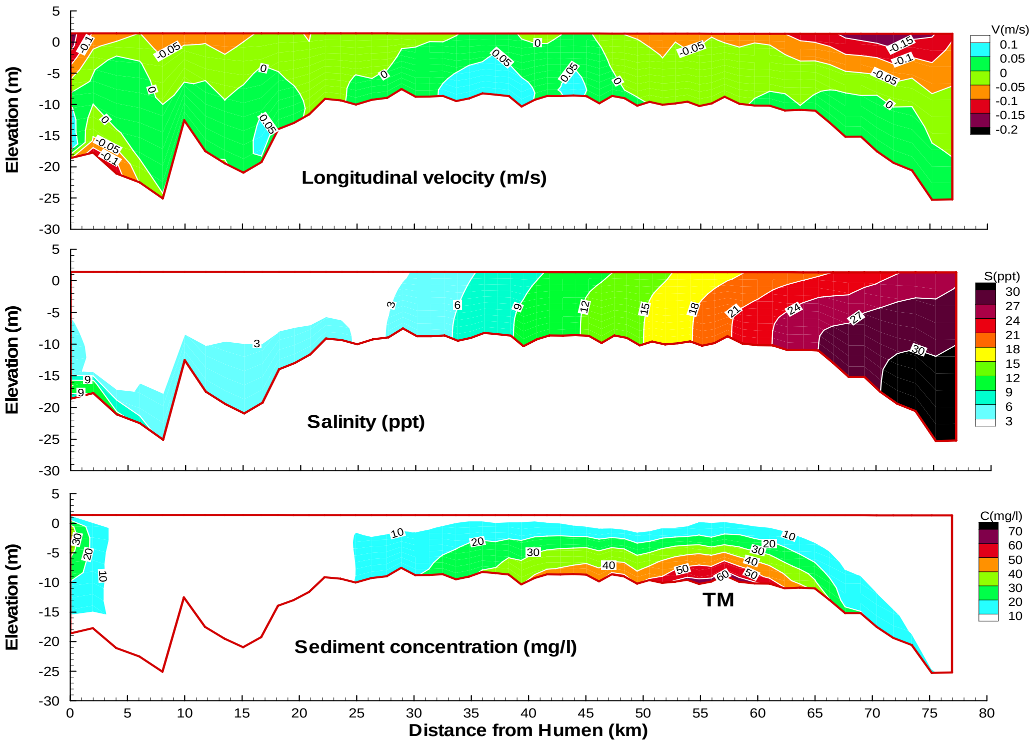

Fig. 6.9 Tidally-averaged profiles of flow, salinity and sediment concentration along the West Channel within a spring tide in the dry season

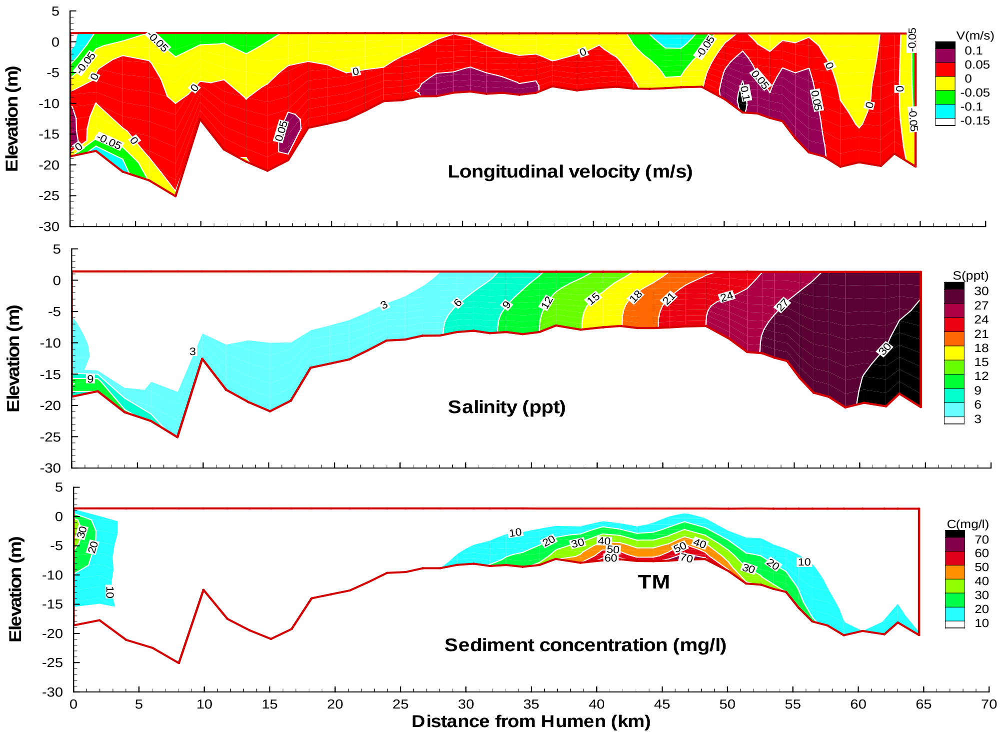

Fig. 6.10 Tidally-averaged profiles of flow, salinity and sediment concentration along the East Channel within a spring tide in the dry season

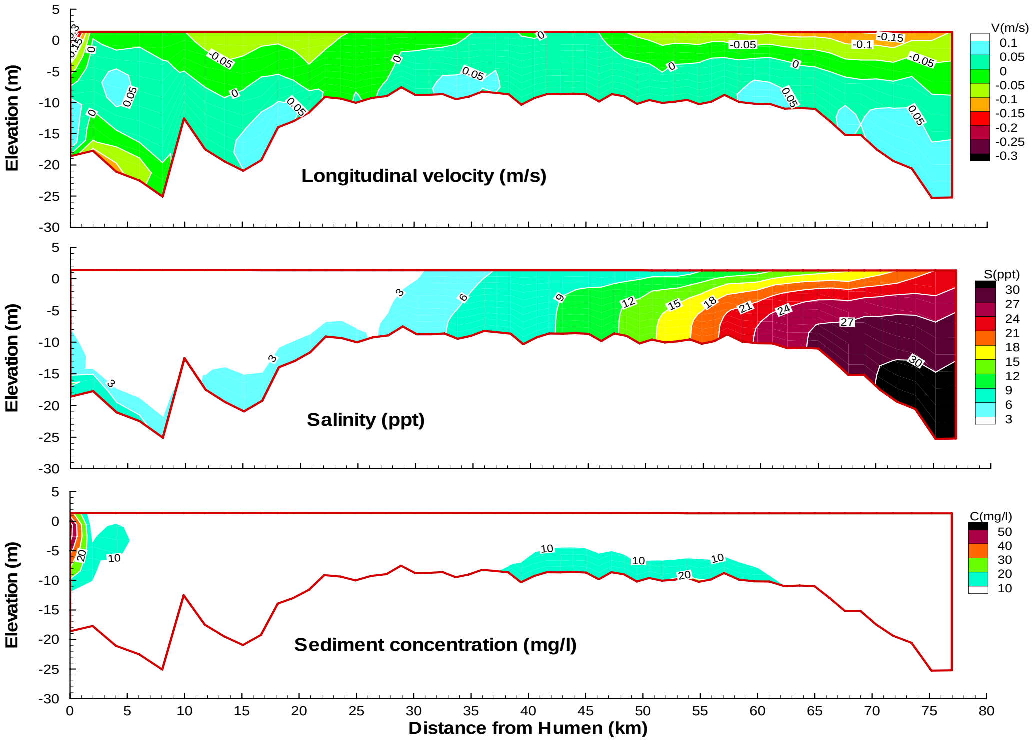

Fig. 6.11 Tidally-averaged profiles of flow, salinity and sediment concentration along the West Channel within a neap tide in the dry season

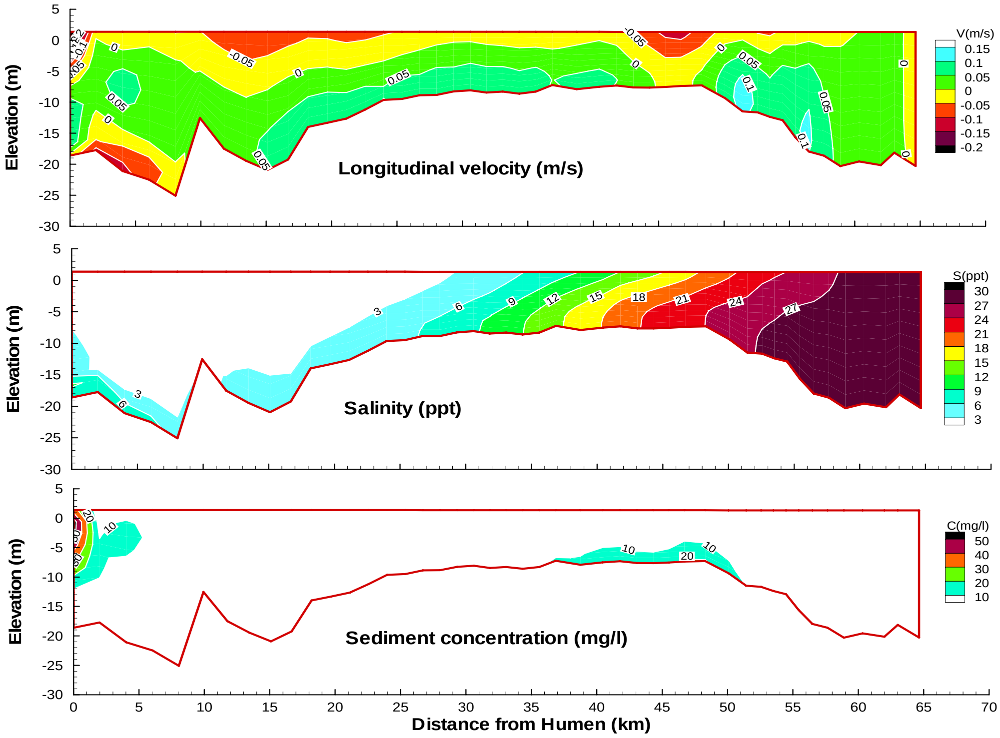

Fig. 6.12 Tidally-averaged profiles of flow, salinity and sediment concentration along the East Channel within a neap tide in the dry season

Fig. 6.13 Tidally averaged sediment concentration contours in a spring tide in the wet season under the conditions of 1.5 times mean seasonal flow rates (solid lines) and mean seasonal flow rate (dots)

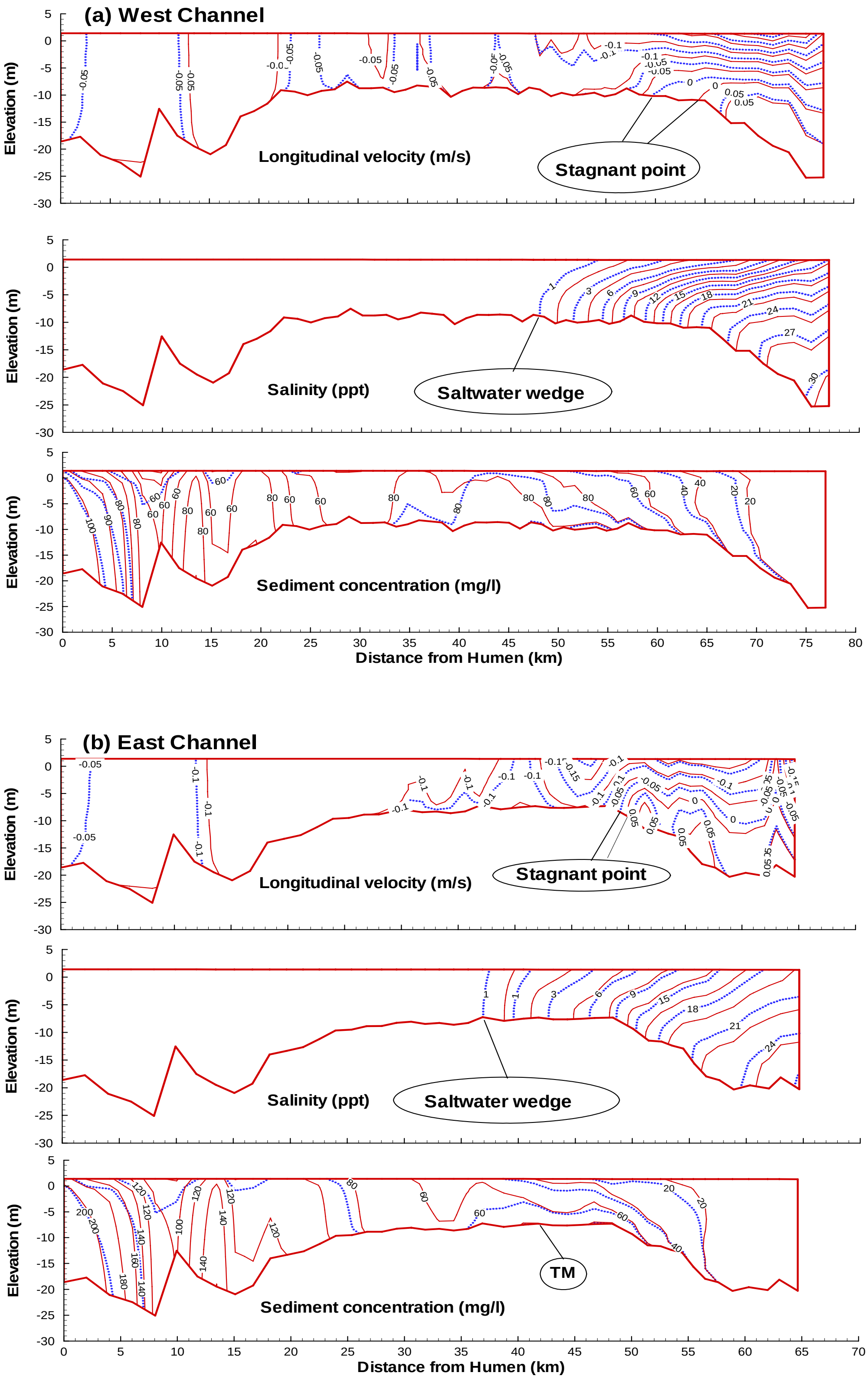

Fig. 6.14 Tidally-averaged profiles along main channels in a spring tide in the wet season under the conditions of 1.5 times mean seasonal flow rates (solid lines) and mean seasonal flow rate (dots)

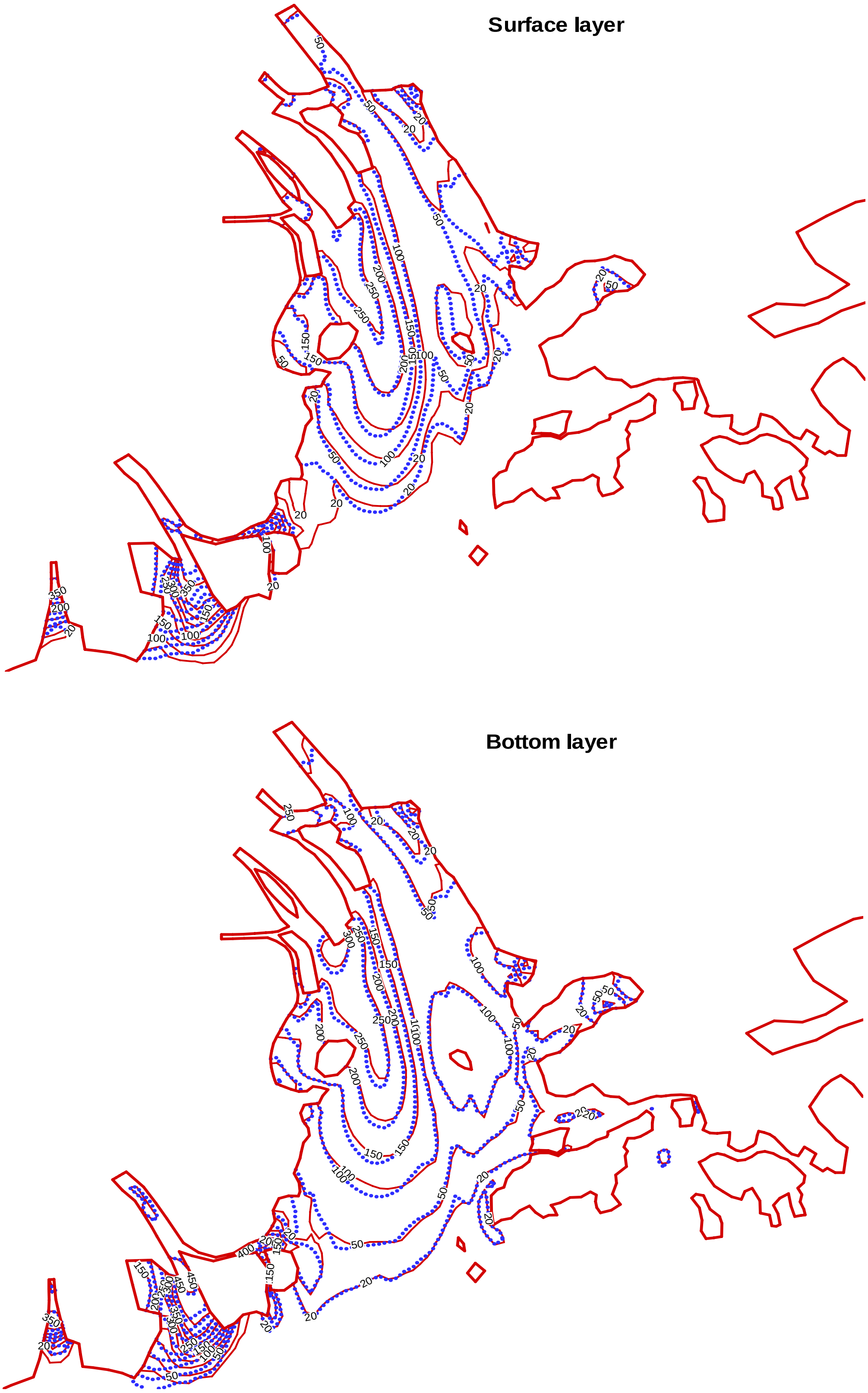

Fig. 6.15 Tidally averaged sediment concentration contours in a spring tide in the wet season with (solid lines) and without (dots) considering wind (5m/s from south)

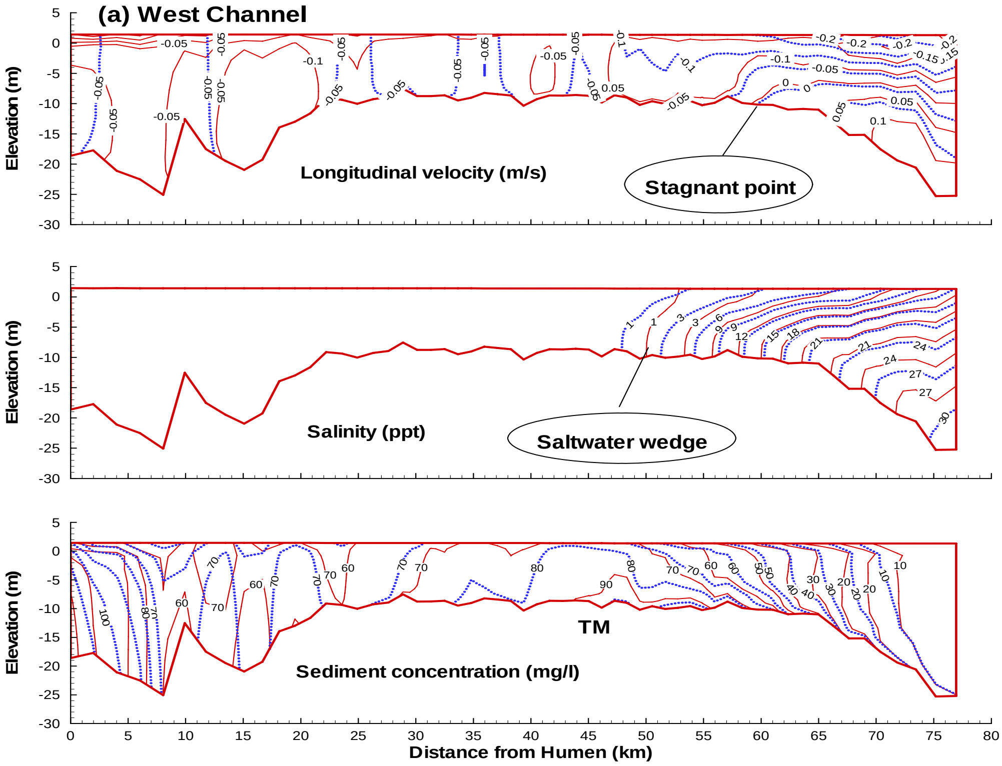

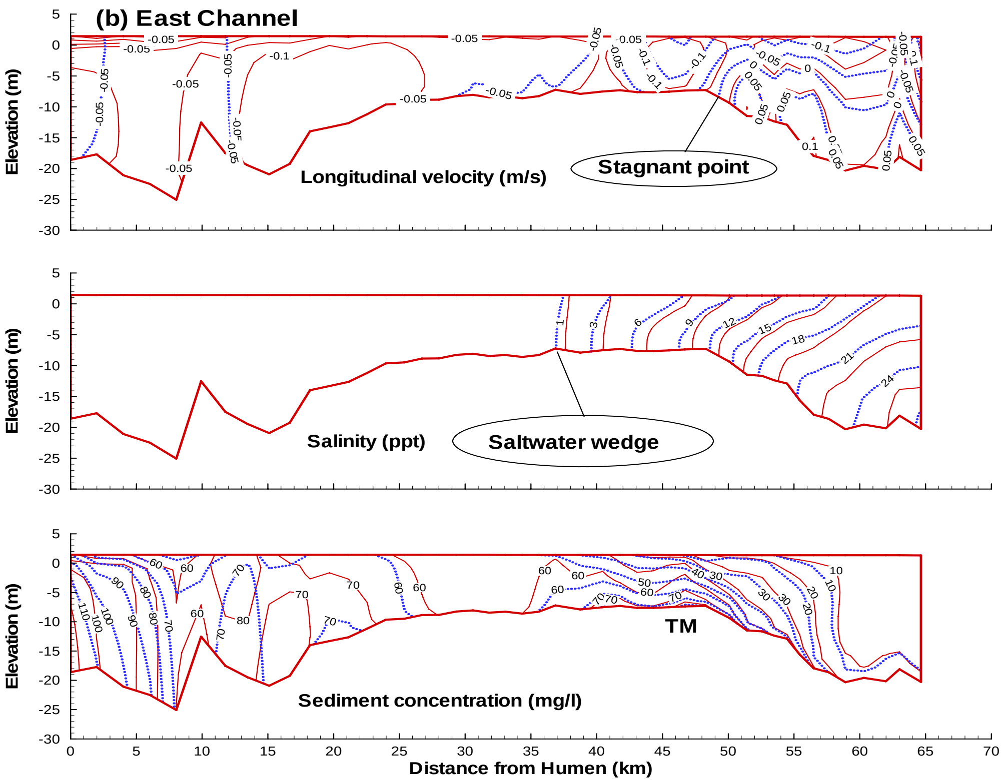

Fig. 6.16 Tidally-averaged profiles along main channels within a spring tide in the wet season with (solid lines) and without (dots) considering wind (5m/s from south)

Fig. 6.17 Tidally averaged sediment concentration contours within a spring tide in the wet season with (solid lines) and without (dots) considering wind (10m/s from south)

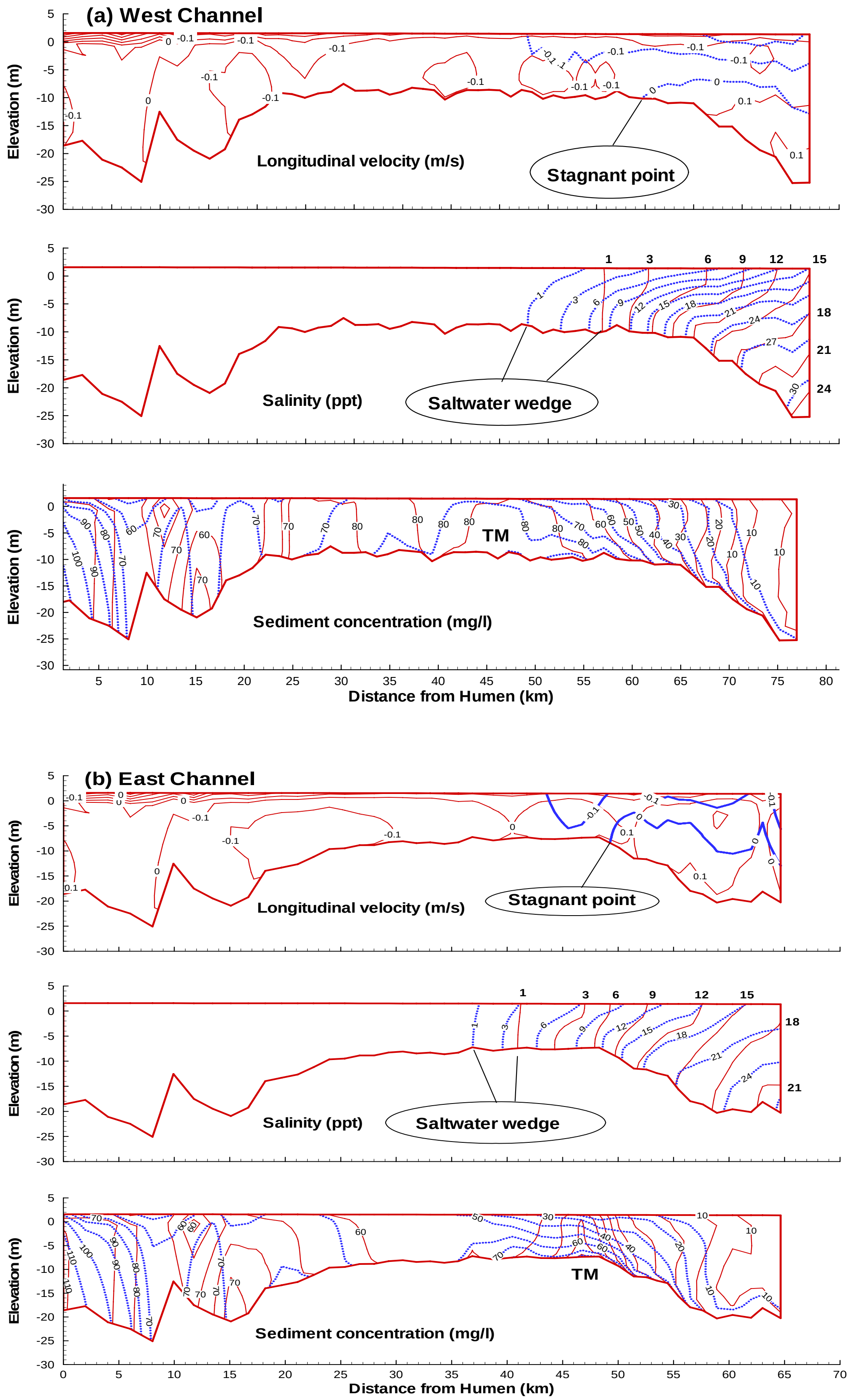

Fig. 6.18 Tidally-averaged profiles along main channels within a spring tide in the wet season with (solid lines) and without (dots) considering wind (10m/s from south)

CHAPTER 7

MODELLING OF WAVE-CURRENT INDUCED TURBIDITY MAXIMUM IN THE PEARL RIVER ESTUARY

7.1 General remarks

Waves always exist in coastal areas. They play an important role in stirring up sediments from the sea bed, as well as giving rise to other motions such as longshore currents and rip currents. The ambient wave conditions must be determined before the sediment transport in large coastal areas can be simulated.

Chen (2001) developed a wave propagation model and successfully applied his model to simulate the wave propagation to the PRE from the open sea. Chen's model is based on the wave action conservation theory and incident and perfectly absorbing wave boundary conditions are imposed on the open sea boundary and land boundary, respectively. The model focuses on the wave propagation in a large-scale domain, taking into account wave refraction and diffraction. However, the model does not consider wave breaking and wave reflection.

The wave propagation model has been validated by Chen (2001) with laboratory data, analytical solutions and field data, which include wave diffraction by a semi-finite breakwater (Wiegel, 1962), wave propagation over a circular shoal (Ito and Tanimoto, 1972) and an elliptic shoal (Berkhoff *et al.*, 1982), and wave propagation in the PRE. Reasonable results were obtained in all cases.

In this chapter, the wave propagation model developed by Chen (2001) was employed and coupled with the three-dimensional hydrodynamic and sediment transport model described in Chapter 5 to study the sediment transport and turbidity maximum in the Pearl River Estuary with wave-current interaction.

The objectives of this chapter are:

1) To couple the 3D hydrodynamics model with the wave model.

2) To study the characteristics of wave propagation in the Pearl River Estuary.

3) To discuss the effect of the wave-current interaction on flow velocity, salinity and sediment concentration in the Pearl River Estuary.

4) To study the effect of wave-current interaction on turbidity maximum in the main channels.

7.2 Wave prorogation model (Chen, 2001)

7.2.1 Wave action conservation equations

The problem of gravity surface wave propagation with wave refraction and diffraction on non-uniform current and bottom friction can be described by the following set of four equations.

a. Irrotationality of wave number vector:

$$\frac{\partial(K \cdot \sin\alpha_w)}{\partial x} - \frac{\partial(K \cdot \cos\alpha_w)}{\partial y} = 0 \tag{7.1}$$

where K is the modified wave number; α_w is the wave propagation direction; and x, y are the Cartesian coordinates.

b. Dispersion relation:

$$[\omega - K \cdot U\cos(\alpha_w - \alpha_c)]^2 = gk \cdot \tanh(k \cdot h) - \frac{1}{4}W^{*2} \tag{7.2}$$

where U is the current velocity; α_c is the current direction; k is the wave number; h is the water depth; ω is the wave angular frequency; g is the acceleration of gravity; and W^* is the bottom friction coefficient, $W^* = \frac{4 f_w H}{3\pi g}\left[\frac{\omega}{\sinh(kh)}\right]^3$, H is the wave height, and f_w is the wave friction factor.

c. Wave action conservation:

$$\frac{\partial A}{\partial t} + \frac{\partial}{\partial x}\left[A\left(\bar{u} + \frac{cc_g}{\omega_r}K\cos\alpha_w\right)\right] + \frac{\partial}{\partial y}\left[A\left(\bar{v} + \frac{cc_g}{\omega_r}K\sin\alpha_w\right)\right] = -W^* \cdot A \tag{7.3}$$

where A is the wave action, $A = \frac{\omega R^2}{2}$, $R = \frac{H}{2\omega}$, H is the wave height; $\bar{u}$ and $\bar{v}$ is the depth-averaged current velocity in the x and y directions, respectively; c is the wave speed; and c_g is the wave group speed; and t is the time.

d. Wave eikonal equation

$$
\begin{aligned}
K^2 = k^2 - \frac{1}{cc_g R}\left[\frac{\partial^2 R}{\partial t^2} + \frac{\partial W^* R}{\partial t} + 2\bar{u}\frac{\partial}{\partial t}\left(\frac{\partial R}{\partial x}\right) + 2\bar{v}\frac{\partial}{\partial t}\left(\frac{\partial R}{\partial y}\right) + \frac{\partial R}{\partial x}\frac{\partial \bar{u}}{\partial t} + \frac{\partial R}{\partial y}\frac{\partial \bar{v}}{\partial t}\right] \\
+ \frac{1}{cc_g R}\left[\frac{\partial}{\partial x}\left(cc_g \frac{\partial R}{\partial x}\right) + \frac{\partial}{\partial y}\left(cc_g \frac{\partial R}{\partial y}\right)\right] \\
- \frac{1}{cc_g R}\left[\frac{\partial}{\partial x}\left(\bar{u}^2 \frac{\partial R}{\partial x} + \overline{uv}\frac{\partial R}{\partial y}\right) + \frac{\partial}{\partial y}\left(\overline{uv}\frac{\partial R}{\partial x} + \bar{v}^2 \frac{\partial R}{\partial y}\right) + \frac{W^{*2}}{4}R\right]
\end{aligned}
\tag{7.4}
$$

7.2.2 Boundary conditions

The conditions at the boundaries enclosing the computational domain must be specified to completely define the problem. Two kinds of boundaries, namely, the incident wave boundaries and absorbing boundaries that absorb all wave energy arriving are considered. Generally, the incident wave boundary is the deepwater wave condition or the measured wave condition at the open boundary and the absorbing boundary is the land boundary.

The wave energy arriving at absorbing boundaries from the fluid domain must be absorbed perfectly. The treatment of this kind of boundary is difficult in numerical modelling. The most commonly used method is the Sommerfeld radiation condition which can be written as:

$$H_t + C_x H_x = 0 \quad \text{and} \quad H_t + C_y H_y = 0 \tag{7.5}$$

where C_x and C_y are the phase speeds along the x and y directions, respectively. In the actual computation, it is difficult to obtain the exact phase speeds and hence, the boundary can still reflect some wave energy.

To eliminate the boundary reflections, a 'sponge' layer proposed by Larsen and Dancy (1983) is placed in front of an absorbing boundary to absorb the incoming wave energy. On the sponge layer, the wave height is divided by a factor, $\mu(x,y)$, after each step. The factor $\mu(x,y)$ takes the following form after extending the one-dimensional form given by Larsen and Dancy (1983) to two dimensions (Li *et al.*, 1999).

$$\mu(x,y) = \begin{cases} \exp\left[\left(2^{-d/\Delta d} - 2^{-d_s/\Delta d}\right)\ln\alpha\right] & 0 \le d \le d_s \\ 1 & d_s < d \end{cases} \tag{7.6}$$

in which d is the distance between the 'sponge' layer and the boundary; Δd is the typical dimension of the elements; d_s is the sponge layer thickness, usually equal to one to two wave lengths and α is a constant to be specified.

7.2.3 Splitting of wave action equation

To increase the numerical stability, an operator splitting method is applied to the wave action Eq. 7.3. A time step is divided into two sub-steps in which the first step is for the advective terms and the second step is for other terms.

In the first sub-step, the advective term is discretized by using an Eulerian-Lagrangian method to increase the numerical stability. The equation in this sub-step is given as:

$$\frac{A^{n+\frac{1}{2}} - A^n}{\Delta t} + \left[\left(\bar{u} + \frac{cc_g}{\omega}\cdot K\cdot\cos\alpha_w\right)\frac{\partial A}{\partial x}\right]^n + \left[\left(\bar{v} + \frac{cc_g}{\omega}\cdot K\cdot\sin\alpha_w\right)\frac{\partial A}{\partial y}\right]^n = 0 \tag{7.7}$$

in which Δt is the time step.

In the second sub-step, the other terms in the wave action equation are calculated using the implicit finite element method. The equation to be solved in this sub-step is:

$$\frac{A^n - A^{n+\frac{1}{2}}}{\Delta t} + A^{n+1} \cdot \left(\overline{u} + \frac{cc_g}{\omega} \cdot K \cdot \cos\alpha_w \right)^{n+\frac{1}{2}} + A^{n+1} \cdot \left(\overline{v} + \frac{cc_g}{\omega} \cdot K \cdot \sin\alpha_w \right)^{n+\frac{1}{2}} = \left(-W^* A\right)^{n+1} \tag{7.8}$$

7.2.4 Numerical scheme and solution procedure

Temporal and spatial solution schemes for the wave action equation are as described in Chapter 5. The time integration of the wave action is performed in two sequential stages, the first stage solves the advective terms and the second stage is for solving the other terms.

To solve the wave number equation for the wave direction, a finite node method (FND) was introduced by Chen (2001) to discretize the equation spatially. To increase the stability in solving the highly non-linear equation, a nominal (or fictitious) temporal derivative term was added to the equation by Chen (2001), transforming Eq. 7.1 to the following form:

$$\frac{\partial \alpha_w}{\partial t'} + \frac{\partial (K \cdot \sin\alpha_w)}{\partial x} - \frac{\partial (K \cdot \cos\alpha_w)}{\partial y} = 0 \tag{7.9}$$

The computation procedure starts from the seaward boundaries in which Eq. 7.1 is first solved for α_w by assuming an initial value of the modified wave number K. Using the values of α_w and K, Eq. 7.2 is then solved for the wave number k. After that, Eq. 7.7 and Eq. 7.8 are solved in two sub-steps to obtain the wave height H. With the known values of the wave direction and wave height, the values of K are updated using Eq. 7.4. The procedure is repeated until convergence is achieved.

7.2.5 Combined wave-current bottom shear stress

One of the important effects of wave on current is the modification of the flow structure, affected through the combined wave-current shear stress. Soulsby's (1993) formulae are used in the model to describe the combined wave-current bottom shear stress.

$$\tau_m = \tau_c \left[1.0 + b \left(\frac{\tau_c}{\tau_c + \tau_w} \right)^p \left(\frac{\tau_w}{\tau_c + \tau_w} \right)^q \right] \tag{7.10}$$

$$\tau_{\max} = \left(\tau_c + \tau_w \right) \left[1.0 + a \left(\frac{\tau_c}{\tau_c + \tau_w} \right)^m \left(\frac{\tau_w}{\tau_c + \tau_w} \right)^n \right] \tag{7.11}$$

where τ_m is the mean combined wave-current bottom shear stress; $\tau_{\max}$ is the maximum combined wave-current bottom shear stress; b, p, q, a, m and n are coefficients (Soulsby, 1997); and τ_c and τ_w are the bed shear stresses due to the current alone and wave alone, respectively.

The seabed shear stress by current is

$$\tau_c = C_c \rho U_c^2 \tag{7.12}$$

where C_c is the friction coefficient of current; ρ is the water density and U_c is the near bed current-induced flow velocity.

The seabed shear stress by wave is

$$\tau_w = \frac{1}{2}\rho f_w U_w^2 \tag{7.13}$$

where f_w is the friction coefficient of wave, and U_w is the near-bed wave orbital velocity amplitude.

7.2.6 Wave-current coupling procedure

Fig. 7.1 shows the flow chart of computational procedures of the 3D wave-current model. The procedure for the implementation of the synchronous coupling of the wave model with the hydrodynamics model is as follows:

1) Assume initial values of tidal level and waves at whole element nodes.

2) The 3D hydrodynamics model is run to obtain the tidal current velocity, current direction and tidal levels.

3) The wave model is employed to obtain the distributions of wave heights and wave directions. The wave is coupled with the tidal current through the depth-averaged current velocities and their directions.

4) The bottom shear stresses under the interactions of wave and current are calculated. The turbulence model is employed to obtain the vertical eddy viscosity coefficients taking into account the interaction of waves and currents.

5) The 3D hydrodynamics model is run to obtain the tidal current taking into account the interaction of waves and currents.

6) Repeat steps (3) to (5) to obtain updated tidal current values and wave values for the next time step.

7.3 Characteristics of wave in the PRE

According to a one-year wave record collected by the Civil Engineering Department of the Hong Kong Government at Wanshan Islands from October 1991 to September 1992, the percentage of swell is estimated to be about 97.2%. The most frequent waves are from the SE and ESE directions. The percentage of wave heights between 0.5 m and 1.5 m is 75.8%.

In the 1998 summer survey, besides the hydrodynamics and water quality measurements, 14-day continuous wave data were also collected at station 7, west to Lantau Islands (see Fig. 5.3), starting from July 6. Fig. 7.2 shows the measured wave height, wave direction and wave period at station 7. The maximum wave height is 1.18 m and the maximum significant wave height is 0.70 m. The wave period is from 3.4 s to 5.3 s and the average wave period is 3.84 s in this survey.

7.4 Wave propagation in quiescent water

To demonstrate the stability of the wave model and to estimate the approximate computer time required to simulate wave propagation from the boundary in the open sea, a pure wave propagating in quiescent water was modelled. Waves of significant wave height 1.5 m, wave period 3.8 s and incoming from the SE were specified as the incident wave conditions at the open sea boundary and an approximate wave height distribution in the computational domain was used as the initial condition.

Fig. 7.3 shows the development of wave height with time at different stations. It can be seen that the stability of the wave model is very good. The waves from open sea propagate to the Lantau Channel after about 24 hours, to the middle reach of the PRE after about 32 hours, and to Humen after about 44 hours. This suggests that a warm up time of about 2 days is needed if the wave model is run from a cold start.

Fig. 7.4 and Fig. 7.5 show the wave heights and directions in the Hong Kong Waters and the Pearl River Estuary, respectively, at the equilibrium state. In these figures, the contours represent the wave heights and arrows give both the wave heights and wave directions. It can be seen from the figures that the wave height in the open sea is relatively uniform. Due to the existence of numerous islands and complex coastlines, refraction and diffractions occur when waves impinge on the obstacles or the irregular land boundaries. The sheltering effects from the two larger islands, Hong Kong Island and Lantau Island, are significant. The wave heights behind them are reduced markedly. The wave heights in the Victoria Harbour are very small, about 0.2 m. This indicates that it is difficult for waves from the open sea to propagate into Victoria Harbour, where waves will be predominantly local wind-induced. The wave heights behind Lantau Island are about 0.2 to 0.4 m because of sheltering.

When waves propagate into the Pearl River Estuary, the shoaling and sheltering effects of islands dissipate the wave energy gradually. Consequently, the wave height diminishes gradually from around 1.4 m near the Waglan Island to about 0.1 m at Humen. The computed wave heights at different stations are listed in Table 7.1.

Table 7.1 Computed wave heights in quiescent water
(Incident wave: H_s =1.5 m, T_s =3.8 s, from SE)

Station	Wave height(m)	Station	Wave height(m)	Station	Wave height (m)
1	0.103	5	0.668	9	1.350
2	0.362	6	0.410	14	0.476
3	0.282	7	0.637	15	0.112
4	0.604	8	1.308	16	0.131

7.5 Combined current and wave modelling

The aim of this chapter is to simulate the sediment transport under the interaction of wave and current. So it is necessary to specify the wave boundary conditions in addition to the hydrodynamic boundary conditions.

The simulation period is the wet season of 1998, which is the same as the period chosen for the 3D hydrodynamics modelling described in Chapter 5. Hence the same hydrodynamics and sediment boundary conditions are specified at the open boundaries.

Table 7.2 Scenarios of combined wave-current modelling

Scenarios	Tidal conditions	Wave conditions		
		Height (m)	Period (s)	Direction
1	Spring tide	1.5	3.8	SE
2	Spring tide	1.5	3.8	S
3	Spring tide	1.5	3.8	SW
4	Spring tide	2.5	3.8	S
5	Spring tide	2.5	8.0	S
6	Neap tide	1.5	3.8	S
7	Neap tide	2.5	3.8	S

Table 7.2 lists the modelling scenarios with different incident wave conditions applied in the open sea boundary. The same incident wave conditions used in the wave propagation modelling in quiescent water with wave height of 1.5m and wave period of 3.8s incoming from the southeast (SE) are also used as the incident wave condition at the open sea boundary in scenario 1. Scenarios 2 and 3 consider incident waves from the south (S) and southwest (SW) with the same incident wave height and wave period as scenario 1 to study the effect of wave directions. In Scenario 4, the incident wave height is 2.5 m, but the incident wave period and wave direction are the same as in scenario 2. Scenario 5 is for studying the effect of wave period on wave pattern and sediment concentration in the PRE, in which the wave period is 8 s and the incident wave height and wave direction are the same as in scenario 4. Scenarios 6 and 7 with incident wave heights of 1.5 m and 2.5m, respectively, are used to study the effect of waves during a neap tide in the wet season. The incident wave period and wave direction are both 3.8 s and from the south in both scenarios.

The time step for wave propagation simulations is 60s. Wave-induced free surface setups are not considered in the modelling of coupled hydrodynamic and wave propagation processes.

7.5.1 Wave propagations over current

Fig. 7.6 to Fig. 7.10 show the tidally averaged wave heights and wave directions during a spring tide in the wet season of scenarios 1 to 5, respectively. Fig. 7.11 and Fig. 7.12 show the tidally averaged wave heights and wave directions during a neap tide in the wet season of scenarios 6 and 7, respectively. Table 7.3 and Table 7.4 list the tidally averaged wave heights and wave directions at different stations. From these figures and tables, we can see the effect of incident wave conditions on the distribution of wave height and the wave directions in the PRE in the presence of tidal currents.

Table 7.3 Computed tidally averaged wave heights at different stations

Stations	Wave height of each scenario						
	1	2	3	4	5	6	7
1	0.12	0.18	0.13	0.27	0.06	0.21	0.31
2	0.09	0.09	0.09	0.14	0.11	0.10	0.15
3	0.23	0.45	0.38	0.67	0.31	0.49	0.76
4	0.82	0.95	0.80	1.43	0.69	0.98	1.53
5	0.65	0.51	0.75	0.84	0.44	0.45	0.74
6	0.90	1.13	0.97	1.63	0.52	0.66	1.04
7	0.73	1.40	0.92	2.33	1.17	1.34	2.23
8	1.43	0.64	0.41	1.19	0.82	0.61	1.01
9	1.35	1.48	1.00	2.45	1.77	1.44	2.40
14	0.53	0.78	0.47	1.22	0.62	0.83	1.30
15	0.15	0.18	0.12	0.23	0.18	0.18	0.22
16	0.16	0.22	0.15	0.32	0.15	0.23	0.32

Wave height is in unit of m

Table 7.4 Computed tidally averaged wave direction at different stations

Stations	Wave direction of each scenario*						
	1	2	3	4	5	6	7
1	103	102	101	102	104	103	103
2	67	65	64	65	65	66	66
3	92	89	88	89	91	90	90
4	77	76	74	76	77	76	76
5	86	82	78	82	86	82	82
6	98	96	95	96	97	97	97
7	99	86	75	86	94	87	87
8	104	90	80	90	93	91	91
9	126	94	72	94	104	95	95
14	103	94	86	94	104	95	95
15	119	118	117	118	123	117	117
16	119	117	115	117	131	117	117

*Wave direction is in unit of deg, anticlockwise from the east

Comparing Fig. 7.7 with Fig. 7.6 and Fig. 7.8, it can be seen in general that the sheltering effect of islands on wave propagating is smallest if waves are coming from the south in the open sea compared with those from either the SE or the SW, especially in the shallow areas. Waves from the S direction propagate further upstream. The wave heights near Neilingding Islands are about 0.8 m, 0.4 m and 0.6 m for waves propagating from the S, SE and SW, respectively. The wave height at Humen is 0.18 m for waves incoming from the south in the open sea. The corresponding wave heights are 0.12 m and 0.13 m for waves from the SE and SW, respectively. Because of the effects of wave reflection and diffraction and shoaling, the contours of wave heights are inclined to the NE direction for waves propagating from the S or the SW in the open sea. However, if waves propagate from the SE, wave energy would tend to concentrate on the shallow waters in the west part of the PRE, resulting in the diminishing of wave heights generally comparing with those of the other two incoming directions, upon propagation into the PRE.

The effect on wave heights in the PRE due to the increase of the incident wave height can be seen by comparing Fig. 7.9 with Fig. 7.7. The increase of the wave height from 1.5 m to 2.5 m in the open sea incoming from the S will correspondingly increase the wave height by about 1 m, 0.4 m and 0.2 m at the entrance of the PRE, near Neilingding Island and at Humen, respectively.

Comparing Fig. 7.10 with Fig. 7.9, it can be seen clearly that an increase in the wave period results in the decrease of wave height. The wave height will reduce by about 0.7 m, 0.4 m and 0.2 m at the entrance of the PRE, near Neilingding Island and at Humen, respectively if the incident wave period increases from 3.8

to 8.0 s in the open sea for an incident wave height of 2.5 m and coming from the S.

It can be seen that the wave heights and directions propagating during a neap tide are in general similar to those propagating during a spring tide in most of the areas of the PRE by comparing Fig. 7.11 with Fig. 7.7 and Fig. 7.12 with Fig. 7.9. Large differences can only be found in the navigation waterways around Lantau Island, where a stronger ebbing current would result in larger wave heights during the spring tide.

Fig. 7.13 to Fig. 7.15 show the time series of wave heights and tidal levels of scenario 5 at the different stations during a spring tide in the wet season to show the interaction of waves and current in the PRE. Table 7.5 gives the minimum and maximum wave heights in the tidal cycle. The result indicates the significant effect of tidal level on the wave height in the PRE. The variations of wave height during the spring tide at these stations are from 0.078 m at station 2 to 0.547 m at station 13. At stations 5 and 7 to 10, located downstream of the estuary, the wave heights basically have a phase lag of a quarter of the tide period, which results in the increase of wave height during the ebbing current and decrease of wave height during the flooding current. The effect of the ebbing flow on waves is significant. At the stations near the river outlets, differences between phases of tidal level and wave height reduce. The high and low wave heights appear before the high tidal slack and low tidal slack respectively, by about 2 to 3 hours.

Table 7.5 Variations of wave heights within a spring tide (Scenario 5)

Station	Wave height (m)			Station	Wave height (m)		
	$H_{\min}$	$H_{\max}$	$H_{\max} - H_{\min}$		$H_{\min}$	$H_{\max}$	$H_{\max} - H_{\min}$
1	0.016	0.114	0.098	9	1.594	2.029	0.436
2	0.063	0.141	0.078	10	1.929	2.292	0.363
3	0.168	0.409	0.242	11	2.222	2.483	0.261
4	0.550	0.780	0.230	12	2.278	2.585	0.307
5	0.363	0.539	0.176	13	0.536	1.085	0.547
6	0.441	0.600	0.159	14	0.465	0.727	0.261
7	1.044	1.272	0.230	15	0.035	0.351	0.316
8	0.655	1.043	0.386	16	0.050	0.243	0.193

7.5.2 Effect of wave on saltwater intrusion

Fig. 7.16 compares the computed contours of tidally averaged salinity induced by the combined action of wave and current (Scenario 2) with those by current only. It can be seen that the saltwater contours have shifted downstream in the presence of waves, which increase the flow turbulence. The front (1 ppt contour) of saltwater intrusion retreats about 2.5 km along the East and West channels, and that in the Middle Shoal moves downstream to the Neilingding Island. Fig. 7.17 indicates the effect of waves on saltwater intrusion at the different stations. In the presence of waves, salinity at the bottom layer of station 2 reduces by about 5 ppt, and that at station 5 reduces by 1 to 10 ppt during tidal flooding and ebbing. At station 14, the maximum reduction is about 4 ppt. Saltwater hardly intrudes into station 3, which is located at the north corner of the Neilingding Island.

7.5.3 Effect of wave on sediment concentration

Using the same hydrodynamic conditions, we can compare the simulated sediment concentration distribution under the combined action of wave and current with that due to current only to shed light on the effect of wave on the sediment concentration in the Pearl River Estuary. From the analysis of wave propagation over quiescent water in the PRE, it is known that waves incoming from the south could propagate further upstream than those from other directions, therefore, the results of scenarios 2 and 4 are chosen to discuss the effect of waves on sediment concentration in the PRE. Fig. 7.18 and Fig. 7.19 compare the wave-current induced near bed sediment concentration with that of current only. Fig. 7.20 and Fig. 7.21 compare the time series of near bed sediment concentrations at different stations induced by wave and current and by current only. From these figures, we can see that the sediment concentrations in the bottom layer under the interaction of wave and current are in general larger than that induced by current only. The contours of sediment concentration move seaward and the concentration around Neilingding Island increases. However, the increase in sediment concentration is not very high, at most 10% except for a short duration in the tidal cycle at certain locations. Although the wave height in the south-eastern part of the estuary is relatively higher, the deeper water there weakens the sediment resuspension by the wave. On the West shoal, the interaction of wave and current increases the bottom layer sediment concentration by about 10-20 mg/l. In the other parts, the increase in sediment concentration in the presence of waves is less than 10 mg/l. On some isolated very shallow locations, wave could increase the sediment concentration by more than 30-50 mg/l.

It can also be seen that the differences of sediment concentrations between scenarios 2 and 4 are slight. Once the wave propagates into the PRE, especially upstream of Neilingding Island, due to the effects of bathymetry, shoaling and sheltering, the differences of wave heights in the up-estuary region are not very large between incident wave heights of 1.5m (scenario 2) and 2.5 m (Scenario 4), which result in the slight differences of sediment concentration.

7.5.4 Wave-current induced turbidity maximum

The turbidity maximum occurs in the Pearl River Estuary at shoals, where sediment particles are easily resuspended within tidal cycles, and at some downstream locations away from the river outlets, where congregation occurs when sediment particles are routed to the estuary.

To discuss the effect of wave on the turbidity maximum in the Pearl River Estuary, tidally averaged sediment concentration profiles along the East and West navigational channels within a spring tide in the wet season under the interaction of wave and current are compared with the profiles by tidal current only in Fig. 7.22 and Fig. 7.23, respectively. It can be seen that waves increase the sediment concentration on the sand bars of the main channels. With the water depth decreasing and the wave energy dissipating upstream of the bars, the effect of wave on sediment concentration beyond the sand bars is considerably weakened, and can be considered negligible. Waves have practically no influence on the location of turbidity maximum in the main channels. However, wave-current interaction would resuspend sediment particles to the upper water column, resulting in a thicker core and higher sediment concentration in the turbidity maximum. The increase of sediment concentration induced by the wave is more than 10 mg/l in the center of the turbidity maxima in the main channels.

Fig. 7.24 and Fig. 7.25 show the effect of the interaction of wave and current on the tidally averaged sediment concentration along the East and West channels within a neap tide. The results show that wave increases the sediment concentration in the neap tide, but we still can not find any turbidity maximum in the main channels during the neap tide. This implies that wave itself can not cause the formation of turbidity maximum. For low wave heights, tidal current is the dominant force that controls the sediment deposition and resuspension within tidal cycles. However, if the wave is strong enough, the wave and current interaction greatly increases the flow turbulence. As a result, stratification is easily destroyed and sediment particles eroded from the seabed will be resuspended uniformly along the water column, which makes the sediment particles difficult to be entrained to form the turbidity maximum.

7.6 Summary

In this chapter, a wave model was introduced to couple with the 3D hydrodynamics and sediment transport model. After analyzing the simulated results of wave propagation and sediment concentration taking into account the interaction of wave and current, the findings can be summarized as follows.

1) The coupled model can be applied efficiently to solve combined problems of wave propagation, hydrodynamics and sediment transport.

2) Waves propagating from the open sea would be attenuated significantly when they enter into the Pearl River Estuary, with their energy

dissipating due to sheltering by islands and the shallow water depth in the estuary.

3) Wave-current interaction increases the sediment concentration in the Pearl River Estuary mainly in the sand bars and shoals.

4) Wave-current action resuspends sediment particles to the upper water column, resulting in a broader and thicker turbidity maximum with higher sediment concentration.

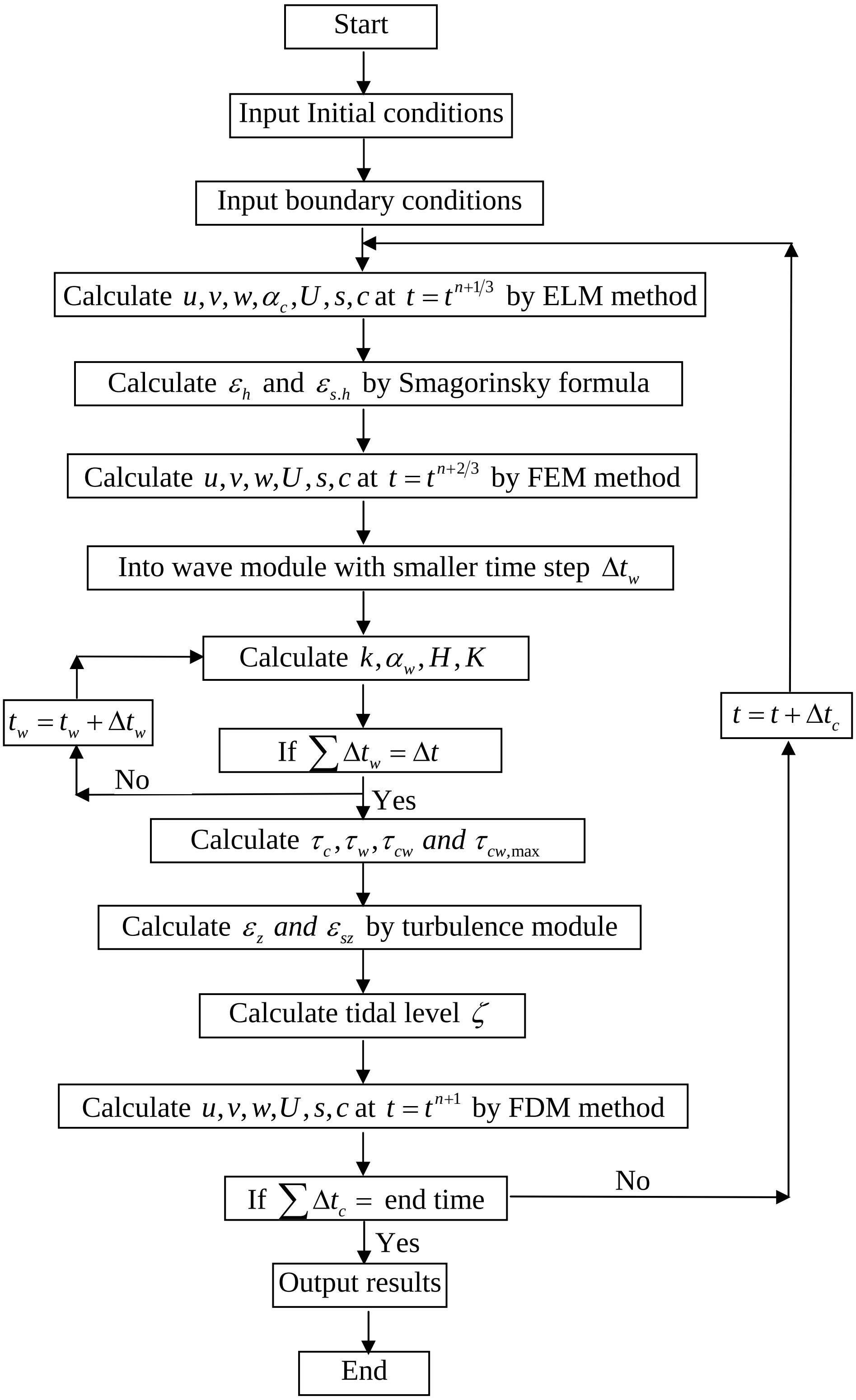

Fig. 7.1 Flow chart of wave-current modelling

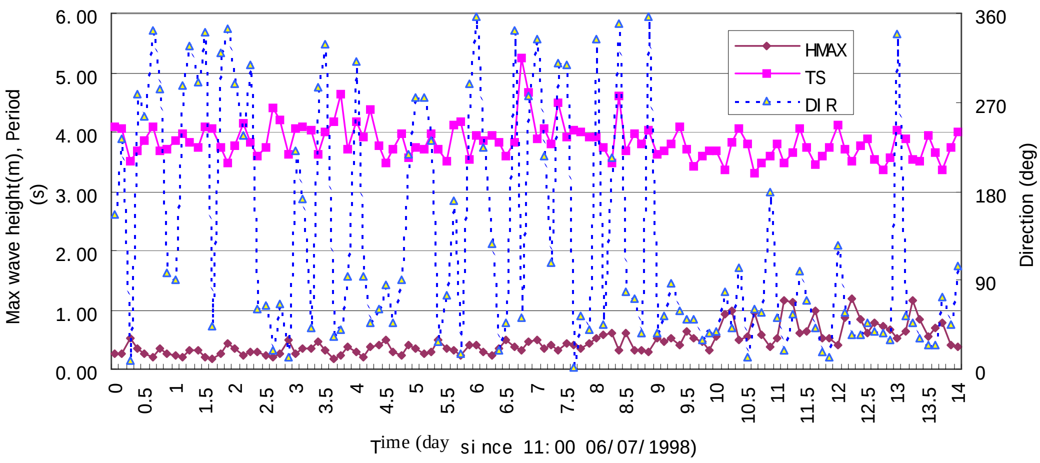

Fig. 7.2 Measured wave height, direction and period at station 7

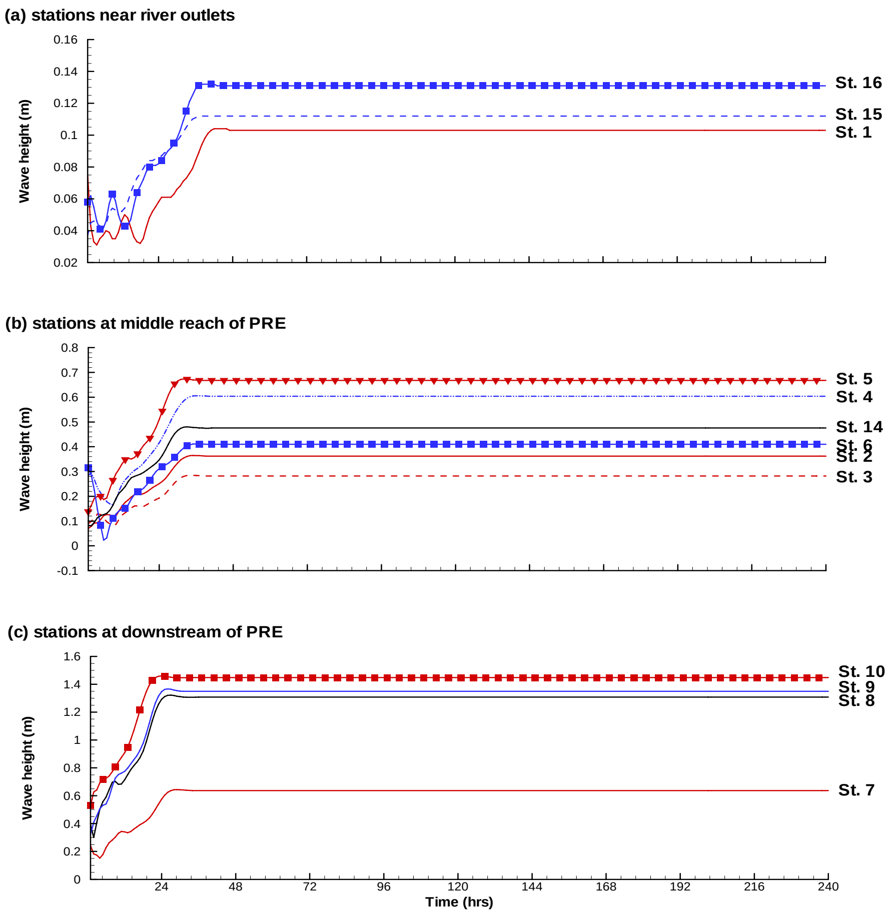

Fig. 7.3 Development of wave height with time in quiescent water at different stations

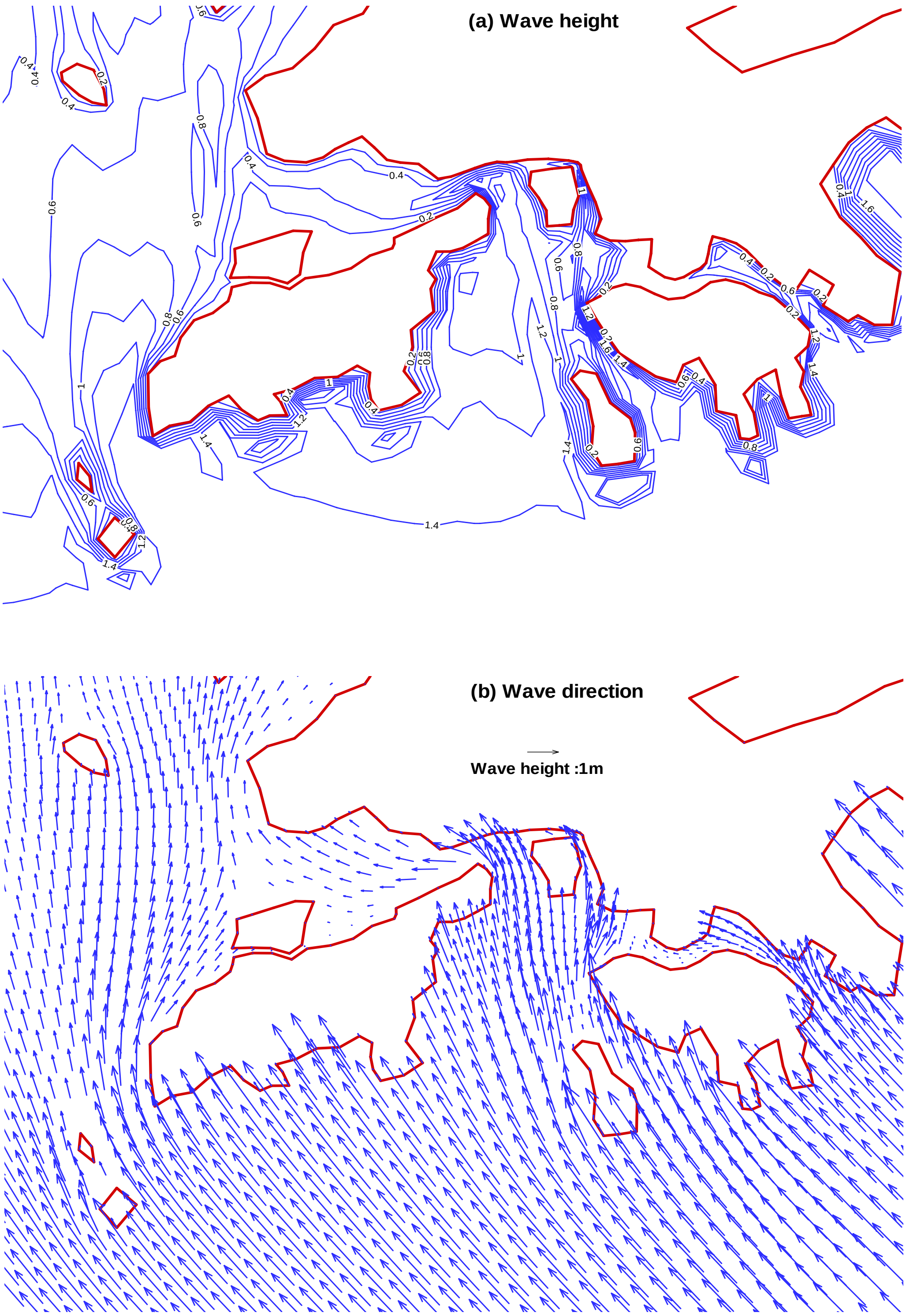

Fig. 7.4 Simulated wave heights and directions in quiescent water in Hong Kong waters (incident wave conditions: H_s =1.5 m, T_s =3.8 s, from SE)

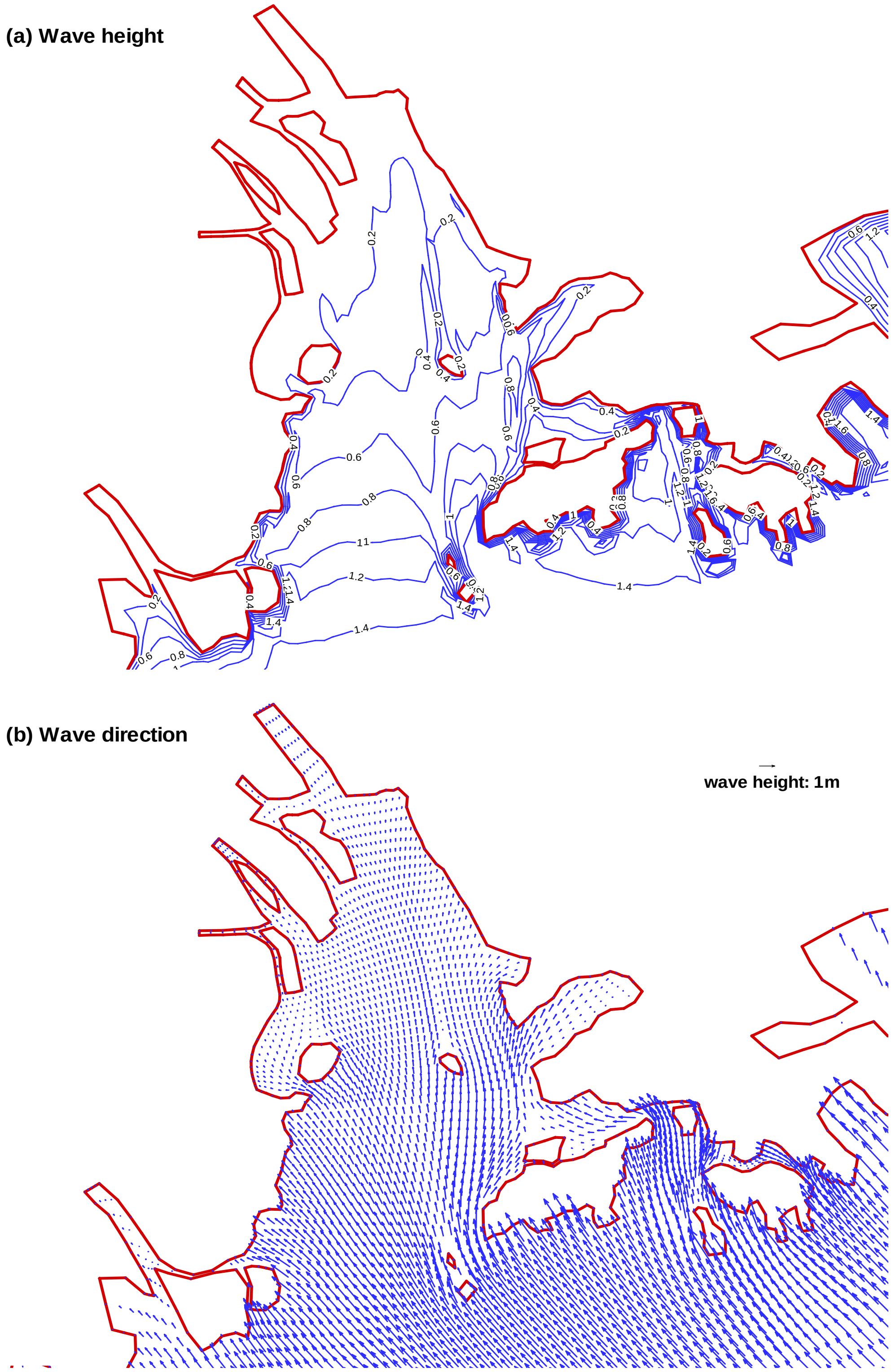

Fig. 7.5 Simulated wave heights and directions in quiescent water
(Incident wave conditions: H_s =1.5 m, T_s =3.8 s, from SE)

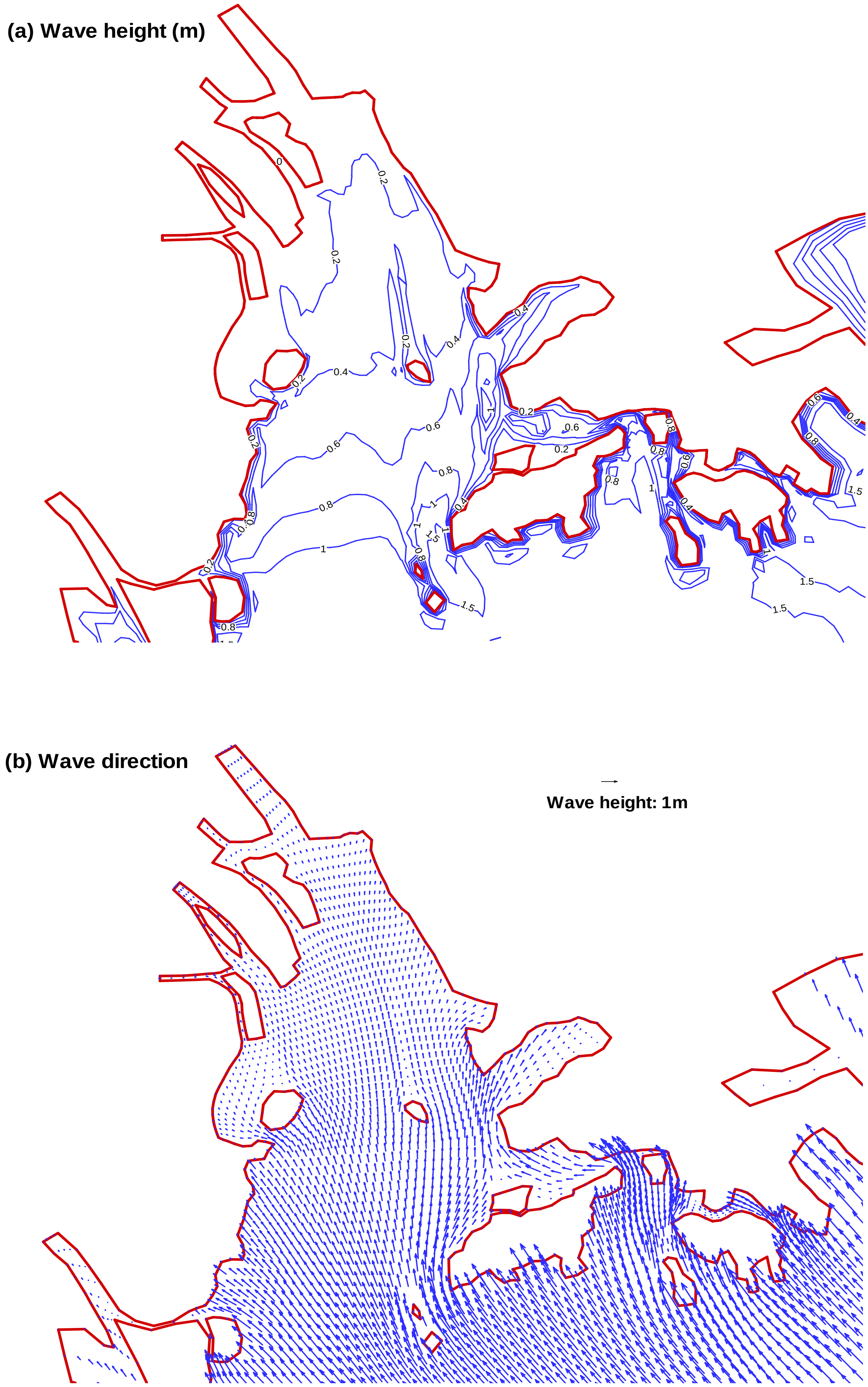

Fig. 7.6 Simulated wave heights and directions of Scenario 1
(Wet season, spring tide, H_s =1.5 m, T_s =3.8 s, from SE)

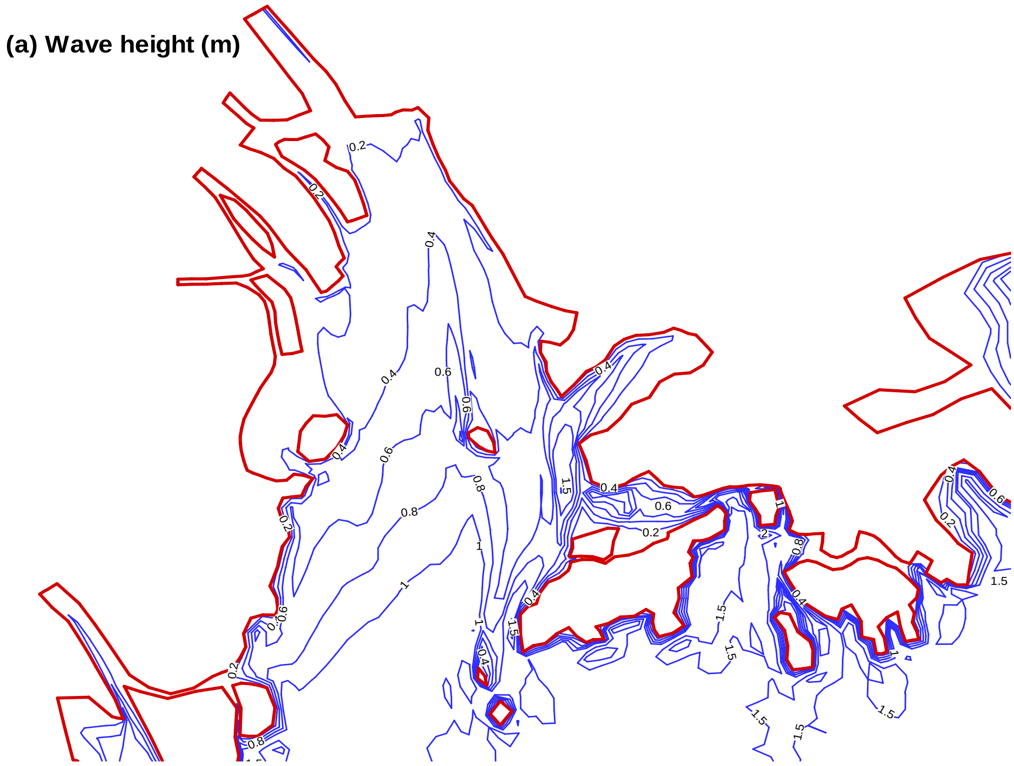

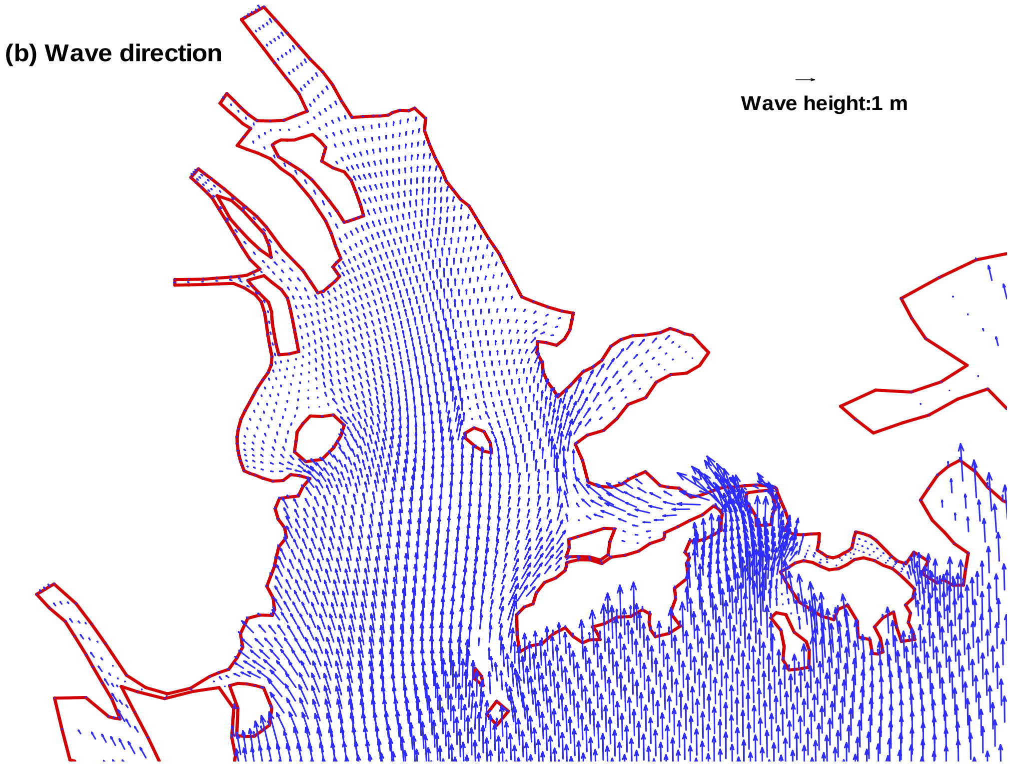

Fig. 7.7 Simulated wave heights and directions of Scenario 2
(Wet season, spring tide, H_s =1.5 m, T_s =3.8 s, from S)

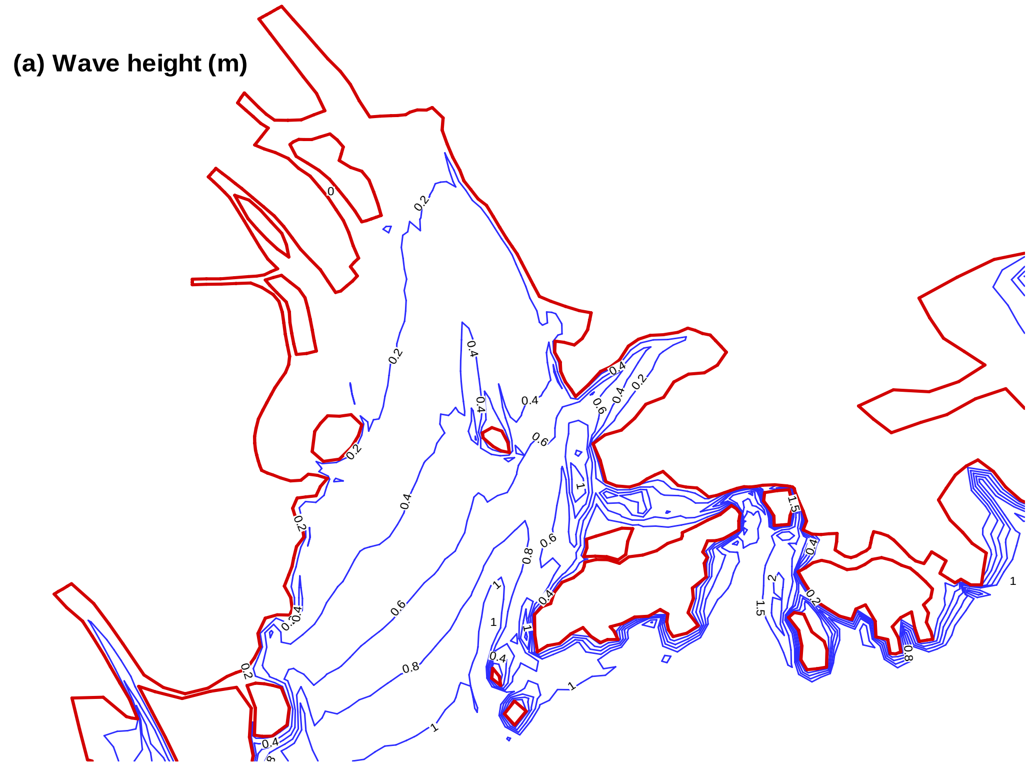

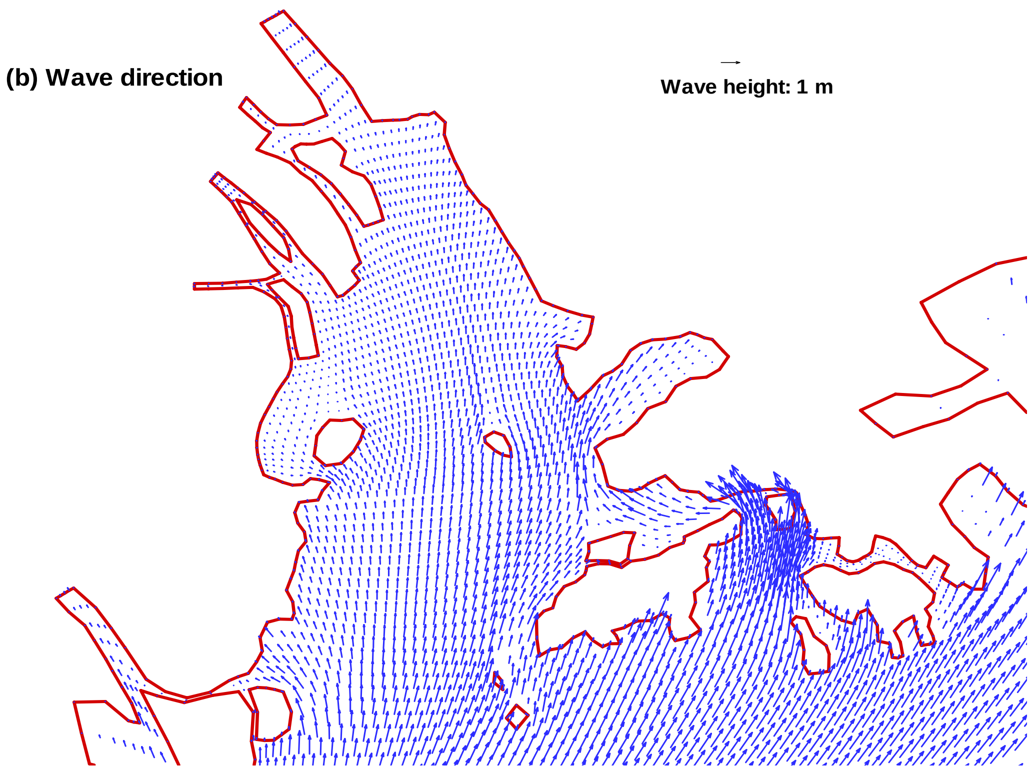

Fig. 7.8 Simulated wave heights and directions of Scenario 3
(Wet season, spring tide, H_s =1.5 m, T_s =3.8 s, from SW)

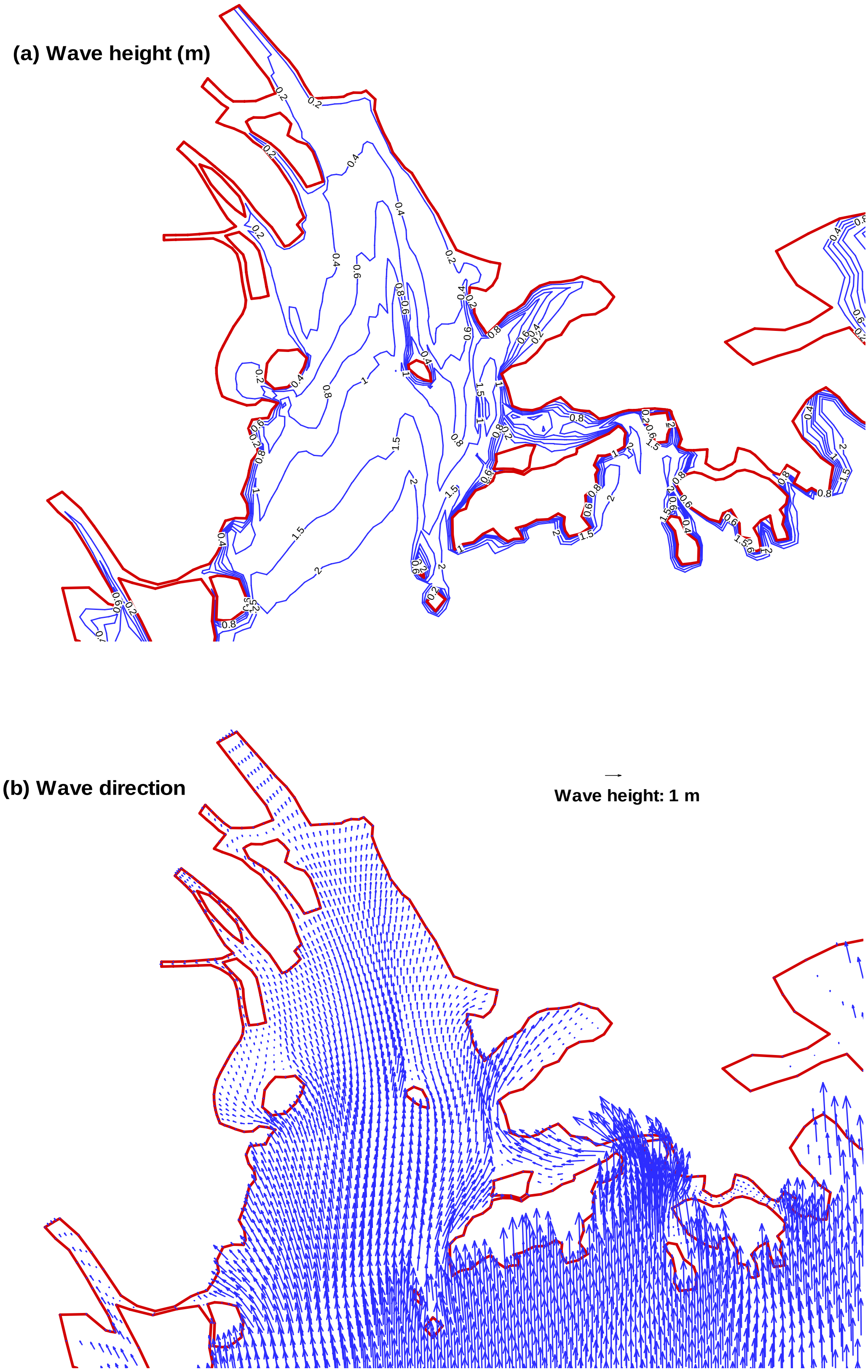

Fig. 7.9 Simulated wave heights and directions of Scenario 4
(Wet season, spring tide, H_s =2.5 m, T_s =3.8 s, from S)

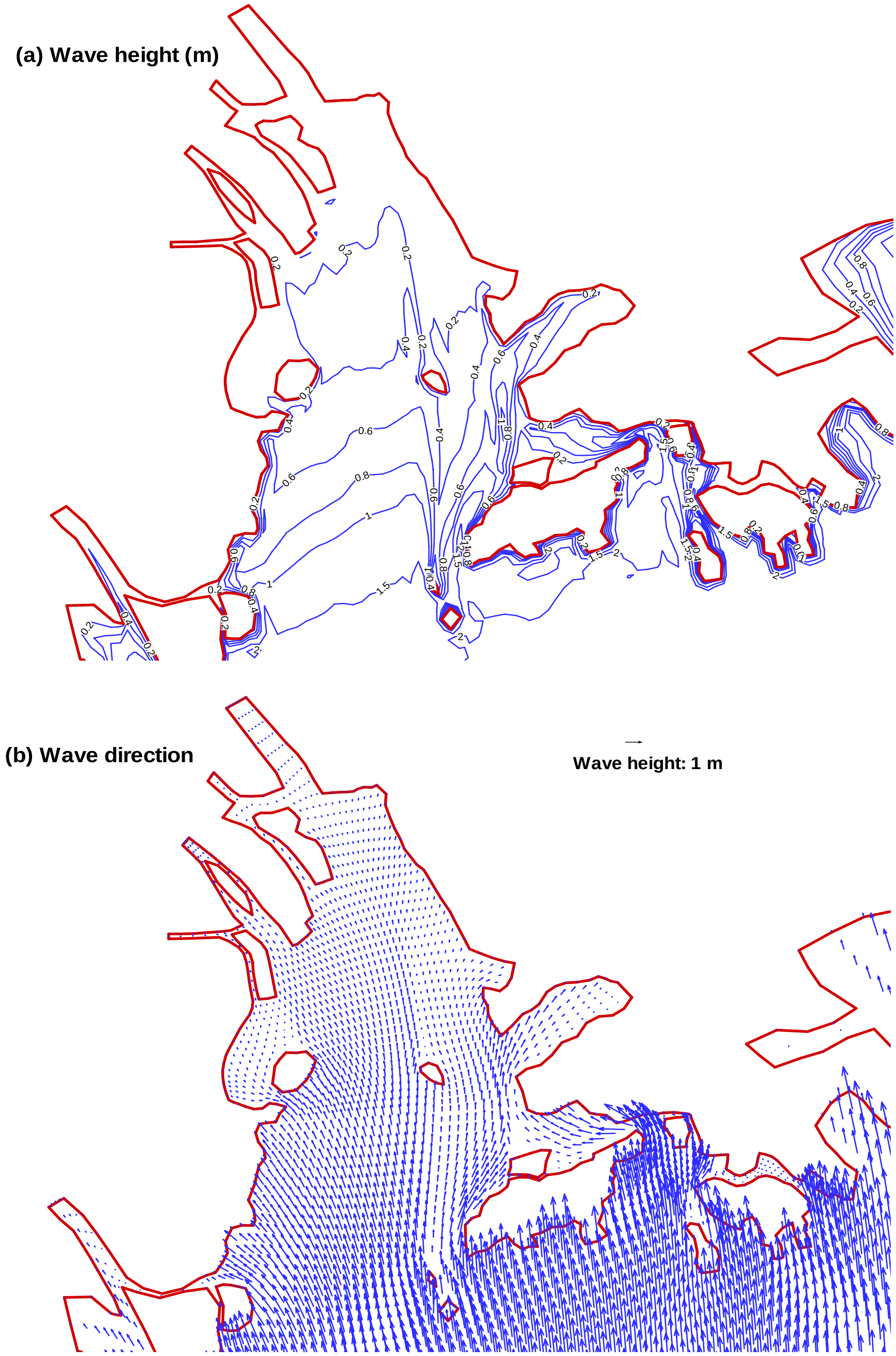

Fig. 7.10 Simulated wave heights and directions of Scenario 5
(Wet season, spring tide, H_s =2.5 m, T_s =8.0 s, from S)

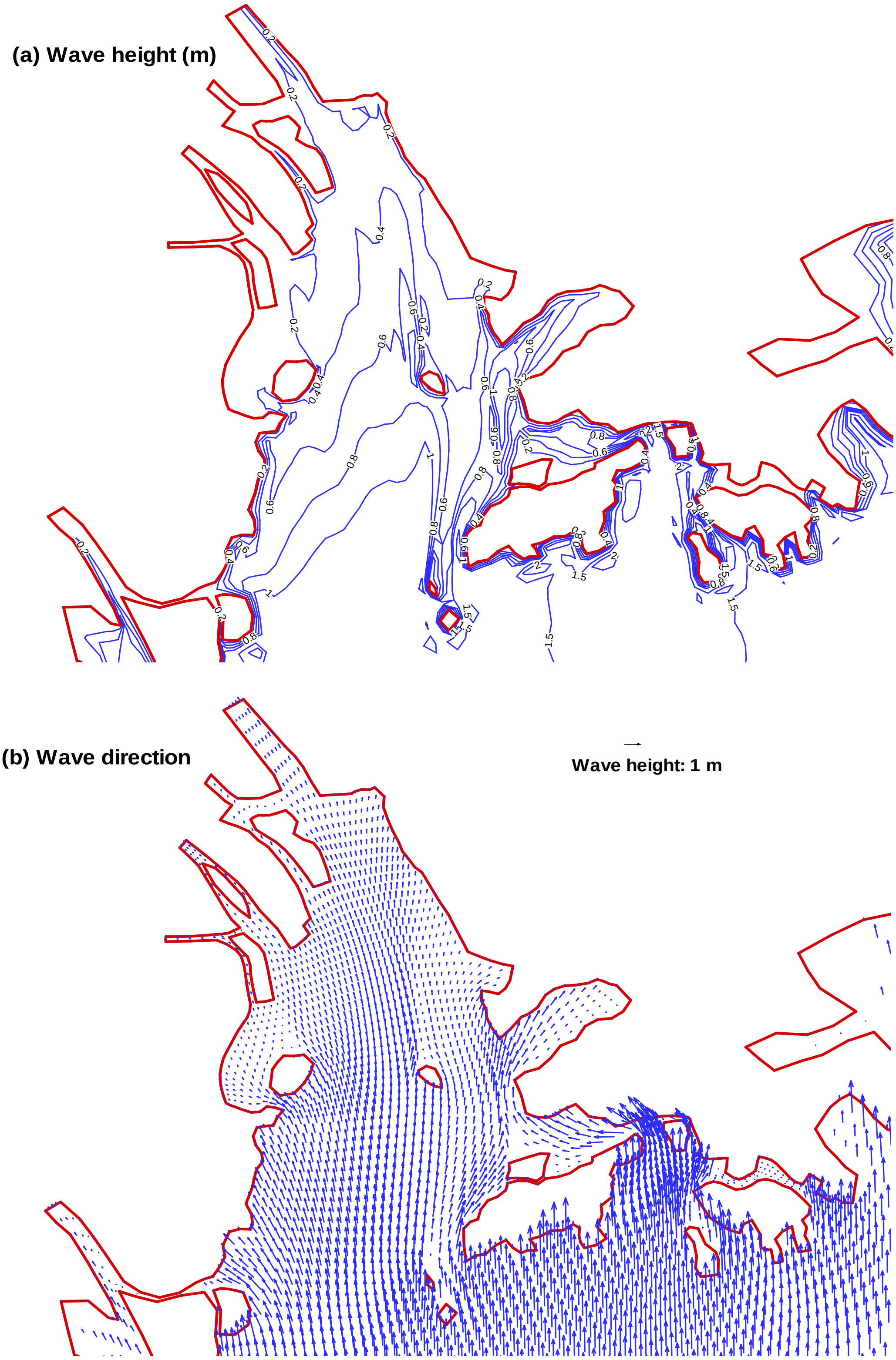

Fig. 7.11 Simulated wave heights and directions of Scenario 6
(Wet season, neap tide, H_s =1.5 m, T_s =3.8 s, from S)

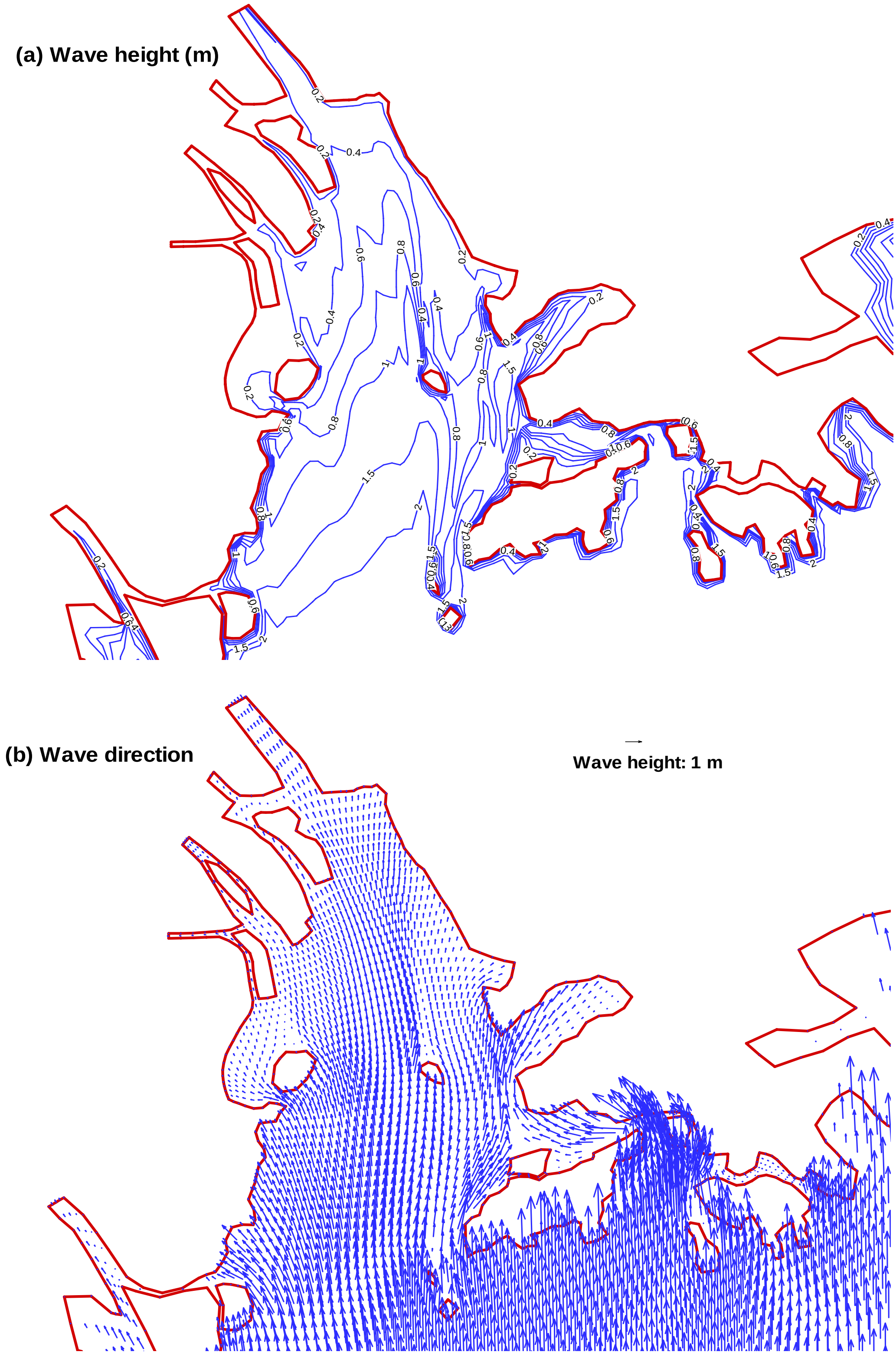

Fig. 7.12 Simulated wave heights and directions of Scenario 7
(Wet season, neap tide, H_s =2.5 m, T_s =3.8 s, from S)

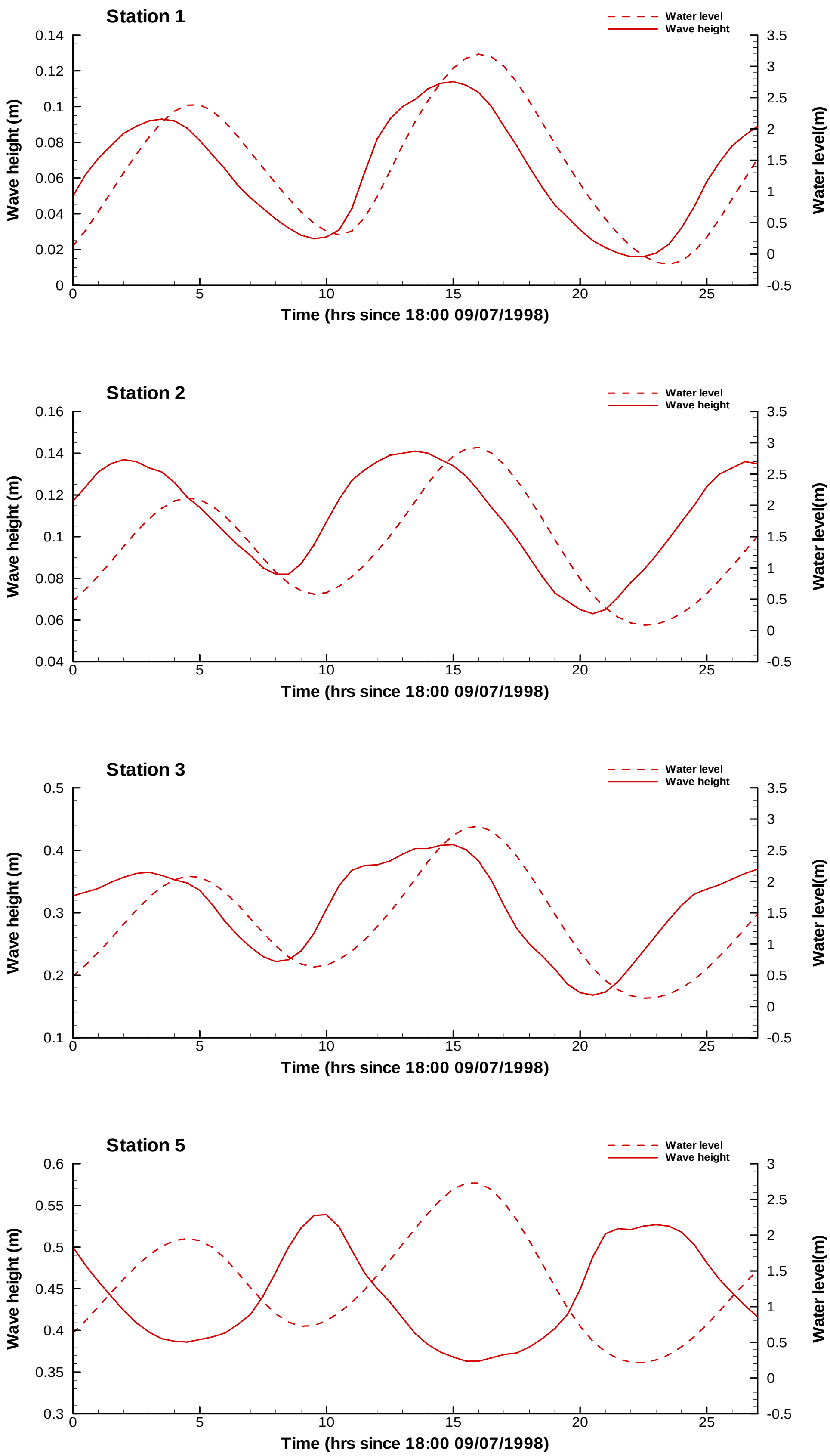

Fig. 7.13 Time series of computed wave height at stations 1 to3 and 5 (Scenario 5)

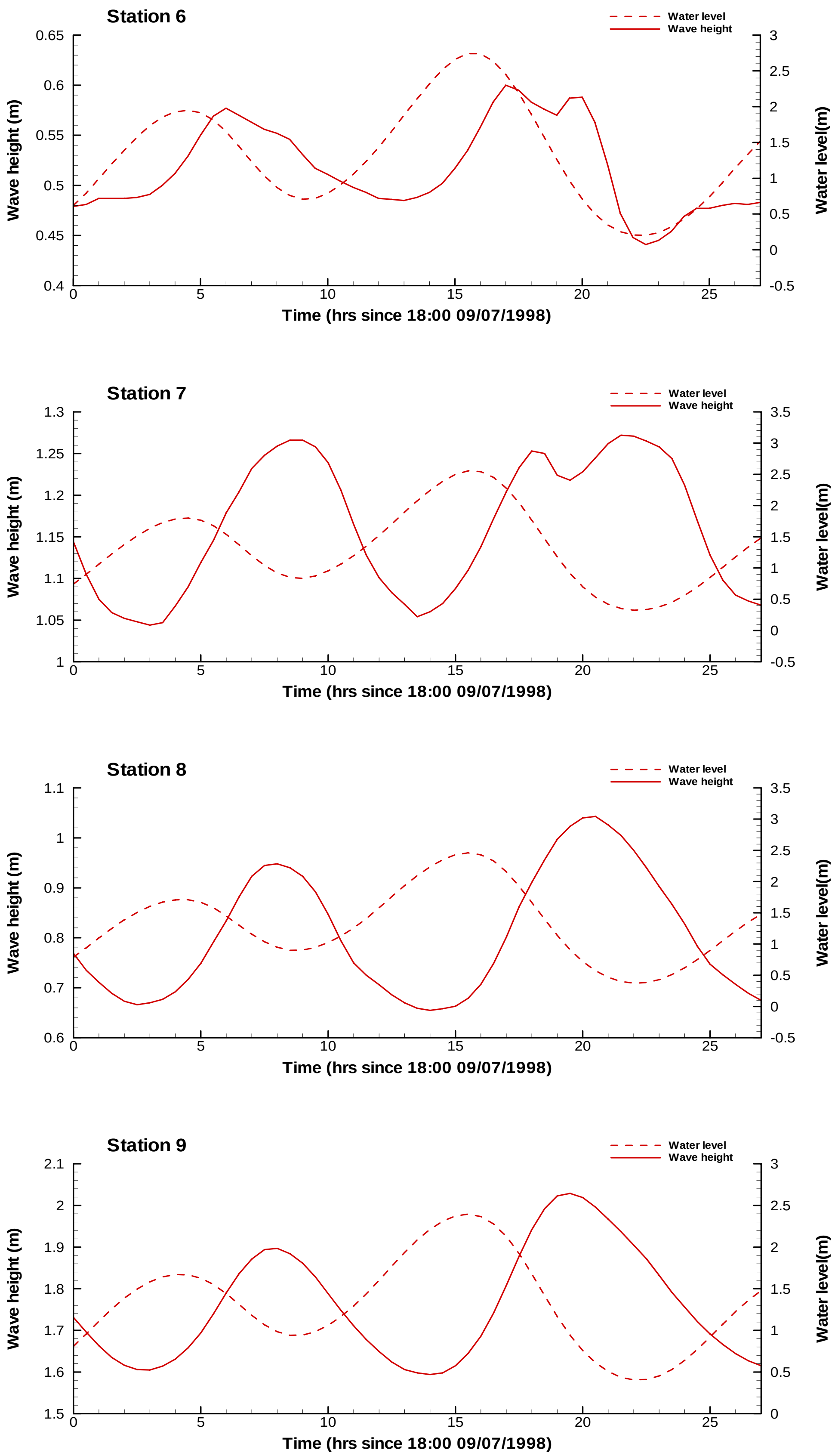

Fig. 7.14 Time series of computed wave height at stations 6 to 9 (Scenario 5)

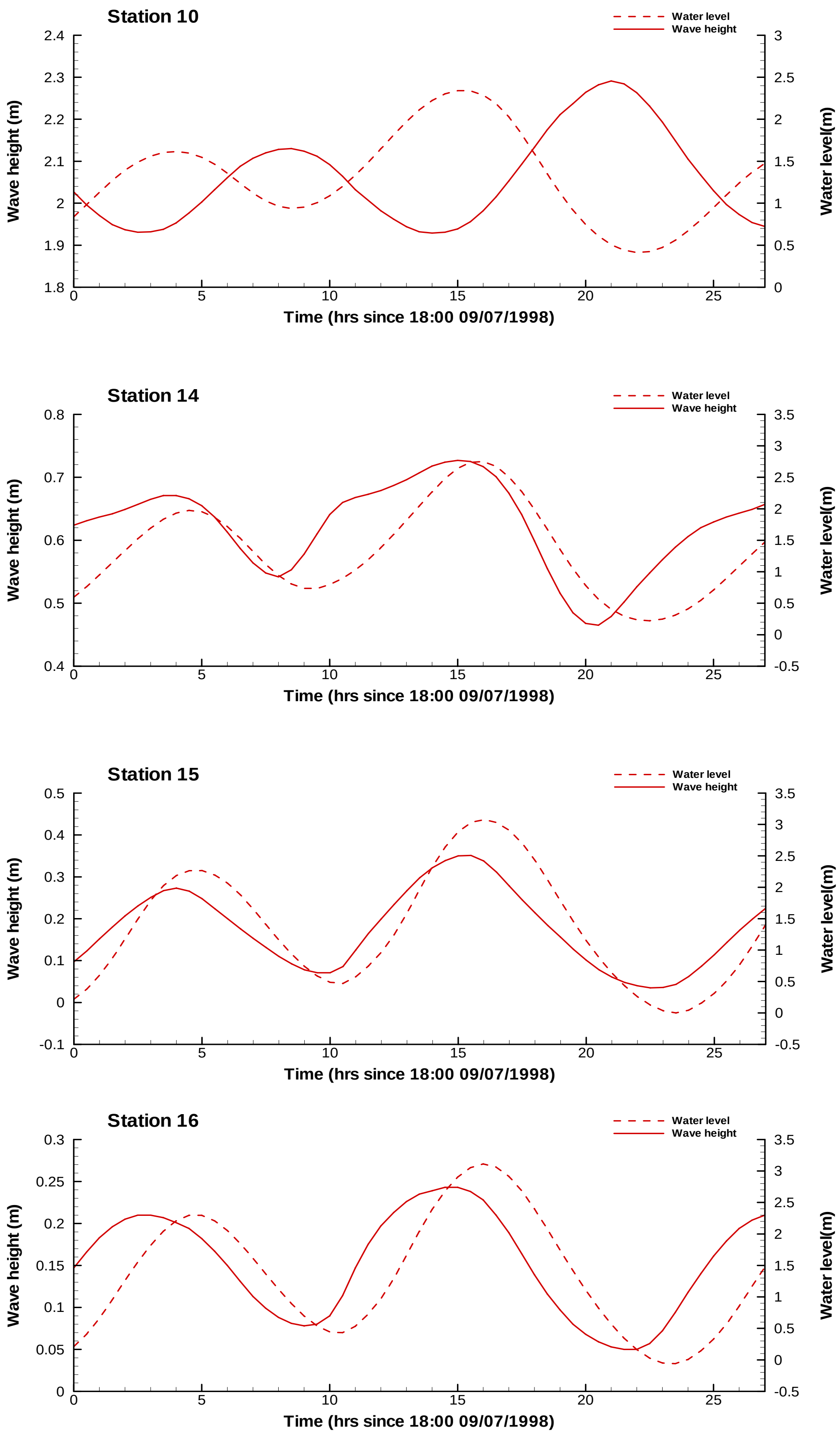

Fig. 7.15 Time series of computed wave height at stations 10, 14 to 16 (Scenario 5)

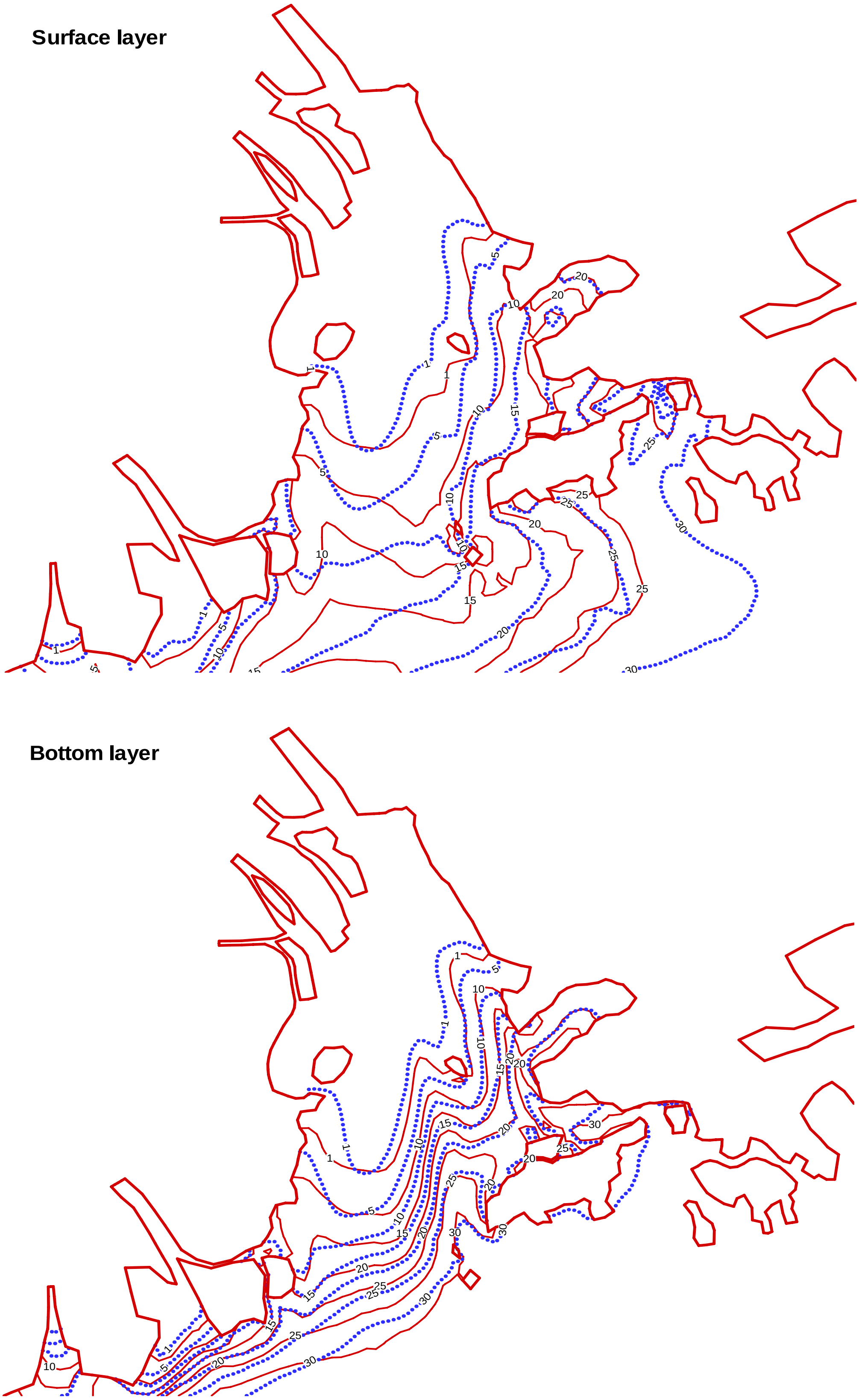

Fig. 7.16 Contours of tidally averaged salinity induced by wave and current (Scenario 2, solid lines) and current only (dots)

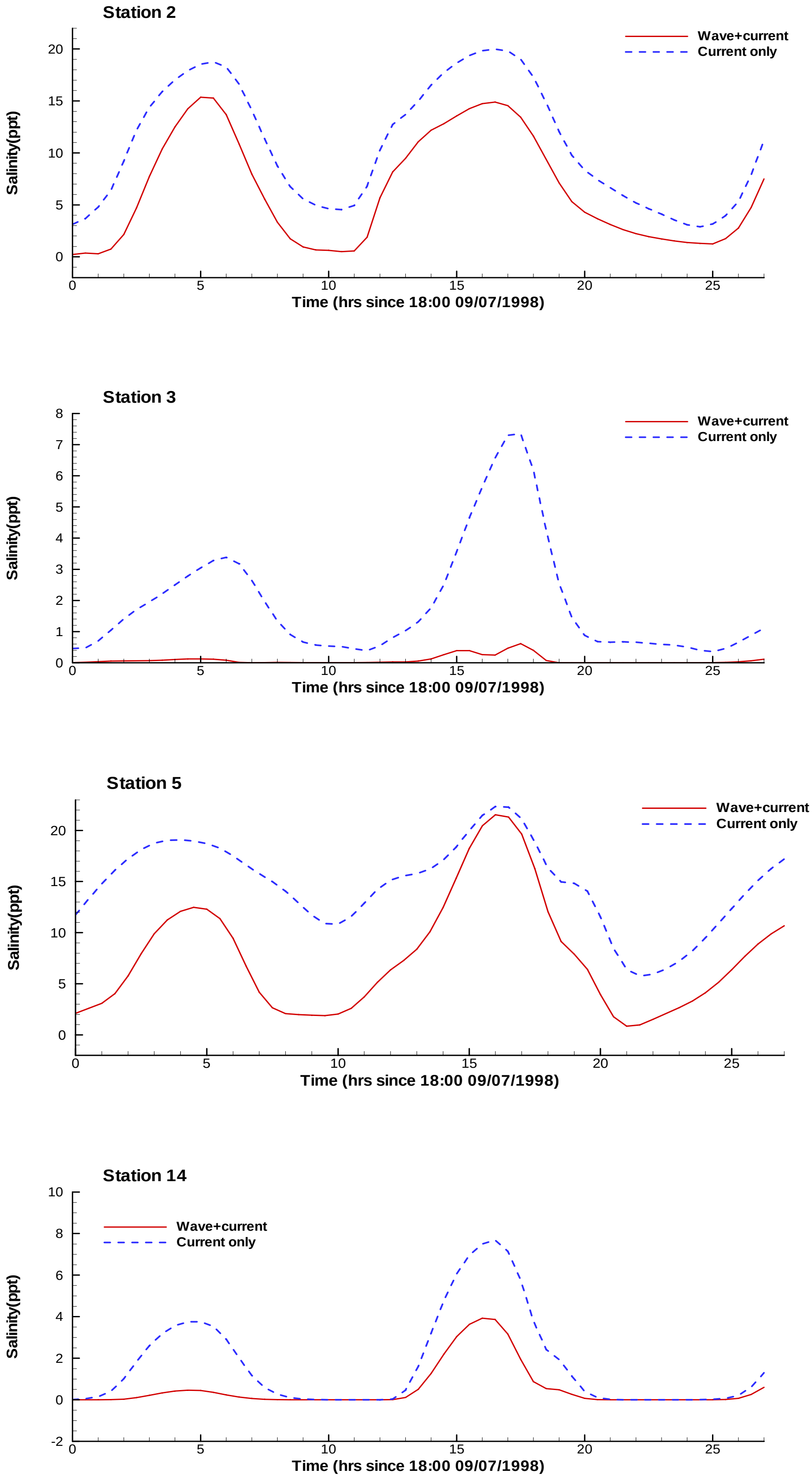

Fig. 7.17 Time series of near bed salinity induced by wave and current (Scenario 2, solid lines) and current only (dash lines)

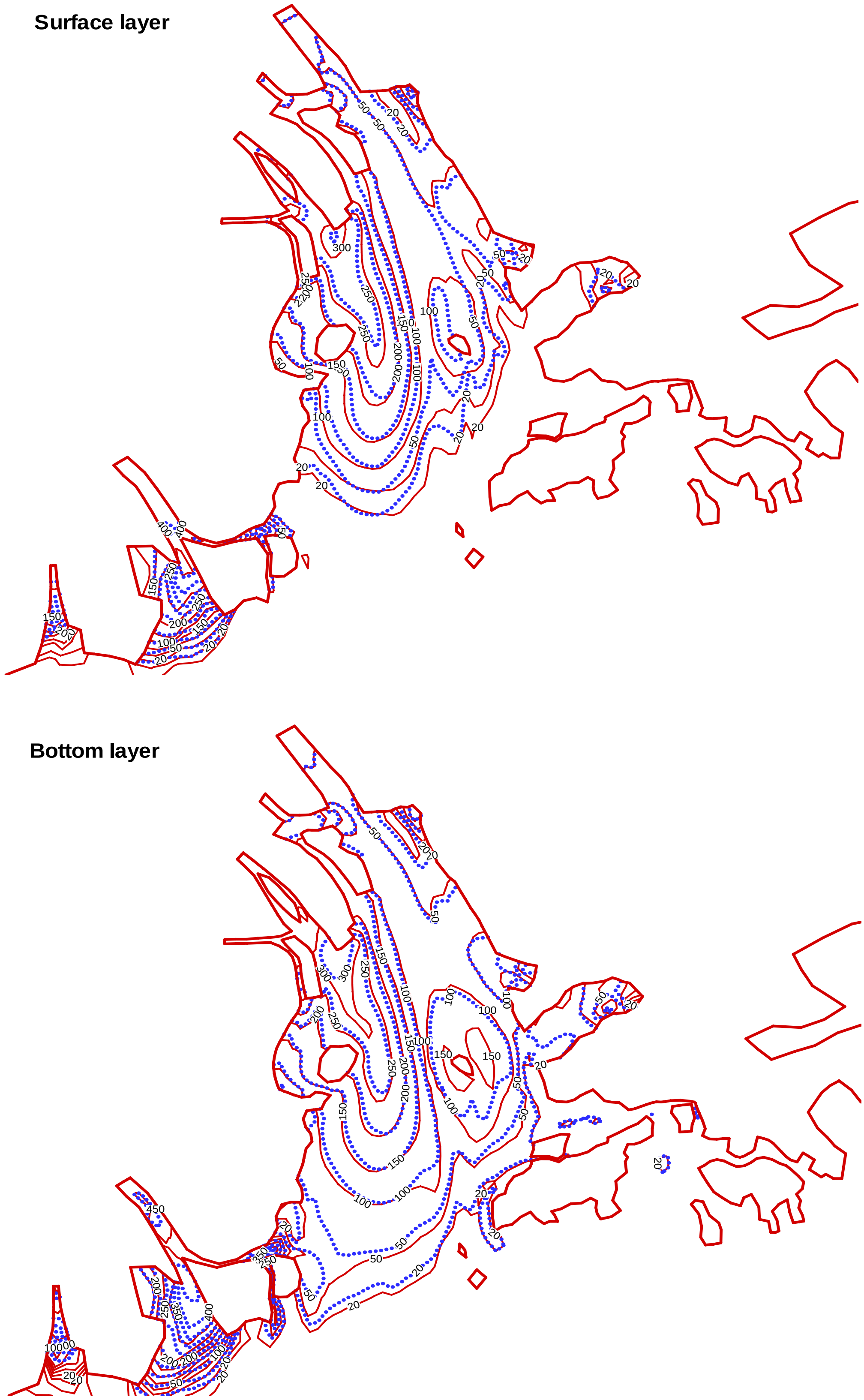

Fig. 7.18 Contours of tidally averaged sediment concentration induced by wave and current (Scenario 2, solid lines) and current only (dots)

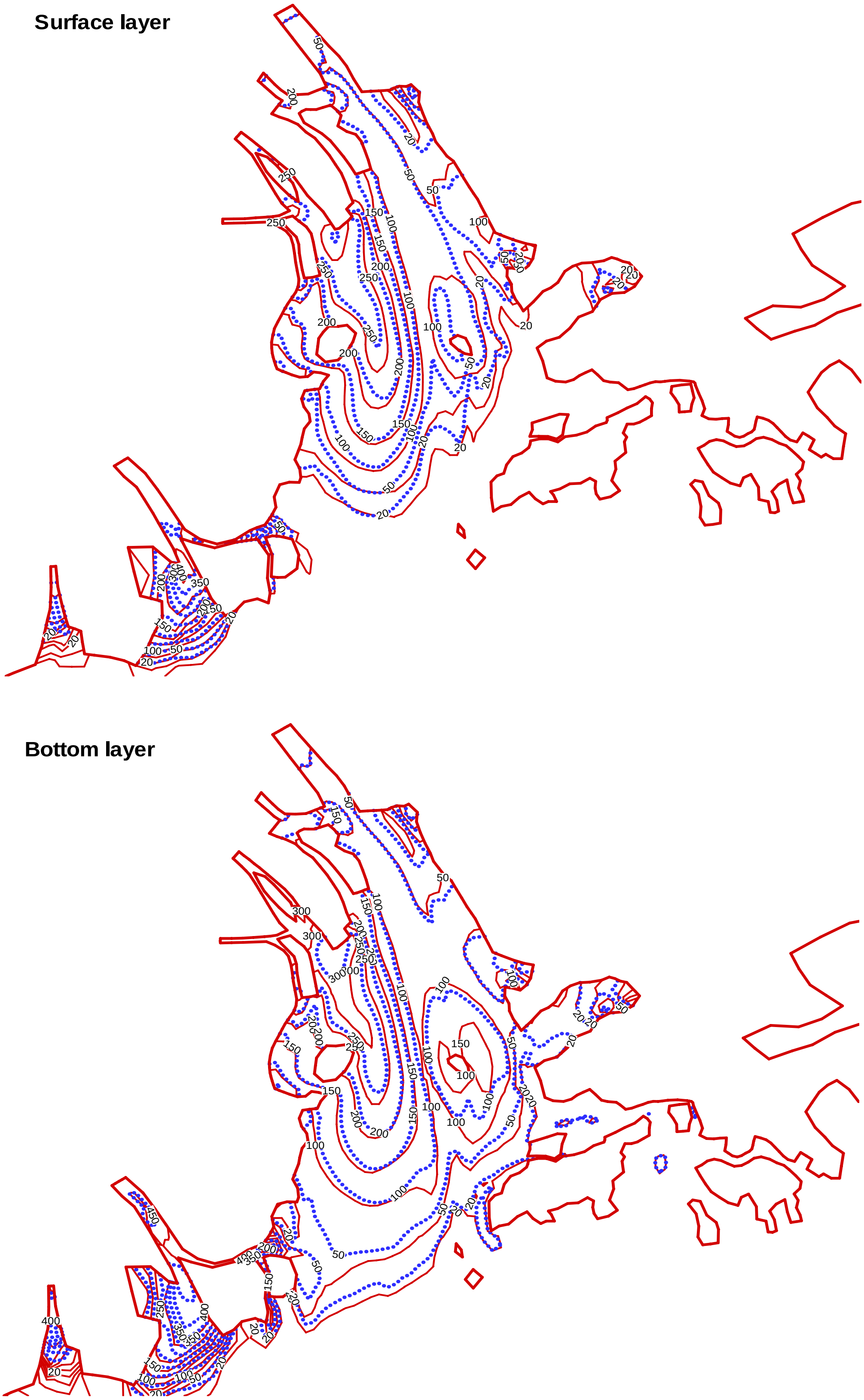

Fig. 7.19 Contours of tidally averaged sediment concentration induced by wave and current (Scenario 4, solid lines) and current only (dots)

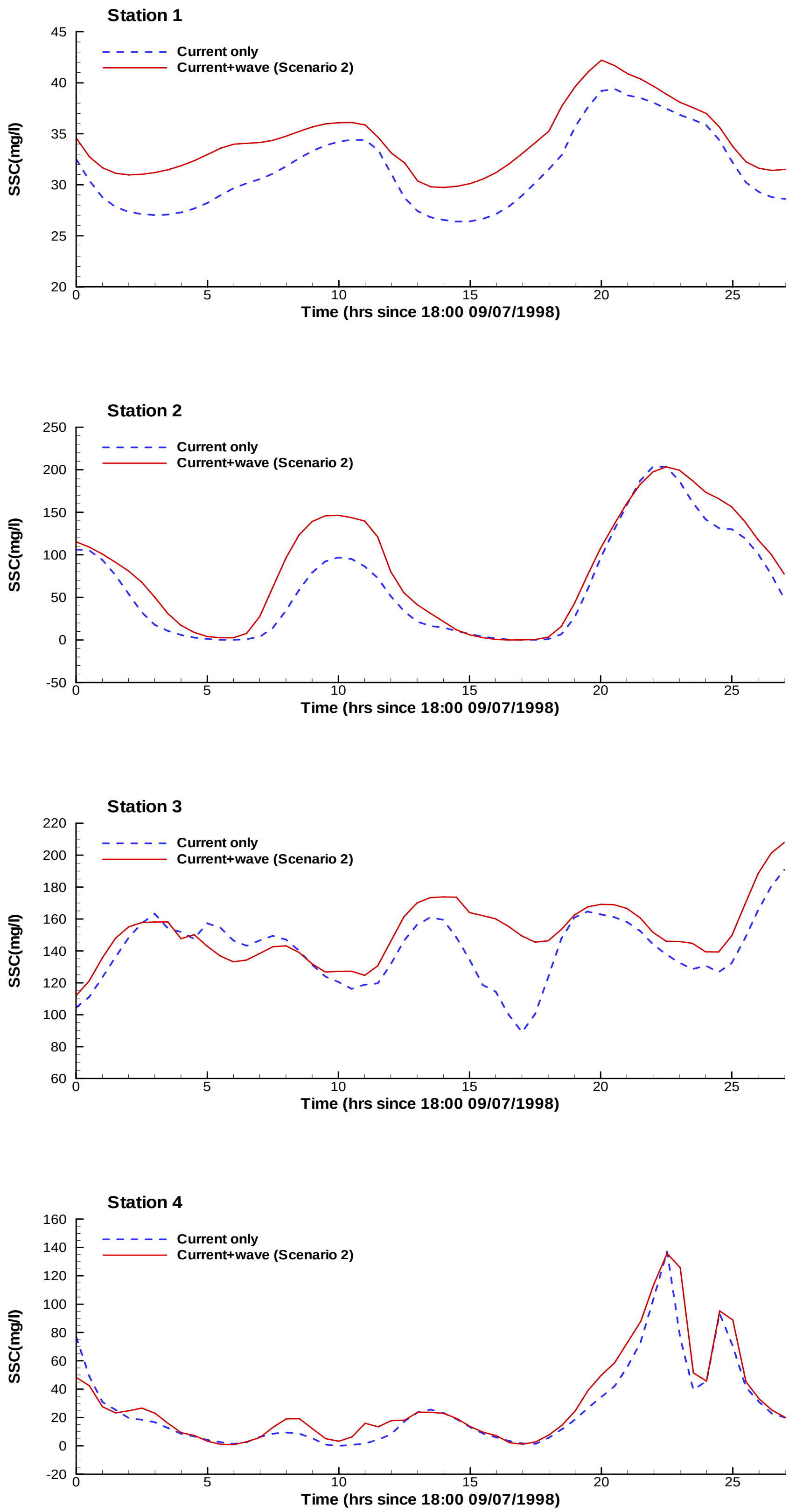

Fig. 7.20 Time series of near bed sediment concentration induced by wave and current (Scenario 2, solid lines) and current only (dash lines) at stations 1 to 4

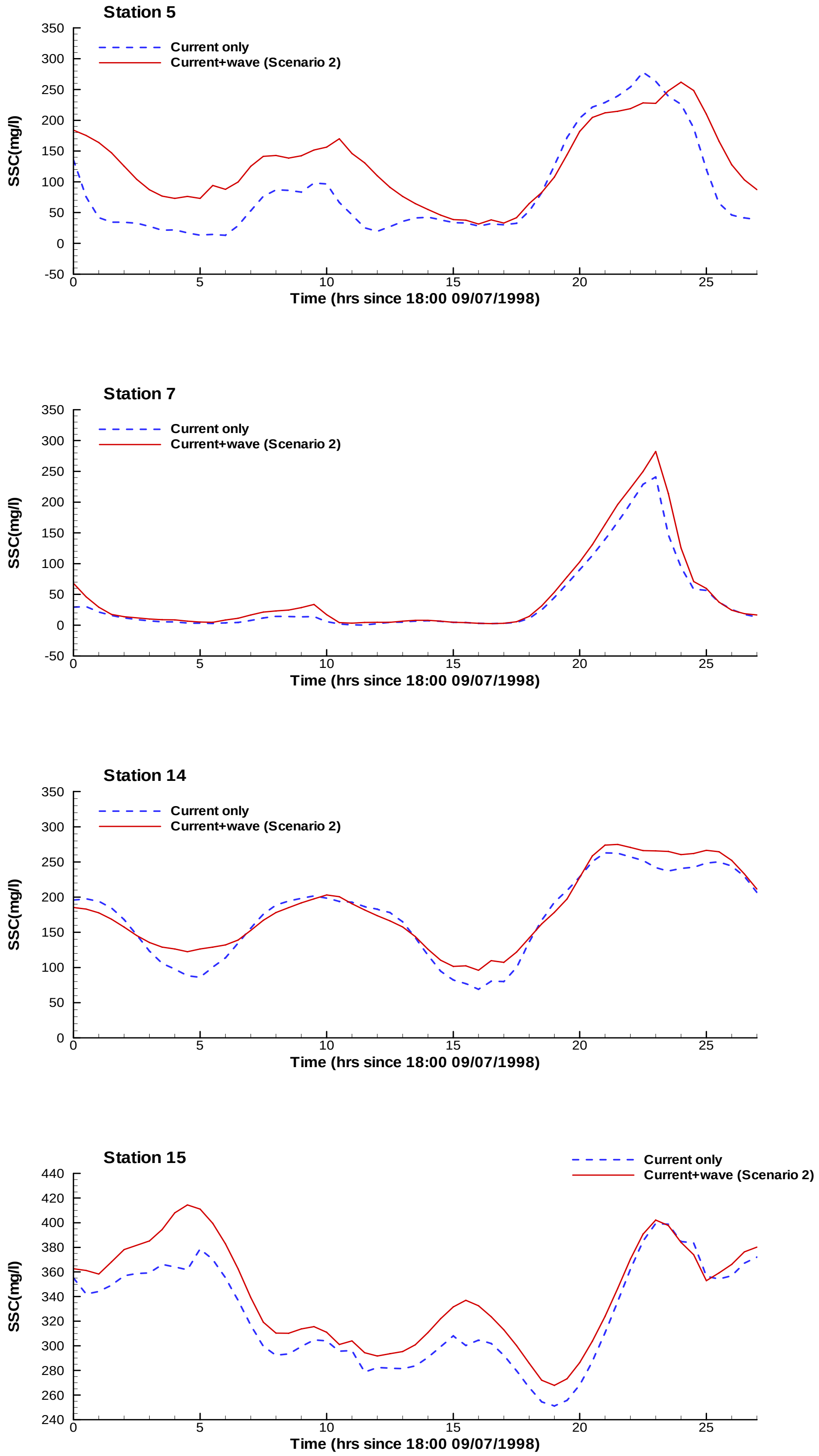

Fig. 7.21 Time series of near bed sediment concentration induced by wave and current (Scenario 2, solid lines) and current only (dash lines) at stations 5,7,14 and 15

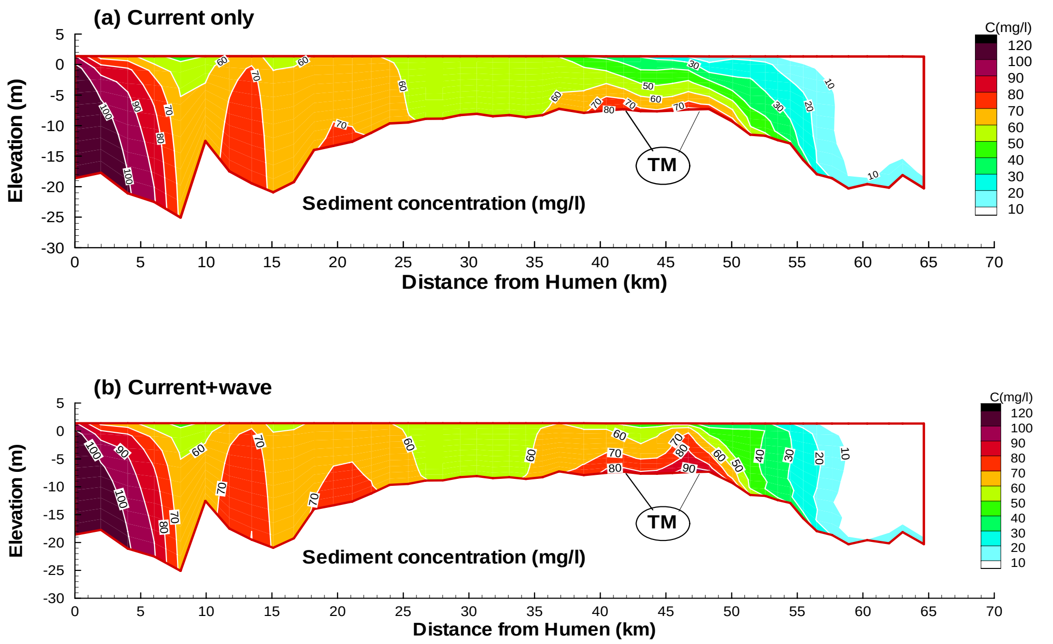

Fig. 7.22 Tidally averaged profiles of sediment concentration along the East Channel induced by wave and current (Scenario 2) and current only in a spring tide in the wet season

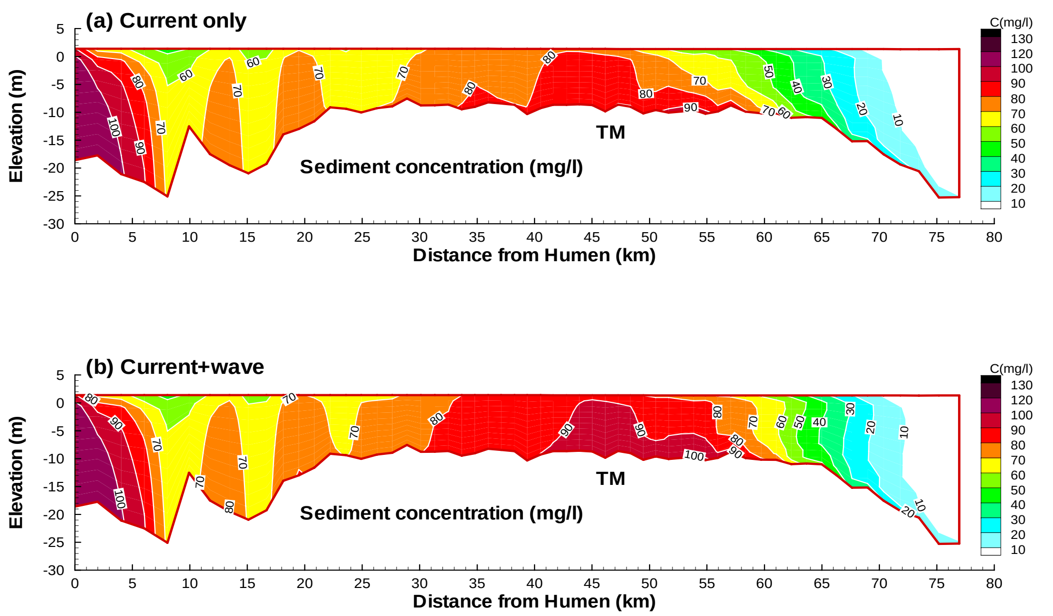

Fig. 7.23 Tidally averaged profiles of sediment concentration along the West Channel induced by wave and current (Scenario 2) and current only in a spring tide in the wet season

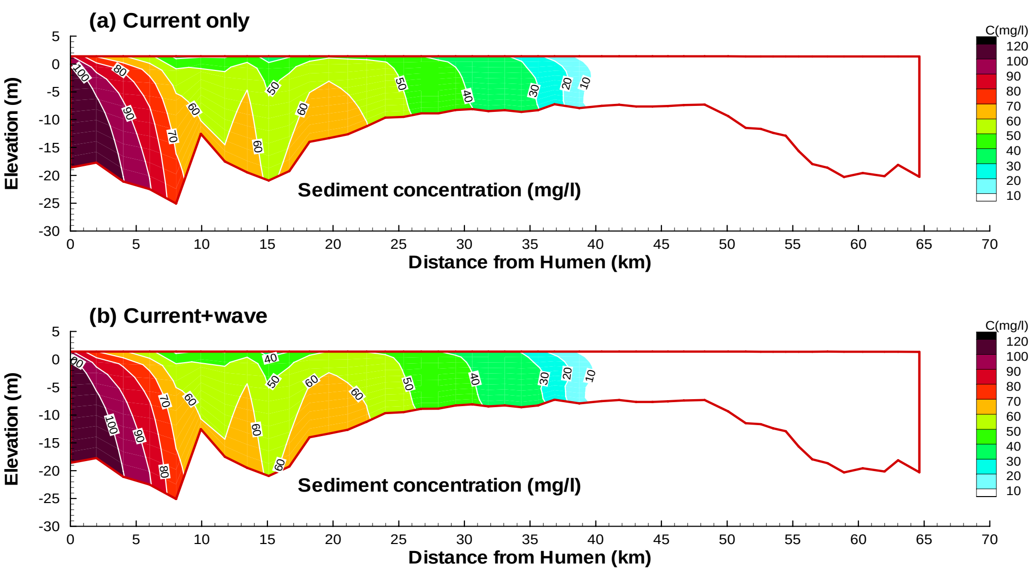

Fig. 7.24 Tidally averaged profiles of sediment concentration along the East Channel induced by wave and current (Scenario 6) and current only in a neap tide in the wet season

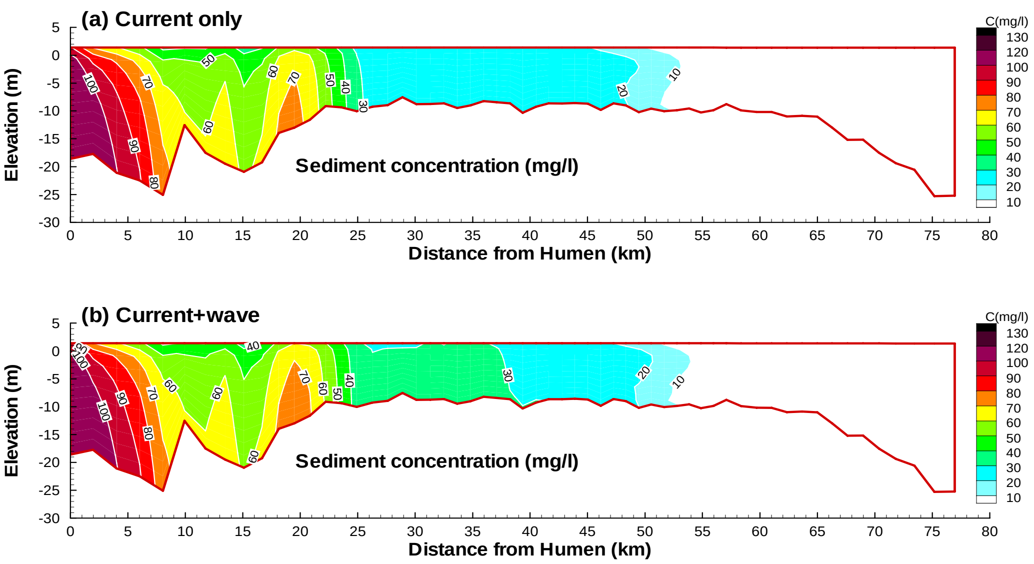

Fig. 7.25 Tidally averaged profiles of sediment concentration along the West Channel induced by wave and current (Scenario 6) and current only in a neap tide in the wet season

CHAPTER 8

CONCLUSIONS AND RECOMMENDATIONS

8.1 Conclusions

The main objectives of this research are to understand the hydrodynamics and sediment transport characteristics of the Pearl River Estuary, to analyze the formation mechanisms of turbidity maximum, to develop a 3D hydrodynamics and sediment transport model, and to couple it with a wave model to study the formation and development processes of turbidity maximum under the interaction of both wave and current. After the systematic data analysis and a series of numerical modelling by 2D and 3D models on the hydrodynamics and sediment transport in the Pearl River Estuary, the conclusions given in the following sections can be drawn.

8.1.1 Numerical models

8.1.1.1 2D hydrodynamics and mass transport model

Based on the work of Wai *et al*. (1996), a depth-integrated two-dimensional hydrodynamics and mass transport model was developed by simplifying the original multi-layer three-dimensional model. The governing equations in the model are solved in finite element meshes using an explicit temporal finite difference scheme. The concept of vertically-averaged sediment carrying capacity is introduced in the model to overcome the difficulties and uncertainty in using the near bed reference sediment concentration.

The computed tidal levels and currents are verified by numerous measurement data. The computed results are in good agreement with the field data, generally. The simulated sediment concentration pattern by this model is in qualitative agreement with that from a satellite image.

8.1.1.2 3D hydrodynamics and sediment transport model

The 2D model can only be used in waters with relatively simple bathymetry, and its results can not reveal the physical processes in the vertical direction. Hence, a 3D hydrodynamics and sediment transport model is developed based on the work of Wai and Lu (1998). The efficiency and accuracy of the original model are enhanced. The improved model has the following characteristics:

1) An operator splitting scheme is employed to solve the governing equations in which an explicit Eulerian-Lagrangian method is applied to the advection terms. The horizontal diffusion terms are discretized by an implicit finite element method and the vertical diffusion term is solved by the finite difference method.

2) An algorithm is introduced to generate linear equations, resulting in a matrix with symmetric, positive coefficients which can be much more efficiently solved than an asymmetric matrix.

3) The salinity conservation equation is solved, taken into account including the baroclinic terms due to the horizontal density gradient in

the governing equation. The range of applicability of the model is thus expanded to include highly stratified flows.

4) The fine cohesive sediment processes in estuaries, such as flocculation and flocs settling of fine sediment particles, are included in the model.

5) The Level 2.5 turbulence closure scheme is coupled with the Navier-Stokes equations, resulting in a more elaborated vertical turbulence structure, which is not only linked to the flow pattern, but is also influenced by the flow stratification caused by the vertical density gradient due to sediment concentration and salinity. The horizontal eddy viscosity is calculated from the Smagorinsky formula to overcome the problem of an under-estimated horizontal diffusivity from the turbulence closure, which is more reasonable than the constant diffusivity coefficient adopted in the original model.

The 3D model is validated comprehensively by tidal level, current, salinity and sediment concentration in a spring tide and a neap tide using field data obtained in July, 1998. Modelling results are in good agreement with measurements, generally. The 3D model can be used to simulate the fine cohesive sediment transport in a partially-mixed and highly stratified estuary, and it is also a useful tool for studying the formation and development processes of turbidity maximum in the Pearl River Estuary.

8.1.1.3 3D wave-current interaction model

A wave propagation model based on wave action conservation, developed by Chen (2001), is coupled with the 3D hydrodynamics and sediment model.

Applications in the Pearl River Estuary show that the coupled wave-current model can solve combined wave-current problems efficiently.

8.1.2 Hydrodynamics in the Pearl River Estuary

Modelling results show that: a) Tidal flow can penetrate more riverward along the East and West channels. However, in the west shoals, shallow water causes rapid dissipation of the tidal and wave energy. The flooding current is relatively weaker and the ebbing current is stronger due to the strong riverine runoff. b) The Eulerian residual current from non-tidal drift is the dominant force in the PRE. The maximum residual velocity is about 0.3 m/s and the direction of the residual flow is consistent with the direction of tidal flooding and ebbing. c) The Stokes drift velocity is less than 0.05 m/s, but it is an important source of power to drive the mass transport from the open sea. d) The effect of Coriolis force on magnitude of tidal current is insignificant. However, Coriolis force will drive the ebbing flow and Eulerian residuals to the west. This is one of the important factors contributing to higher sediment concentration in west shoals. e) Monsoons in the PRE will influence Eulerian residuals significantly. In the wet season, wind from SW will reverse the direction of the Eulerian residual current from SW to NE when it flows out of Lingding Sea. In the dry season, because of the consistence of wind direction with the Eulerian residual flow, wind will enhance the Eulerian residual current, and this helps to transport more sediment through west shoals into the open sea.

8.1.3 Wave propagation in the Pearl River Estuary

Waves frequently propagate from the open sea into the Pearl River Estuary. The wave height in the open sea is relatively uniform. However, due to sheltering by islands and shoaling effects, wave heights are much smaller on the shoals and in the upper estuary. The wave height downstream of Neilingding Island is smaller than 0.8 m, while upstream of Neilingding Island it varies between 0.2 m and 0.4 m.

8.1.4 Salinity in the Pearl River Estuary

The pattern of salinity intrusion in the PRE changes semi-diurnally, fortnightly and seasonally with the tidal flooding and ebbing, the change from spring tide to neap tide and the variation of freshwater input between seasons.

Salt water intrudes along deep channels, with the wedge of salt water moving back and forth in a range of about 10-15 km. The head of the wedges can extend to the middle reach in the East Channel and to the upstream side of Neilingding Island in the West Channel during spring tide in the wet season. Most regions of the Pearl River Estuary are salty in the dry season, and the salt water can even intrude into the Humen channel.

The maximum difference of salinity within a tidal cycle could reach 15 ppt in the surface layer, and 25 ppt in the bottom layer. The location of the sharp changing zone is on the seaward side of sand bars in the East and West channels.

Wave propagation has little effect on the salinity and salt water intrusion in the Pearl River Estuary.

8.1.5 Sediment transport in the Pearl River Estuary

Characteristics of suspended sediment concentration are also investigated. Model results show that sediment concentration in the West Shoal is high due to the inputs from the Pearl River, the Coriolis force effect and local resuspension. Resuspension plays an important role within tidal cycles because of the surplus sediment-carrying capacity. Sediment concentration in deep channels is smaller than that in the nearby shoals.

Because of the horizontal distribution of sediment concentration, the turbid zones are located around the three western outlets and the middle shoal around Neilingding Island. Both sediment particles from the Pearl River, especially through the western three outlets, and from deposition and resuspension within tidal cycles are responsible for the sediment concentration patterns. Generally, the suspended sediment concentration in the Pearl River Estuary is lower in channels than in shoals, is lower in the East Channel than in the West Channel, and is lower during dry seasons than during wet seasons.

Wave-current action increases the sediment concentration in the Pearl River Estuary, mainly near the sand bars and in shoals. The magnitude of sediment concentration increase is not very high, about 10% over that by current alone.

8.1.6 Turbidity maximum in the Pearl River Estuary

The turbidity maximum in the Pearl River Estuary exists on shallow shoals and downstream of the outlets of the Pearl River. It occurs during spring tides and disappears during neap tides both in the wet season and dry season, and fully develops when ebbing during a spring tide in the wet season.

The turbidity maximum in the West Channel is located at the upstream limit of the wedge head of salt water intrusion. Because tidal flow is the dominant factor of salt water intrusion and the freshwater from the three western outlets stratifies the flow downstream of the wedge head, the turbidity maximum in the East Channel has two peaks of sediment concentration.

The turbidity maximum moves back and forth from the middle reach to the downstream reach of the sand bars in the main channels within tidal cycles with a cruising range of about 22 km in the wet season.

Wave-current interaction resuspends sediment particles to the upper water column, resulting in a broader and thicker center with higher sediment concentration in the turbidity maximum.

Sediment flux analyses based on the synchronous field survey conducted in 1978 show that gravitational circulation and tidal trapping are the principal formation mechanisms of the turbidity maximum located adjacent to the head of saltwater intrusion wedge. Turbidity maximum in the East Channel is mainly caused by the sediment resuspension and deposition processes. Gravitational circulation is the predominant formation mechanism of turbidity maximum in the West Channel. Numerical results confirm further that gravitational circulation, tidal pumping and resuspension are the main factors for the formation of the turbidity maximum in the Pearl River Estuary. Gravitational circulation and tidal pumping induce favourable hydrodynamic conditions to congregate sediment particles. Local resuspension is the main sediment source for the development of turbidity maximum. In the wet season, all the three factors play important roles in the formation of turbidity maximum in the West Channel. For the turbidity maximum in the East Channel, tidal pumping and gravitational circulation dominate the upstream and downstream peaks of sediment concentration, respectively. Local resuspension is the main cause of turbidity maximum formation in the dry season.

8.2 Recommendations for future work

Studying the turbidity maximum in the Pearl River Estuary is an interesting and meaningful work. However, it is also full of challenges. The irregular topography, coupled with complex hydrodynamic and hydro-meteorological conditions, create a lot of difficulties to the modeler. Furthermore, the scarcity of field data in this large water body and the insufficiency of background knowledge on sediment transport processes in the Pearl River Estuary make the study of turbidity maximum in the PRE even more difficult. The following aspects require further investigation.

1) The knowledge of fine cohesive sediment transport in the Pearl River Estuary should be improved, especially the cohesive sediment settling velocity, mechanism of flocculation, sediment carrying capacity, cohesive sediment critical threshold velocity and critical shear stress for erosion and deposition.

2) Further improvement of the stability of the wave model and incorporation of wind-induced waves.

3) More field data of tidal current, salinity, sediment concentration and wave should be collected to further verify the numerical model and analyze the sediment flux in the Pearl River.

4) The bathymetry near the Pearl River outlets should be updated. With the economy developing rapidly in the Pearl River Delta region in the past decades, the topography near the river outlets has been changed drastically by the numerous reclamation and hydraulic engineering projects.

5) The upstream river boundary in the model should be extended to eliminate the possibility of salt water intrusion crossing the model boundary. It is better to couple the 3D model of the estuary with a 1D model of the river system.

REFERENCES

Allen, G.P. (1973). “Etude des processus sedimentaires dans l’estuaire de la Gironde.” *These Doct. Sci. Nat.* Bordeaux. p. 314.

Allen, G.P., Salomon, J. C., Bassoulet, P., Du Penhoat, Y. and De Grandpre, C. (1980). “Effects of tides on mixing and suspended sediment transport in macrotidal estuaries.” *Sediment. Geol*., 26, pp. 69-90.

ASCE Task Committee. (1988). “Turbulence modelling of surface water flow and transport: Part 1 to 5.” *Journal of Hydraulic Engineering*, Vol. 114, No. 9, pp. 970-1073.

Bagnold, R.A. (1973). “The nature of saltation and of bed load transport in water.” *Proc. Royal Soc*., London, Ser. A, Vol. 332, pp. 473-504.

Balas, L. and Özhan, E. (2000). “An implicit three dimensional numerical model to simulate transport processes in coastal water bodies.” *International Journal of Numerical Methods in Fluids*, Vol. 34, pp. 307-339.

Balas, L. and Özhan, E. (2001). “Applications of a 3-D numerical model to circulation in coastal waters.” *Coastal Engineering Journal*, Vol. 43, pp. 99-120.

Balas, L. and Özhan, E. (2002). “Three-dimensional modelling of stratified coastal waters.” *Estuarine, Coastal and Shelf Science*, Vol.54, Issue1, pp. 75-87.

Berkhoff, J.C.W., Booij, N. and Radder, S.C. (1982). “Verification of numerical wave propagation models for simple harmonic linear water waves.” *Coastal Engineering*, Vol. 6, pp. 255-396.

Bi, O.H. and Sun, Z.L. (1984) “Primary study on the sediment processes in the Jiao Jiang Estuary.” *Journal of Sediment Research*. No. 3, pp.12-26. (in Chinese)

Bloss, S., Lehfeldt, R., and Patterson, J. C. (1988). ‘‘Modeling turbulent transport in stratified estuary.’’ J. Hydr. Engrg., ASCE, Vol. 114, No. 9, pp. 1115-1133.

Blumberg, A.F. and Mellor, G. A. (1987). “Description of a three dimensional coastal ocean circulation model.” In: Heaps NS, editor. *Three-dimensional Coastal Ocean Models*. Washington, DC: American Geophysical Union, pp. 1-16.

Blumberg, A.F., Galperin, B. and O'Connor, D.J. (1992). “Modeling vertical structure of open-channel flows.” *Journal of Hydraulic Engineering*, ASCE, No. 8, pp. 1119-1134.

Cao, Z.D and Wang, G.F. (1993). “Numerical modelling of sediment erosion by wave and sediment transport by tidal current.” *Acta Oceanologoca Sinica*, Vol. 15, No. 1, pp.111-118. (in Chinese)

Chen, Y., Wai, W.H.O., Li, Y.S. and Lu, Q.M. (1999). “Three-dimensional numerical modeling of cohesive sediment transport by tidal current in the Pearl River Estuary.” *International Journal of Sediment Research*, Vol. 14, No.2, pp.107-123.

Chen, Y. (2001). “Sediment transport by waves and currents in the Pearl River Estuary.” Ph.D. thesis, Department of Civil and Structural Engineering, The Hong Kong Polytechnic University, Hong Kong.

Chien, N. and Wan, Z.H. (1999). “Mechanics of sediment transport.” ASCE Press, Virginia, US.

Davesne, M., and Lepetit, J.P. (1980). “Dynamics of silt in estuary: residual currents or flocculation, which prevails?” *17th Int. Conf. on Coastal Engineering*, Sydney, pp. 338-339.

Dou, G.R. (1995). “The capacity to transport sand under wave and current.” *Chinese Science Bulletin*, Vol. 40, No. 5, pp. 443-446. (in Chinese)

Dronkers, J. (1986). “Tide-induced residual transport of fine sediment.” In *Physics of Shallow Estuaries and Bays*, ed. J. van de Kreeke, Springer, Berlin, pp. 228-244.

Dyer, K.R. (1986). “Coastal and estuarine sediment dynamics.” John Wiley & Sons Chichester. p. 342.

Dyer, K.R. (1988). “Fine sediment particle transport in estuaries.” In: *Physical Processes in Estuaries*, eds J. Dronkers and W. van Leussen, pp. 295-310, Springer, Berlin.

Dyer, K.R. (1989). “Sediment processes in estuaries: further research requirements.” *J. Geophysical Research*, Vol. 94, pp. 14327-14339.

Dyer, K.R. (1997). “Partially mixed and well-mixed estuaries. In: *Estuaries—A Physical Introduction.*” 2nd edition, pp. 136-164.

Dyer, K.R., Bale, A.J., Christie, M.C., Feates, N., Jones, S. and Manning, A.J. (2002). “The turbidity maximum in a mesotidal estuary, the Tamar Estuary, UK:II. The floc properties.” INTERCOH-2000, Elsevier, Fine sediment dynamics in the marine environment, *Proceedings in Marine Science*, ed. J.C. Vol. 5, pp. 219-232.

Einstein, H.A. and Krone, R.B. (1962). “Experiments to determine modes of cohesive sediment transport in salt water.” *J. G. Res.*, Vol. 67, No. 4.

Fan, S.J., Chieng, C.M. and Yu, Z.Y. (1999). “Resuspension and dispersion transport of cohesive fine-grained sediment in wave boundary layer.” *J. Sedi. Res*. No.2. (in Chinese).

Fang, C.M. (1998). “Cross section equilibrium in depth-integrated modeling of suspended sediment transport.” *Proceeding of the Seventh International Symposium on River Sedimentation*, Hong Kong, pp. 39-44.

Fennessy, M.J., Dyer, K.R. and Huntley, D.A. (1994). “Size and settling velocity distributions of flocs in the Tamar Estuary during a tidal cycle.” *Neth. Jour. Aquatic Ecology*, Vol. 28, pp. 275-282.

Festa, J.F. and Hansen, D.V. (1978). “Turbidity maximum in partially mixed estuaries: a two-dimensional numerical model.” *Estuarine, Coastal and Shelf Science*, Vol.7, pp. 347-359.

Fettweis, M., Sas, M. and Monbaliu J. (1998). “Seasonal, neap-spring and tidal variation of cohesive sediment concentration in the Scheldt Estuary, Belgium.” *Estuarine, Coastal and Shelf Science*, Vol. 47, pp. 21-36.

Fisher, H.B., List, E. J., Koh, R.C.Y. *et al*. (1979). “Mixing in inland and coastal waters.” Academic, San Diego, Calif.

Fredsøe, J. (1984). “Turbulent boundary layer in wave-current motion.” *J. Hydr. Engrg* ASCE, Vol. 110, No. 8, pp. 1103-1120.

Gelfenbaum, G. (1983). “Suspended-sediment response to semi-diurnal and fortnightly tidal variations in a mesotidal estuary: Columbia River, U.S.A.” *Marine Geology*, Vol. 52, pp. 39-57.

Geyer, W.R. (1993). “The importance of suppression of turbulence by stratification on the estuarine turbidity maximum.” *Estuaries*, Vol. 16, No. 2, pp. 113-125.

Gibbs, R.J., Tschudy, D.M., Konwar, L. and Martin, J.M. (1989). “Coagulation and transport of sediments in the Gironde Estuary.” *Sedimentology*, Vol. 36, pp. 987-999.

Glangeaud, L. (1938). “Transport et sedimentation clans l’estuairs et a l’embouchure de la Gironde.” *Bulletin of Geological Society of France*, Vol. 8, pp. 599-630.

Grant, W.D. and Madsen, O.S. (1979). “Combined wave and current interaction with a rough bottom.” *Journal of Geophysical Research*, Vol. 84, pp. 1797-1807.

Gross, E.S., Koseff, J.R. and Monismith, S.G. (1999). “Three-dimensional salinity simulation of South San Francisco Bay.” *Journal of Hydraulic Engineering*, ASCE, Vol. 125, No. 11, pp. 1199-1299.

Guan, W.B., Wolanski, E. and Dong, L.X (1998). “Cohesive sediment transport in the Jiaojiang River Estuary, China.” *Estuarine, Coastal and Shelf Science*, Vol. 46, pp. 861-871.

Hamblin, P.F. (1988). “Observations of suspended sediment flux over a tidal circle in region of the turbidity maximum of the upper St. Lawrence River Estuary, hydrodynamic and sediment dynamics of tidal inlet.” *Lecture Notes on Coastal and Estuarine Studies*, pp. 29,245-29,256.

Hamblin, P.F. (1989). “Observation and Model of Sediment Transport Near the Turbidity Maximum of the Upper Saint Lawrence Estuary.” *Journal of Geophysical Research*. Vol. 94, No. C10, pp. 14,419-14,428.

Han, N.B. and Lu, Z.Y. (1982). “Settling characteristics of sediments in the Yangtze River Estuary in salt water.” *Research paper of Nanjing Institute of Hydraulics*. (in Chinese)

Han, Q.W. and He, M.M. (1987). “One-dimensional model for reservoir sedimentation and fluvial processes.” *Journal of Sediment Research*, No.3, pp. 14-29. (in Chinese).

Han, Q.W. and He, M.M. (1990). “A mathematical model for reservoir sedimentation and fluvial processes.” *International Journal of Sediment Research.*

Hansen, D.V. and Rattray, M. (1966). “New dimensions in estuary classification.” *Limnol Oceanogr.*, Vol. 11, No. 3, pp. 319-326.

He, M.M. and Han, Q.W. (1989). “Concepts of size distribution for sediment carrying capacity and effective size distribution of bed materials.” *Journal of Hydraulic Research*, No. 3, pp. 7-26. (in Chinese)

He, M.M. and Han, Q.W. (1990). “Quantifying to size distribution for sediment carrying capacity and effective size distribution of bed materials.” *Journal of Hydraulic Research*, No. 3, pp. 1-12. (in Chinese)

He, S.L. (1983). “Analysis of the formation of deposition zones inside and outside the Ou Jiang Estuary.” *Acta Oceanologica Sinica.*, Vol. 5, No. 5, pp. 612-623. (in Chinese).

Huang, J.W. (1987). “Experiments of cohesive sediment settling velocity in still water.” *Journal of Sediment Research*, No. 2. (in Chinese).

Huang, J.W. (1989). “The experimental study of the scouring and settling properties of cohesive sediment.” *The Ocean Engineering*, Vol. 7, No. 1, pp. 61-70. (in Chinese).

Huang, Q.Z., Wang, W.Z. and Chen, J.C. (1994). “Tides, tidal currents and storm surge set-up of South China Sea.” *Oceanology of China Seas*, Edited by Zhou Di *et al*., Balkema, pp. 321-326.

Ippen, A. T. (1966). “Estuary and coastline hydrodynamics.” McGraw-Hill Book Company Inc., New York, pp52-61.

Ito, Y. and Tanimoto, K. (1972). “A numerical method of analysis of wave propagation – Application to wave diffraction and refraction.” *Proc. Conf. Coastal Engineering*, 13th, Chapter 26, pp. 503-522.

Jay, D.A. and Musiak J.D. (1994). “Particle trapping in estuarine tidal flows.” *J. Geophy. Res.* Vol. 99, No. C10. pp. 20,445-20,461.

Jewell, P.W., Stallard, R.F. and Mellor, G.L. (1993). “Numerical studies of bottom shear stress and sediment distribution on the Amazon continental shelf.” *J. Sedi. Petro.*, Vol. 63, No. 4, pp. 734-745.

Jiang, Y.W. (2003). “Three-dimensional numerical modelling of sediment and heavy metal transport in surface waters.” Ph.D. Thesis, Department of Civil and Structural Engineering, the Hong Kong Polytechnic University, Hong Kong.

Kawahara, M., Nakazawa, S., Ohmori, S., Hasegawa, K. and Tsunami (1978). “Wave propagation analysis by the finite element method.” *Finite Elements in Water Resources,* pp. 2131-2150.

Kranch, K. (1981). “Particulate matter grain-size characteristics and flocculation in a partially mixed estuary.” *Sedimentlogy*, Vol. 28, pp. 107-114.

Kranch, K. (1984). “Settling behavior of cohesive Sediment”. *Estuarine Cohesive Sediment Dynamics*.” Springer-Verlag Berlin Heidelberg New York Tokyo. Vol. 14, pp. 151-169.

Lang, G. *et al* (1989). “Data interpolation and numerical modeling of the mud and suspended sediment experiment”. *J. Geophysical Research*, 94, C10, pp. 14381-14394.

Large, G. and Pond, S. (1981). “Open ocean momentum flux measurements in moderate to strong winds.” *Journal of Physical Oceanography,* Vol. 11, pp. 324-336.

Larsen, J. and Dancy, H. (1983). “Open Boundary in short wave simulation – a new approach.” *Coastal Eng.* Vol. 7, No. 3, pp. 285-297.

Lavelle, J.W., Mofjeld, H.O. and Baker, E.T. (1984). “An in-situ erosion rate for a fine-grained marine sediment.” *J. Geophys. Res.*, Vol. 89, pp. 6543-6552.

Li, B.G., Xie, Q.C. and Xia, X.M. (1999). “Particle size distribution in the turbidity maximum and its responding to the tidal flow in Jiao Jiang Estuary.” *Journal of Sediment Research*, No. 1, pp. 18-26. (in Chinese)

Li, Y.S., Liu, S.X., Yu, Y.X. and Lai, G.Z. (1999). "Numerical modeling of Boussinesq equations by finite element method." *Coastal Engineering*, Vol. 37, pp. 97-122.

Li, Z.H., Nguyen, K.D., Brun-Cottan, J.D. and Martin, J.M. (1994). "Numerical simulation of the turbidity maximum transport in the Gironde Estuary (France)." *Oceanologica Acta*, Vol. 17, No. 5, pp. 479-500.

Lian, J.J. and Zhao, Z.D. (1998). "Cohesive sediment entrainment from soft muddy bed by waves." *J. Hydr. Engrg.* No. 8, pp. 47-51. (in Chinese).

Lick, W., Huang, H. and Jepsen, R. (1993). "Flocculation of fine-grained sediments due to differential settling." *J. Geographical Research*, Vol. 98, C. 6, pp. 10279-10288.

Lin, B.L. and Falconer, R.A. (1996). "Numerical modelling of three-dimensional suspended sediment for estuarine and coastal waters." *J. Hydr. Res.*, Vol. 34, No. 4, pp. 435-455.

Lin, B.L., and Falconer, R.A. (1997). "Three-dimensional layer-integrated modeling of estuarine flows with flooding and drying." *Estuarine, Coastal and Shelf Science*, Vol. 44, pp. 737-751.

Liu, J.J. (1992). "Sediment transport under the action of wave." *Proceeding, Symposium of Basic Sediment Movement Theory*, Beijing, pp. 145-177. (in Chinese)

Liu, W.C., Hsub, M.H. and Kuo, Y. (2002). "Application of different turbulence closure model for stratified tidal flows and salinity in an estuarine system." *Mathematics and Computers in Simulation*, Vol. 59, pp. 437-451.

Lu, Q. (1997). "Three-dimensional modeling of hydrodynamics and sediment transport with parallel algorithm." Ph.D. thesis, Department of Civil and Structural Engineering, The Hong Kong Polytechnic University, Hong Kong.

Lu, Q., and Wai, O. (1998). "An efficient operator splitting scheme for three-dimensional hydrodynamic computations." *International Journal of Numerical Methods in Fluids*, Vol. 26, pp. 771-789.

Martin, J.M., Mouchel, J.M. and Thomas, A.J. (1986). "Time concepts in hydrodynamics systems with an application to be in the Gironde estuary." *Mar. Chem*, Vol. 18, pp. 369-392.

Marin, F. (1999). "Velocity and turbulence distributions in combined wave-current flows over a ripple bed." *J. Hydr. Res.*, Vol. 37, No. 4, pp. 501-518.

Mehta, A.J. (1984). "Characterization of cohesive sediment properties and transport processes in estuaries. Estuarine cohesive sediment dynamics." *Lecture Notes in Coastal and Estuarine Studies*. Spring-Verlag Berlin Heidelberg New York Tokyo, No.14.

Mellor, G.L., and Yamada, T. (1982). "Development of a turbulence closure model for geophysical fluid problems." *Reviews of Geophysics and Space Physics*, Vol. 20 , No.4, pp. 851-875.

Mellor, G.L., Oey, L.Y. and Ezer, T. (1998). "Sigma coordinate pressure gradient errors and the seamount problem." *Journal of Atmospheric and Oceanic Technology*, Vol. 15, pp. 1122-1131.

Migniot, C. (1968). "Study on physical properties of various silt and its properties under flow dynamics." *La Houille Blanche*, No. 7.

Mimura, N. (1993). "Rates of erosion and deposition of cohesive sediment under wave action." *Nearshoal and Estuarine Cohesive Sediment Transport*, ed. by Mehta A.J., pp. 247-264.

Mitchell, S.B., West, J.J., Arundale, A.M.W., Guymer, I. and Couperthwaite, J.S. (1998). "Dynamics of the turbidity maximum in the Upper Humber Estuary System, UK." *Marine Pollution Bulletin*. Vol. 37, Nos. 3-7, pp. 190-205.

Nicholson, J. and O'Connor, B.A. (1986). "Cohesive sediment transport model." *J. Hydr. Engrg.*, ASCE, Vol. 112, No. 7, pp. 621-640.

Odd, N.V. and Owen, M.W. (1972). "A two-layer model of mud transport in the Thames estuary." *Proceedings ICE,* 7517S, pp. 175-205.

Oey, L.Y., Mellor, G.L. and Hires, R.I. (1985a). "A Three-dimensional simulation of Hudson-Raritan estuary. Part I. Description of the model and model simulations." *J. Phys. Oceanogr.*, Vol. 15, pp. 1676-1692.

Oey, L.Y., Mellor, G.L. and Hires, R. I. (1985b). "A three-dimensional simulation of the Hudson Raritan estuary. Part II: Comparison with observation." *J. Phys. Oceanogr.*, Vol. 15, pp. 1693-1709.

Oey, L.Y., Mellor, G.L., and Hires, R.I. (1985c). "A three-dimensional simulation of the Hudson Raritan estuary. Part III: Salt flux analyses." *J. Phys.Oceanogr.*, Vol. 15, pp. 1711-1720.

Officer, C.B. (1980). "Discussion of the turbidity maximum in partially mixed estuaries." *Estuarine Coastal Mar. Sci*., Vol. 10, pp. 239-246.

Officer, C.B. and Nichols, M.M. (1980). "Box model application to a study of suspended sediment distributions and fluxes in partially mixed estuaries." *Estuarine Perspectives*, pp. 329-340.

Office, C.B. (1981). "Physical dynamics of estuarine suspended sediments." *Marine Geology*, Vol. 40, pp.1-14.

Orton, P.M. and Kineke, G.C. (2001). "Comparing calculated and observed vertical suspended-sediment distributions from a Hudson River Estuary turbidity maximum." *Estuarine, Coastal and Shelf Science*, Vol. 52, pp. 401-410.

Owen, M.W. (1975). "Erosion of aronmouth mud hydraulics research station." *Report INT*, p. 150.

Pan, D.A., Shen, H.T. and Mao, Z.C. (1999). “Formation mechanisms and characteristics of the turbidity maximum in the Changjiang Estuary.” *Acta oceanologica sinica.* Vol. 21, No. 4, pp. 62-69. (in Chinese)

Pang, C.G., Yang, Z.S., Zhang, J. and Lei, K. (2000). “Characteristics and the temporal and spatial variation of the turbidity maximum in the Yellow River Estuary.” *Journey of Oceanography of Huanghai and Bohai Seas*. Vol. 18, No. 3, pp. 1-6. (in Chinese).

Parthenaides, E. (1962). “A study of erosion and deposition of cohesive soils in salt water.” Ph.D. thesis. University of California, Berkeley, 182p.

Pickens, K., Chroneer, Z., Patel, P. and Lick, W. (1993). “The formation of a turbidity maximum in an estuary.”. *J. Great Lakes Res.*

Postma, H. (1967). “Sediment transport and sedimentation in the estuarine environment.” In G.H.Lauff (ed.), *Estuaries*. American Association for the Advancement of Science. Washington, D.C. ,pp. 158-179.

Qin, C.R. (1991). “Computation of bedload transport rate under the interaction of shallow water wave and tidal current.” *J. Hydr. Engrg.* No. 9, pp. 49-54. (in Chinese).

Rijn, L.C. van (1984). “Sediment transport, Part 2: Suspended load transport.” *J. Hydr. Engg*. ASCE. Vol. 110, No. 11, pp. 1,613-1,641.

Rijn, L.C. van (1986). “Mathematical modeling of suspended sediment in nonuniform flows.” *J. Hydr. Engg*. ASCE. Vol. 112, No. 6, pp. 433-455.

Rijn, L.C. van (1987). “Mathematical modeling of morphological processes in the case of suspended sediment transport.” Thesis presented to Delft University of Technology, at Delft, the Netherlands, in partial fulfillment of the requirements for the degree of Doctor of Philosophy.

Rijn, L.C. van (1990). “Field verification of 2-D and 3-D suspended-sediment models.” *J. Hydr. Engg*. ASCE. Vol. 116, No. 10, pp. 1,270-1,287.

Rodi, W. (1993). “Turbulence models and their application in hydraulics.” IAHR *Monograph Series*, Third Edition, The Netherlands.

Rouse, H. (1937). “Modern conceptions of the mechanics of fluid turbulence.” *Transactions of the American Society of Civil Engineers*, Vol. 102, pp. 463-541.

Sauvaget, P. (1987). “Modelisation numerique des ecoulements stratifies en estuaries et reservoirs.” These de docteur de 1’INPG, p. 173.

Schmitz (1996). “Turbidity maximum in the Weser Estuary.” Ph.D. thesis, University of Birmingham, UK.

Schubel, J.R. (1968). “Turbidity Maximum of the Northern Chesapeake Bay.” *Science*, Vol. 161, pp. 1013-1015.

Schubel, J.R. and Carter, H.H. (1984). “The estuary as a filter for fine-grained, suspended sediment.” In: *The Estuary as A Filter*, ed. V.S. Kennedy, Academic Press Inc, New York, pp. 81-105.

Shen, H.T. *et al.*, (1980). “The variation and formation causes of turbidity maximum in the Changjiang estuary.” *Proceedings of Research Results in the Changjiang Estuary*. Department of estuarine and coastal research, China Eastern Normal University. (in Chinese).

Shen, H.T., Li, J.F. and Zhu, H.F. (1986). “Sediment transport in the Yangtze River Estuary.” *Journal of Sediment research* , No. 1. (in Chinese)

Shen, H.T., He, S.L., Pan, D.A. and Li, J.F. (1992). “A study of turbidity maximum in the Yangtze river estuary.” *ACTA Geographic Sinica*. Vol. 47, No. 5, pp. 472-479. (in Chinese).

Shen, H.T, He, S.L., Mao, Z.C. and Li, J.F (2001). “On the turbidity maxima in Chinese estuaries.” *Journal of Sediment Research*, No. 1, pp. 23-29. (in Chinese).

Shen J., Shen H.T., Pan D.A. and Xiao C.Q. (1995). “Analysis of transport mechanism in turbidity maximum in the Yangtze River estuary.” *Acta Geographica Sinica*, Vol. 50, No. 5, pp. 411-419. (in Chinese)

Sheng, Y.P. and Lick, W. (1979). “The transport and resuspension of sediments in a shallow lake.” *J. Geophy. Res.*, Vol. 84, pp. 1809-1826.

Sheng, Y.P. and Villaret, C. (1989). “Modeling the effect of suspended sediment stratification on bottom exchange processes.” *J. Geophy. Res.*, AGU. Vol. 94, C10, pp. 14,429-14,444.

Shi, W.R. (1993). “Variation of turbidity maximum with tidal scale and its formation analysis in Yangtze River estuary.” *Acta Geographyca Sinica*, Vol. 48. No. 5, pp. 412-419. (in Chinese)

Shi, W.R. and Li, J.F. (1995) “Sediment resuspension in the Changjiang Estuary.” *International Journal of Sediment Research*, Vol. 10, No. 1, pp. 32-45.

Shi, Z. and Chen, W.S. (2000). “Sediment Processes of the Turbidity Maximum in North channel in Changjiang River estuary.” *J. Sediment Research*, No. 1, pp. 1-13. (in Chinese)

Shields, A. (1936). “Anwendung der Ahnlichkeitsmechanik und der Turbulenz-forschung auf die geschiebebewegung.” Mitt. Der Preuss. Versuchsanst. Fur Wasserbau und Schiffbau, Helf 26, Berlin, Germany.

Soulsby, R.L. (1993). “Modeling of Coastal Processes.” *Proc. 1993 MAFF Conf. of River and Coastal Engineering, Loughborough*, UK, pp. 111-118. Ministry of Agriculture, Fisheriers and Food, London, UK.

Soulsby, R.L. (1997). “Dynamics of Marine Sands.” *A Manual for Practical Applications.*

Su, J.L. and Wang, K.S. (1989) “The suspended sediment balances in Changjiang Estuary.” *Estuarine, Coastal and Shelf Science,* Vol. 23, pp. 81-98.

Sylaios, G. and Boxall, S.R. (1998). “Residual currents and flux estimates in a partially-mixed estuary.” *Estuarine, Coastal and Shelf Science*, Vol. 46, pp. 671-682.

Tang, C.B. (1963). “The law of sediment initiation.” *Journal of Hydraulic Engineering*, No. 2, pp. 1-12. (In Chinese)

Thorn, M.F.C. and Parsons, J.G. (1980). “Erosion of cohesive sediments in estuaries: An engineering guide.” *Proceedings, Third international Symposium on Dredging Technology*, paper F1.

Tian, X.P. (1986). “A Study on Turbidity Maximum in Lingdingyang Estuary of the Pearl River.” *Tropic Oceanology*, Vol. 5, No. 2, pp. 27-35. (in Chinese)

Tong, Z.Y. (1986). “Primary analysis of equilibrium between water and sediment, erosion and deposition in Lingding sea.” *Proceeding of Researches and Investigations of Coastal Researches in the Pearl River Estuary*, Guangzhou Science and Technology Press, 4, pp. 210-230. (in Chinese).

Uncles, R.J. and Jordan, M.B. (1979). “Residual fluxes of water and salt at two stations in the Severn estuary.” *Estuarine, and Coastal Marine Science*, Vol. 9, pp. 287-302.

Uncles, R.J., Elliott, R.C.A. and Weston, S. A. (1985a). “Dispersion of salt and suspended sediment in a partially mixed estuary.” *Estuaries* , Vol. 8, pp. 256-269.

Uncles, R.J., Elliott, R.C.A and Weston, S.A. (1985b). “Lateral distributions of water, salt and sediment transport in a partly mixed estuary.” *Proceedings of the Coastal Engineering Conference*, Vol. 3, pp. 3067-3077.

Uncles, R.J., Stephens, J.A., Woodrow, T.Y. (1988). “Seasonal cycling of estuarine sediment and contaminant transport.” *Estuaries.* Vol. 11, No. 2, pp. 108-116.

Uncles, R.J. and Stephens, J. A. (1989). "Distribution of suspended sediment at high water in a macrotidal estuary." *Journal of Geophysical Research*, Vol. 94, No. C10, pp. 14,395-14,405.

Uncles, R.J., Easton A.E., Griffiths, M.L., Harris C., Howland, R.J.M. King R.S., Morris A.W. and Plummer D.H. (1998). "Seasonality of the Turbidity Maximum in the Humber-Ouse Estuary, UK." *Marine Pollution Bulletin*, Vol. 37, Nos. 3-7, pp. 206-215.

Wai, W.H.O., Lu, Q.M. and Li, Y.S. (1996). "Multi-layer modeling of three-dimensional hydrodynamic transport processes." *Journal of hydraulic research*, Vol. 34, No. 5, pp. 677-693.

Wai, W.H.O. and Lu, Q. (1998). "An efficient operator splitting scheme for three-dimensional hydrodynamic computations." *International Journal of Numerical Methods in Fluids*, Vol. 26, pp. 771-789.

Wai, W.H.O. and Lu, Q.M. (1999). "Gradient-adaptive-sigma (GAS) grid for 3D mass-transport modeling." *J. Hydr. Engg.*, ASCE. Vol. 125, No. 2, pp. 141-151.

Wai, W.H.O. and Lu, Q.M. (2000). "An efficient parallel model for coastal transport process simulation." *Advances in Water Resources*, Vol. 23, No. 7, pp. 747-764.

Wang, C.H., Wai, W.H.O. and Li. Y.S. (2001). "Two-dimensional characteristics of hydrodynamics and sediment transport in the Pearl River Estuary." in: *Proceedings of XXIX IAHR Congress*, ed. Wang, Z.Y., Pettijean A. and Fisher R.K., pp. 396-401.

Wang, J.M., Yu, G.Y. and Chen, Z.Y. (1992). "Numerical modelling of tidal current in Lingding Sea PRE." *ACTA Oceanologiga Sinica*, Vol. 14, No. 2, pp. 26-34. (in Chinese)

Wellershaus, S. (1981). "Turbidity maximum and mud shoaling in the Weser Estuary." *Archiva Hydrobiologica*, Vol. 92, pp. 161-198.

Wells, J.T. and Kemp, G.P. (1994). “Interaction of surface waves and cohesive sediments: Field observations and geologic significance.” *Estuarine Cohesive Sediment Dynamics*, Springer-Verlag Berlin Heidelberg New York Tokyo. Vol. 14, pp. 43-65.

Wiegel, R.L. (1962). “Diffraction of waves by a semi-infinite breakwater.” *J. Hydraulics Div.*, ASCE, Vol. 88, No. HY1, pp. 27-44.

Winterwerp, J.C. and Kranenburg, C. (1997a) “Erosion of fluid mud layer. I: entrainment model.” *Journal of Hydraulic Engineering*, ASCE, Vol. 123, No. 6, pp. 504-511.

Winterwerp, J.C. and Kranenburg, C. (1997b). “Erosion of fluid mud layer. II: Experiments and model validation.” *Journal of Hydraulic Engineering*, ASCE, Vol. 123, No. 6, pp. 512-519.

Wu, Y., Falconer, R.A. and Uncles, R.J. (1998). “Modelling of wave flows and cohesive sediment fluxes in the Humber Estuary UK.” *Marine Pollution Bulletin*, Vol. 37, Nos. 3-7, pp. 182-189.

Xing, J. and Davies, A.M. (1996). “Application of turbulence energy models to the computation of tidal currents and mixing intensities in shelf edge regions.”, *J. Phys. Oceanogr*. Vol. 26, pp. 417-447.

Xu, J.L., Li, Y.X., Can, F. X and Chen, Q.D. (1985). “Evolution of channels and shoals in Lingding Sea, PRE.” Ocean Press, Beijing. (in Chinese).

Yalin, M.S. (1972). *Mechanisms of Sediment Transport*, Pergamon Press, Oxford.

Ying, Z. F, Luo, Z.R, Wu, C.Y., Chen, Z.X. and Wang, H.S. (1993). “Dynamic deposition environment and navigation channel selection in Lingding Sea.” *Study on coastal dynamic physiography and its application in harbor infrastructure in South China*, 1995, edited by Yang G.R *et al*., Zhongshan University Press, China. (in Chinese)

Zhang, R.J. (1963). “Discussion of gravitation theory and mechanism of sediment suspension.” *Chinese J. of Hydraulic Research*, Vol. 3, pp. 11-23. (in Chinese)

Zhou, H.J. (1992). “Characteristics of the turbidity maximum in the Changjiang River Estuary and 3-D hydrodynamic and sedimentation numerical model.” Ph.D. dissertation of the Ho Hai University, Nanjing, China.

Zhou, J.J. and Lin, B.N. (1998). “One-dimensional mathematical model for suspended sediment by lateral integration.” *Journal of Hydraulic Engineering*, Vol. 124, No. 7, pp. 712-717.

Zhu, J.R., Fu, D.J., Wu, H. and Qi, D.M. (2004). “Hydrodynamic models and numerical experiments of the formation of turbidity maximum.” *The Ocean Engineering*, Vol. 22, No. 1, pp. 66-73. (in Chinese).

Zhu, J.R., Qi, D.M., Xiao, C.Q. and Wu, H. (2004). “Impacts of change of river discharge on estuarine turbidity maximum zone.” *Acta oceanologica sinica.* Vol. 26, No. 5, pp. 12-22. (in Chinese).